

UNIVERSITY OF ICELAND

Ph.D. Dissertation

in Geophysics

Volcano-tectonic Controls on Ground Deformation across Temporal Scales: Insights from the Krafla Volcanic System, Iceland

Yilin Yang

January 2026

FACULTY OF EARTH SCIENCES

Volcano-tectonic Controls on Ground Deformation across Temporal Scales: Insights from the Krafla Volcanic System, Iceland

Yilin Yang

Dissertation submitted in partial fulfillment of a
Philosophiae Doctor degree in Geophysics

Ph.D. Committee
Freysteinn Sigmundsson
Halldór Geirsson
Joachim Gottsmann
Vincent Drouin

Opponents
Corné Kreemer
Raphaël Grandin

Faculty of Earth Sciences
School of Engineering and Natural Sciences
University of Iceland
Reykjavik, January 2026

Volcano-tectonic Controls on Ground Deformation across Temporal Scales: Insights from the Krafla Volcanic System, Iceland

Dissertation submitted in partial fulfillment of a *Ph.D.* degree in Geophysics

Copyright © 2026 Yilin Yang
All rights reserved

Faculty of Earth Sciences
School of Engineering and Natural Sciences
University of Iceland
Sæmundargata 2
102 Reykjavik
Iceland

Telephone: 525 4000

Bibliographic information:
Yilin Yang, 2026, Volcano-tectonic Controls on Ground Deformation across Temporal Scales: Insights from the Krafla Volcanic System, Iceland, Ph.D. dissertation, Faculty of Earth Sciences, University of Iceland.

Author ORCID: 0000-0001-8123-2257
ISBN: 978-9935-9877-0-9

Abstract

Measurements of ground movements in volcanic regions and interpretation of observed deformation is important for understanding of volcano behavior and their subsurface processes. Observed deformation often reflects the combined effects of multiple processes. The Krafla volcanic system in North Iceland lies at the divergent plate boundary between the North American and Eurasian plates. A rifting episode in 1975–1984, five decades of geothermal exploitation and extensive geodetic observations make Krafla an ideal natural laboratory to investigate volcano deformation across multiple temporal scales and explore underlying geophysical processes. For short-term deformation, a period of accelerated westward motion during 2014–2015 at Krafla is identified from Global Navigation Satellite System (GNSS) time series using Bayesian inference. These deformation anomalies occurred concurrently with the near-field precursors of the 2014 Bárdarbunga dike intrusion, ~120 km to the south, indicating potential coupling between volcanic systems along the rift. For the decadal deformation associated with the 1975–1984 rifting episode, a revised numerical model of repeated dike intrusions is developed to incorporate realistic dike geometries and crustal behavior. The model reproduces first-order regularities of the 1975–1984 dike sequence and highlights the critical role of tectonic stress and topography in driving lateral dike propagation, allowing magma flow into dikes or eruptions under low pressure. For long-term deformation, velocity fields derived from GNSS (2002–2024) and Interferometric Synthetic Aperture Radar (InSAR; 2015–2023) constrain a six-segment plate boundary model for central Krafla. The inferred plate boundary central axis follows recent eruptive fissures and aligns with mapped fracture orientations. Locking depth variation along the fissure swarm implies a dome-shaped rheological transition. Residual velocities reveal three local deflation patterns related to geothermal activity and lava subsidence. Together, these results advance understanding of volcano-tectonic interactions at divergent plate boundaries, while the methodological developments have broader practical value.

Útdráttur

Mælingar á jarðskorpuhreyfingum á eldvirkum svæðum og túlkun á mældri aflögun eru mikilvægar til að auka skilning á hegðun eldfjalla og ferlum sem eiga sér stað í rótum þeirra. Við túlkun á aflögun þarf að hafa í huga að mældar jarðskorpuhreyfingar stafa oft af samspili margra samverkandi ferla. Eldstöðvakerfi Kröflu liggur á flekaskilunum á milli Norður-Ameríku og Evrasíu flekanna í Norðurgosbelti Íslands. Sprungusveimur Kröflu og Krófluaskjan, tvö jarðhitasvæði, gliðnunartímabil 1975–1984, jarðhitanýting í fimm áratugi og yfirgripsmiklar mælingar á jarðskorpuhreyfingum gera Kröflu að hentugu rannsóknarsvæði til að rannsaka þau ferli sem valda eldfjallaaflögun. Í þessari ritgerð eru rannsakaðar jarðskorpuhreyfingar í Kröflu yfir mismunandi tímaskala til að kanna þau ferli sem valda jarðskorpuhreyfingum. Fyrir aflögun á stuttum tímaskala, þá var rannsakað tímabil aukinnar tilfærslu til vesturs árið 2014-2015 í Kröflu sem greint var í tímaröðum jarðskorpuhreyfinga sem ákvarðaðar voru út frá GNSS (Global Navigation Satellite System) landmælingum og svokölluðu Bayesísku líkindamati (e. Bayesian inference). Þessi frávik í jarðskorpuhreyfingum byrjuðu fyrir myndun kvikugangs í eldstöðvakerfi Bárðarbungu árið 2014, um 120 km sunnan við Kröflu, og áttu sér stað á sama tíma og fyrirboðavirkni mældist í og við Bárðarbungu. Þetta bendir til mögulegrar tengingar milli eldstöðvakerfi í Norðurgosbelti Íslands. Fyrir aflögunartímabil sem nær yfir áratug, þá voru rannsakaðar jarðskorpuhreyfingar sem urðu á gliðnunartímabilinu 1975-1984. Endurbætt reiknilíkan af endurteknum kvikugöngum sem myndast við lárétt flæði bergkviku í jarðskorpunni var þróað til að taka tillit til raunsærrar lögunar kvikuganga og hegðunar jarðskorpunnar. Líkanið endurskapar helstu reglubundna eiginleika kvikuganganna sem mynduðust 1975–1984. Það dregur fram mikilvægt hlutverk tektónísks spennusviðs og landslags í að knýja áfram lárétta útbreiðslu kvikuganga, sem gerir kviku kleift að flæða inn í ganga eða valda eldgosum við lágan þrýsting – jafnvel undir bergþyngdarþrýstingi (e. lithostatic pressure). Þegar kemur að langtímabreytingum eru hraðasvið, metin út frá GNSS gögnum (2002–2024) og bylgjuvíxlmælingum með ratsjárgervitunglum (e. Interferometric analysis of synthetic aperture radar satellite images, InSAR) (2015–2023), notuð til að ákvarða líkan af flekaskilum fyrir miðhluta eldstöðvakerfis Kröflu, skipt upp í sex búta. Ályktað er að ás flekaskilanna liggi þar sem nýlegar gossprungur eru og stefna hans sé í samræmi við kortlagðar sprungur. Læsingardýpi (e. locking depth) flekaskilanna er minnst, eða um 3.5 km undir Krófluöskjunni, og eykst í um 4,3 km til norðurs og í um 6.8 km til suðurs. Þessi breytileiki í læsingardýpi endurspeglar breytingar í efnishegðun jarðskorpunnar. Frávikshraðar sýna þrjú staðbundin samdráttarsvæði sem tengjast jarðhitavirkni og sigi hrauns. Niðurstöður ritgerðarinnar auka skilning á samspili eldvirkni og tektóníska ferla á flekaskilum, og þróun sem unnið var að í aðferðafræði hefur víðtækt hagnýtt gildi.

Table of Contents

List of Figures ..... **xi**

List of Publications ..... **xvii**

Abbreviations ..... **xix**

Variables ..... **xxi**

Acknowledgements ..... **xxv**

1 Introduction **1**
1.1 The Krafla Volcanic System 2
1.1.1 Tectonic Setting 2
1.1.2 Volcanic Activities 4
1.1.3 Geothermal Fields 5
1.2 Geodetic Measurements at the Krafla Volcanic System 6
1.2.1 Terrestrial Geodetic Techniques 7
1.2.2 Space Geodetic Techniques 10
1.3 Modeling Transient Deformation 19
1.3.1 GNSS Coordinate Time Series Analysis 20
1.3.2 Modeling Velocity Changes in Deformation Time Series 24
1.4 Modeling Dike Intrusions 26
1.4.1 Dike Initiation 27
1.4.2 Dike Propagation 28
1.4.3 Dike Sequence 31
1.5 Modeling Plate Boundary Deformation 32
1.5.1 Plate boundary deformation models 33
1.5.2 Global plate motion models 35
1.5.3 Regional plate boundary models for Krafla 36

2 Paper I: Joint Bayesian Modeling of Velocity Break Points, Noise Characteristics, and Their Uncertainties in GNSS Time Series: Far-Field Velocity Anomalies Concurrent with Magmatic Activity in Iceland **39**
2.1 Summary 39
2.2 Main Results 40

3 Paper II: Role of tectonic stress and topography on repeated lateral dikes: application to the 1975–1984 Krafla and 2023–2025 Svartsengi rifting episodes in Iceland **43**
3.1 Summary 43
3.2 Main Results 45

4 Paper III: Plate divergence at the Krafla volcanic system, Iceland: Insight from GNSS geodesy and Sentinel-1 Satellite Radar Interferometry in 2002–2024 ..... **47**

4.1 Summary 47
4.2 Main Results 48

5 Conclusions and outlook 51

References 55

Paper I 77

Paper II 121

Paper III 153

List of Figures

Figure 1.1 a) A map of Iceland with the black rectangle indicating the main extent of the Northern Volcanic Zone (NVZ) of Iceland. The light cyan areas show the glaciers. The purple line is a simplified schematic representation of the plate boundary axis. **b) A map of the main extent of the NVZ** with volcanic systems: Askja (A), Fremri-Námar (F), Krafla (K), and Þeistareykir (Th). The Tjörnes Fracture Zone (TFZ) and the Húsavík-Flatey fault (H) are also shown. The black rectangle indicates the central part of the Krafla volcanic system. The purple dashed line indicates the plate boundary axis. The shaded background map shows the topograghy. **c) A map of the main study area.** The black arrows indicate the direction of plate spreading. Eruptive fissures shown are the Holocene eruptive fissures. Fissure swarms, central volcanos, calderas, and fractures in Figure 1.1(b) are from Jóhannesson and Sæmundsson (2009); the plate boundary axis shown is combined from Metzger et al. (2013), Drouin et al. (2017a) and Drouin and Sigmundsson (2019). Fractures in Figure 1.1(c) are from Hjartardóttir et al. (2016) supplemented by fractures from Jóhannesson and Saemundsson (2009) near the Þeistareykir central volcano. Topography is from Landmælingar Íslands [LMÍ] (2020). 3

Figure 1.2 Overview of ground deformation in the Krafla volcanic system during 1974–1995. a) Zoomed-in map of the Krafla caldera with leveling benchmarks (black dots) presented in Figure 1.2(b). The shaded background map shows the topography. The yellow shaded areas show the fissure swarms. The grided lines show the Krafla caldera and the dashed lines shows the southern boundary of the Krafla central volcano. The brown lines are the roads. The red star shows the location of the Krafla power plant. The light red area shows the lava field from the 1975–1984 rifting episode inside the caldera. The green triangle shows the referenced benchmark of Figure 1.2(c). **b) Surface elevation change along a leveling line between December 1975 and March 1976.** The leveling line extends eastward from KÓNGSP (near Lake Mývatn) and continues northward along Hlíðardalur after benchmark FM115. The leveling line follows approximately the roads. Black dots indicate observed elevation changes and white dots are interpolated according to the observations. Modified from Björnsson and Eysteinsson (1998). **c) Elevation time series at the center of the Krafla caldera (benchmark FM5596)**. The time series are based on leveling measurements (1975–1976), with the temporal gaps filled using tilt measurements inside the power plant (1976–1990) and in Hlíðardalur (1990–1995). The elevation is relative to the benchmark FM6414. Modified from Björnsson and Eysteinsson (1998). **d) Elevation profile along the Krafla fissure swarm,** smoothened using the Savitzky-Golay filter (Savitzky and Golay, 1964). **e) Cumulative surface widening in the fissure swarm during the 1975–1984 Krafla rifting episode** estimated with distance measurements, adapted from Tryggvason (1984). The elevation profile is extracted from a digital elevation model from Landmælingar Íslands [LMÍ] (2020). 9

Figure 1.3 a) Schematic figure of GNSS trilateration. The blue circle represents the Earth, while other circles indicate all locations determined from the distance ranging of satellites. Source: GIS Commons by Michael Schmandt, licensed under CC BY-SA 3.0, accessed on 4 July 2025 at https://giscommons.org/chapter-2-input/. **b) Continuous GNSS station THRC at Þeistareykir. c) Coordinate time series from the cGNSS site THRC.** The dots indicate the coordinate values (one value per day) and the grey lines are their uncertainties. The vertical dashed line indicates the beginning of an inflation period at Þeistareykir reported by Gudnasson et al. (2024). **d) Campaign GNSS site RAHO in the Krafla caldera. e) Coordinate time series from the campaign site RAHO.** Symbols have the same meanings as in Figure 1.3(c). The values in Figure 1.3(c) and (e) are the last digits of the coordinates under a topocentric reference system (NEU). The integer parts of the coordinates are (7335594, 15593234, 374) for site THRC and (7314748, 15717186, 623) for site RAHO (in meters). The coordinates are relative to ITRF2014 (Altamim et al., 2016). 13

Figure 1.4 **a) The distribution of GNSS sites in the central part of the Krafla volcanic system.** All the sites mentioned in this chapter are labeled. The purple dashed lines indicate the plate boundary axis, combined from Metzger et al. (2013) and Drouin et al. (2017a). **b), c) and d) Summary of campaign GNSS observations during 2002–2024.** 14

Figure 1.5 a) Illustration of InSAR line-of-sight direction for a right-looking satellite. Right looking indicates that the microwave pulses are transmitted to the right of the satellite orbit. Roman alphabets have the same meaning as in Equation (4) and (5). Source: adapted from Fuhrmann and Garthwaite (2019), licensed under CC BY, originally published in Remote Sensing, https://doi.org/10.3390/rs11030241. **b) Interferogram generated with Sentinel-1 satellite ascending SAR acquisitions (Track 147) on 2 September 2021 and 3 September 2022.** The map area is the same as in Figure 1.1(b). Dashed lines indicate central volcanoes. Dense fringes inside the Askja central volcano (white rectangle) show rapid inflation reported by Parks et al. (2024). Other areas show no significant pattern, indicating small displacement within one year and that the interferogram is largely affected by the atmospheric errors. The arrows indicate the satellite directions of motion (long) and look side (short). Accessed from COMET-LiCS Sentinel-1 InSAR portal (https://comet.nerc.ac.uk/comet-lics-portal/; Lazecký et al., 2020). **c) Interferogram generated with Sentinel-1 satellite descending SAR acquisitions (Track 111) on 12 September 2021 and 25 September 2022. d-e) Zoomed-in views of the dense fringes in the Askja central volcano (white rectangle in Figure 1.5(b) and (c)), for ascending (d) and descending (e) tracks, respectively.** 16

Figure 1.6 Temporal coverage of different SAR satellite missions over the study area. The legend indicates the microwave frequency band and wavelength of the radar satellites. Revisit time refers to the interval between successive SAR acquisitions of the same area by a satellite, determined by its orbit, sensor characteristics, and imaging schedule. 18

Figure 1.7 a) Deterministic models (colored lines) fitting the cGNSS coordinate time series (black dots) at station THRC and b) their corresponding residuals. Grey lines indicate the observation uncertainties. Vertical dashed lines indicate the onset timing of the inflation period reported by Gudnasson et al. (2024). The deterministic model only includes linear deformation velocity, annual signal, and semi-annual signal. 21

Figure 1.8 cGNSS coordinate time series demonstrating an instantaneous coseismic offset and a transient post-seismic deformation signal of the 2020 Mw 6.4 Nima Earthquake in Central Tibet, China. The interseismic line corresponds to the linear deformation velocity in Equation (6) of this thesis. Source: adapted from Liu, X, et al. (2023), licensed under CC BY, originally published in Frontiers in Earth Science, https://doi.org/10.3389/feart.2022.1012773. 22

Figure 1.9 Stacked power spectra of cGNSS residual time series with annual and semi-annual signals removed (unfiltered). The stacked power spectra shown here is the spectrum of all the residual time series from a cGNSS network are aligned together and averaged at each frequency. The cGNSS network here is Crustal Movement Observation Network of China. The grey line shows the characteristic of flicker noise. The filtered curve is the spectra of residuals further with spatially correlated noise removed. Vertical black and gray lines indicate the annual (1 cpy) and draconitic (1.04 cpy) oscillations and their harmonics up to the 4th. Vertical green lines indicate the frequencies of 24.75, 25.74, and 26.74 cpy from semidiurnal tides. Source: from Yuan et al. (2018), licensed under CC BY, originally published in Remote Sensing, https://doi.org/10.3390/rs10091472 24

Figure 1.10 A synthetic cGNSS coordinate time series with the velocity change from 5 mm/yr to -5 mm/yr at decimal year 2021.5, modeled with a second-degree polynomial. No periodic signal is simulated in the synthetic time series. A white noise with an amplitude of 1 mm and a flicker noise with an amplitude of 4 $mm/yr^{0.25}$ are included in the synthetic time series. 25

Figure 1.11 a) Schematic figure of the kinematic back-slip model. The green lines show the plate boundary axis. The red rectangle with red arrows shows the back-slip dislocation. **b) Schematic figure of the buried dislocation model.** The vertical dark blue rectangle indicates the opening dislocation below the locking depth. **c) Comparison among deformation velocities predicted by the back-slip, buried dislocation and arctangent function models.** The strike-perpendicular coordinate indicates the distance from the plate boundary axis (vertical green line) along its strike-perpendicular direction. The deformation velocity is perpendicular to the strike of the plate boundary axis. The grey shaded area shows where the back-slip and buried dislocation models predict minimal ground deformation near the plate boundary axis. The blue short-dashed and red dashed lines overlap with each other. The full spreading rate is 20 mm/yr and the locking depth is set to 6 km. 34

Figure 1.12 Plate spreading rates and directions in the Krafla volcanic system predicted from different global plate motion models and regional plate boundary models. Krafla caldera center (16.80°W, 65.71°N) is used to calculate the horizontal velocities from the global plate motion models. Thin lines indicate the uncertainties of the model predictions. Shapes without thin lines indicate the corresponding models do not have uncertainty or the uncertainties are too large and thereby omitted. The vertical dashed and dash-dotted lines are the plate spreading rates from Árnadóttir et al. (2009) and Cao et al. (2023), respectively. The yellow shaded area is the uncertainty of Árnadóttir et al. (2009) spreading rate while the orange shaded area is the range of spreading direction given by Cao et al. (2023). Barreto et al. (2025) has two solutions, depending on whether the Húsavík-Flatey fault is modeled as one or two segment(s). Euler pole location uncertainties are omitted for APKIM2005 and REVEL2000 since they lead to rather large uncertainty in plate spreading. Global models are: ITRF2000 (Altamimi et al., 2002), ITRF2008 (Altamimi et al., 2012), ITRF2014 (Altamimi et al., 2017), ITRF2020 (Altamimi et al., 2023), NUVEL-1 (Argus and Gordon, 1991), NUVEL-1A (DeMets et al., 1994), NUVEL-HS2 (Gripp and Gordon, 1990), NUVEL-HS3 (Gripp and Gordon, 2002), APKIM2000 (Drewes, 1998), APKIM2005 (Drewes, 2009), MORVEL1 (DeMets et al., 2010), MORVEL56 (Argus et al., 2011), GSRMv1.2 (Kreemer et al., 2003), GSRMv2 (Kreemer et al., 2014), CGPS2004 (Prawirodirdjo and Bock, 2004), REVEL2000 (Sella et al., 2002), and GEODVEL2010 (Argus et al., 2010). The global plate motions are calculated with GAGE Plate Motion Calculator (https://www.unavco.org/software/geodetic-utilities/plate-motion-calculator/pla te-motion-calculator.html). 37

Figure 2.1 Comparison between the onset timing of deformation anomalies in the Krafla volcanic system during 2014–2015 and the near-field precursors prior to the 2014 Bárðarbunga dike intrusion. a) A map showing the locations of the Krafla (K) and Bárðarbunga (B) volcanic systems. The shaded background map shows the topography and the white area is the Vatnajökull ice cap. The black dashed lines indicate central volcanoes and the black ticked lines indicate calderas. The blue rectangle outlines the area as in Figure 1.1(c). The red line indicates the 2014 Bárðarbunga dike intrusion. The yellow areas show the fissure swarms. The purple rectangle shows the location of cGNSS site VONC, as shown in Figure 2.1(c). **b) Marginal posterior probability distribution of the deformation anomaly onset timings at Krafla with 95% confidence interval.** The colored shaded areas start and end at the lower and higher limit of the 95% confidence interval, respectively. The vertical solid and dashed lines indicate the optimal and mean estimates, respectively. The gray area indicates the period after the onset of the Bárðarbunga dike intrusion. **c) The horizontal displacement in direction N279.4°E (the azimuth of maximum horizontal motion) at VONC station (11 km west of the Bárðarbunga, location shown in Figure 2.1(a)) from detrended GNSS time series. d) Seismicity at Bárðarbunga versus time (left axis) and accumulated seismic moment (right axis) prior to**

the dike intrusion. Data in Figure 2.1(c) and (d) are from Sigmundsson et al. (2020). Fissure swarms, central volcanos, calderas are from Jóhannesson and Sæmundsson (2009), and topography is from Landmælingar Íslands [LMÍ] (2020). 40

Figure 3.1 A schematic figure of the modified dike sequence model. a) Illustration of magma flow from a magma domain, through the fissure swarm inlet and to a dike along the least compressive stress plane. The figure is not on scale. **b)–c) Dike driving pressure from topographic effects and tectonic stress prior to 1975–1984 Krafla rifting episode.** The topographic effect is calculated with a simplified piecewise elevation profile along the Krafla fissure swarm, and an average host rock density of 2510 kg/m^3 (Scott et al., 2019). The tensile tectonic stress is assumed to be 12 MPa with two stress barriers on both ends of the Krafla fissure swarm (Buck et al., 2006). **d) Dike driving pressure supplied by the topographic effects and tectonic stress summing up Figure 3.1(b) and (c).** The combined value shown is the sum of values in Figure 3.1(b) and (c). 44

Figure 4.1 a) Long-term horizontal deformation velocity fields in the central part of the Krafla volcanic system derived from GNSS (2002–2024, black arrows) and InSAR (2015–2023, color map). The ellipses indicate uncertainties (95% confidence). The blue line with segments separated by white diamonds shows the inferred plate boundary central axis. The color from light to dark blue indicates segment location from south to north for visual distinction, also applied for Figure 4.1(b). The vertical dashed lines show the median estimates. **b) Marginal posterior probability distribution of the locking depth for each plate boundary axis segment.** The vertical extent of each panel corresponds to their latitude range in Figure 4.1(a**). c)–e) Marginal posterior probability distribution of spreading parameters and horizontal GIA scaling factor.** 48

List of Publications

Paper I:

Yang, Y., Sigmundsson, F., and Geirsson, H. (2023). Joint Bayesian modeling of velocity break points, noise characteristics, and their uncertainties in GNSS time series: Far-field velocity anomalies concurrent with magmatic activity in Iceland. *Geophysical Research Letters*, 50, e2023GL103432. https://doi.org/10.1029/2023GL103432.

Paper II:

Yang, Y., Sigmundsson, F., Geirsson, H., and Gottsmann, J. (2025) Role of tectonic stress and topography on repeated lateral dikes: application to the 1975–1984 Krafla and 2023–2025 Svartsengi rifting episodes in Iceland. *Bulletin of Volcanology*, 87, 105. https://doi.org/10.1007/s00445-025-01897-y

Paper III (draft manuscript)**:**

Yang, Y., Sigmundsson, F., Geirsson, H., Biggs, J., Drouin, V., Araya J. S., Hreinsdóttir S., Lanzi C., Gottsmann, J., Broerse, T., and Verhagen, S. Plate divergence at the Krafla volcanic system, Iceland: Insight from GNSS geodesy and Sentinel-1 Satellite Radar Interferometry in 2002–2024. *Journal of Geophysical Research: Solid Earth*.

Contribution of the author:

Paper I: The research question was developed by me and Freysteinn Sigmundsson (FS). The methodology was designed by me under the guidance of FS. Programming, experiments, formal analysis and visualization are mainly carried out by myself. Interpretation was done together with FS and Halldór Geirsson (HG). I wrote the initial draft of the manuscript. All authors contributed to review and editing.

Paper 2: The research question and modeling framework were developed by me and FS. Programming, experiments, formal analysis and visualization were mainly completed by myself. Results interpretation involved discussion with FS, HG, and Joachim Gottsmann (JG). I prepared the initial draft of the manuscript with input from FS. All authors contributed to manuscript review and editing.

Paper 3: The research question was formulated mainly by myself. InSAR data processing was conducted together with Juliet Biggs (JB) and Josefa Sepúlveda Araya. GNSS data processing was based on work by Sigrún Hreinsdóttir. Chiara Lanzi contributed to the regional subsidence model. Methodology development, programming, formal analysis and visualization were conducted by me under suggestions from FS and JB. Interpretation is led by me through discussions with FS, JB, CL and Taco Broerse. I drafted the initial manuscript, and all authors contributed to its review and editing.

Abbreviations

This list contains abbreviations used in this thesis in alphabetical order:

AR	Autoregressive Process
cGNSS	Continuous GNSS
DEM	Digital Elevation Model
EDM	Electronic Distance Measurement
EnviSat	Environmental Satellite
ERS	European Remote-Sensing Satellite
FLN	Flicker Noise
GIA	Glacial Isostatic Adjustment
GLONASS	Globalnaya Navigatsionnaya Sputnikovaya Sistema
GNSS	Global Navigation Satellite System
GPS	Global Positioning System
HFF	Húsavík-Flatey Fault
InSAR	Interferometric Synthetic Aperture Radar
IQR	Interquartile Range
LiDAR	Light Detection and Ranging
LLR	Lunar Laser Ranging
LOS	Line-of-sight
LSE	Least Square Estimation
MAD	Median Absolute Deviation
MOR	Mid-ocean Ridge
NVZ	Northern Volcanic Zone of Iceland
PLN	Power-law Noise
PPP	Precise Point Positioning
PS-InSAR	Persistent Scatterer InSAR
RP	Relative Positioning
RWN	Random-walk Noise
SAR	Synthetic Aperture Radar
SBAS-InSAR	Small Baseline Subset InSAR
SLR	Satellite Laser Ranging
TFZ	Tjörnes Fracture Zone
VLBI	Very Long Baseline Interferometry
WN	White Noise

Variables

This list contains variables used in the main text of the thesis, ordered based on meanings:

P_r	Code pseudorange measurement of GNSS
Φ	Carrier phase measurement of GNSS
r	Distance between a satellite and a antenna
c	Speed of light
Δt_r	GNSS receiver clock error
Δt_s	GNSS satellite clock error
I	Ionospheric error of GNSS observation
T	Tropospheric error of GNSS observation
λ	Wavelength of GNSS signal
N	Integer ambiguity in GNSS carrier phase measurement
ε_P	Residual errors of GNSS code pseudorange measurement
ε_Φ	Residual errors of GNSS carrier phase measurement
$\Delta\varphi_{int}$	Phase difference between two SAR images
$\Delta\varphi_{geom}$	InSAR phases difference from satellite orbital positions at two acquisitions and a perspective effect from topography
$\Delta\varphi_{def}$	InSAR phase difference from surface deformation
$\Delta\varphi_{atm}$	InSAR phase difference from atmospheric conditions
$\Delta\varphi_{pixel}$	InSAR phase difference due to individual scatterers within an image pixel
d_{los}	Displacements in the satellite line-of-sight direction
d_{los}^{asc}	Displacements in the satellite line-of-sight direction for ascending observations
d_{los}^{des}	Displacements in the satellite line-of-sight direction for descending observations
d_u	Displacements in the vertical component
d_e	Displacements in the east component
d_n	Displacements in the north component
θ	Incidence angle of the satellite line-of-sight vector
θ^{asc}	Incidence angle of the satellite line-of-sight vector for ascending observations

θ^{des}	Incidence angle of the satellite line-of-sight vector for descending observations
α	Azimuth of the satellite line-of-sight vector
α^{asc}	Azimuth of the satellite line-of-sight vector for ascending observations
α^{des}	Azimuth of the satellite line-of-sight vector for descending observations
y	Coordinates in GNSS time series
t	Observation epoch
a	Initial position of a GNSS site (intercept)
b	Deformation velocity (linear trend from GNSS coordinate time series)
d^1	Amplitude of the sine harmonic of a periodic signal in GNSS coordinate time series
d^2	Amplitude of the cosine harmonic of a periodic signal in GNSS coordinate time series
δ	Transient deformation signal in GNSS coordinate time series
ω	Angular frequency of a periodic signal
ε	Residuals
m	Magnitude of a transient deformation signal
h	Magnitude of a velocity change
τ	Relaxation time of post-seismic deformation
Δt	Elapsed time after an earthquake
t_0	Epoch of an offset
t_1	Timing of a velocity change (break point)
P	Power spectral density
f	Frequency
P_0	Spectral amplitude of a power spectrum at the reference frequency
f_0	Reference frequency of a power spectrum
κ	Spectrum index
$\mathbf{J}_\kappa$	Covariance matrix of a time series
ΔT	Sampling interval of a time series
σ	Stress with subscripts 1, 2 and 3 indicating maximum, intermediate and minimum principal stress
σ_e	Deviatoric stress
σ_d	Effective normal stress acting on the dike plane

I_1	First stress invariant
J_2	Second invariant of deviatoric stress tensor
T_0	Tensile strength of the host rock
φ	Internal friction angle of the host rock
C_0	Cohesion of the host rock
E	Young's modulus of the host rock
μ	Shear modulus of the host rock
p_m	Magma overpressure
p_m^d	Magma pressure in a dike
p_b	Buoyancy pressure due to the density difference between the magma and the host rock
p_u	Pressure due to a buoyant magma body increases in thickness
P_o	Failure limit of the host rock
$P_{driving}$	Driving pressure of dike propagation
Δp	Pressure change in a magma body
ΔM	Mass change in a magma body
M	Total mass of magma in a magma body
ΔV	Volume change of a magma body
V	Volume of a magma body
ρ_m	Magma density
$\Delta\rho$	Density difference between the magma and the host rock
β_m	Intrinsic compressibility of magma
β_c	Elastic compressibility of a magma body
$\overline{\beta_c}$	Effective compressibility of a magma body
r_v	Ratio of injected and extruded magma volume to the volume change in the magma domain
A, B, C	Semi-axis lengths of a penny-shaped body
g	Gravitational acceleration
V_A	Plate boundary deformation velocity at a given location A
V_{plate}	Full plate spreading rate
d_A	Distance from a given location A to the plate boundary axis
D	Width of the velocity transition zone
v_n	North-component plate boundary deformation velocity
v_e	East-component plate boundary deformation velocity

R	Earth's radius
$\mathbf{w}$	Angular velocity vector of a plate motion (Euler vector)
w	Angular velocities with subscripts x, y, and z indicating different components in Cartesian coordinate system
$\mathbf{r}$	Unit position vector
$\mathbf{r_0}$	Unit position vector of a Euler pole
B	Latitude of a ground point
L	Longitude of a ground point

Acknowledgements

This Ph.D. project received funding from the European Union's Horizon 2020 research and innovation programme under grant agreement No. 858092 (IMPROVE), and from Landsvirkjun.

First, I would like to thank my supervisors, **Freysteinn Sigmundsson, Halldór Geirsson, Joachim Gottsmann, and Vincent Drouin**. Thanks to **Freysteinn** for making all this possible by replying to the very first, and somehow random, email from me, and for being so supportive and patient throughout the journey. Thanks to **Halldór** for his kind guidance, inspiring discussions, and of course, the ice cream on the way back from the field. Thanks to **Jo** for the 'premier' COMSOL lessons and for offering valuable feedback on my research. Thanks to **Vincent** for invaluable support, both technically and mentally.

I am also grateful to many others who provided trainings or help during my Ph.D.: **Juliet Biggs and Milan Lazecký** for InSAR data processing; **Giuseppe Puglisi, Francesco Guglielmino, and Alessandro Bonforte** for high-rate GNSS data processing and GNSS-InSAR integration; **Sigrún Hreinsdóttir** for GNSS data processing; **Páll Einarsson** and **Bryndís Brandsdóttir** for sharing their knowledge of Icelandic volcanoes; **Yosuke Aoki** for fruitful discussions on Japanese volcanoes; **Andy Hooper** for his insightful comments on my studies; and **Steffen Mischke** as the external coordinator of my Ph.D. project.

People in IMPROVE have made this journey so much more lively and pleasant. I would like to thank **Paolo Papale, Magnús Tumi Guðmundsson, and all supervisors in IMPROVE** for their support and training offered throughout the project. Heartfelt thanks to all my friends in IMPROVE – **Ana, Alejandra, Patricia, Andrew, Lisa, Regina, Roberto, Joe, Gabriel, Maurice, Owen, Clothilde, Giulio, and Beatrice**. Together we went through the chilly summer with COVID at Krafla, endured the heat wave and wildfires in Sicily, shared sandwiches and whiskey in Ireland, and enjoyed the concert and boat ride in Berlin – all the dramas and fun that made this journey unforgettable.

Beyond all the travels, friends and colleagues in Iceland kept me grounded and smiling. Special thanks to **Chiara, Daniel V., Tingting, Patricia** (again)**, Siqi, Birhan, Dong, and others** for being there through everything – dinners, drinks, groceries, pools, and random chats. Thanks to **Sonja, Greta, Cat, Ylse, Jonas, Nico, Gabrielle, Didas, Daniel C. and many others** for companionship in the office, lunches, coffee breaks, and board games. Thanks also to the people who made my four-month stay in the Britain so joyful: **Tianyuan, Evie, Simon, Lyn, Ben, Cindy, and more in Bristol**; **the group in Leeds** for welcoming my unexpected visits; **Josefa** for our fieldwork and hikes together and for sharing experiences. The GNSS campaigns at Krafla with **Sveinbjörn, Taco, Sandra, Freek, Wietske, Paco, and the students from TU Delft** gave me both learning and joy – thanks to them as well. I am grateful for every meeting and encounter.

While far from home, my family and friends in China have been an incredible source of support. **My parents** have always supported all my decisions – thank you for everything. Thanks to **Xiaohui Zhou and Yifang Ma** for caring about my research and life. Thanks to

Tao Xue, Qian You, Xiaoqi Chen, Zejia Chen, Luoyixin Zheng, Zhuang Ma, and others for laughter via calls and chats.

Finally, when the gate to a planned destination closes, how does one find another path toward the dreamland? Perhaps it takes endurance, courage, and efforts. Thanks to **myself** for not giving up and for passing countless checkpoints along the way – I hope it is not only an improved understanding of ground deformation at a volcano, but also a better understanding of life.

1 Introduction

More than 8% of the world's population lives within 100 km of an active volcano, exposed to volcanic risks (Small and Naumann, 2011; Freire et al., 2019). Meanwhile, active volcanoes often host geothermal systems, highlighting their potential as valuable energy resources (Stelling et al., 2016). Monitoring and interpreting volcano deformation is important for understanding volcano evolution and revealing their internal processes, which thereby enhances volcanic hazard assessments and geothermal resource management.

Volcano deformation features inherent complexity, driven by various processes including magma emplacement, tectonics, and geothermal activity (Dvorak and Dzurisin, 1997). These processes act across distinct temporal and spatial scales (e.g., Biggs et al., 2014; Ebmeier et al., 2018). For example, precursory deformation signals start typically a few days to several months prior to volcano eruptions (Dzurisin, 2003). Volcano conduit processes can induce minute-scale deformation (Ripepe et al., 2021), while the gravitational spreading of volcano edifice can persist for decades or longer (e.g., Borgia et al., 1992; Lundgren et al., 2004; Tizzani et al., 2010). Spatially, precursory crater contraction before eruptions may occur within a few kilometers (Bonaccorso and Davis, 1999; Himematsu et al., 2024), while deformation at the scale of volcanic edifice and calderas typically spans on the order of ~10 km (e.g., Meertens and Smith, 1991; Bonforte and Puglisi, 2003), and rift-scale inflation can affect >100-km-wide area (La Rosa et al., 2024). Combined effects from multiple processes complicate the interpretation of deformation observations and require comprehensive modeling approaches.

Improved characterization of individual deformation signals and their underlying causal factors provides valuable insights into Earth's internal properties and dynamic behavior. For example, deformation driven by viscoelastic stress relaxation offers constraints on the viscosity of the crust (e.g., Bonafede, 1995; Novoa et al., 2019; Li et al., 2022), and temporal changes and spatial patterns in surface deformation can reflect variations and different processes of volcano and hydrothermal systems, thereby assisting in modeling approaches (e.g., Wang et al., 2019; Le Mével et al., 2021; Liu, F. et al., 2023; Kebede et al., 2025).

Considering realistic Earth properties is a critical component of a comprehensive modeling approach to ensure model accuracy and reliability. Different deformation processes at a volcano may be controlled by different properties of the Earth. One example is the incorporation of realistic deformation mechanisms. For instance, beyond conventional assumption of homogeneous elastic crust, a long-lived magma body can induce thermo-viscoelastic deformation as it alters the thermal structure of the crust and involves ductile behavior (e.g., Dragoni and Magnanensi, 1989; Head et al., 2021; Weber et al., 2025). Other constraints include crustal heterogeneities and more realistic boundary conditions of models (e.g., Manconi et al., 2007; Hautmann et al., 2010; Anderson and Segall, 2013; Greiner and Geirsson, 2024).

This study investigates the deformation at the Krafla volcanic system, northeast Iceland, across multiple temporal scales. Th objectives are to collect new ground

deformation data, refine previous modeling approaches, and explore possible processes causing the observed deformation. For short-term deformation signals, I study deformation anomalies observed during the 2014–2015 period and their possible causes from rift processes (Chapter 2). The decadal-scale unrest during 1975–1984 Krafla rifting episode is revisited to examine how tectonic stress and topographic effects influence the spatial distribution of sequential dike intrusions under more realistic Earth behavior (Chapter 3). New observations and models of long-term plate divergence are presented to provide insights into the local crustal structure, volcano-tectonic interactions and potential local deformation processes (Chapter 4). Finally, Chapter 5 summarizes the main conclusions, methodological advances, and perspectives for future research.

The following two sections briefly introduce the Krafla volcanic system and its history of geodetic measurements. Subsequent sections provide necessary background for modeling deformation in the three temporal scales addressed in this thesis. Section 1.3 reviews time series analysis theory for geodetic data, the theoretical basis for modeling short-term deformation anomalies. Section 1.4 summarizes the initiation conditions of dike intrusions, previous dike propagation models, and the simple elastic model of rifting by Buck et al. (2006). Section 1.5 reviews different types of plate boundary models and previous studies of the plate divergence that include the Krafla volcanic system.

1.1 The Krafla Volcanic System

1.1.1 Tectonic Setting

The Krafla volcanic system lies within the Northern Volcanic Zone (NVZ) of Iceland. It is a segment of the divergent boundary between the Eurasian and North American plates along the Mid-Atlantic Ridge (Figure 1.1). Mid-ocean ridge (MOR) systems are the most common type of divergent plate boundary and account for about 75% of Earth's volcanism (Bennett et al., 2019). The subaerial portion of the global MOR system represents less than 2% of its total length, and Iceland provides one of the few locations where surface observations allow direct investigation of rifting and magmatic accretion processes. Within this subaerial ridge segment, the Krafla volcanic system serves as a natural laboratory for studying volcano-tectonic interactions and their associated ground deformation in an active rift setting.

Plate spreading at Krafla occurs in the direction N283.0°–286.7°E at rates of 16.3–18.6 mm/yr according to global plate motion models (DeMets et al., 1994; DeMets et al., 2010; Argus et al., 2010). The volcanic system consists of a central volcano with a radius of ~25 km, a 9×7 km caldera formed ~110,000 years ago at the center of the central volcano, and a 4–10-km-wide fissure swarm (rift zone) extending 40 km south and 50 km north from the caldera (Opheim and Gudmundsson, 1989; Sæmundsson, 1991; Hjartardóttir et al., 2012). Most normal faults, extension fractures and eruptive fissures in the Krafla fissure swarm have orientation N to NNE with an average strike of N9.5°E (Corti et al., 2021). The density of these geological structures decreases northward and southward from the caldera (Pedicini et al., 2024). Two main high-temperature geothermal fields are located in the study area: Krafla and Bjarnarflag (Figure 1.1(c)).

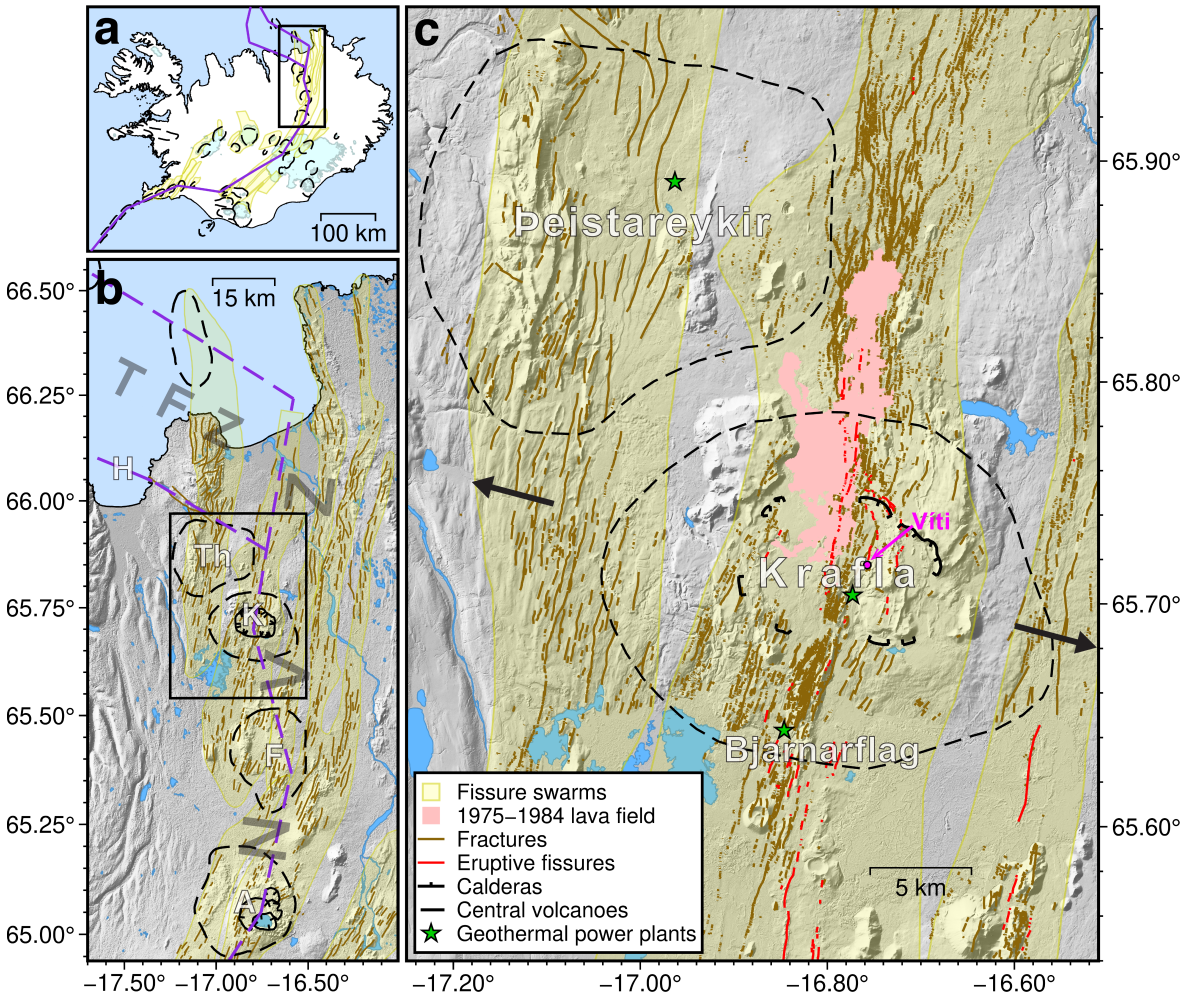


Figure 1.1 a) A map of Iceland *with the black rectangle indicating the main extent of the Northern Volcanic Zone (NVZ) of Iceland. The light cyan areas show the glaciers. The purple line is a simplified schematic representation of the plate boundary axis.* ***b) A map of the main extent of the NVZ*** *with volcanic systems: Askja (A), Fremri-Námar (F), Krafla (K), and Þeistareykir (Th). The Tjörnes Fracture Zone (TFZ) and the Húsavík-Flatey fault (H) are also shown. The black rectangle indicates the central part of the Krafla volcanic system. The purple dashed line indicates the plate boundary axis. The shaded background map shows the topograghy.* ***c) A map of the main study area.*** *The black arrows indicate the direction of plate spreading. Eruptive fissures shown are the Holocene eruptive fissures. Fissure swarms, central volcanos, calderas, and fractures in Figure 1.1(b) are from Jóhannesson and Sæmundsson (2009); the plate boundary axis shown is combined from Metzger et al. (2013), Drouin et al. (2017a) and Drouin and Sigmundsson (2019). Fractures in Figure 1.1(c) are from Hjartardóttir et al. (2016) supplemented by fractures from Jóhannesson and Saemundsson (2009) near the Þeistareykir central volcano. Topography is from Landmælingar Íslands [LMÍ] (2020).*

The inferred boundary of the Þeistareykir central volcano is located only ~5 km northwest of the Krafla central volcano boundary, and the southern Þeistareykir fissure swarm overlaps the westernmost part of the Krafla central volcano (Figure 1.1). Near the northern edge of the Þeistareykir central volcano, the Þeistareykir fissure swarm connects to

the Tjörnes Fracture Zone (TFZ) transform. One main lineament of TFZ is the Húsavík-Flatey fault (HFF), a right-lateral strike-slip fault with a length of ~100 km and a strike of N116.3°–124.4°W (Metzger et al., 2013). Geodetic models show that the HFF accommodates about 30–40% of the full plate transform motion (Geirsson et al., 2006; Metzger and Jónsson, 2014; Barreto et al., 2025). Earthquake and fracture distributions suggest a possible southeastward subsurface prolongation of the HFF, potentially intersecting the Krafla fissure swarm (Hjartardóttir et al., 2012; Tibaldi et al., 2016). The northern parts of the Fremri-Námar and Askja fissure swarms are present east of Krafla, where the former overlaps the easternmost part of the Krafla central volcano and the latter lies ~5 km to the east of the Krafla central volcano boundary. All these fissure swarms share similar N to NNE strikes, controlled by regional tectonic stress (e.g., Tibaldi et al., 2020).

1.1.2 Volcanic Activities

Magma is distributed over a wide range of depths beneath the Krafla caldera. Magma has been directly encountered at ~2.1 and ~2.6 km depth during drilling of two boreholes (Mortenson et al., 2010, 2014, 2015). Studies of seismic shear wave shadows and seismic tomography have inferred shallow magma presence at 3–7 km depth (Einarsson, 1978; Brandsdóttir et al. 1997; Schuler et al., 2015). Similarly, reflection seismology identified strong reflectors at ~2.1 km and ~4 km depth (Kim et al., 2020). Geodetic models using a point pressure source in a homogeneous elastic half-space (Mogi, 1958) inferred shallow deformation sources at ~3–4.3 km depth (e.g., Tryggvason, 1980; Johnsen et al. 1980; Árnadóttir et al. 1998; Heimisson et al. 2015). Geodetic models suggested deeper magma bodies down to the lower crust at ~21 km depth (e.g., de Zeeuw-van Dalfsen et al., 2004).

Petrological and geochemical analyses have revealed bimodal volcanism at the Krafla volcanic system, with a series of basaltic–andesitic rocks and a cluster of rhyolitic rocks (e.g., Jónasson, 1994). Two main phases of rhyolitic activity occurred during the last interglacial, when the Krafla caldera formed, and during the last glacial, when a ring dike was intruded. Quenched glass from two boreholes also indicates the presence of rhyolitic magma within basaltic crust (Zierenberg et al., 2012; Rule, 2020). Recent studies highlighted the roles of both hydrothermal alteration and fractional crystallization in the generation of these rhyolites (Hampton et al., 2021; Rooyakkers et al., 2021). Evolved basaltic magma crystallizes and assimilates altered crust at ~3–4 km depth, forming crystal mushes and interstitial silicic melts. These melts ascend further to ~2–3 km depth where they interact with similar mush or intrusive bodies (Rooyakkers et al., 2022). The evolved basaltic magma itself is inferred to reside at ~8 km depth and is likely fed by more primitive magma from ~14–19 km depth (Rooyakkers et al., 2022, 2024).

Two most recent rifting episodes in the volcanic system occurred in 1724–1729 (the Mývatn rifting episode) and in 1975–1984 (the Krafla rifting episode). The Mývatn rifting episode began with a magmatic-hydrothermal eruption that formed the Víti crater (Montanaro et al., 2021; for location see Figure 1.1). During its first three years, the rifting episode featured short and sharp events, with intense seismic swarms, fault movements and vertical ground displacements, but followed in the last two years by long-lived effusive eruptions (Thorarinsson, 1979; Grönvold, 1984). During this episode, ~0.45 km^3 of basaltic lava erupted from discontinuous fissures ~11 km in length, covering an area of 30 km^2.

The 1975-1984 Krafla rifting episode consisted of about twenty rifting events with dike intrusions affecting different portions of the Krafla fissure swarm, nine of which led to basaltic eruptions (e.g., Björnsson et al., 1977; Tryggvason, 1980; Einarsson, 1991; Wright et al., 2012). Similar as during the Mývatn episode, the events generated seismic swarms, faulting, and surface widening, while all later events after March 1980 included eruptions. The cumulative surface widening averaged 4–5 m, corresponding to 200–250 years of accumulated spreading (Tryggvason, 1984; Hollingsworth et al., 2012). Geodetic data revealed gradual inflation of the caldera up to 7–10 mm/day between diking events, followed by sudden deflation beginning at the onset of each dike intrusion (Tryggvason, 1980). The first intrusion in December 1975 was the largest in the episode, affecting a ~60-km-long segment of the fissure swarm, causing subsidence up to 2 m at the caldera center (Björnsson et al., 1977; Tryggvason, 1980). The total erupted lava volume during the 1975–1984 period is estimated to be ~0.26 km^3 covering 36 km^2 (Table 1 in Rooyakkers et al., 2024, and references therein). Petrochemical analyses of the erupted lava revealed a clear compositional bimodality in the erupted basalts across the north caldera rim, where basalts erupted inside the caldera is more evolved (quartz tholeiite with MgO = 5.7–6.4 wt%) and inferred to be from a shallow body (~7–9 km), whereas primitive basalts (mainly olivine-normative with MgO = 6.4–8.7 wt%) erupted outside the caldera is inferred to be from a lower-crustal body (~14–19 km) (e.g., Grönvold and Mäkipää, 1978; Rooyakkers et al., 2024).

The rifting episodes at Krafla show similar mechanisms to those observed in other subaerial portions of the MOR system, such as Afar region in Africa (Grandin et al., 2009; Grandin et al., 2010; Wright et al., 2012). Rifting in both regions features: (i) repeated lateral dike intrusions over many kilometers from a source near the rift zone center, (ii) magma supplied from multiple storage zones at different locations and (or) depths, (iii) dike propagation guided by regional extensional tectonic stress, (iv) sequences of smaller dikes following an initial main intrusion, and (v) deformation and stress release dominated by magma injection rather than seismicity. Investigating the volcano-tectonic interactions and their associated deformation at Krafla therefore contributes to a broader understanding of the rifting cycles of the global MOR system.

Moreover, the mechanisms inferred from a magma-rich rift systems such as Krafla and Afar also have broader implications for understanding both magma-poor rift systems and dike intrusions in non-rift volcanoes. For instance, comparing the styles of strain localization between the Krafla volcanic system and less magmatically active rift segments in East Africa (e.g., Muirhead et al., 2019) may provide insights into the evolution and segmentation of continental rifts. In non-rift volcano settings, the interplay between magma overpressure and local stress field observed at rift settings also explain the formation of circumferential and radial dike patterns (e.g, Chadwick and Dieterich, 1995; Acocella and Neri, 2009).

1.1.3 Geothermal Fields

The Krafla volcanic system hosts two major geothermal fields, the Krafla and Bjarnarflag geothermal fields (Figure 1.1). They cover a total surface area of around 280 km^2 (Guðmundsson et al., 1971). The Krafla field occupies the center of the Krafla caldera with an estimated geothermal reservoir temperature up to 350°C at 2 km depth (Ármannsson et

al., 1987; Bodvarsson et al., 1984). The Bjarnarflag field is located ~9 km south of the caldera near the Námafjall ridge, where the downhole measurements have recorded the highest temperature of 320°C at ~1.5 km depth (Gudmundsson and Arnórsson, 2002). Geothermal exploitation began in 1969 at Bjarnarflag and 1977 at Krafla, with over 50 wells drilled across the two fields over decades (Gudmundsson and Arnórsson, 2002; Mortensen et al., 2015). The initial production capacity at Krafla was 30 MW, which was increased to 60 MW in 1997, providing electricity to towns in northeast Iceland. Bjarnarflag's power station had an installed capacity limit at 3 MW and was increased to 5 MW in 2019 (e.g., Drouin, 2024). At Bjarnarflag, the extraction rate has been relatively stable at 1500–2500 kilotons per year during 1993–2015 (Drouin et al., 2017b). In contrast, the Krafla power plant doubled extraction rate in 1995, averaging ~9000 kilotons per year during 2000–2018. Most wells at the Krafla field are used for geothermal fluid extraction, while a few are used for the reinjection of cold water. The reinjection of water into the geothermal reservoir at Krafla started in 1999, increasing gradually to more than 4000 kilotons per year after 2014 (Drouin et al., 2017b; Lanzi et al., 2023).

1.2 Geodetic Measurements at the Krafla Volcanic System

Surface deformation recorded by geodetic measurements has supported investigations of various geophysical processes in the Krafla volcanic system. Before, during and after the 1975–1984 Krafla rifting episode, geodetic techniques such as leveling, ground tilt measurements, and electronic distance measurements (EDM) provided valuable constraints on inflation-deflation cycles, surface widening due to dike intrusions, post-rifting processes, and more (e.g., Moller and Ritter, 1980; Tryggvason, 1980; Tryggvason, 1984; Sturkell et al., 2008; Wright et al., 2012). The 1975-1984 rifting episode was the first instrumentally observed subaerial rifting episode, with detailed observations that are still important today.

Over the past several decades, the development of space geodetic techniques, especially Global Navigation Satellite System (GNSS) and Interferometric analysis of Synthetic Aperture Radar satellite images (InSAR), has enabled continuous, high-precision monitoring of crustal deformation under almost all-weather conditions and with high spatiotemporal resolution. These advances offer new opportunities to understand deformation processes across multiple spatiotemporal scales.

The following text briefly reviews the terrestrial geodetic techniques and their contributions to monitoring crustal deformation at Krafla before, during and after the 1975–1984 rifting episode. Then it introduces the principles, data processing workflows, and observational histories at Krafla of GNSS and InSAR, as well as their specific contributions to this thesis. Other techniques, such as satellite optical imagery (Hollingsworth et al., 2012, 2013) and airborne Light Detection and Ranging (LiDAR; Bramham, 2014) have also been used to measure the surface deformation at Krafla. However, I do not discuss them further as they do not form a major part of this thesis.

1.2.1 Terrestrial Geodetic Techniques

Leveling

Geodetic leveling conventionally determines height differences between ground points with differential, trigonometric, or barometric methods (e.g., Vanicek et al., 1980; National Oceanic and Atmospheric Administration [NOAA], 2017; Lyon et al., 2018; Noll and Rydlund, 2020). Vertical ground deformation can be derived from height time series by repeated leveling measurements. In the Krafla volcanic system, both differential and trigonometric leveling were applied. In differential leveling, a leveled surveying instrument is set up at a fixed position and readings are taken of height difference between two calibrated rods placed vertically on benchmarks (the backsight and foresight). The trigonometric method calculates height differences from measured slope distances and zenith angles between two points.

Early trigonometric leveling surveys across North Iceland were conducted by German and Austrian scientists in 1938, 1964 and 1965, to test the validity of the continental drift theory, which established long-term benchmarks at Krafla for later geodetic measurements (e.g., Niemczyk, 1943; Spickernagel, 1966). Differential leveling was carried out at Krafla in 1974 along the road from Lake Mývatn to the Krafla caldera, supplemented by benchmarks measured with trigonometric leveling (Johnsen et al., 1980). During the Krafla rifting episode, leveling surveys were carried out regularly and used to infer the locations and depths of the pressure sources associated with magmatic activity (e.g., Björnsson et al., 1979; Tryggvason, 1980; Ewart et al., 1991; Árnadóttir et al., 1998; Sturkell et al., 2006; Heimisson et al., 2015). After the rifting episode, additional leveling surveys were conducted in 1989, 1995, 2000, 2005 and 2010, providing insights into the post-rifting adjustment of the volcanic system and magmatic processes, as well as deformation related to geothermal exploitation (Björnsson and Eysteinsson, 1998; Ágústsson, 2001; Theodórsson and Búi, 2006; Sturkell et al., 2008; Theodórsson and Búi, 2011; Drouin et al., 2017b). Figure 1.2 (b) shows the elevation change during the early stage of the Krafla rifting episode in 1975–1976 based on leveling measurements.

Tilt Measurements

Tilt measurement determines angular movements of the ground relative to the horizontal (e.g., Dzurisin, 2003; Gambino et al., 2014). Three types of tilt monitoring were implemented at Krafla: water-tube tiltmeters, electronic tiltmeters, and short-array optical leveling (e.g., Tryggvason, 1978, 1979; Sturkell et al., 2008). These measurements were initiated in 1976–1977, shortly after the first dike intrusion of the Krafla rifting episode. Although tilt data are not directly used in this thesis, they provided important constraints on the inflation-deflation cycles during the 1975–1984 rifting episode (e.g., Johnsen et al., 1980; Tryggvason, 1986, 1994). Figure 1.2(c) shows the time series of elevation at a geodetic benchmark at the Krafla caldera center during 1975–1995 combining leveling and tilt measurements.

After the 1975–1984 rifting episode, water-tube tiltmeter readings became less frequent and stopped 17 January 1990 (Tryggvason, 1995), while electronic tiltmeter operation continued until December 1994. Post-rifting tilt measurements using optical leveling were conducted 24 times between October 1984 and July 1994 (Tryggvason, 1995).

Measurements showed general inflation at Krafla ceased in 1989 and a slow deflation commenced. Optical leveling tilt measurements were resumed during the 2000–2005 period (Sturkell et al., 2008) and compared with the observations from 1994. During and after the rifting episode, the station closest to the inferred inflation-deflation center exhibited an upward tilt pointing away from the geothermal area. Because no tilt is expected directly above an inflation-deflation center, this observation indicates local deflation likely associated with geothermal exploitation (Tryggvason, 1995; Sturkell et al., 2008). Such a pattern helps distinguish geothermal-related deformation from broader tectonic or magmatic processes.

Electronic Distance Measurements

Electronic Distance Measurements (EDM) determines the distances between ground points using electromagnetic waves, typically in the visible or near-infrared spectrum (e.g., Rüeger, 2012; Bonforte et al., 2024). An instrument at one ground point transmits a modulated electromagnetic wave toward a corner-cube reflector at the other point and the distance is derived from either the travel time or the phase shift between the transmitted and reflected signals.

An early triangulation network in the NVZ was established to detect relative displacements between ground points and test Wegener's continental drift hypothesis (Niemczyk, 1943). In 1965, EDM was integrated with triangulation observations to remeasure the geodetic network, and subsequent surveys were conducted every few years (Gerke, 1974; Wendt et al., 1985). These surveys revealed slight contraction in the Krafla volcanic system between 1965 and 1971, prior to the rifting episode (Moller and Ritter, 1980). During the Krafla rifting episode, significant surface widening across the fissure swarm was recorded with EDM, providing constraints on the geometry of dikes formed during the rifting episode (Tryggvason, 1984; Hollingsworth et al., 2013). Figure 1.2(d) illustrates the cumulative widening along the Krafla fissure swarm during the 1975–1982 period, estimated from EDM data. When combined with other geodetic datasets, EDM observations also contributed to monitoring conditions within the magmatic system beneath the Krafla caldera, such as pressure changes in relation to inflation and deflation (e.g., Tryggvason, 1994; Árnadóttir et al., 1998). In this thesis, leveling and EDM data in Figure 1.2 provide important constraints to the numerical modeling of sequential dike intrusions during the 1975–1984 rifting episode.

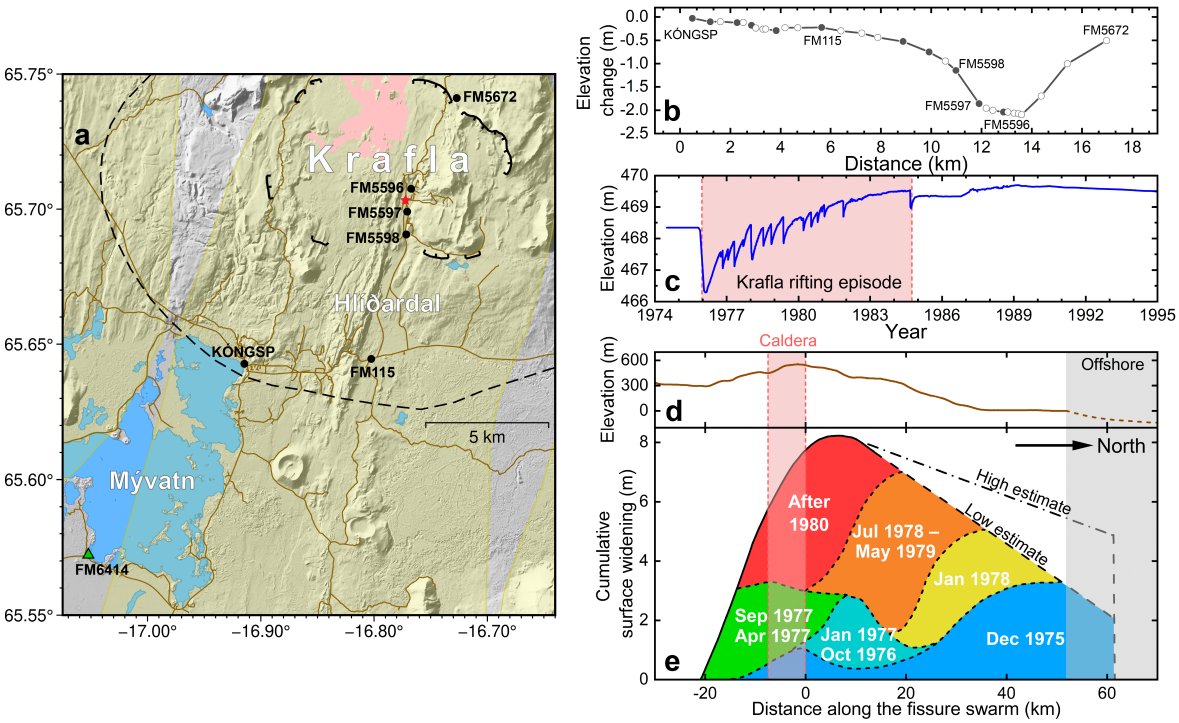


Figure 1.2 Overview of ground deformation in the Krafla volcanic system during 1974–1995. a) Zoomed-in map of the Krafla caldera with leveling benchmarks (black dots) presented in Figure 1.2(b). *The shaded background map shows the topography. The yellow shaded areas show the fissure swarms. The grided lines show the Krafla caldera and the dashed lines shows the southern boundary of the Krafla central volcano. The brown lines are the roads. The red star shows the location of the Krafla power plant. The light red area shows the lava field from the 1975–1984 rifting episode inside the caldera. The green triangle shows the referenced benchmark of Figure 1.2(c).* ***b) Surface elevation change along a leveling line between December 1975 and March 1976.*** *The leveling line extends eastward from KÓNGSP (near Lake Mývatn) and continues northward along Hlíðardalur after benchmark FM115. The leveling line follows approximately the roads. Black dots indicate observed elevation changes and white dots are interpolated according to the observations. Modified from Björnsson and Eysteinsson (1998).* ***c) Elevation time series at the center of the Krafla caldera (benchmark FM5596)****. The time series are based on leveling measurements (1975–1976), with the temporal gaps filled using tilt measurements inside the power plant (1976–1990) and in Hlíðardalur (1990–1995). The elevation is relative to the benchmark FM6414. Modified from Björnsson and Eysteinsson (1998).* ***d) Elevation profile along the Krafla fissure swarm,*** *smoothened using the Savitzky-Golay filter (Savitzky and Golay, 1964).* ***e) Cumulative surface widening in the fissure swarm during the 1975–1984 Krafla rifting episode*** *estimated with distance measurements, adapted from Tryggvason (1984). The elevation profile is extracted from a digital elevation model from Landmælingar Íslands [LMÍ] (2020).*

1.2.2 Space Geodetic Techniques

Global Navigation Satellite System

Global Navigation Satellite System (GNSS) geodesy can determine three-dimensional coordinates of ground points with millimeter-level precision (e.g., Hofmann-Wellenhof et al., 2008; Fernández et al., 2017; Aoki and Kreemer, 2024). GNSS refers to satellite constellations that provide positioning, navigation and timing services, including Global Positioning System (GPS, operated by the United States), Globalnaya Navigatsionnaya Sputnikovaya Sistema (GLONASS, operated by Russia), Galileo (operated by the European Union), and Beidou (operated by China). These satellites continuously transmit modulated electromagnetic signals, which are received by GNSS antennas connected to GNSS receivers, where the signals are recorded and preprocessed. From these signals, both the encoded information (used for code pseudorange) and carrier phases can be used to measure the distance between a satellite and the antenna.

The GNSS phase and code measurements are affected by various error sources from satellites, receivers, and the signal propagation. The observation equation can be written as (Hofmann-Wellenhof et al., 2008):

$$P_r(k) = r(k) + c\Delta t_r(k) - c\Delta t_s(k) + I(k) + T(k) + \varepsilon_P, \quad (1)$$

$$\Phi(k) = r(k) - \lambda N + c\Delta t_r(k) - c\Delta t_s(k) + I(k) + T(k) + \varepsilon_\Phi, \quad (2)$$

where $P_r(k)$ and $\Phi(k)$ represent the code pseudorange and carrier phase measurements at observation epoch k, respectively. Δt_s and Δt_r are the satellite and receiver clock errors, respectively. $r(k)$ denotes the distance between the satellite and the antenna. $I(k)$ and $T(k)$ represent the errors from signal propagating through the ionosphere and troposphere, respectively, and ε_P and ε_Φ denote other residual errors. The code pseudorange P_r is obtained by multiplying the signal propagation time by the speed of light c. The carrier phase Φ is the phase difference between the received signal and a locally generated reference, which also depends on precise timing of signal transmission and reception. To derive the absolute distance from carrier phase observations, the integer ambiguity N, namely the number of full wavelengths λ in signal propagation, must be resolved. GNSS carrier signals have wavelengths of ~20 cm, much shorter than the several-meter resolution of code-based measurements. As a result, phase observations offer much higher precision and are important for detecting small-magnitude deformation signals.

Since satellite and receiver clock errors (Δt_s and Δt_r, respectively) directly affect the signal timing, they have significant impact on positioning. While satellites have on-board atomic clocks, GNSS receivers typically use less stable but cheaper quartz clocks, of which the errors cannot be modeled empirically and must be estimated during positioning. Illustrated in Figure 1.3(a), each satellite distance measurement defines a sphere centering the satellite and a radius equal to the measured distance. The intersection of spheres from three satellites yields two possible antenna positions. A fourth satellite is required to simultaneously solve for the receiver clock error and eliminate the spurious solution, resulting in a unique antenna position. This is sometimes referred to as GNSS trilateration. Then the antenna's precise location can be translated to a ground point (benchmark) location.

To achieve millimeter-level accuracy in GNSS-based deformation monitoring, several conditions must be met, including dual-frequency observations (to eliminate ionospheric errors), sufficiently long observation durations (typically several hours or daily sessions), and appropriate error mitigation strategies (Bock and Melgar, 2016). Two primary GNSS positioning strategies are commonly applied: relative positioning (RP) based on network solutions, and Precise Point Positioning (PPP) based on single-station solutions (Hofmann-Wellenhof et al., 2008). RP, utilized by, e.g., the GAMIT/GLOBK software (Herring et al., 2018), eliminates common-mode errors with so-called double-difference observations, which are constructed by differencing simultaneous observations between GNSS sites and then between satellites. RP yields baseline vectors between sites that together form a baseline network. Then the baseline network can be aligned to a reference frame using reference stations with known positions and velocities, yielding absolute coordinates for all sites. PPP, utilized by, e.g., the GIPSY-X and PRIDE-PPP software (Bertiger et al., 2020; Geng et al., 2019) determines site coordinates independently of reference stations or baselines by applying corrections for satellite orbits and clocks, and modeling atmospheric delays and other error sources. Millimeter-level accuracy can be achieved using PPP with integer ambiguity resolution (PPP-AR), which fixes carrier phase ambiguities to integers by estimating ambiguity parameters using precise satellite products.

GNSS observations for ground deformation are conducted in either continuous (cGNSS) or campaign modes. cGNSS stations collect data continuously while campaign GNSS sites are measured episodically. Figure 1.3(b) and (d) show examples of a cGNSS station and a campaign site in the central part of the Krafla volcanic system, respectively. Data from both observation modes can be processed using the RP or PPP strategy to obtain daily coordinate time series. For continuous stations, this results in long-term deformation records. For campaign sites, multiple-day observations during each survey also enhance the reliability of deformation analysis. cGNSS stations offer good temporal resolution and coverage, and can capture transient volcanic deformation signals with high temporal resolution, but their spatial distribution is usually sparse due to cost and logistic limitations. The denser spatial coverage of campaign GNSS sites is useful for detecting various deformation patterns. GNSS coordinate time series analysis theory will be introduced in section 1.3, as well a background for short-term deformation anomaly detection.

GNSS measurements at Krafla began in 1986 as part of Iceland's first country-wide GNSS survey (Foulger et al., 1987), followed by a large-scale survey of the NVZ in 1987 to observe tectonic deformation and related processes (Jahn et al., 1990). Additional surveys were conducted between 1990 and 2002 to investigate post-rifting relaxation after the Krafla rifting episode and to support routine volcanic monitoring (e.g., Foulger et al., 1992; Heki et al., 1993; Hofton and Foulger, 1996; Sturkell et al., 2008). Since then, surveys have been conducted annually for evaluating deformation due to the multiple processes, including plate spreading, magmatic and geothermal processes. The GNSS network in the area has been densified since 2012, partly by incorporating benchmarks originally installed for gravimetric surveys by the Icelandic Geosurvey (ÍSOR) (Drouin et al., 2017b). In recent years, GNSS measurements have been coordinated by University of Iceland in collaboration with, and support from: Landsvirkjun (the National Power Company of Iceland), the IMPROVE project under EU Horizon 2020, and the Delft University of Technology, Netherlands.

Today there are more than 100 GNSS benchmarks across the Krafla and its surrounding areas, with an average of 78 sites measured every summer during 2010–2024 (e.g., Yang et al., 2025). Six cGNSS stations are operating by the time of writing: BJAC

since 2012, MYVA since 2006, KRAC since 2011, LHNC since 2019, SPBC since 2019, and THRC since 2011. Figure 1.4 shows the distribution of all GNSS sites and the temporal coverage of campaign surveys from 2002 to 2024. cGNSS data are downloaded daily at University of Iceland and processed with both RP and PPP strategies using GAMIT/GLOBK and GIPSY software, respectively. After each annual campaign, all GNSS data from Krafla are processed together with reference stations across Iceland and globally using GAMIT/GLOBK software (e.g., Hersir et al., 2020; Lanzi et al., 2022; Yang et al., 2023).

In this thesis, cGNSS coordinate time series enable the investigation of the magnitude and onset timing of the short-term deformation anomalies at Krafla during 2014–2015 and thereby their possible causes in Chapter 1. Moreover, long-term deformation recorded by GNSS surveys over the past two decades offers insights into both regional plate boundary processes and persistent localized deformation, studied in Chapter 3. These analyses are mainly based on the solutions derived using the GAMIT/GLOBK software.

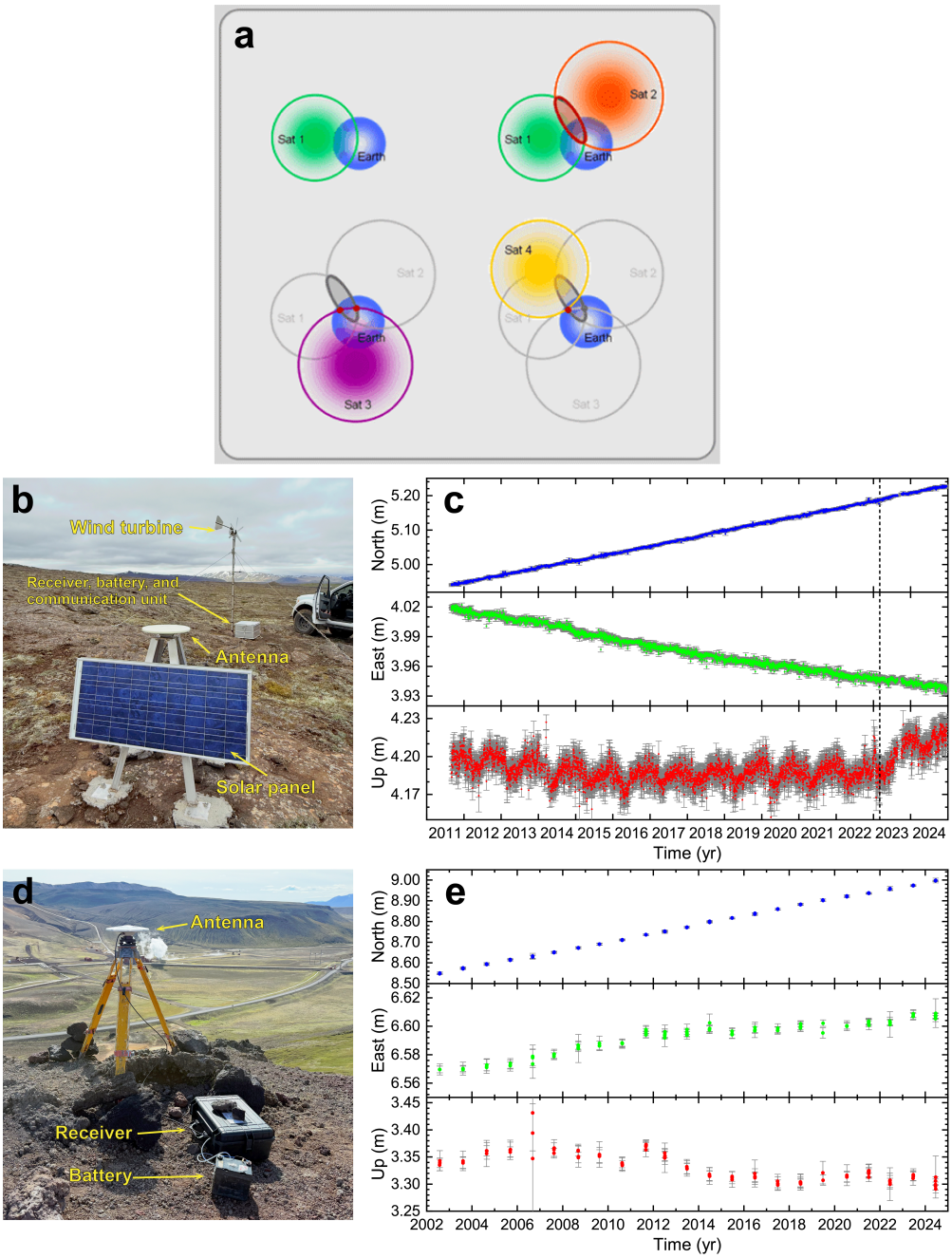


Figure 1.3 a) Schematic figure of GNSS trilateration. *The blue circle represents the Earth, while other circles indicate all locations determined from the distance ranging of satellites. Source: GIS Commons by Michael Schmandt, licensed under CC BY-SA 3.0, accessed on 4 July 2025 at https://giscommons.org/chapter-2-input/.* ***b) Continuous GNSS station THRC at Þeistareykir. c) Coordinate time series from the cGNSS site THRC.*** *The dots indicate the coordinate values (one value per day) and the grey lines are their uncertainties. The vertical dashed line indicates the beginning of an inflation period at Þeistareykir reported by Gudnasson et al. (2024).* ***d) Campaign GNSS site RAHO in the Krafla caldera. e) Coordinate time series from the campaign site RAHO.*** *Symbols have the same meanings as in Figure 1.3(c). The values in Figure 1.3(c) and (e) are the last digits of the coordinates under a topocentric reference system (NEU). The integer parts of the coordinates are (7335594, 15593234, 374) for site THRC and (7314748, 15717186, 623) for site RAHO (in meters). The coordinates are relative to ITRF2014 (Altamim et al., 2016).*

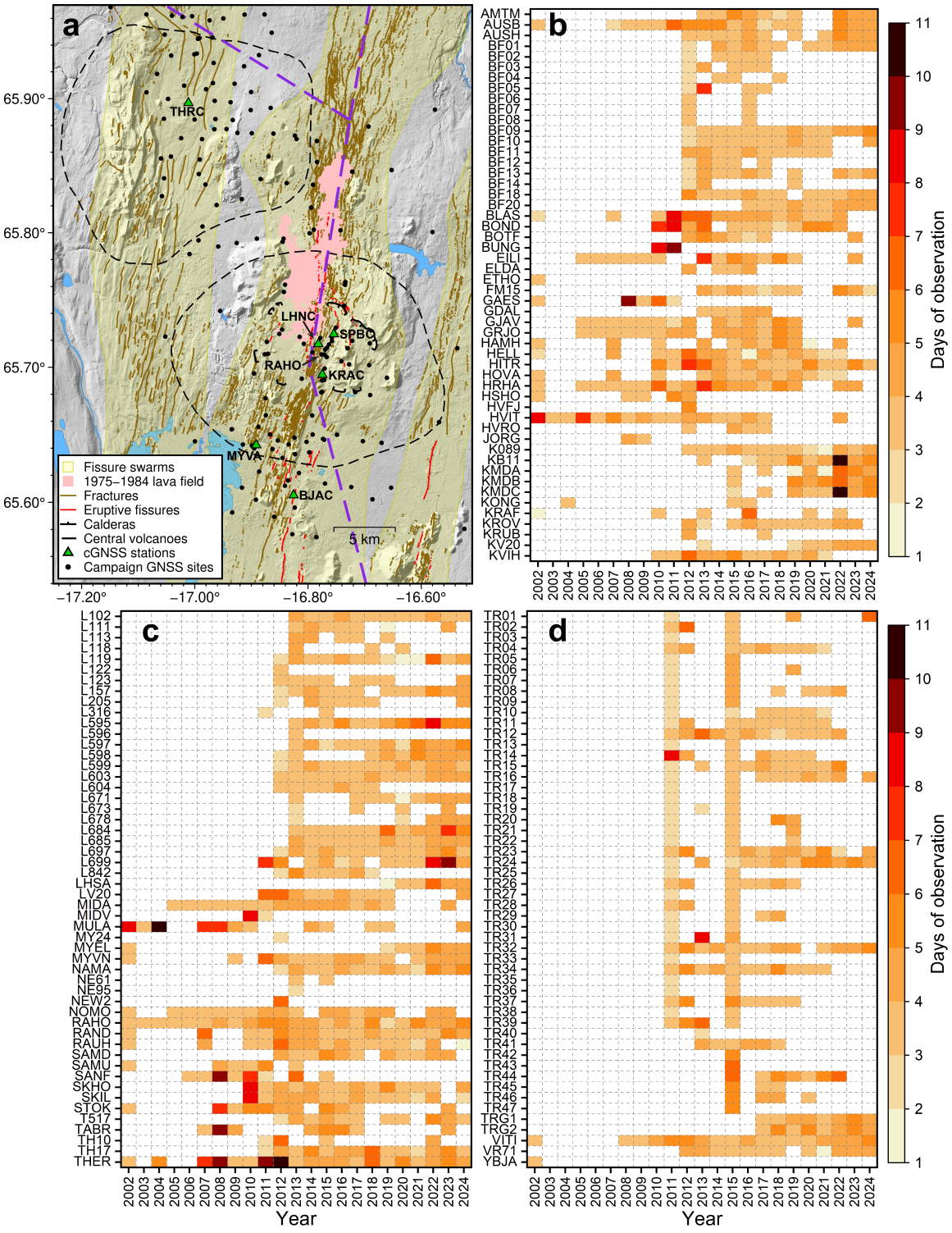


Figure 1.4 ***a) The distribution of GNSS sites in the central part of the Krafla volcanic system.*** *All the sites mentioned in this chapter are labeled. The purple dashed lines indicate the plate boundary axis, combined from Metzger et al. (2013) and Drouin et al. (2017a).* ***b), c) and d) Summary of campaign GNSS observations during 2002–2024.***

Interferometric Synthetic Aperture Radar

Interferometric analysis of synthetic aperture radar images (InSAR) can be used to determine one-dimensional ground displacements, projected along the line-of-sight (LOS) direction from a radar satellite to a location on the ground (Figure 1.5(a)). This is done by analyzing Synthetic Aperture Radar (SAR) images acquired at different epochs over the same area from the same satellite location (e.g., Massonnet et al., 1993; Hanssen, 2002; Ferretti et al., 2007). SAR synthesizes a large antenna aperture by combining successive microwave echoes acquired along the satellite flight path, to capture high-resolution images of ground targets. These images provide both intensity and phase information of the backscattered microwaves. Interferometric analysis of the complex-number phase signal from repeated SAR acquisitions is carried out to produce interferograms that contain phase differences ($\Delta\varphi_{int}$) resulting from several factors, expressed as (e.g., Sigmundsson et al., 2018):

$$\Delta\varphi_{int} = \Delta\varphi_{geom} + \Delta\varphi_{def} + \Delta\varphi_{atm} + \Delta\varphi_{pixel}, \quad (3)$$

where $\Delta\varphi_{geom}$ is the phases contribution from differences in satellite orbital position between acquisitions and a perspective effect from topography, $\Delta\varphi_{def}$ arises from surface deformation, $\Delta\varphi_{atm}$ is caused by variations in atmospheric conditions between acquisitions, and $\Delta\varphi_{pixel}$ is due to individual scatterers within an image pixel. The satellite positions required for calculating $\Delta\varphi_{geom}$ are obtained from high-precision orbit products by operating agencies. A digital elevation model (DEM), or multiple SAR acquisitions, can be used to reduce the topographic components in $\Delta\varphi_{geom}$ and derive ground displacements. Because the radar signal is periodic, interferometric analysis can only resolve the difference between two waveforms within one single cycle. Thus, the measured phase difference is wrapped within the range from $-\pi$ to π, where phase difference of $\pm\pi$ corresponds to a displacement equal to half of the radar wavelength along the LOS.

The near-polar orbits (Figure 1.5(a)) and mostly right-looking acquisition mode of SAR satellites (microwave pulses transmitted to the right of the satellite orbit) yield two main viewing geometries of interferograms, namely ascending (satellite moving from south to north) and descending (satellite moving from north to south). Figure 1.5(b) and (c) show examples of interferograms from ascending and descending tracks, respectively.

The reliability of a single interferogram is limited by atmospheric delays $\Delta\varphi_{atm}$ affecting the electromagnetic waves transmitted by radar satellites upon their travel to and from the Earth, temporal decorrelation due to changes in scattering properties of ground targets, and other noise sources (e.g., Zebker and Villasenor, 1992). To overcome these limitations, InSAR time series analysis using a stack of interferograms has been developed for continuous long-term deformation monitoring (e.g., Ferretti et al., 2001; Berardino et al., 2003; Hooper et al., 2004; Lanari et al., 2007). Two main approaches for InSAR times series analysis are so-called Persistent Scatterer InSAR (PS-InSAR) and Small Baseline Subset InSAR (SBAS-InSAR).

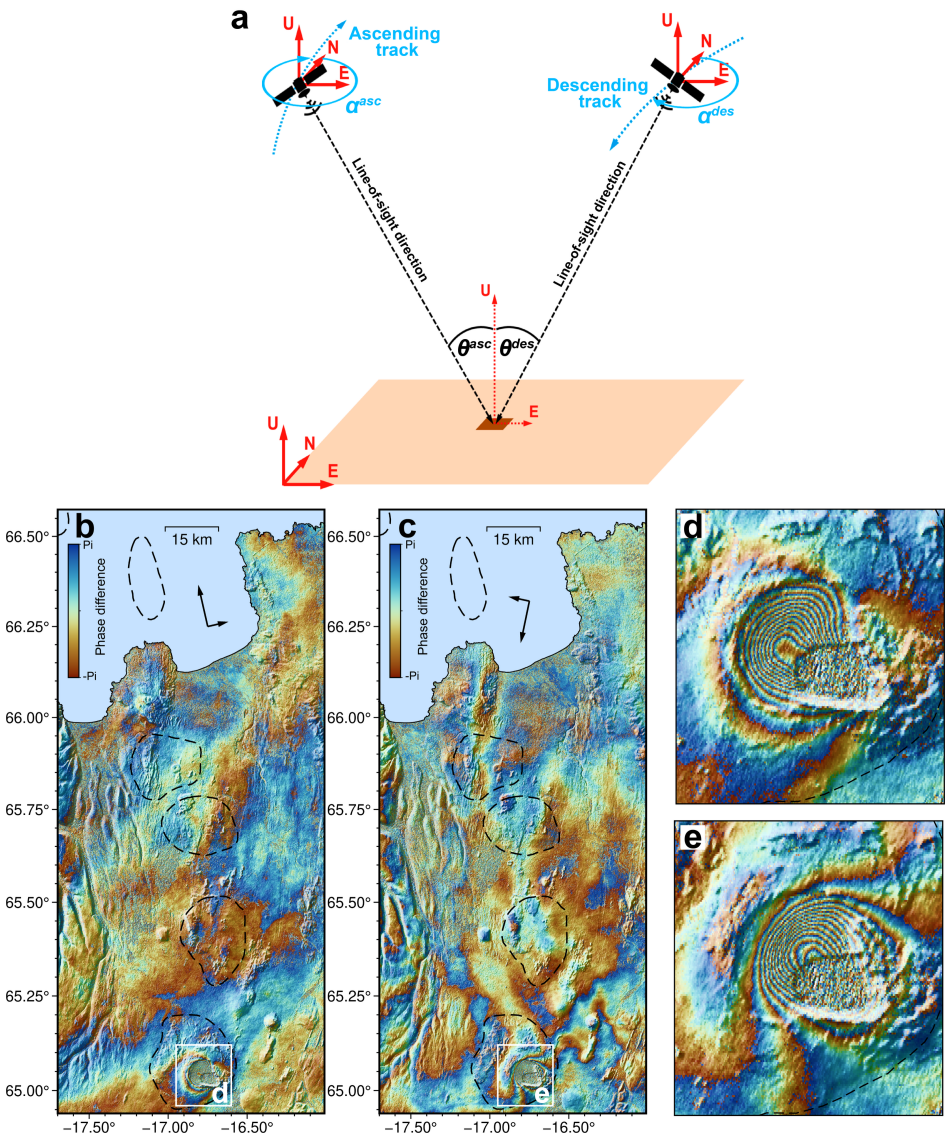


Figure 1.5 a) Illustration of InSAR line-of-sight direction for a right-looking satellite. *Right looking indicates that the microwave pulses are transmitted to the right of the satellite orbit. Roman alphabets have the same meaning as in Equation (4) and (5). Source: adapted from Fuhrmann and Garthwaite (2019), licensed under CC BY, originally published in Remote Sensing, https://doi.org/10.3390/rs11030241.* ***b) Interferogram generated with Sentinel-1 satellite ascending SAR acquisitions (Track 147) on 2 September 2021 and 3 September 2022.*** *The map area is the same as in Figure 1.1(b). Dashed lines indicate central volcanoes. Dense fringes inside the Askja central volcano (white rectangle) show rapid inflation reported by Parks et al. (2024). Other areas show no significant pattern, indicating small displacement within one year and that the interferogram is largely affected by the atmospheric errors. The arrows indicate the satellite directions of motion (long) and look side (short). Accessed from COMET-LiCS Sentinel-1 InSAR portal (https://comet.nerc.ac.uk/comet-lics-portal/; Lazecký et al., 2020).* ***c) Interferogram generated with Sentinel-1 satellite descending SAR acquisitions (Track 111) on 12 September 2021 and 25 September 2022. d-e) Zoomed-in views of the dense fringes in the Askja central volcano (white rectangle in Figure 1.5(b) and (c)), for ascending (d) and descending (e) tracks, respectively.***

PS-InSAR uses one SAR image as a reference and generates interferograms by pairing it with other acquisitions. It identifies point targets with stable scattering properties over time (namely persistent scatterers). The observed phase differences at these points are typically modeled to separate ground deformation from error sources such as atmospheric delays, satellite orbit inaccuracies, and topographic residuals. Since all interferograms share the same reference acquisition, variations in satellite geometry and ground scattering behavior across the observation period can obscure the identification of PS points and consequently impair the spatial coverage of PS-InSAR results (e.g., Ferretti et al., 2001). In contrast, SBAS-InSAR generates interferograms from SAR image pairs with small temporal intervals and satellite geometry differences to maintain the similarities of target scattering properties between acquisitions (known as coherence), and to increase observational redundancy. Deformation derived from all interferograms is processed using a least-square method to obtain deformation time series. The error sources can be modeled jointly with the deformation, or reduced by preprocessing of interferograms or postprocessing of deformation field using spatiotemporal filtering (e.g., Lanari et al., 2007; Fattahi et al., 2017; Morishita et al., 2020).

Overall, the precision of displacement measurements and velocity estimates from InSAR time series analysis can reach a few millimeters and sub-millimeter-per-year level, respectively, in the LOS direction, depending on the microwave frequency bands of different satellite missions, the spatiotemporal geometry of SAR acquisitions, data coherence, and error mitigation strategies (e.g., Lanari et al., 2007; Fattahi and Amelung, 2014, 2015). Longer-wavelength InSAR signals (e.g., L-band with a wavelength of ~24 cm) offer better penetration and coherence over vegetated or decorrelating surfaces, but generally provide lower measurement precision compared to shorter-wavelength systems (e.g., X- or C-band with wavelengths of ~3 and ~5.6 cm, respectively). The spatial resolution of interferograms ranges from sub-meter to hundreds of meters, according to different SAR imaging modes and the number of pixels combined during analysis (multi-looking) to increase coherence (e.g., Tadono et al., 2024; De Wit et al., 2024). The spatial resolution of PS-InSAR deformation fields depends on the density of PS points, whereas for SBAS-InSAR it is usually several tens of meters to 100 m determined by multi-looking. The temporal coverage and resolution vary with operational periods and revisit cycle of specific satellite missions, respectively (see Figure 1.6 for satellites covering the Krafla volcanic system). SAR satellites are typically designed for an operational period of 5–7 years but often operate for ten years or longer with proper maintenance and sufficient power supply.

The one-dimensional observations of distance change in the LOS direction is influenced by ground displacement both in horizontal and vertical components, which can be expressed as:

$$d_{los} = d_u \cos\theta - (d_e \cos\alpha - d_n \sin\alpha) \sin\theta, \quad (4)$$

where d_{los} presents the displacements in the LOS direction, d_u, d_e and d_n represent the displacements in up, east, and north components, respectively, α is the azimuth of the LOS vector, and θ is the incidence angle (shown in Figure 1.5(a); Motagh et al., 2017).

When InSAR observations are available from different viewing geometries, LOS displacement vectors can be decomposed into geographically meaningful components. However, limited to the two main viewing geometries (ascending and descending), InSAR observations are least sensitive to north-south displacements and it is difficult to resolve

three-dimensional ground displacements (e.g., Wright et al., 2004; Brouwer and Hanssen, 2024). Assuming north-south displacements have negligible influence on the LOS displacements, one ascending and one descending observation can be combined to decompose the ascending and descending LOS displacements into approximate estimates of east (near-east) and vertical (near-up) components:

$$\begin{pmatrix} d_{los}^{asc} \\ d_{los}^{des} \end{pmatrix} \approx \begin{pmatrix} \cos\theta^{asc} & -\cos\alpha^{asc}\sin\theta^{asc} \\ \cos\theta^{des} & -\cos\alpha^{des}\sin\theta^{des} \end{pmatrix} \begin{pmatrix} d_u \\ d_e \end{pmatrix}, \tag{5}$$

where the superscripts asc and des indicate the ascending and descending observations. Note that this can also be achieved using two ascending or descending observations with different viewing angles (Samsonov et al., 2017).

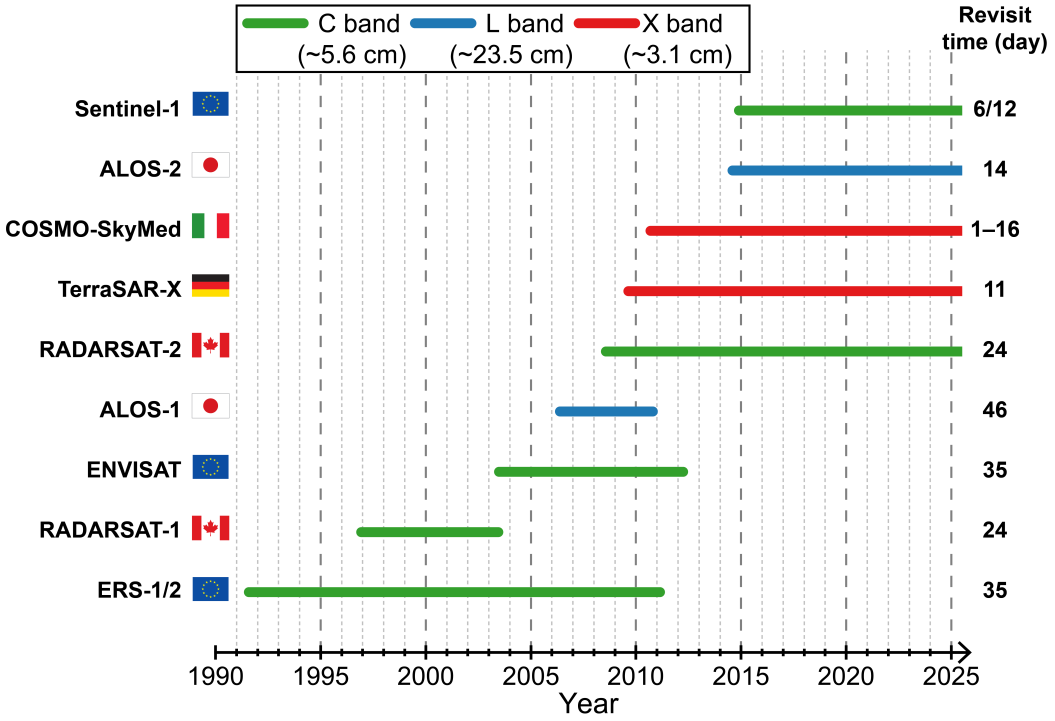


Figure 1.6 Temporal coverage of different SAR satellite missions over the study area. *The legend indicates the microwave frequency band and wavelength of the radar satellites. Revisit time refers to the interval between successive SAR acquisitions of the same area by a satellite, determined by its orbit, sensor characteristics, and imaging schedule.*

InSAR observations from multiple satellite missions have been used to monitor crustal deformation at Krafla. Sigmundsson et al. (1997), de Zeeuw-van Dalfsen et al. (2004), Henriot and Villemin (2005) and Ali and Feigl (2012) applied the InSAR technique to images from the European Remote-Sensing (ERS) satellite to study magmatic processes and post-rifting deformation in the 1992–1999 period, after the 1975–1984 Krafla rifting episode. Ali et al. (2014) further incorporated data from the European Environmental Satellite (EnviSat) to extend the observation span to 1993–2008. Metzger and Jónsson (2014)

implemented SBAS-InSAR technique with ERS images to investigate plate boundary deformation in north Iceland during 1992–2009. A more comprehensive analysis was conducted by Drouin et al. (2017b), by using both PS-InSAR and SBAS-InSAR techniques on images from ERS, EnviSat, RADARSAT-2, and TerraSAR-X missions, mainly to resolve geothermal deformation signals in the area. Since 2015, Sentinel-1 constellation, due to its open access and short revisit cycle (6 or 12 days), has played an important role in monitoring deformation processes across Iceland (Drouin and Sigmundsson, 2019; Cao et al., 2023) and in the Krafla volcanic system (e.g., Lanzi et al., 2023, 2024; Yang et al., 2025). Figure 1.6 shows the temporal coverage of these satellite missions for the area. In this thesis, Sentinel-1 SAR interferograms analyzed with SBAS-InSAR technique are used to estimate long-term deformation velocities in the central part of the Krafla volcanic system and to constrain the plate boundary deformation model in Chapter 3.

1.3 Modeling Transient Deformation

Transient deformation refers to time-varying, non-steady displacements, typically lasting from days to years, in contrast to long-term deformation velocities resulting from, e.g., tectonics, glacier isostatic adjustment (GIA), and some persistent magmatic activities. Transient deformation signals are induced from diverse geophysical processes, including post-seismic or post-rifting viscoelastic relaxation, after-slip following large earthquakes, poroelastic rebound due to fluid pressure change, slow slip events on faults, short-term hydrological forcing such as floods or droughts, and short-term magmatic activity (e.g., Dragert et al., 2001; Freed and Bürgmann, 2004; Borsa et al., 2014; Sobrero et al., 2020; Li et al., 2022; Eskandari and Scaioni, 2024; Wallace and Rollins, 2024). Characterizing the timing, duration and magnitude of transient signals is important for understanding Earth's realistic rheological and hydrological properties, as well as for improving geohazard assessments. For instance, timescales and magnitudes of viscoelastic relaxation deformation reflect the effective viscosity of lower crust and upper mantle (e.g., Suito, 2017; Lee et al., 2025). Transient deformation driven by extreme rainfalls reveals possible influences on urban infrastructures such as roads and underground (Li et al., 2024).

cGNSS coordinate time series provide a powerful tool for capturing transient signals, taking advantages from its long temporal coverage, daily resolution and millimeter precision. However, the detection and interpretation of these signals require vigorous analysis framework, where GNSS time series analysis theory offers a robust methodological foundation. In the Krafla volcanic system, a transient deformation signal is observed during 2014–2015 from cGNSS time series, featuring possible variations in the deformation velocity (Lanzi et al., 2023). This observation motivates a review of GNSS time series analysis theory, focusing on modeling transient signals of velocity changes, to support the investigation of short-term deformation at Krafla in Chapter 2.

1.3.1 GNSS Coordinate Time Series Analysis

Deterministic model

Conventionally, a cGNSS coordinate time series can be modeled as follows (Nikolaidis, 2002):

$$y = a + bt + \sum_{i=1}^{n}[d_i^1 \sin(\omega_i t) + d_i^2 \cos(\omega_i t)] + \sum_{j=1}^{q} \delta_j(t) + \varepsilon, \quad (6)$$

where y is the coordinate at time t, a represents initial site position, b represents the linear deformation velocity, and ε represents the residuals. The third term indicates periodic signals, with n being the number of them, ω_i being their angular frequencies, and d_i^1 and d_i^2 representing the amplitudes of their sine and cosine harmonics, respectively. The fourth term $\delta_j(t)$ accounts for transient or instantaneous signals (discussed in a subsequent paragraph), with q denoting the number of such events or components.

The most significant periodicities are the annual ($\omega = 2\pi$) and semi-annual ($\omega = 4\pi$) signals. These originate from both realistic geophysical processes and non-geophysical artifacts. Geophysical sources include atmospheric, oceanic and hydrological loadings, as well as thermal expansion of the surrounding host rock (e.g., Tregoning and van Dam, 2005; Fu et al., 2012; Li et al., 2025). Non-geophysical factors can involve systematic errors in data and thermal expansion of GNSS monuments (e.g., Yan et al., 2009; Hohensinn et al., 2024). Additional periodicities haven been also observed and modeled (e.g., Altamimi et al., 2023; Ma et al., 2025). These include the GPS draconitic harmonics (351.2 days and its integer submultiples), resulted from repeating orbital geometry of GNSS constellations; the Chandlerian signal (~433 days) related to the wobble of Earth's rotation axis; and fortnightly signals (13–15 days) due to residuals in tidal corrections (e.g., Penna et al., 2007; Ray et al., 2008; Amiri-Simkooei et al., 2017). Figure 1.7 shows simple deterministic models fitting cGNSS time series at station THRC in Figure 1.3 (c) and their corresponding residuals.

The term $\delta_j(t)$ in Equation (6) represents various transient or instantaneous signals. For example, post-seismic deformation signal in a cGNSS time series may be described using a combination of logarithmic and/or exponential functions, expressed as:

$$\delta_1(t) = m_1 \ln(1 + \frac{\Delta t}{\tau_1}), \quad (7)$$

$$\delta_2(t) = m_2 \left(1 - e^{-\frac{\Delta t}{\tau_2}}\right), \quad (8)$$

where m_1 and m_2 are the amplitudes of the transient, τ_1 and τ_2 are relaxation times, and Δt is the elapsed time after the earthquake occurrence, with $\Delta t > 0$ (e.g., Tobita, 2016; Bevis et al, 2020; Sobrero et al., 2020). Instantaneous offsets in the time series, typically resulting from antenna maintenance, earthquakes or changes in processing strategies, can be modeled using a Heaviside step function (Gazeaux et al., 2013):

$$\delta_3(t) = m_3 \cdot \mathrm{H}(t - t_0), \quad (9)$$

where m_3 is the offset magnitude, t_0 is epoch of the offset, and H( ) is the Heaviside function:

$$\mathrm{H}(t - t_0) = \begin{cases} 0, & t < t_0 \\ 1, & t \geq t_0 \end{cases}. \tag{10}$$

These are only two representative components of $\delta(t)$ and the same function can be added for multiple times to account for successive transient or instantaneous events. Therefore, the formulation of $\delta(t)$ is tailored based on local conditions and research objectives. Figure 1.8 shows an example of transient and instantaneous deformation signals induced by an earthquake.

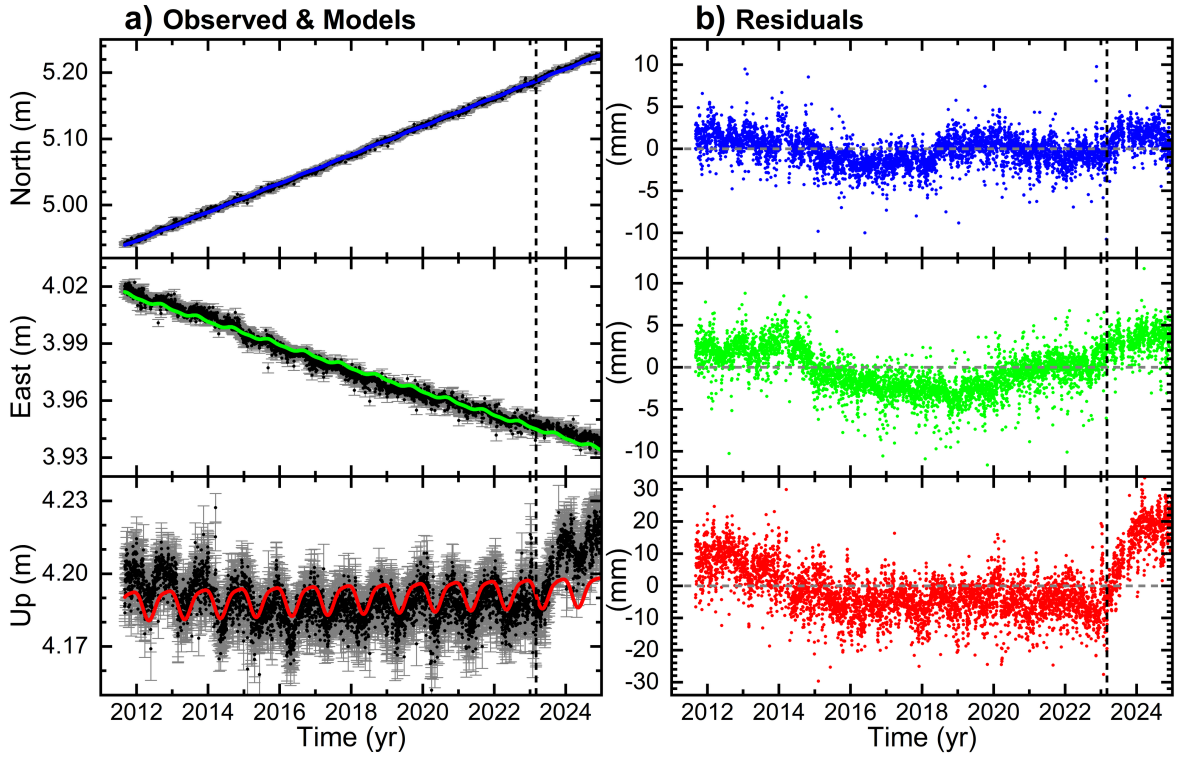


Figure 1.7 a) Deterministic models (colored lines) fitting the cGNSS coordinate time series (black dots) at station THRC and b) their corresponding residuals. *Grey lines indicate the observation uncertainties. Vertical dashed lines indicate the onset timing of the inflation period reported by Gudnasson et al. (2024). The deterministic model only includes linear deformation velocity, annual signal, and semi-annual signal.*

However, some parameters in these terms, for example, angular frequencies ω_i, relaxation times τ and the offset timing t_0 cannot be estimated simultaneously with their amplitudes due to strong mutual correlations. Instead, angular frequencies ω_i are commonly determined from frequency-domain analysis or similar time-domain estimation (e.g., Amiri-Simkooei et al., 2007; Feng et al., 2017; Zhou et al., 2019). Offset epochs t_0 are usually acquired from station operation logs, earthquake catalogues or manual inspection while the relaxation times τ can be estimated via non-linear inversions. Once these parameters are fixed, a simple least square estimation (LSE) method can be applied to estimate all the amplitudes together with the linear trends and initial position. Additionally, the amplitudes

of periodicities can be time-varying due to the dynamics of their geophysical contributors (e.g., Klos et al., 2018; Wu et al., 2023; Deng et al., 2025).

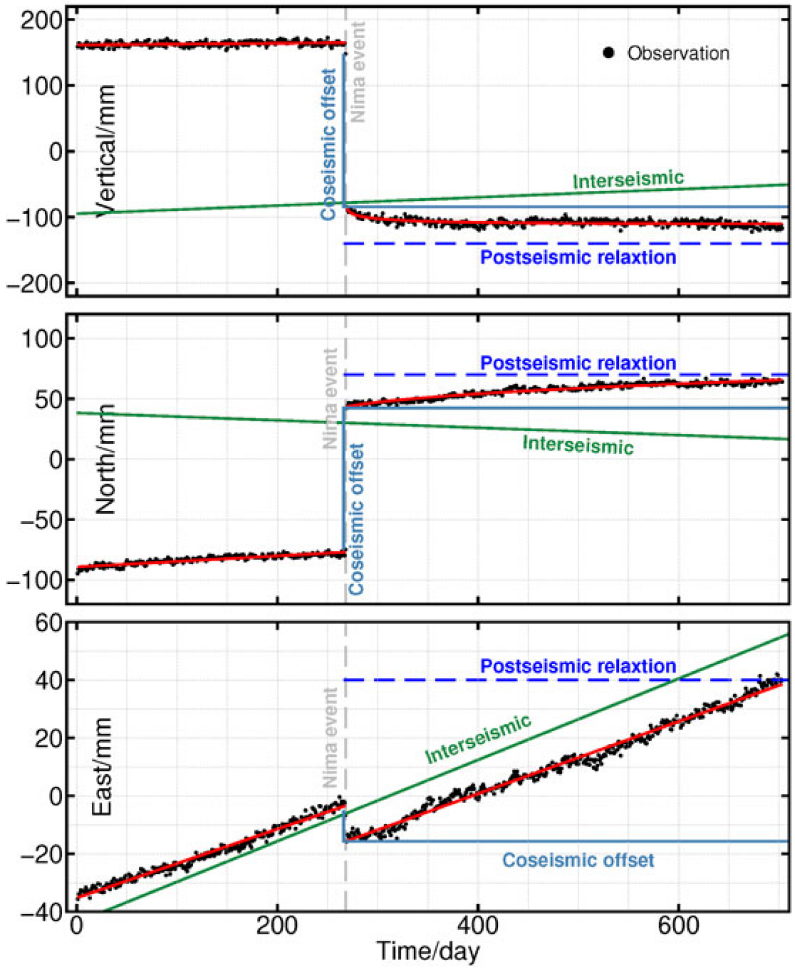


Figure 1.8 cGNSS coordinate time series demonstrating an instantaneous coseismic offset and a transient post-seismic deformation signal of the 2020 Mw 6.4 Nima Earthquake in Central Tibet, China. *The interseismic line corresponds to the linear deformation velocity in Equation (6) of this thesis. Source: adapted from Liu, X, et al. (2023), licensed under CC BY, originally published in Frontiers in Earth Science, https://doi.org/10.3389/feart.2022.1012773.*

Outliers may exist in cGNSS time series due to poor observation conditions or temporary measurement anomalies. If not properly addressed, they can bias model estimation significantly. Therefore, for many methods that are not robust to such deviations, outlier removal is necessary. This is often implemented by first estimating a simplified deterministic model and then analyzing the residuals using statistical criteria or more advanced methods (e.g., Nikolaidis, 2002; Qianqian and Qingming, 2013; Klos et al., 2015). Commonly used criteria include Interquartile Range (IQR), Median Absolute Deviation (MAD) and standard-deviation-based confidence intervals. Outlier removal, together with

offset detection and correction, are usually implemented iteratively prior to accurate estimation of the deterministic model, denoted as the preprocessing of GNSS coordinate time series (e.g., Altamimi et al., 2016; Altamimi et al., 2023).

Stochastic model

The LSE method assumes that the residuals ε are white noise (WN), which are uncorrelated between epochs and follow a Gaussian distribution. However, complex periodicities with temporal variations in GNSS coordinate time series cannot be fully addressed using simplified deterministic models, particularly those only including constant-amplitude annual and semi-annual signals. Model misfits, as well as unmodeled transient and instantaneous signals, lead to time-correlated residuals. Such time-correlation can be described using power-law noise (PLN), characterized in the frequency domain by:

$$P(f) = P_0 \left(\frac{f}{f_0}\right)^{\kappa}, \tag{11}$$

where $P(f)$ is the power spectral density at frequency f, and P_0 and f_0 are constants (Williams, 2003). The spectral index κ is the slope of the power spectrum, ranging from -2 to 0 in GNSS time series. When κ is 0, -1 and -2, the noise behaves as WN, flicker noise (FLN) and random-walk noise (RWN), respectively. Figure 1.9 illustrates the power spectra from residual time series of a cGNSS network.

In the time domain, PLN behavior can be expressed through the covariance matrix ($\mathbf{J}_\kappa$) of the time series:

$$\mathbf{J}_\kappa = \mathbf{T}\mathbf{T}^T, \tag{12}$$

where $\mathbf{T}$ is the Toeplitz matrix:

$$\mathbf{T} = \Delta T^{-\kappa/4} \begin{bmatrix} \psi_0 & 0 & 0 & \cdots & 0 \\ \psi_1 & \psi_0 & 0 & \cdots & 0 \\ \psi_2 & \psi_1 & \psi_0 & \cdots & 0 \\ \vdots & \vdots & \vdots & \ddots & \vdots \\ \psi_n & \psi_{n-1} & \psi_{n-2} & \cdots & \psi_0 \end{bmatrix}, \tag{13}$$

$$\psi_n = \frac{-\frac{\kappa}{2}\left(1-\frac{\kappa}{2}\right)\cdots\left(n-1-\frac{\kappa}{2}\right)}{n!}, \tag{14}$$

where ΔT is the sampling interval of the time series (Williams, 2003). Mao et al. (1999) showed that ignoring time-correlated noise can cause underestimated uncertainties by up to an order of magnitude. To obtain realistic estimate uncertainties, the residuals from the LSE method must be assessed (e.g., Bos et al., 2008; Langbein, 2012; Bos et al., 2013). Typically, noise amplitudes are estimated using maximum likelihood estimation while the optimal combination of different noise types is selected based on statistical model selection criteria.

While PLN is widely used, other stochastic models, for instance, generalized Gauss-Markov process, t-distributed deviations, and time-varying variance, have also been applied for stochastic modeling of GNSS time series (e.g., He et al., 2019; Dorndorf et al., 2021; Wang et al., 2022). When sufficient periodicities are included in the deterministic model,

temporal correlation in residuals can be represented by a first-order autoregressive process (AR(1)), where each residual is correlated only with the one at its previous epoch (Amiri-Simkooei et al., 2007). Studies of spatially correlated noise have further enhanced our understanding on the behavior and causal factors of the GNSS residuals (e.g., Wdowinski et al., 1997; Shen et al., 2014; Niu et al., 2023). Noise assessments can also be performed using other methods such as least square variance component estimation.

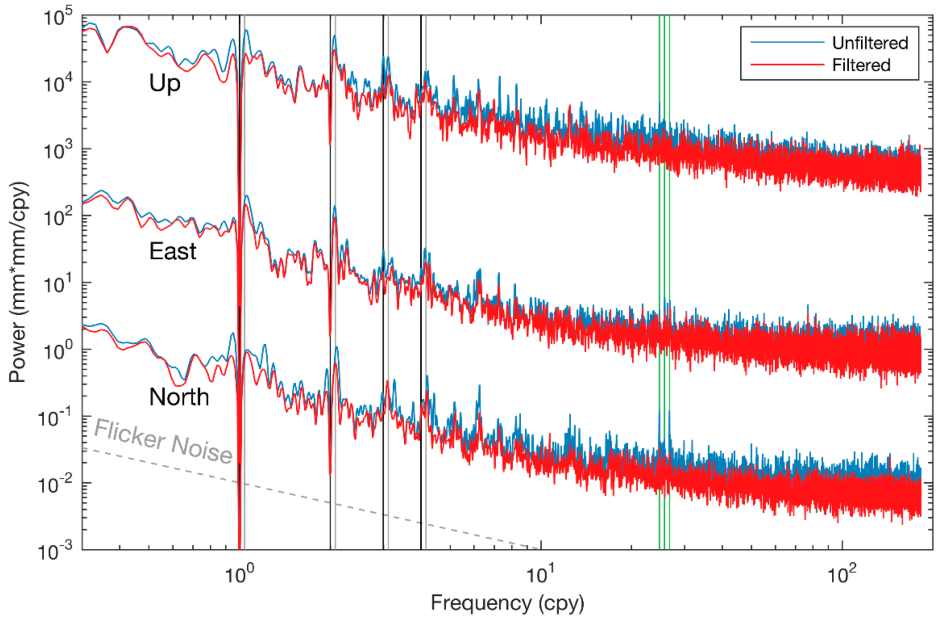


Figure 1.9 Stacked power spectra of cGNSS residual time series with annual and semi-annual signals removed (unfiltered). *The stacked power spectra shown here is the spectrum of all the residual time series from a cGNSS network are aligned together and averaged at each frequency. The cGNSS network here is Crustal Movement Observation Network of China. The grey line shows the characteristic of flicker noise. The filtered curve is the spectra of residuals further with spatially correlated noise removed. Vertical black and gray lines indicate the annual (1 cpy) and draconitic (1.04 cpy) oscillations and their harmonics up to the 4th. Vertical green lines indicate the frequencies of 24.75, 25.74, and 26.74 cpy from semidiurnal tides. Source: from Yuan et al. (2018), licensed under CC BY, originally published in Remote Sensing, https://doi.org/10.3390/rs10091472.*

1.3.2 Modeling Velocity Changes in Deformation Time Series

Equation (6) models the linear deformation velocity of GNSS sites with the term bt. However, this assumption of constant velocity does not always hold. Temporal changes in deformation velocity can, for example, manifest short-term volcanic-hydrothermal processes, tectonic slow slip events, and variations in groundwater level (e.g., Davis et al., 2006; Borsa et al., 2014; Geirsson et al., 2010). Timings of velocity changes, defined as velocity break points, provide valuable information of these underlying processes, while magnitudes of velocity changes are essential for following geophysical modeling and interpretation. Two

main types of methods have been developed to model these velocity changes: continuous time-varying models and piecewise linear models.

Continuous time-varying models capture velocity changes using advanced mathematical methods. For instance, Bos et al. (2020) extended the linear term bt in Equation (6) to a higher-order polynomial to accommodate varying deformation velocity. Kalman filter offers a recursive framework allowing continuous variations of deformation velocity as the observations are incorporated sequentially (Didova et al., 2016). Moreover, methods such as wavelet analysis and singular spectrum analysis decompose the time series into components with different temporal scales. The lower-frequency or smooth components are often interpreted as underlying trends (Borghi et al., 2012; Wang et al., 2016; Shi et al., 2025). Figure 1.10 shows a synthetic GNSS time series with a velocity change, modeled using a polynomial. It demonstrates that these continuous models can flexibly fit the observations and thereby help identify potential variations in deformation velocity. However, they do not report explicit estimates of velocity break points and change magnitudes, which requires additional analysis for further interpretation. Thus, despite the modeling accuracy, such methods may lack intuitiveness to discrete geophysical processes.

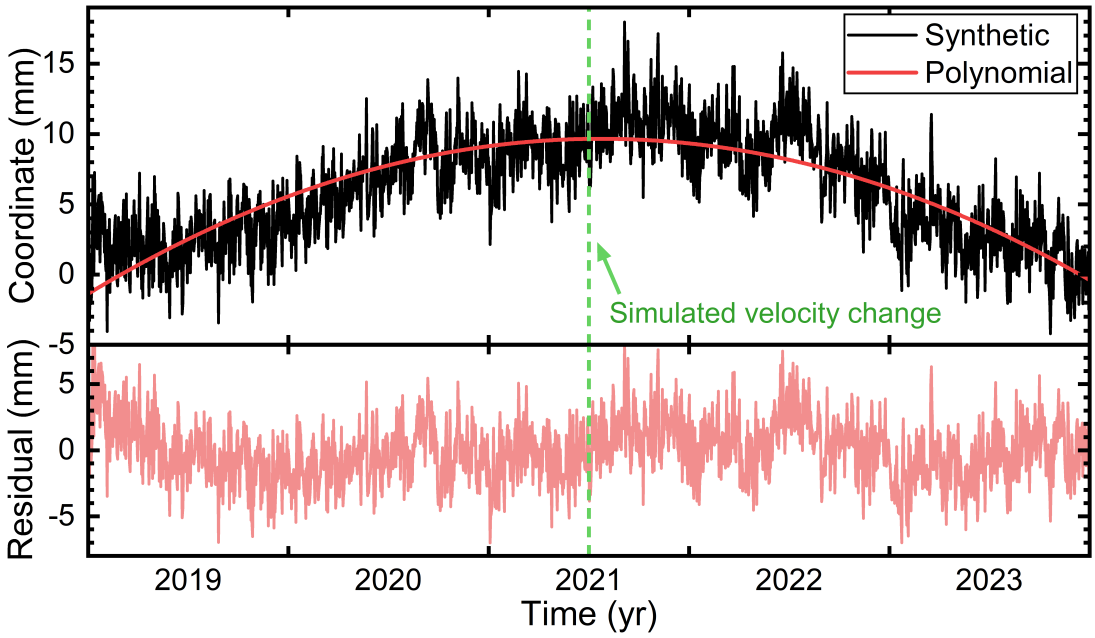


Figure 1.10 A synthetic cGNSS coordinate time series with the velocity change from 5 mm/yr to -5 mm/yr at decimal year 2021.5, modeled with a second-degree polynomial. *No periodic signal is simulated in the synthetic time series. A white noise with an amplitude of 1 mm and a flicker noise with an amplitude of 4 mm/yr$^{0.25}$ are included in the synthetic time series.*

Piecewise linear models are transparent for estimating both break points and velocity change magnitudes, by introducing a new component of transient deformation:

$$\delta_4(t) = h(t - t_1)\mathrm{H}(t - t_1), \tag{15}$$

where h is the magnitude of velocity change and t_1 is the break point. The Heaviside function $\mathrm{H}(t - t_1)$ equals zero before the break point t_1 and one afterwards (Equation (10)). Similar to other transient components in Equation (7), (8), and (9), the velocity change magnitude cannot be jointly estimated with its break point using a simple LSE framework, due to strong mutual correlation. Previous studies have applied statistical criteria to determine break points in advance (e.g., Benciolini et al., 2012; Vitti, 2012; Bos et al., 2018; Wu et al., 2018). These criteria are usually based on minimizing the misfit of the deterministic model and yield only optimal break points. Then the velocity change magnitudes can be estimated from the LSE method. Nevertheless, these methods do not report uncertainties for the detected break points, which impairs the reliability of subsequent geophysical interpretation. Another approach to detect break points with uncertainties is Bayesian modeling, which infers the posterior distribution of model parameters and thereby obtains estimates and their uncertainties jointly. For instance, Liu, Elliott, et al. (2023) determined the onset of volcanic unrest with break points in cGNSS time series inferred from Bayesian modeling, and Oelsmann et al. (2023) established piecewise linear model with instantaneous offsets for coastal vertical deformation time series using Bayesian modeling. However, these Bayesian approaches did not consider FLN in the residuals, which may undermine the accuracy of modeling and uncertainty assessments.

Chapter 2 in this thesis addresses these issues by developing a Bayesian modeling scheme that jointly estimates break points, velocity change magnitudes, stochastic model of PLN, and their uncertainties. This method is applied to infer the short-term deformation anomalies at Krafla during 2014–2015 and thereby to explore their possible causal factors and potential indications on realistic Earth's properties.

1.4 Modeling Dike Intrusions

Dike intrusion is a fundamental process transporting magma vertically and laterally in the Earth's crust (e.g., Dahm 2002; Daniels and Menand 2015; Urbani et al. 2018). Dikes are usually fed by subterranean magma bodies, that are distributed across a range of depth, from a few kilometers beneath the surface down to the crust-mantle boundary (Cashman et al., 2017; Edmonds et al., 2019). Geochemical analyses of erupted lavas have revealed that dike intrusions in a short period (months to years) in the same area can be fed by multiple sources (e.g., Árnadóttir et al., 1998; Ayele et al., 2009; Matthews et al., 2025). Therefore, I here denote the crustal volume that accumulates magma and feeds dike intrusions as a magma domain, consisting of partial melt, magma mush and hot solid rock, distributed over a depth interval, as defined by Sigmundsson et al. (2024). Prior to diking, magma accumulation within the domain increases internal pressure. When the pressure exceeds a failure limit of the magma domain, magma flows out and initiates a dike. Subsequent dike propagation is affected by a variety of factors, inducing variations in propagation direction, rate and geometry of dikes (e.g., Roper and Lister, 2007; Maccaferri et al., 2010; Sumita and Ota, 2011). Therefore, to understand how dike intrusions initiate and evolve, this section first reviews the failure conditions of magma domains and the physical models describing dike propagation.

At extensional plate boundaries such as Krafla, repeated lateral dike intrusions often occur in rifting episodes lasting from months to years, with individual dikes propagating up to tens of kilometers along rift zones. The Mývatn and Krafla rifting episodes are both classic

examples, where temporal sequences of dikes during rifting episodes release stress in plate boundary deformation zones accumulated over large timescales (centuries) due to plate movements (e.g., Abdallah et al. 1979; Paquet et al. 2007; Wright et al. 2012). Such dikes can cause meter-scale ground deformation, trigger normal faulting, and lead to eruptions (e.g., Björnsson et al. 1977; Biggs et al. 2009; Grandin et al. 2010; Parks et al. 2023, 2025). To further understand the controlling factors of dike sequences in a rifting episode, a numerical model proposed by Buck et al. (2006) is reviewed.

1.4.1 Dike Initiation

Dike intrusions initiate when the failure limit of magma domains is achieved. Understanding the failure criteria for host rocks is important to determine the initial conditions of dike propagation. Brittle failure criteria, including tensile and shear failure, describe the conditions where host rock undergoes brittle fracturing, and have been applied to dike initiation studies since the 1970s. Blake (1981) derived the maximum magma volume in a magma body based on tensile failure. Since then, the tensile failure criterion has been widely used in dike models. The tensile failure criterion applied to the host rock around a magma domain can be expressed as (Zhan and Gregg, 2019):

$$-\sigma_3 - T_0 > 0, \tag{16}$$

where σ_3 represents the least compressive stress (minimum principal stress, taking compression as positive hereinafter), and similarly σ_1 and σ_2 are the maximum and intermediate principal stress, respectively. T_0 is the tensile strength of the host rock. Although the tensile failure criterion is mathematically simple, the inferred values of T_0 span a wide range depending on the observational or experimental method. Blake (1981) suggested a value of 10–50 MPa for T_0, while later laboratory measurements reported lower values of ~1–~20 MPa (Zhan and Gregg, 2019) and geodetic inversions inferred T_0 values below 10 MPa (Jónsson, 2012).

Although the shear failure is not usually related to dike initiations, once happened prior to the tensile failure, it can redistribute the stress around a magma domain and weaken the host rock so that the tensile failure can follow (e.g., Gerbault et al., 2012; Currenti and Williams, 2014; Zhan and Gregg, 2019; Gregg et al., 2022). The Mohr-Coulomb criterion of shear failure can be written as (Zhan and Gregg, 2019):

$$\frac{\sigma_1-\sigma_3}{2}\cos\varphi - \frac{\sigma_1+\sigma_3}{2}\tan\varphi > C_0, \tag{17}$$

where C_0 represents the cohesion of the host rock, and φ is the internal friction angle which ranges 15°–35°. C_0 can be estimated empirically with Young's modulus (E) based on rock experiments, where $C_0 = E \times 10^{-3}$ (Hoek, 1990; Bradford et al., 1998; Dinçer et al., 2004; Jaeger et al., 2007). Taking E of 5–80 GPa, C_0 ranges from 5 to 80 MPa. This implies that the failure limit of a magma domain may not strictly follow the tensile strength of host rock.

In addition, host rock behavior may deviate from pure elasticity once the elastic limit is exceeded. For instance, Head et al. (2021) demonstrated that, under a geotherm of 30 K/km and a representative reservoir depth of 5 km, thermo-viscoelastic deformation allows

magma bodies to sustain overpressure ~10% to ~45% higher than in an elastic model before tensile failure occurs. Plastic deformation can also occur when the crustal thermal structure is disturbed by long-lived magma domains, or when the relevant deformation occurs near the brittle-ductile transition zone (e.g., Del Negro et al., 2009; Simakin and Ghassemi, 2010; Head et al., 2021). Therefore, Currenti and Williams (2014) adopted the Drucker-Prager criterion as a failure condition, assuming perfect plastic deformation of the host rock:

$$K + \alpha I_1 - \sqrt{J_2} = 0, \tag{18}$$

where I_1 and J_2 represent the first stress invariant and second invariant of deviatoric stress tensor, respectively. Namely, $I_1 = \sigma_1 + \sigma_2 + \sigma_3$ and $J_2 = \frac{1}{6}[(\sigma_1 - \sigma_2)^2 + (\sigma_2 - \sigma_3)^2 + (\sigma_3 - \sigma_1)^2]$. The coefficients K and α are related to the internal friction angle φ and cohesion C_0:

$$K = \frac{6C_0 \cos\varphi}{\sqrt{3}(3 - \sin\varphi)}, \tag{19}$$

$$\alpha = \frac{2\sin\varphi}{\sqrt{3}(3 - \sin\varphi)}. \tag{20}$$

Combining the shear failure and this condition, Currenti and Williams (2014) explored the mechanical stability of magma domains surrounded by a ductile shell. However, the relationship between this failure condition and dike initiations remains unclear.

Although plastic and viscoelastic behaviors can influence the mechanical responses of host rock, in the upper crust with relatively low temperature and pressure, brittle failures are still representative indicators of the stress status around magma domains (Lengline et al., 2008). Based on tensile failure criterion, Albino et al. (2018) considered the contribution of pore fluid pressure to the failure of magma bodies, and Sigmundsson et al. (2020) developed the failure limit of a buoyant magma body under external stresses, which can be expressed as:

$$p_m + p_b + p_u > P_o + \sigma_e, \tag{21}$$

where p_m is the magma overpressure in the magma domain, p_b is the buoyancy pressure due to the density difference between the magma and the host rock, p_u indicates a buoyant magma body increases in thickness, P_o is the failure limit of the host rock, and σ_e is the deviatoric stress at the boundary of the magma domain due to all external processes acting perpendicular to the plane of failure, including tectonics, surface loading, and topographic effects. This study (Chapter 3) uses this criterion to evaluate the initial condition for failure of a magma domain and further incorporates additional buoyancy pressure generated during vertical magma ascent in the crust prior to lateral emplacement.

1.4.2 Dike Propagation

Dike propagation models primarily aim to predict the temporal evolution of a single dike, including its geometry, propagation velocity, and magma pressure distribution. Traditionally, there have been two main schools of thought for modeling vertical propagation of a single

dike (Nakashima, 1993; Rivalta et al., 2015). One emphasizes the resistance of host rock to fracturing, deriving dike geometry from the minimum fluid pressure required to maintain equilibrium of an open fluid-filled crack, known as the Weertman school of thought (Weertman, 1971; Weertman, 1973). The other emphasizes the stress in viscous magma flow to predict dike propagation dynamics, known as the lubrication-theory school of thought (e.g., Lister and Kerr, 1991; Roper and Lister, 2007).

For the Weertman school of thought, dike propagation is modeled as a fracture process that is mechanically independent of its feeding source(s) and driven solely by buoyancy. The buoyancy-induced stress within the magma must overcome the mechanical resistance of the surrounding host rock, which is characterized by its fracture toughness. From the mechanical equilibrium between buoyant stress and the fracture resistance, these models derive dike geometry for a given volume of intruded magma. However, observations of dike intrusions at many volcanoes indicate that shallow dikes often remain hydraulically or mechanically coupled to their feeding source(s) over at least partial propagating distance (e.g., Tryggavason, 1984; Owen et al., 2000; Nishimura et al., 2001; Wright et al., 2006). Thus, it is important to consider the source-dike connection when modeling dike propagation.

Correspondingly, the lubrication-theory school of thought models dike propagation as viscous fluid flow continuously supplied by a connected magma body over a finite propagating distance (Taisne and Jaupart, 2009; Rivalta et al., 2015). The basic models simplify the Navier-Stokes equations by assuming laminar flow of incompressible magma in a thin fracture (known as the lubrication approximation). By incorporating mass conservation law, and assuming constant magma flux and elastic deformation of the host rock, these models derive the pressure distribution and associated geometry of the dike. However, to address the discrepancies between inferred volume changes in the magma domain and in the dike intrusion, the compressibility of both magma and magma domain must be considered (e.g., Johnson et al., 2000; Hreinsdóttir et al., 2014; Sigmundsson et al., 2024). Moreover, the assumption of a constant flux from magma bodies may not hold due to the dynamic behavior of magmatic systems and coupled models between magma bodies and dike intrusions are developed.

Compressibility of magma and magma domain

Rivalta et al. (2015) defined the ratio between the relative mass extraction of compressible magma from a magma body and the resulting pressure drop (effective compressibility, $\overline{\beta_c}$) as:

$$\frac{\Delta M/M}{\Delta p} = \frac{(\rho_m \Delta V + V \Delta \rho_m)/(\rho_m V)}{\Delta p} = \frac{1}{V}\frac{\Delta V}{\Delta p} + \frac{1}{\rho_m}\frac{\Delta \rho_m}{\Delta p} = \beta_c + \beta_m = \overline{\beta_c}, \tag{22}$$

where ΔM is the mass of extracted magma, M is the total mass of magma in the body, V is the volume of the magma body, Δp is the pressure change due to magma extraction and ρ_m is the magma density. Here, β_c represents the so-called elastic compressibility of the magma body, which relates to how much the boundary of a magma body will deform upon magma extraction, while β_m is the intrinsic compressibility of the magma itself. Assuming a magma domain as a single volumetric unit, β_c can be generalized for the entire domain. Then, the ratio (r_v) of the injected and extruded magma volume to the volume change in the magma domain is given by (Rivalta, 2010; Shreve et al., 2021):

$$r_v = 1 + \frac{\beta_m}{\beta_c}, \tag{23}$$

Assuming specific magma domain geometries, β_c can be derived analytically (Amoruso and Crescentini, 2009). For instance, for a spherical magma domain (McTigue, 1987),

$$\beta_c = \frac{3}{4\mu}, \tag{24}$$

and for a penny-shaped magma domain,

$$\beta_c = \frac{3}{\mu}\left(\frac{A}{C}\frac{1}{2\pi} - \frac{1}{5}\right), \tag{25}$$

where μ represents the shear modulus of the host rock, and A, B and C are the principal axes of the penny-shaped body with $A = B \gg C$. Anderson and Segall (2011) further estimated β_c under assumptions of intermediate geometries using finite element calculations.

Shreve et al. (2021) summarized that β_c ranges 3.8×10^{-10}–22×10^{-10} Pa^{-1} for $\mu = 2$ GPa, with the lower bound corresponding to the spherical case and the higher bound to the penny-shaped geometry with $\frac{A}{C} \approx 10$. In contrast, magma compressibility β_m usually ranges from 0.4×10^{-10} to 15×10^{-10} Pa^{-1}, dependent on pressure conditions and gas content (e.g., gas-free, or with exsolved gas; Spera, 2000; Segall et al., 2020; Sigmundsson et al., 2020). Therefore, the effective compressibility $\overline{\beta_c}$ can vary between 4.2×10^{-10} and 37×10^{-10} Pa^{-1}, highlighting that even modest magma extraction can induce significant pressure drops and observable surface deflation of the domain. Correspondingly, r_v can typically range from ~1 to ~4, implying that magma volume changes of a magma domain inferred from surface deformation can be smaller than that of its fed dikes by up to four times.

Coupled models between magma domain and dike intrusions

An early coupled model linking a magma body and a vertical dike intrusion was proposed by Mériaux and Jaupart (1995), based on the principles of the lubrication-theory school of thought. In this model, the magma body is simplified as having an elliptical vertical cross-section, which yields the analytical relationship between its dimensions and internal pressure. The internal pressure of a magma body feeding dikes evolves over time according to a time-dependent external magma supply. Assuming incompressible magma and applying mass conservation law, the magma flux into the dike is controlled by the varying cross-sectional geometry of the magma body, and therefore the viscous flow within the dike also varies with time. This model assumes incompressible magma. Moreover, it assumes that dikes open already at the boundary of the magma body and is therefore controlled directly by the internal pressure of the magma body. Both assumptions limit the model's capability to represent more complex coupling mechanism between magma bodies and dike intrusions.

During the 1997 dike intrusion at Kīlauea volcano, Hawaii, ground deformation indicated that major dike opening occurred ~14 km southeast of the caldera (Segall et al., 2001). This differs from the assumption in the Mériaux and Jaupart (1995) model that major dike opening occurs in the immediate vicinity of the magma body. Such observation motivated the development of an alternative coupled model to account for distant dike

propagation (Segall et al., 2001). This model takes the dike as a half-ellipsoid, allowing for analytical expression of dike propagation under varying driving pressure ($P_{driving}$), that is:

$$P_{driving} = \begin{cases} p_m^d - \sigma_d & \text{for lateral propagation,} \\ p_m^d - \sigma_d - \Delta\rho g & \text{for vertical propagation,} \end{cases} \quad (26)$$

where p_m^d is the magma pressure in the dike, $\Delta\rho$ is the density difference between magma and host rock, g is the gravitational acceleration, and σ_d is the effective normal stress acting on the dike plane. The term $\Delta\rho g$ reflects that the vertical dike propagation needs to overcome the buoyancy force. Dike driving pressure is coupled to the pressure in the magma body by applying the mass conservation law, considering magma flow through a connecting conduit, and accounting for the compressibility of both the magma and the magma body. As the dike expands, pressure in the magma body decreases, which in turn reduces dike driving pressure. When driving pressure is too low to maintain dike propagation, or a quasi-equilibrium is reached between the dike and the magma body, dike propagation stops. This model also examines the eruption conditions and the associated pressure loss in the dike.

To better characterize the temporal evolution of the dike propagation, Rivalta (2010) modified the Segall et al. (2001) model. First, the connecting conduit between the magma body and the dike is modeled as a cylindrical pipe with Poiseuille flow, allowing accurate evaluation of the viscous flow. In addition, the model was extended to include various geometries of magma body and dike. Finally, the model was generalized to incorporate multiple magma bodies and dikes for more complex magmatic systems. The model presented in Segall et al. (2001) and Rivalta (2010) can be further refined for shallow, water-rich arc volcanoes to account for phase changes of dissolved volatiles during dike intrusion. Townsend and Huber (2020) introduced an enthalpy-based formulation to capture the latent heat effects associated with water exsolution from magma, which impacts the thermal and mechanical evolution of dike propagation.

To summarize, coupled models fundamentally rely on mass conservation and the pressure gradient between the magma domain and the dikes to capture their temporal evolutions, under assumptions regarding magma flow dynamics and component geometries. However, these models typically do not resolve the spatial location of dike opening or incorporate the interaction between dike intrusion and regional tectonics, such as at a divergent plate boundary like Krafla. These limitations bring difficulties to understand how repeated lateral dike intrusions jointly accommodate plate extension and release accumulated stress at a divergent plate boundary like Krafla.

1.4.3 Dike Sequence

To reproduce the spatial distribution of dike intrusions during the Krafla rifting episode and investigate its controlling factors, Buck et al. (2006) proposed a simple numerical model for dike sequence formation. The model defines a one-dimensional profile of tectonic and topographic stress along the rift zone, which contributes to the dike driving pressure. Host rock deformation follows Hooke's law, indicating that tensile stress is proportionally reduced with dike opening. Dike height is fixed throughout the rift zone, representing its vertical extent.

The model performs a numerical search to determine where along the fissure swarm dikes open and how far they extend laterally. It assumes that stress changes induced by dike intrusions are controlled by the difference between magma pressure and stress conditions along the fissure swarm due to tectonic stress and topographic effects. Pressure increase in the dikes and corresponding pressure drops in the source due to magma extraction re-establish quasi-equilibrium between the source and the dikes. The resulting dike intrusion alters the local stress field, and feeds into the next iteration of search. Repeating this process yields a full sequence of dikes throughout a rifting episode. The model successfully reproduces the observed spatial distribution of dike at Krafla and explains the gradual ground uplift in the Krafla caldera at dike initiations.

However, there is scope for improvement. For instance, the model assumes a uniform stress distribution along the dike at the end of an intrusion, with dike opening that can be larger than expected from accumulated tensile stress from plate spreading prior to a rifting episode. Observations show, however, single dike may only partially relieve preexisting tectonic stress, and that the total stress released during a rifting episode is often limited by the amount of tectonic stress accumulated beforehand (e.g., Wright et al., 2012; Parks et al., 2023, 2025; Greiner et al., 2025). Additional limitation lies in the assumed dike geometry. The Buck et al. (2006) model assumed a vertical dike extent of 10 km at Krafla, whereas geodetic observations suggest a range of 2–5 km (Hollingsworth et al., 2013). The lateral distribution of dike opening in the model can also be modified according to the surface widening.

Therefore, to better reflect realistic Earth's properties, and gain new insights into the Krafla rifting episode, this study (Chapter 3) further develops this model by (i) assuming a three-section dike geometry with tapering toward its far end, (ii) restricting the tectonic stress released by individual dike intrusions as well as by the entire dike sequence, (iii) incorporating magma compressibility in mass conservation between a magma domain and a set of dikes, and (iv) determining the part of dike opening along the fissure swarm according to the stress profile before resolving opening distribution.

1.5 Modeling Plate Boundary Deformation

Five decades after the 1975–1984 Krafla rifting episode, large-scale deformation at Krafla is currently dominated by plate spreading and GIA, with only minor influences from decayed post-rifting processes and small-magnitude volcano-tectonic-geothermal processes. That is, the deformation in the Krafla volcanic system has become relatively steady and well suitable for studying the plate divergence at the subaerial part of mid-Atlantic ridge using extensive space geodetic observations (e.g., Ali et al., 2014; Drouin et al., 2017a; Drouin et al., 2017b; Lanzi et al., 2023).

Moreover, quantifying plate divergence at Krafla is important for monitoring volcanic, geothermal, and rift-related activities. For instance, Sturkell et al. (2008) suggested that the subsidence from deflation of a shallow magmatic body below Krafla (~2.5 km depth) decayed from 50 mm/yr in 1989 – 1992 to 3 mm/yr during 2002–2005. Geothermally-related surface deformation in the study area has been generally inferred to be smaller than 6 and 15

mm/yr in horizontal and vertical components, respectively, with sources shallower than 2.5 km (Drouin et al., 2017b; Lanzi et al., 2023). Recent transient deformation signals at Krafla also exhibit relatively small magnitudes, as studied in Chapter 2 of this thesis. Accurate estimation of background plate spreading enhances our capability to detect and model these small deformation signals.

This section reviews four types of models used to predict the secular horizontal velocity field at divergent plate boundaries in Iceland. It includes a summary of the plate divergence across the Krafla predicted by various global plate motion models. It also reviews previous regional plate boundary deformation models, highlighting potential improvements therein.

1.5.1 Plate boundary deformation models

The first type of model assumes that the plate spreading is fully accommodated by the viscoelastic response of Earth's crust to lateral dike intrusions during rifting episodes (e.g., Foulger et al., 1992; Heki et al., 1993). Near the plate boundary axis, deformation is primarily governed by elastic upper crust, which responses to dike intrusions in short timescales. This results in episodic surface widening during rifting episodes but minimal inter-rifting deformation. In contrast, further away from the plate boundary, deformation is increasingly influenced by the viscoelastic lower crust. The gradual post-rifting relaxation of the ductile part of the crust thereby accommodates long-term inter-rifting plate divergence and contributes to the cumulative extension over multiple rifting cycles. This type of model requires knowledge of time intervals between rifting episodes and average opening during each of them, which are often poorly constrained.

The second type of model is the kinematic back-slip model (e.g., Savage and Prescott, 1978; Ali et al., 2014; Drouin and Sigmundsson, 2019; Metzger and Jónsson, 2014; Barreto et al., 2025). The model assumes that two tectonic blocks (plates) are locked from the surface down to a certain depth but move freely below. The free movement at depth is implemented by assigning half of the full spreading rate to each side of the plate boundary axis. The locked part is implemented by superimposing a back-slip deformation field generated by a vertical dislocation from the surface to the locking depth along the axis in a uniform elastic half-space (Okada, 1992), moving opposite to the spreading direction at the same rate. Figure 1.11(a) shows a schematic figure of the back-slip model.

The third type of model is the so-called buried dislocation model (e.g., LaFemina et al., 2005; Árnadórttir et al., 2006). This model implements a vertical tensile dislocation along the plate boundary axis, extending from its locking depth to infinite depth (Figure 1.11(b)). The crust is assumed to be a uniform elastic half-space following Okada (1992). This dislocation represents the free movement of the ductile part of the crust and opens at a rate equal to the full plate spreading. The buried dislocation model and the back-slip model produce similar results for the horizontal displacements (Figure 1.11(c)), though both models have an unphysical singularity at the locking depth (Bonafede and Danesi, 1997).

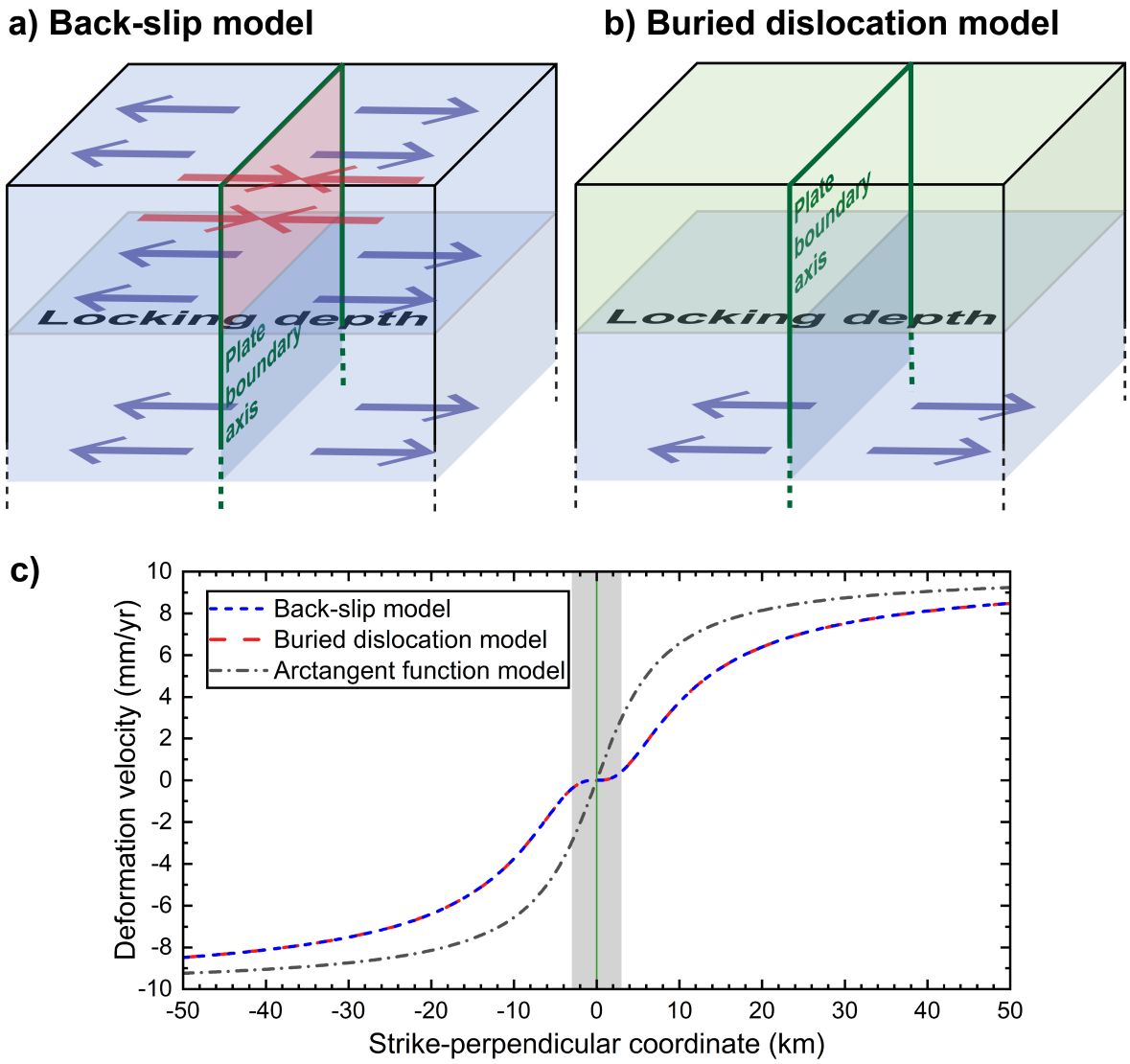


Figure 1.11 a) Schematic figure of the kinematic back-slip model. *The green lines show the plate boundary axis. The red rectangle with red arrows shows the back-slip dislocation.* ***b) Schematic figure of the buried dislocation model.*** *The vertical dark blue rectangle indicates the opening dislocation below the locking depth.* ***c) Comparison among deformation velocities predicted by the back-slip, buried dislocation and arctangent function models.*** *The strike-perpendicular coordinate indicates the distance from the plate boundary axis (vertical green line) along its strike-perpendicular direction. The deformation velocity is perpendicular to the strike of the plate boundary axis. The grey shaded area shows where the back-slip and buried dislocation models predict minimal ground deformation near the plate boundary axis. The blue short-dashed and red dashed lines overlap with each other. The full spreading rate is 20 mm/yr and the locking depth is set to 6 km.*

A fourth modeling approach uses an arctangent function to describe the transition of ground deformation velocity across the plate boundary (e.g., Savage and Beurford, 1973; Árnadóttir et al., 2006; Heimisson et al., 2015; Islam and Sturkell, 2015; Drouin et al., 2017a). The velocity perpendicular to the plate boundary axis at a given location A (V_A) is calculated as:

$$V_A = \frac{V_{plate}}{\pi} \cdot \arctan(\frac{d_A}{D}), \quad (27)$$

where V_{plate} is the full plate spreading rate, and d_A is the distance from point A to the axis. D represents the locking depth at the plate boundary axis, or the brittle-ductile transition in the crust, which controls the width of the velocity transition zone.

Figure 1.11(c) compares the deformation velocity predicted by the latter three models using similar parameter settings. The results shows that both back-slip and buried dislocation models predict a narrow area of near-zero ground deformation next to the plate boundary central axis (grey-shaded area in Figure 1.11(c)). In contrast, the arctangent function model yields a steeper velocity gradient across the axis. However, distinguishing among these models is challenging because an arctangent function model with a deflation source may generate similar strike-perpendicular deformation profile to the other two. Moreover, these fundamental models typically assume that the spreading direction is perpendicular to the plate boundary axis and neglect deformation along the axis (strike-parallel component). Regional spreading direction is not necessarily perpendicular to the axis. Incorporating strike-parallel component allows more realistic representation of spatial deformation patterns at plate boundaries (e.g., McCaffrey et al., 2000; Geirsson et al., 2012). Accordingly, in Chapter 4 of this thesis, the back-slip model is modified to include the strike-parallel component of deformation and is then applied to interpret the long-term deformation field across the Krafla volcanic system.

1.5.2 Global plate motion models

Global plate motion models provide an overall constraint on plate boundary deformation across the Krafla volcanic system, though local deviations may exist due to tectonic complexity and interactions with the volcanic system. Plate motion models are typically established by first delineating plate boundaries and then estimating relative plate motions using various datasets. Tectonic plate motions can be described as a rigid body rotation centering a location (Euler pole) on a spherical Earth (Euler, 1765) and the horizontal displacement velocity at any point is calculated as:

$$\begin{bmatrix} v_n \\ v_e \end{bmatrix} = \mathbf{T} \cdot R \cdot (\mathbf{w} \times \mathbf{r}), \quad (28)$$

where v_n and v_e are the north and east velocity components, respectively, R is Earth's radius, $\mathbf{w}$ is the angular velocity (Euler vector) of the plate, $\mathbf{r}$ is the unit position vector of the ground point, and $\mathbf{T}$ is the transformation matrix that projects the Cartesian velocities into the local topocentric frame. The unit position vector $\mathbf{r}$ at a point with latitude B and longitude L is given by:

$$\mathbf{r} = \begin{bmatrix} \cos B \cos L \\ \cos B \sin L \\ \sin B \end{bmatrix}. \quad (29)$$

The angular velocity vector $\mathbf{w}$ can be expressed either as a Cartesian vector $[w_x \quad w_y \quad w_z]^{\mathrm{T}}$, or as a scalar angular rate $|\mathbf{w}|$ combined with the unit position vector of the Euler pole $\mathbf{r_0}$:

$$\mathbf{w} = |\mathbf{w}|\mathbf{r_0}. \tag{30}$$

The transformation matrix **T** is:

$$\mathbf{T} = \begin{bmatrix} -\sin B \cos L & -\sin B \sin L & \cos B \\ -\sin L & \cos L & 0 \end{bmatrix}. \tag{31}$$

The difference of velocity predictions from two adjacent plates at a given location yields the relative plate motion.

Plate boundaries can be inferred from multiple geological and geophysical observations, including: (i) earthquake epicenter distribution and moment tensors; (ii) seafloor magnetic anomalies and fracture zones that trace spreading centers and transform faults; (iii) topography or bathymetry; (iv) subaerial volcano locations; and (v) geodetic measurements (e.g., Sella et al., 2002; Bird, 2003; Müller et al., 2008; Argus et al., 2011). Updates to plate motion parameters and consistency analysis at triple junctions, where three plate boundaries meet, also contribute to fine adjustments of these boundary locations (e.g., DeMets et al., 1990; Argus et al., 2011). Estimation of plate motion parameters relies on a combination of long-term and short-term indicators, such as (i) earthquake slip vectors; (ii) transform fault azimuths; (iii) magnetic anomalies that record plate motions over millions of years; (iv) tracks of hotspots from volcano locations and ages; (v) modern space geodetic observations including GNSS, very long baseline interferometry (VLBI), satellite laser ranging (SLR), lunar laser ranging (LLR) and InSAR (e.g., DeMets et al., 1990; Altamimi et al., 2002; Gripp and Gordon, 2002). Figure 1.12 shows the predicted plate spreading rates and directions in the Krafla volcanic system from a variety of global plate motion models.

1.5.3 Regional plate boundary models for Krafla

Regional models for Krafla have been developed using ground deformation observations. By fitting observed deformation fields with plate boundary models in section 1.5.1, key parameters such as the plate boundary axis location, spreading rate and direction can be inferred. The first countrywide plate boundary model constrained by GNSS data was presented by Árnadóttir et al. (2009) using the buried dislocation model. Later models benefited from denser GNSS networks and focused on regional-scale deformation in north Iceland. For instance, Metzger et al. (2013) and Barreto et al. (2025) studied the TFZ, Þeistareykir and Krafla areas, while Drouin et al. (2017a) analyzed the plate boundary deformation across the NVZ. Countrywide InSAR analysis by Drouin and Sigmundsson (2019) and Cao et al. (2023) have also contributed to the estimation of plate boundary models for the whole Iceland. Metzger and Jónsson (2014) implemented the first joint inversion of GNSS and InSAR data covering the Krafla volcanic system, spanning 1992–2009, to better identify plate motion, fault slip rate and volcanic deformation in North Iceland. Figure 1.12 compares the inferred plate spreading rates and directions from these regional models with those predicted by global plate motion models.

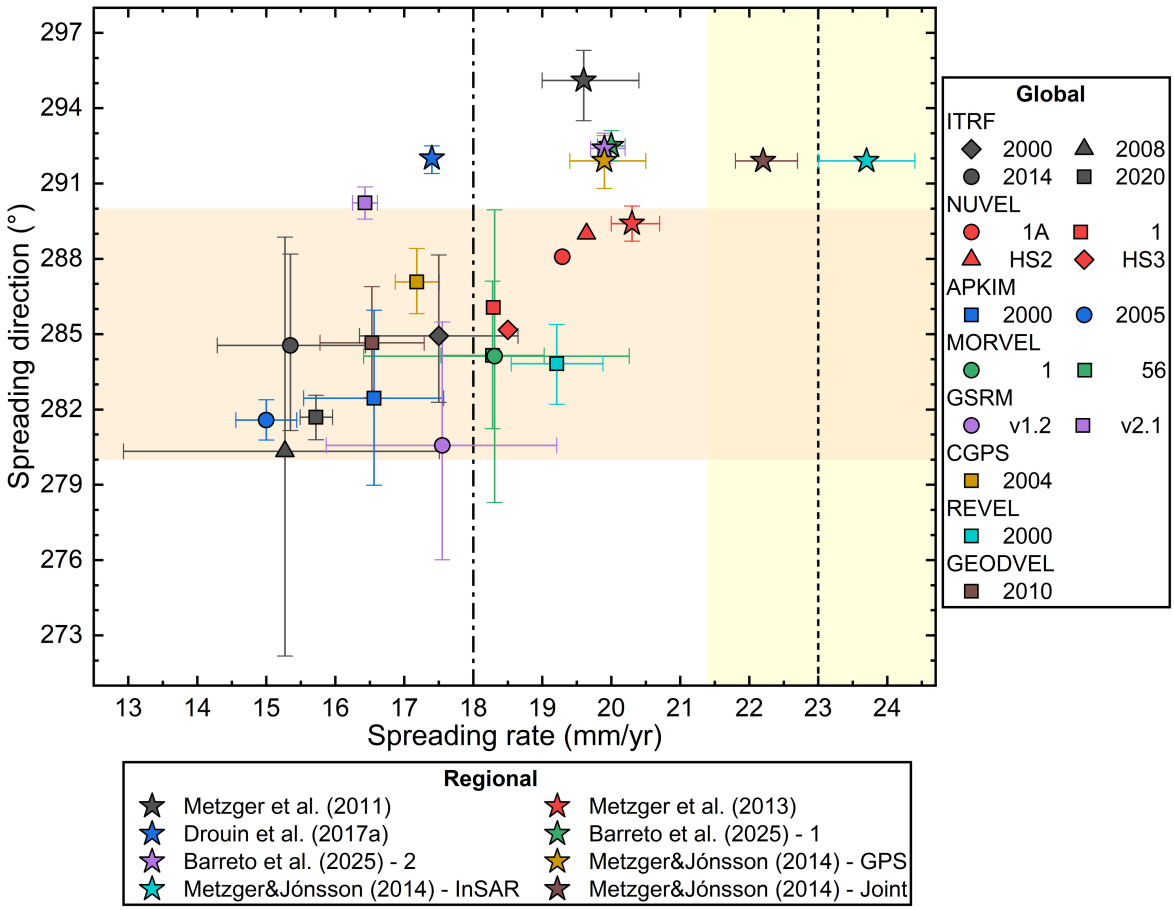


Figure 1.12 Plate spreading rates and directions in the Krafla volcanic system predicted from different global plate motion models and regional plate boundary models. *Krafla caldera center (16.80°W, 65.71°N) is used to calculate the horizontal velocities from the global plate motion models. Thin lines indicate the uncertainties of the model predictions. Shapes without thin lines indicate the corresponding models do not have uncertainty or the uncertainties are too large and thereby omitted. The vertical dashed and dash-dotted lines are the plate spreading rates from Árnadóttir et al. (2009) and Cao et al. (2023), respectively. The yellow shaded area is the uncertainty of Árnadóttir et al. (2009) spreading rate while the orange shaded area is the range of spreading direction given by Cao et al. (2023). Barreto et al. (2025) has two solutions, depending on whether the Húsavík-Flatey fault is modeled as one or two segment(s). Euler pole location uncertainties are omitted for APKIM2005 and REVEL2000 since they lead to rather large uncertainty in plate spreading. Global models are: ITRF2000 (Altamimi et al., 2002), ITRF2008 (Altamimi et al., 2012), ITRF2014 (Altamimi et al., 2017), ITRF2020 (Altamimi et al., 2023), NUVEL-1 (Argus and Gordon, 1991), NUVEL-1A (DeMets et al., 1994), NUVEL-HS2 (Gripp and Gordon, 1990), NUVEL-HS3 (Gripp and Gordon, 2002), APKIM2000 (Drewes, 1998), APKIM2005 (Drewes, 2009), MORVEL1 (DeMets et al., 2010), MORVEL56 (Argus et al., 2011), GSRMv1.2 (Kreemer et al., 2003), GSRMv2 (Kreemer et al., 2014), CGPS2004 (Prawirodirdjo and Bock, 2004), REVEL2000 (Sella et al., 2002), and GEODVEL2010 (Argus et al., 2010). The global plate motions are calculated with GAGE Plate Motion Calculator (https://www.unavco.org/software/geodetic-utilities/plate-motion-calculator/plate-motion-calculator.html).*

In most of these studies, the plate boundary across the Krafla volcanic system is simplified into two linear segments in line. However, Metzger and Jónsson (2014) and Drouin et al. (2017a) found that the locking depth of the plate boundary varies significantly at Krafla, ranging at least from ~3 to 6 km. Moreover, the geometric simplification of using long, straight plate boundary segments (Drouin and Sigmundsson, 2019; Cao et al., 2023) causes the inferred plate boundary being offset from the Krafla fissure swarm (Hjartardóttir et al., 2015), and inconsistent with the observed fracture strikes (Corti et al., 2021). These observations suggest that a simplified plate boundary axis cannot adequately represent the local stress field. A spatially variable plate boundary profile along the NVZ, such as in Drouin et al. (2017a), can solve this issue. Their profile, with variable strike, also shows the variability in locking depth across the Krafla area, but it suffers from large uncertainties in locking depth of ~10 km due to the sparse distribution of GNSS sites.

The vast increase in available geodetic data (both GNSS and InSAR) allows us to derive an improved plate boundary model with a more precise description of geometry and locking depths. In earlier studies, Metzger and Jónsson (2014) used 92 interferograms and Drouin et al. (2017) included ~35 GNSS sites from Krafla. As described in section 1.2.2, the GNSS network at Krafla has expanded since 2012, and annual campaign GNSS measurements have been conducted since 2010. Meanwhile, Sentinel-1 InSAR data since 2015 provides consistent and long-term measurements. Our current datasets including more than 100 GNSS sites and thousands of SAR interferograms covering the central part of the Krafla volcanic system can provide better constraint on the plate divergence. Integrating these two types of datasets also combines the strengths of the wide spatial coverage from InSAR and three-dimensional displacement measurements from GNSS, leading to more reliable plate boundary models than using only one of them. Therefore, this study (Chapter 4) builds on these recent datasets to gain better insights into the long-term deformation in the area with a refined plate boundary model.

2 Paper I: Joint Bayesian Modeling of Velocity Break Points, Noise Characteristics, and Their Uncertainties in GNSS Time Series: Far-Field Velocity Anomalies Concurrent with Magmatic Activity in Iceland

2.1 Summary

The study in this chapter is motivated by short-term deformation anomalies observed in the Krafla volcanic system during 2014–2015 and their chronological relationship with the 2014 Bárðarbunga rifting episode, ~120 km to the south. These anomalies manifest as velocity changes in cGNSS coordinate time series. A Bayesian inference approach is developed to jointly estimate velocity break points, velocity change values and their uncertainties, where GNSS time series modeling incorporates a deterministic model with piecewise linear functions and a stochastic model including both WN and PLN components. Synthetic data experiments are implemented to investigate the lower limits of detectable velocity changes under different noise levels. The method is then applied to east-component GNSS time series from Krafla and the results indicates that westward movement at Krafla accelerated prior to the Bárðarbunga dike intrusion and resumed its pre-anomaly velocity in early 2015. Detailed comparison further suggests these inferred onset timings of far-field deformation anomalies coincide with near-field precursors of enhanced ground deformation and seismicity prior to the Bárðarbunga dike intrusion (shown in Figure 2.1). After reviewing seismicity at Krafla during this period and historical records of concurrent activities among volcanic systems at the NVZ, these results suggest that the volcanic systems at NVZ may be coupled eventually through a partial melt zone that can channel pressure variations. The study also addresses: (i) effects of time series lengths and other transient signal components on velocity change modeling; (ii) supplementary observations from InSAR and campaign GNSS; and (iii) comparisons to other studies of coupling between volcanoes and/or magma bodies.

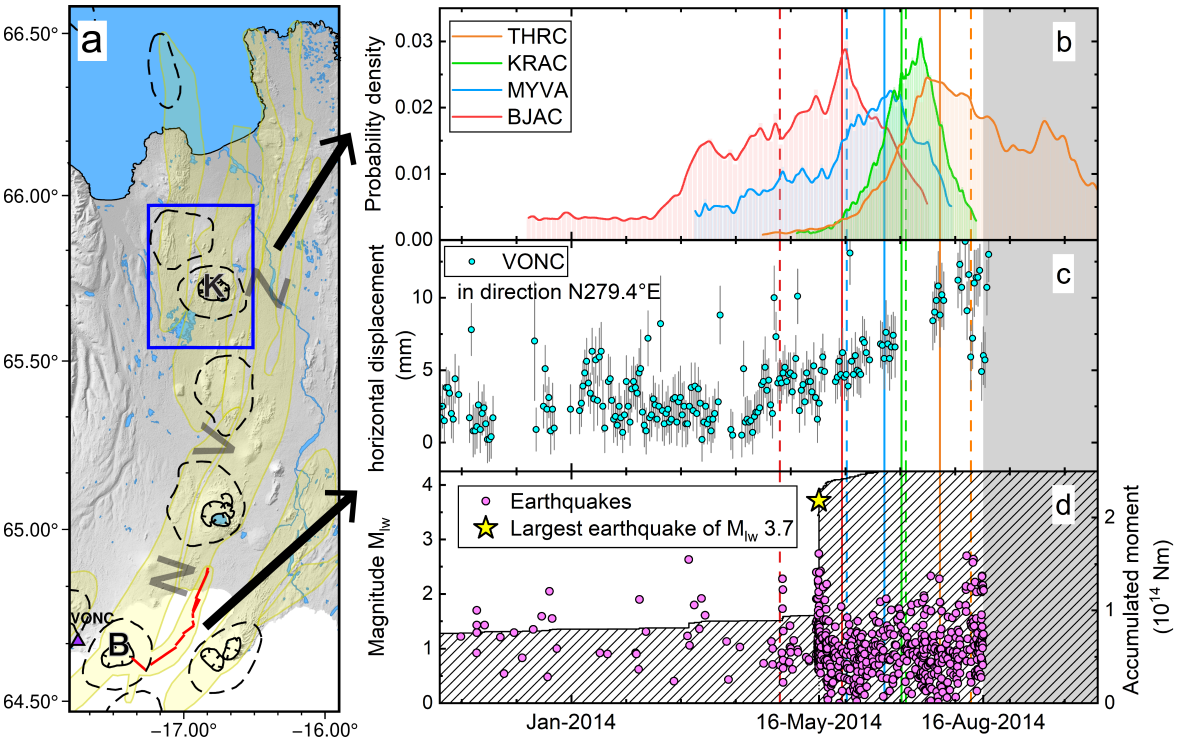


Figure 2.1 Comparison between the onset timing of deformation anomalies in the Krafla volcanic system during 2014–2015 and the near-field precursors prior to the 2014 Bárðarbunga dike intrusion. a) A map showing the locations of the Krafla (K) and Bárðarbunga (B) volcanic systems. *The shaded background map shows the topography and the white area is the Vatnajökull ice cap. The black dashed lines indicate central volcanoes and the black ticked lines indicate calderas. The blue rectangle outlines the area as in Figure 1.1(c). The red line indicates the 2014 Bárðarbunga dike intrusion. The yellow areas show the fissure swarms. The purple rectangle shows the location of cGNSS site VONC, as shown in Figure 2.1(c).* ***b) Marginal posterior probability distribution of the deformation anomaly onset timings at Krafla with 95% confidence interval.*** *The colored shaded areas start and end at the lower and higher limit of the 95% confidence interval, respectively. The vertical solid and dashed lines indicate the optimal and mean estimates, respectively. The gray area indicates the period after the onset of the Bárðarbunga dike intrusion.* ***c) The horizontal displacement in direction N279.4°E (the azimuth of maximum horizontal motion) at VONC station (11 km west of the Bárðarbunga, location shown in Figure 2.1(a)) from detrended GNSS time series. d) Seismicity at Bárðarbunga versus time (left axis) and accumulated seismic moment (right axis) prior to the dike intrusion.*** *Data in Figure 2.1(c) and (d) are from Sigmundsson et al. (2020). Fissure swarms, central volcanos, calderas are from Jóhannesson and Sæmundsson (2009), and topography is from Landmælingar Íslands [LMÍ] (2020).*

2.2 Main Results

- Time-correlated noise in GNSS coordinate time series can cause spurious estimates of break points for small velocity change.

- Velocity change with its value exceeding 7.5, 10 and 15 mm/yr can be satisfactorily detected in a 5-yr-length time series under FLN amplitude of 3, 4, and 5 mm/yr$^{0.25}$, respectively.

- Maximum likelihood estimates suggest that the deformation anomalies at Krafla begin during 31 May to 3 July 2014 with the westward movement increased by 7.6–9.8 mm/yr.

- Inferred onset timings of the deformation anomalies precede by 23–77 days the 2014 Bárðarbunga dike intrusion on 16 August 2014 with 95% confidence interval.

- Deformation anomalies at Krafla occur in the same period as enhanced near-field seismicity and deformation prior to the 2014 Bárðarbunga dike intrusion, based on their maximum likelihood estimates.

- Distant volcanic systems along the NVZ may be coupled, eventually through a deep partial melt zone that can channel pressure variations.

3 Paper II: Role of tectonic stress and topography on repeated lateral dikes: application to the 1975–1984 Krafla and 2023–2025 Svartsengi rifting episodes in Iceland

3.1 Summary

The study in this chapter reexamines the effects of tectonic stress and topography on repeated lateral dikes during rifting episodes, by modifying the simplified elastic model proposed by Buck et al. (2006). In the modified model, magma flows into all the dikes and eruptions through approximately the same horizontal location in the fissure swarm, referred to as the fissure swarm inlet (Figure 3.1). In addition to intrinsic magma pressure, extrinsic tectonic stress and topographic gradient contribute to the driving pressure of lateral dike propagation. Dikes in the model will propagate in the direction with larger positive gradient of dike driving pressure near the inlet, continuing toward an area where the driving pressure reaches its local maximum and no longer increases. The model searches for the opening distribution of dikes by considering the hydraulic coupling between the fissure swarm inlet and dikes, and the amount of pre-diking stored tectonic stress. As successive dikes intrude and redistribute stress, the most favorable segment for dike intrusion along the fissure swarm shifts. The modifications include: (i) assuming a three-section dike geometry with tapering toward its far end, (ii) restricting the tectonic stress released by individual dike intrusions as well as by the entire dike sequence, (iii) incorporating magma compressibility in mass conservation between a magma domain and a set of dikes, and (iv) determining where dike tapering begins based on the cumulative stress profile before resolving the spatial distribution of dike opening.

The model is applied to the 1975–1984 Krafla rifting episode, with key parameters adjusted against deformation observations. Model predictions reproduce the first-order regularities of the dike sequence. Low inlet magma pressure at dike initiations is inferred due to significant contribution from the extrinsic factors (up to an order of magnitude larger than the magma overpressure). Fitting model prediction to the vertical ground deformation suggests the pressure limit to initialize the first dike is larger than for later ones. A larger failure limit for the first dike compared to later dikes, a significant tectonic stress component along the dikes' paths and the compressibility of the magma domain permit magma flow into later dikes even when pressure conditions are below lithostatic at the LNB. Additionally, the model is adapted for the first three dikes in the 2023–2025 Svartsengi rifting episode, SW Iceland, during November 2023 to January 2024. There, tectonic stress and magma buoyancy effects enable dike initiations when the overpressure from magma supply in the

domain is 3 MPa below lithostatic. Tectonic stress inhibited eruption from the initial dike of the Svartsengi rifting episode. Our findings demonstrate that tectonic stress and topographic effects are critical factors driving lateral dike propagation, allowing magma flow into dikes or eruptions under low magma pressure, even lower than lithostatic pressure.

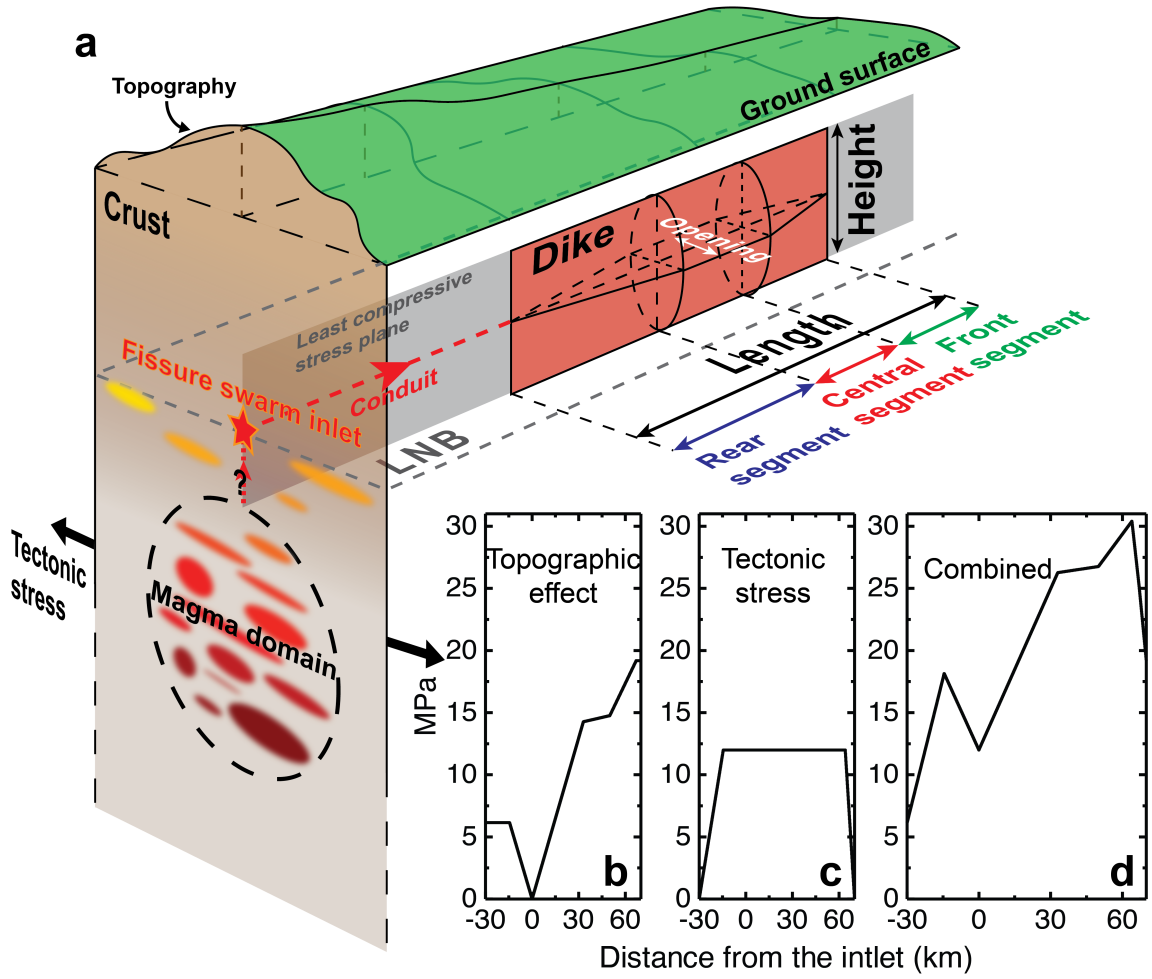


Figure 3.1 A schematic figure of the modified dike sequence model. a) Illustration of magma flow from a magma domain, through the fissure swarm inlet and to a dike along the least compressive stress plane. *The figure is not on scale.* ***b)–c) Dike driving pressure from topographic effects and tectonic stress prior to 1975–1984 Krafla rifting episode.*** *The topographic effect is calculated with a simplified piecewise elevation profile along the Krafla fissure swarm, and an average host rock density of 2510 kg/m^3 (Scott et al., 2019). The tensile tectonic stress is assumed to be 12 MPa with two stress barriers on both ends of the Krafla fissure swarm (Buck et al., 2006).* ***d) Dike driving pressure supplied by the topographic effects and tectonic stress summing up Figure 3.1(b) and (c).*** *The combined value shown is the sum of values in Figure 3.1(b) and (c).*

3.2 Main Results

1975–1984 Krafla rifting episode:

- Tectonic stress and topographic effects can contribute up to 30 MPa to dike driving pressure, which account for >90% of driving pressure of lateral dike propagation in the early stage of the Krafla rifting episode if an initial inlet magma pressure of 3 MPa is assumed.

- Failure limit for initiating the first dike is higher than later dikes by a factor of 1.8–2.2, suggested by fitting predicted inlet magma overpressure to the observed elevation change.

- Inferred inlet magma pressure at the initiation of the first dike is ~1–10 MPa above the lithostatic stress.

- The model suggests that the second to fifth dike intrusions are initiated at an inlet magma pressure below the lithostatic because of the lower failure limit and tectonic stress.

- The fissure swarm inlet for the Krafla rifting episode may offset from the caldera center, by ~2–4 km toward the north.

2023–2025 Svartsengi rifting episode:

- Topographic effects affect less than 3 MPa of dike driving pressure, due to small elevation variation in the area.

- Tectonic stress (assumed 8 MPa) and significant buoyancy pressure (estimated 9 MPa) enabled dike initiations with the pressure from magma supply in the domain 3 MPa lower than the lithostatic.

- Tectonic stress inhibited eruption from the initial dike of the Svartsengi rifting episode by favoring lateral magma transport rather than vertical ascent to the surface.

4 Paper III: Plate divergence at the Krafla volcanic system, Iceland: Insight from GNSS geodesy and Sentinel-1 Satellite Radar Interferometry in 2002–2024

4.1 Summary

The study in this chapter develops a detailed plate boundary model for the Krafla volcanic system using the kinematic back-slip model and long-term deformation velocity fields from GNSS data in 2002–2024 and Sentinel-1 InSAR interferograms in 2015–2023. Both GNSS horizontal and InSAR near-east velocity fields reveal a consistent extensional deformation pattern across the study area, supporting their joint constraints on the plate boundary model. Vertical displacements show overall uplift, with millimeter-scale subsidence every year concentrated at Bjarnarflag, at the Krafla caldera center, and at the center of the Þeistareykir central volcano. Here, the back-slip model is extended to include deformation components parallel to the plate boundary axis when the spreading direction is locally non-perpendicular to the axis. A two-step Bayesian inversion strategy is implemented to balance the spatial resolution, modeling precision and inversion stability. The inversion considers GIA deformation and jointly solves for the axis geometry, spreading parameters and segmental locking depths. A six-segment geometry of the plate boundary axis is resolved across the central part of the Krafla volcanic system (Figure 4.1). The inferred axis aligns with recent eruptive fissures and strike variations of the mapped fractures. The inferred locking depth variations coincide with the depth distribution of seismicity in the area. These results provide insights into the regional stress accumulation, rheological transition and volcano-tectonic interactions. Residual velocity fields, along with vertical displacements corrected for GIA and regional subsidence due to rheological anomalies and plate spreading, highlight local contraction and subsidence at the Bjarnarflag and Krafla geothermal fields, and the northernmost part of the 1975–1984 lava field. Further analysis of InSAR displacement time series reveals their temporal variations in 2015–2023.

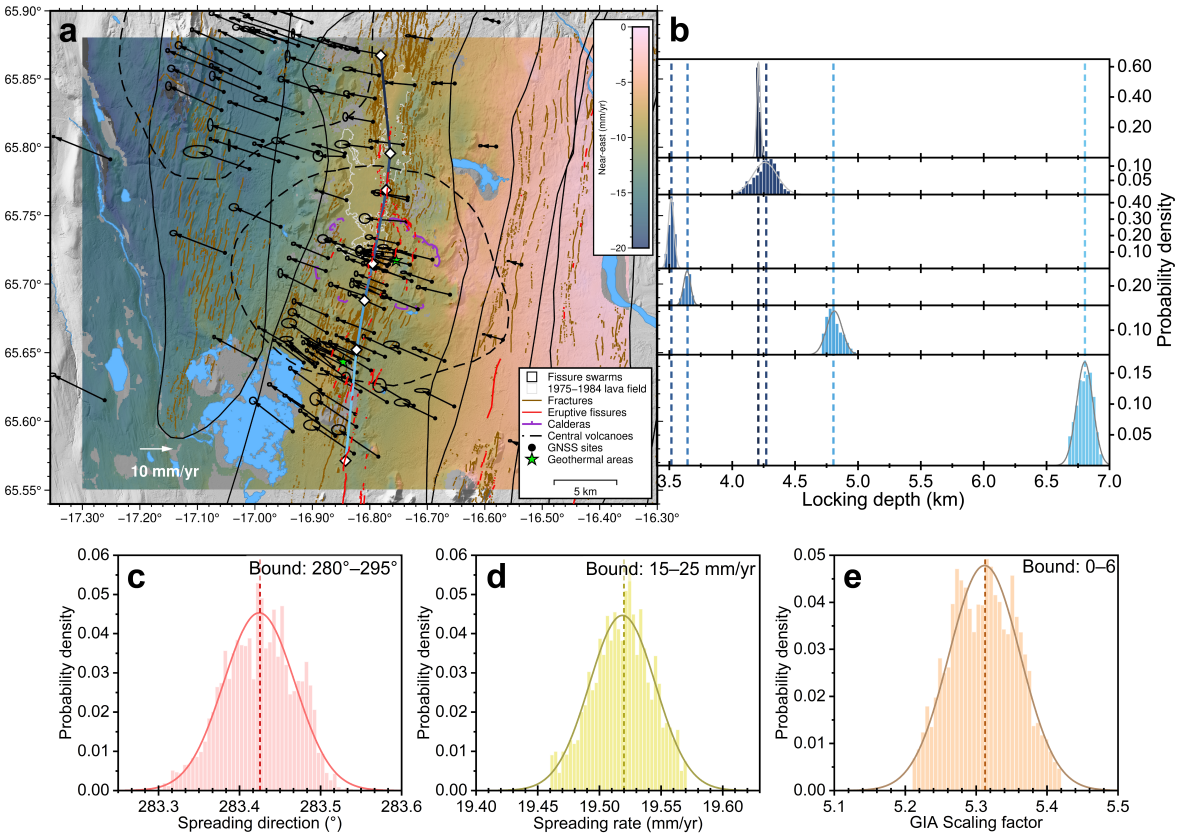


Figure 4.1 a) Long-term horizontal deformation velocity fields in the central part of the Krafla volcanic system derived from GNSS (2002–2024, black arrows) and InSAR (2015–2023, color map). *The ellipses indicate uncertainties (95% confidence). The blue line with segments separated by white diamonds shows the inferred plate boundary central axis. The color from light to dark blue indicates segment location from south to north for visual distinction, also applied for Figure 4.1(b). The vertical dashed lines show the median estimates.* ***b) Marginal posterior probability distribution of the locking depth for each plate boundary axis segment.*** *The vertical extent of each panel corresponds to their latitude range in Figure 4.1(a).* ***c)–e) Marginal posterior probability distribution of spreading parameters and horizontal GIA scaling factor.***

4.2 Main Results

- Inferred segments of the plate boundary axis strike N3.8°–15.5°E. For the southern three segments, strike angles increase south-to-north, whereas for the northern three segments the strike shift from NNE-SSW to NNW-SSE.

- Inferred plate spreading is $19.52^{+0.05}_{-0.06}$ mm/yr in an azimuth of $283.4°^{+0.1°}_{-0.1°}$ at Krafla, with formal uncertainties corresponding to the 95% confidence interval of the Bayesian inversion results

- Locking depth varies significantly along the axis: it is shallowest within ($3.52^{+0.03}_{-0.06}$ km) and just north ($3.64^{+0.05}_{-0.06}$) of the Krafla caldera and deepens to $4.27^{+0.15}_{-0.23}$ km and $6.81^{+0.11}_{-0.13}$ km northward and southward, respectively.

- Inferred plate boundary axis aligns with the recent eruptive fissures and strike variations of the mapped fractures.

- Comparison between the inferred locking depth and the depth distribution of seismicity indicates shallow brittle-ductile transition inside and just north of the Krafla caldera, forming a dome-like crustal structure.

- Residual velocity fields reveal three local deformation patterns with millimeter-level contraction and several millimeters of subsidence per year, at the Bjarnarflag and Krafla geothermal fields, and at the northernmost part of the 1975–1984 lava field.

5 Conclusions and outlook

This study aims to improve the understanding of ground deformation in the Krafla volcanic system, northeast Iceland, across multiple temporal scales and investigate how observed deformation signals reflect internal Earth processes. Together, these analyses provide insights into different stages of the rifting cycle: long-term plate divergence leads to strain accumulation along the plate boundary, which is released through dike intrusions during rifting episodes, such as the decadal-scale unrest of the 1975–1984 Krafla rifting episode. Additional transient deformation, on the other hand, may occur and modulate the long-term deformation signals. The main findings include:

(i) Short-term deformation anomalies during 2014–2015 at Krafla are identified, manifesting as accelerated westward movement recorded by four cGNSS stations. These anomalies occurred simultaneously with enhanced near-field seismicity and deformation preceding the 2014 dike intrusion in the Bárdarbunga volcanic system, ~120 km to the south of Krafla. This inferred concurrent activity provides new evidence for potential coupling between volcanic systems in the NVZ, possibly through a deep partial melt zone.

(ii) A modified numerical model of repeated lateral dike intrusions successfully reproduces the first-order regularities of the decadal-scale deformation during the 1975–1984 Krafla rifting episode. The model suggests that magma may flow into all the dikes and eruptions through approximately the same horizontal location along the fissure swarm, and that stored tectonic stress prior to rifting episodes may not be fully released by a single dike intrusion. Tectonic stress and topography play a critical role in driving lateral dike propagation, allowing magma flow into dikes or eruptions even when magma pressure is lower than the lithostatic.

(iii) Long-term deformation velocity field is derived for the Krafla volcanic system using GNSS data (2002–2024) and InSAR data (2015–2023), which subsequently constrain a six-segment plate boundary model. The inferred plate boundary axis aligns with recent eruptive fissures and fracture orientations. Locking depth is shallowest beneath the Krafla caldera and ~3 km to its north, indicating a dome-like crustal structure along the central part of the Krafla fissure swarm. Model residuals further reveal three local deformation patterns with protracted deflation.

The methodologies developed in this thesis include deformation time series analysis, numerical modeling of temporal lateral dike sequences, and joint inversion strategy for plate boundary models. They provide broad practical contributions to geodesy and volcanology:

(i) The Bayesian modeling framework for velocity changes in cGNSS time series incorporates piecewise linear functions in deterministic model and time-correlated noise in stochastic model, yielding joint estimation of velocity break points and their uncertainties and thereby supporting reliable geophysical

interpretations. This approach is broadly applicable to both GNSS and InSAR time series across various contexts, such as volcanic unrest, slow-slip events or hydrologically induced deformation.

(ii) The modified numerical model of dike sequence here assumes a fissure swarm inlet into lateral dikes, allowing for the maximum dike opening zone to offset laterally from the underlying magma domain. The modified model enables closer and detailed comparison of model predictions with geodetic observations and models. Importantly, the model is not limited to the Krafla rifting episode. Its application to the 2023–2025 Svartsengi rifting episode in SW Iceland demonstrates its generalizability, encouraging future applications to other volcanoes.

(iii) The two-step inversion strategy for plate boundary model reduces its reliance on a priori information of plate spreading. This allows more data-driven models and helps identify discrepancies between observations and known geophysical processes. A key methodological improvement is the adaptively defined segment lengths along the plate boundary axis, which improves the trade-offs among spatial resolution, model precision and inversion stability.

There remain open questions and methodological limitations that direct future research. For the short-term deformation anomalies during 2014–2015 at Krafla, the optimal estimates from Bayesian inference suggest a chronological onset order with a decreasing magnitude from the south to north. This supports the hypothesis of a deep partial melt zone channeling pressure pulses. However, the interpretation is limited by the sparse distribution of cGNSS stations, and the associated uncertainties do not permit solid conclusions. The spatial characteristics of these anomalies should be further assessed by combining additional campaign GNSS and InSAR data with the temporal information inferred from Paper I. Although the magnitudes of the first and second velocity changes are broadly similar but opposite in sign, up to 20% of the velocity anomalies were not fully recovered after the second break point. Marginal posterior probability distributions also show changes in the correlation between the second break point and its velocity change at all four cGNSS stations, suggesting that part of the anomalous deformation may have persisted or decayed non-linearly (e.g., exponentially or logarithmically). Further investigation of the second velocity changes could provide new insights into the transient processes. Methodologically, the number of velocity break points are prescribed in this research and only one component of the time series is analyzed at a time. The modeling framework can be further generalized to infer the number of velocity changes directly from the data, and to jointly estimate velocity changes across all components.

For dike sequences, the current model primarily focuses on the end-member states, that is, dike initiation and eventual quasi-equilibrium between each dike and the magma domain. Future improvement could incorporate magma flow dynamics to investigate flow rates during intrusions and inter-diking magma accumulation. The model builds on a series of simplifications and assumptions. For instance, the central depth of dikes is fixed, and the tectonic stress is assumed uniform along the rift zone. However, Hollingsworth et al. (2013) suggested that dike depth increases northward away from the Krafla caldera. Paper III inferred that the brittle-ductile transition depth, and therefore the elastic thickness, also increases away from the caldera along the fissure swarm. Such variations may influence the distribution of tectonic stress, dike driving pressure, and dike geometry (e.g., Qin and Buck,

2008; Grandin et al., 2012; Kjøll et al., 2019). Accounting for these effects may improve the physical realism of future models and better explain the observed along-rift variation in deformation. Additionally, applying the model to other volcanic systems may reveal additional mechanisms of lateral dike propagations. Magma, for instance, may be supplied from multiple sources (Wright et al., 2006; Grandin et al., 2009; Rivalta, 2010), or, in some cases, from a portion of the rift zone (Poland et al., 2014). Lateral dike propagation can also occur in a segmented manner, influenced by external stress conditions (Sigmundsson et al., 2015; Montgomery-Brown and Miklius, 2019). Incorporating these complexities will allow the model to better represent dike behavior in different volcano-tectonic settings.

For long-term deformation in the Krafla volcanic system, this study adopts a regional subsidence model assuming symmetric crustal structure along the rift centered on the Krafla caldera (Lanzi et al., 2024), whereas the new plate boundary model indicates a shallower rheological transition north of the caldera than to its south. This contrast provides a basis for future refinement to numerical models. Moreover, residual velocity field shows additional northwestward motion in the southeast of Bjarnarflag, potentially due to shift of plate boundary central axis from the Krafla volcanic system to other systems in the south, or GIA model inaccuracies. Updating GIA deformation model and extending the InSAR data coverage southeastward could better investigate these effects. Finally, the back-slip and numerical model of Lanzi et al. (2024) used in Paper III represent two conceptually different approaches. The former is kinematic, describing elastic strain accumulation at a divergent plate boundary, whereas the latter is dynamic, accounting for rheological response of the lithosphere under extension. Because of these differences, the horizontal and vertical deformation fields are analyzed independently, with the vertical component used only for qualitative interpretation. Future studies could integrate these two formulations within a coupled model to jointly resolve deformation processes at divergent plate boundaries.

Beyond these specific aspects, all deformation signals studied in this thesis are eventually related to volcano-tectonic interaction in a volcano at a divergent plate boundary. Given the inherent complexity in the spatiotemporal characteristics of deformation at Krafla, future research can benefit from approaches that transcend traditional single-process modeling. For instance, machine learning and artificial intelligence methods could be applied to detect and extract subtle deformation signals from extensive geodetic dataset. Meanwhile, finite element methods, which integrate different deformation mechanisms, e.g., linear elasticity, viscoelasticity, and thermo-poro-elasticity, and various Earth's processes, e.g., dike intrusion, plate spreading and faulting, offer a promising path toward unified models of the Krafla volcanic system. Together, these advances would further enhance our ability to interpret complex geodetic observations and improve hazard assessment and resource managements in volcanic and geothermal areas like Krafla.

References

Acocella, V., and Neri, M. (2009). Dike propagation in volcanic edifices: Overview and possible developments. Tectonophysics, 471(1–2), 67–77. https://doi.org/10.1016/j.tecto.2008.10.002

Abdallah, A., Courtillot, V., Kasser, M., Le Dain, A.-Y., Lépine, J.-C., Robineau, B., et al. (1979). Relevance of Afar seismicity and volcanism to the mechanics of accreting plate boundaries. Nature, 282, 17–23. https://doi.org/10.1038/282017a0

Aden, A. A., Bali, E., Guðfinnsson, G. H., Hersir, G. P., Galeczka, I. M., and Ahmed, K. M. (2025). Characterization and evolution of the basaltic magma reservoir beneath the Asal-Ghoubbet rift, Republic of Djibouti. Journal of Volcanology and Geothermal Research, 108401. https://doi.org/10.1016/j.jvolgeores.2025.108401

Ágústsson, S. M. (2001). Landhæðarbreytingar á Kröflusvæðinu (B.Sc. thesis). University of Iceland, Reykjavik.

Albino, F., Amelung, F., and Gregg, P. (2018). The role of pore fluid pressure on the failure of magma reservoirs: Insights from Indonesian and Aleutian arc volcanoes. Journal of Geophysical Research: Solid Earth, 123, 1328–1349. https://doi.org/10.1002/2017JB014523

Ali, S. T. and Feigl, K. L. (2012). A new strategy for estimating geophysical parameters from InSAR data: Application to the Krafla central volcano in Iceland. Geochemistry, Geophysics, Geosystems, 13, Q06005. https://doi.org/10.1029/2012GC004112

Ali, S. T., Feigl, K. L., Carr, B. B., Masterlark, T. and Sigmundsson, F. (2014). Geodetic measurements and numerical models of rifting in Northern Iceland for 1993–2008. Geophysical Journal International, 196(3), 1267–1280. https://doi.org/10.1093/gji/ggt462

Altamimi, Z., Métivier, L., and Collilieux, X. (2012). ITRF2008 plate motion model. Journal of Geophysical Research: Solid Earth, 117(B07402). https://doi.org/10.1029/2011JB008930

Altamimi, Z., Métivier, L., Rebischung, P., Collilieux, X., Chanard, K., and Barnéoud, J. (2023). ITRF2020 plate motion model. Geophysical Research Letters, 50(18), e2023GL106373. https://doi.org/10.1029/2023GL106373

Altamimi, Z., Métivier, L., Rebischung, P., Rouby, H., and Collilieux, X. (2017). ITRF2014 plate motion model. Geophysical Journal International, 209(3), 1906–1912. https://doi.org/10.1093/gji/ggx136

Altamimi, Z., Rebischung, P., Collilieux, X., Métivier, L., and Chanard, K. (2023). ITRF2020: An augmented reference frame refining the modeling of nonlinear station motions. Journal of Geodesy, 97, 47. https://doi.org/10.1007/s00190-023-01738-w

Altamimi, Z., Rebischung, P., Métivier, L., and Collilieux, X. (2016). ITRF2014: A new release of the International Terrestrial Reference Frame modeling nonlinear station motions. Journal of Geophysical Research: Solid Earth, 121, 6109–6131. https://doi.org/10.1002/2016JB013098

Altamimi, Z., Sillard, P., and Boucher, C. (2002). ITRF2000: A new release of the International Terrestrial Reference Frame for earth science applications. Journal of Geophysical Research: Solid Earth, 107(B10), 2214. https://doi.org/10.1029/2001JB000561

Amiri-Simkooei, A. R., Mohammadloo, T. H., and Argus, D. F. (2017). Multivariate analysis of GPS position time series of JPL second reprocessing campaign. Journal of Geodesy, 91, 685–704. https://doi.org/10.1007/s00190-016-0991-9

Amiri-Simkooei, A. R., Tiberius, C. C. J. M., and Teunissen, P. J. G. (2007). Assessment of noise in GPS coordinate time series: Methodology and results. Journal of Geophysical Research: Solid Earth, 112, B07413. https://doi.org/10.1029/2006JB004913

Amoruso, A., and Crescentini, L. (2009). Shape and volume change of pressurized ellipsoidal cavities from deformation and seismic data. Journal of Geophysical Research: Solid Earth, 114, B02210. https://doi.org/10.1029/2008JB005946

Anderson, K., and Segall, P. (2011). Physics-based models of ground deformation and extrusion rate at effusively erupting volcanoes. Journal of Geophysical Research: Solid Earth, 116, B07204. https://doi.org/10.1029/2010JB007939

Anderson, K., and Segall, P. (2013). Bayesian inversion of data from effusive volcanic eruptions using physics-based models: Application to Mount St. Helens 2004–2008. Journal of Geophysical Research: Solid Earth, 118, 2017–2037. https://doi.org/10.1002/jgrb.50169

Aoki, Y., and Kreemer, C. (2024). Introduction. In Y. Aoki and C. Kreemer (Eds.), GNSS monitoring of the terrestrial environment (pp. 1–10). Elsevier. https://doi.org/10.1016/B978-0-323-95507-2.00001-3

Argus, D. F., and Gordon, R. G. (1991). No-net-rotation model of current plate velocities incorporating plate motion model NUVEL-1. Geophysical Research Letters, 18(11), 2039–2042. https://doi.org/10.1029/91GL01532

Argus, D. F., Gordon, R. G., and DeMets, C. (2011). Geologically current motion of 56 plates relative to the no-net-rotation reference frame. Geochemistry, Geophysics, Geosystems, 12(11). https://doi.org/10.1029/2011GC003751

Argus, D. F., Gordon, R. G., Heflin, M. B., Ma, C., Eanes, R. J., Willis, P., Peltier, W. R., and Owen, S. E. (2010). The angular velocities of the plates and the velocity of the Earth's centre from space geodesy. Geophysical Journal International, 180(3), 913–960. https://doi.org/10.1111/j.1365-246X.2009.04463.x

Ármannsson, H. (1987). Studies on the geochemistry of steam in the Suswa and Longonot areas and water in the Lake Magadi, Kedong Valley and Lake Turkana areas. UNDTCD/Government of Kenya Technical Report, Nairobi, Kenya.

Árnadóttir, T., Jiang, W., Feigl, K. L., Geirsson, H., and Sturkell, E. (2006). Kinematic models of plate boundary deformation in southwest Iceland derived from GPS observations. Journal of Geophysical Research: Solid Earth, 111, B07402. https://doi.org/10.1029/2005JB003907

Árnadóttir, T., Lund, B., Jiang, W., Geirsson, H., Björnsson, H., Einarsson, P. and Sigurdsson, T. (2009). Glacial rebound and plate spreading: results from the first countrywide GPS observations in Iceland. Geophysical Journal International, 177: 691-716. https://doi.org/10.1111/j.1365-246X.2008.04059.x

Árnadóttir, T., Sigmundsson, F., and Delaney, P. T. (1998). Sources of crustal deformation associated with the Krafla, Iceland, eruption of September 1984. Geophysical Research Letters, 25(7), 1043–1046. https://doi.org/10.1029/98GL50655

Ayele, A., Keir, D., Ebinger, C., Wright, T. J., Stuart, G. W., Buck, W. R., et al. (2009). September 2005 mega-dike emplacement in the Manda-Harraro nascent oceanic rift (Afar depression). Geophysical Research Letters, 36, L20306. https://doi.org/10.1029/2009GL039605

Barreto, A., Viltres, R., Matrau, R., Metzger, S., Ófeigsson, B. G., Liu, S., et al. (2025). Interseismic deformation of the Húsavík–Flatey fault (North Iceland) from two

decades of GNSS data. Geophysical Journal International, 241, 1663–1679. https://doi.org/10.1093/gji/ggaf106

Bennett, E.N., Jenner, F.E., Millet, M.-A., Cashman, K.V., and Lissenberg, C.J. (2019). Deep roots for mid-ocean-ridge volcanoes revealed by plagioclase-hosted melt inclusions. Nature, 572, 235–239. https://doi.org/10.1038/s41586-019-1448-0

Benciolini, B., Reguzzoni, M., Venuti, G., and Vitti, A. (2012). Bayesian and Variational Methods for Discontinuity Detection: Theory Overview and Performance Comparison. In Sneeuw, N., Novák, P., Crespi, M., Sansò, F. (Eds.) Berlin, Germany: Springer.

Berardino, P., Fornaro, G., Lanari, R., and Sansosti, E. (2002). A new algorithm for surface deformation monitoring based on small baseline differential SAR interferograms. IEEE Transactions on Geoscience and Remote Sensing, 40(11), 2375–2383. https://doi.org/10.1109/TGRS.2002.803792

Bertiger, W., Bar-Sever, Y., Dorsey, A., Haines, B., Harvey, N., Hemberger, D., et al. (2020). GipsyX/RTGx, a new tool set for space geodetic operations and research. Advances in Space Research, 66(3), 469–489. https://doi.org/10.1016/j.asr.2020.04.015

Bevis, M., Bedford, J., and Caccamise, D. J. II. (2020). The art and science of trajectory modelling. In J. P. Montillet and M. Bos (Eds.), Geodetic Time Series Analysis in Earth Sciences (pp. 1–30). Springer. https://doi.org/10.1007/978-3-030-21718-1_1

Biggs, J., Amelung, F., Gourmelen, N., Dixon, T. H., and Kim, S.-W. (2009). InSAR observations of 2007 Tanzania rifting episode reveal mixed fault and dyke extension in an immature continental rift. Geophysical Journal International, 179(1), 549–558. https://doi.org/10.1111/j.1365-246X.2009.04262.x

Biggs, J., Ebmeier, S., Aspinall, W., Lu, Z., Pritchard, M., Sparks, R. S. J., and Mather, T. (2014). Global link between deformation and volcanic eruption quantified by satellite imagery. Nature Communications, 5, 3471. https://doi.org/10.1038/ncomms4471

Bird, P. (2003). An updated digital model of plate boundaries. Geochemistry, Geophysics, Geosystems, 4(3), 1027. https://doi.org/10.1029/2001GC000252

Björnsson, A., and Eysteinsson, H. (1998). Breytingar á landhæð við Kröflu 1974–1995: Samantekt á landhæðarmælingum: Samvinnuverk Orkustofnunar, Norrænu eldfjallastöðvarinnar og Landsvirkjunar. National Energy Authority Report No. OS-98002, Reykjavík, Iceland.

Björnsson, A., Johnsen, G., Sigurdsson, S., Thorbergsson, G., and Tryggvason, E. (1979). Rifting of the plate boundary in north Iceland 1975–1978. Journal of Geophysical Research, 84(B6), 3029–3038. https://doi.org/10.1029/JB084iB06p03029

Björnsson, A., Saemundsson, K., Einarsson, P., Tryggvason, E., and Grönvold, K. (1977). Current rifting episode in north Iceland. Nature, 266, 318–323. https://doi.org/10.1038/266318a0

Blake, S. (1981). Volcanism and dynamics of open magma chambers. Nature, 289, 783–785. https://doi.org/10.1038/289783a0

Bock, Y., and Melgar, D. (2016). Physical applications of GPS geodesy: A review. Reports on Progress in Physics, 79(10), 106801. https://doi.org/10.1088/0034-4885/79/10/106801

Bodvarsson, G. S., Benson, S. M., Sigurdsson, O., Stefansson, V., and Eliasson, E. T. (1984). The Krafla Geothermal Field, Iceland: 1. Analysis of well test data. Water Resources Research, 20(11), 1515–1530. https://doi.org/10.1029/WR020i011p01515

Bonaccorso, A., and Davis, P. M. (1999). Models of ground deformation from vertical volcanic conduits with application to eruptions of Mount St. Helens and Mount Etna. Journal of Geophysical Research: Solid Earth, 104(B5), 10531–10542. https://doi.org/10.1029/1999JB900054

Bonafede, M. (1995). Interaction between seismic and volcanic deformation: A possible interpretation of ground deformation observed at Vulcano Island (1976–84). Terra Nova, 7(1), 80–86. https://doi.org/10.1111/j.1365-3121.1995.tb00670.x

Bonafede, M., and Danesi, S. (1997). Near-field modifications of stress induced by dyke injection at shallow depth. Geophysical Journal International, 130(2), 435–448. https://doi.org/10.1111/j.1365-246X.1997.tb05659.x

Bonforte, A., Gambino, S., Velardita, R., and Privitera, L. (2024). Review of early ground deformation observations by electronic distance measurements (EDM) on active Sicilian volcanoes: valuable data and information for long-term analyses. Journal of Geodesy, 98, 60. https://doi.org/10.1007/s00190-024-01867-w

Bonforte, A., and Puglisi, G. (2003). Magma uprising and flank dynamics on Mount Etna volcano, studied using GPS data (1994–1995). Journal of Geophysical Research: Solid Earth, 108(B3), 2153. https://doi.org/10.1029/2002JB001845

Borghi, A., Cannizzaro, L., and Vitti, A. (2012). Advanced Techniques for Discontinuity Detection in GNSS Coordinate Time-Series. An Italian Case Study. In Kenyon, S., Pacino, M., Marti, U. (Eds.) Geodesy for Planet Earth. Berlin, Germany: Springer.

Borgia, A., Ferrari, L., and Pasquarè, G. (1992). Importance of gravitational spreading in the tectonic and volcanic evolution of Mount Etna. Nature, 357, 231–235. https://doi.org/10.1038/357231a0

Borsa, A. A., Agnew, D. C. and Cayan, D. R. (2014). Ongoing drought-induced uplift in the western United States. Science, 345(6204), 1587–1590. https://doi.org/10.1126/science.1260279

Bos, M. S., Fernandes, R. M. S., Williams, S. D. P., and Bastos, L. (2008). Fast error analysis of continuous GPS observations. Journal of Geodesy, 82, 157–166. https://doi.org/10.1007/s00190-007-0165-x

Bos, M. S., Fernandes, R. M. S., Williams, S. D. P., and Bastos, L. (2013). Fast error analysis of continuous GNSS observations with missing data. Journal of Geodesy, 87, 351–360. https://doi.org/10.1007/s00190-012-0605-0

Bos, M. S., Montillet, J. P., Williams, S. D. P., and Fernandes, R. M. S. (2020). Introduction to geodetic time series analysis. In J. P. Montillet and M. Bos (Eds.), Geodetic Time Series Analysis in Earth Sciences. Springer Geophysics. Springer, Cham. https://doi.org/10.1007/978-3-030-21718-1_2

Bradford, I. D. R., Fuller, J., Thompson, P. J., and Walsgrove, T. R. (1998). Benefits of assessing the solids production risk in a North Sea reservoir using elastoplastic modelling. In SPE/ISRM Rock Mechanics in Petroleum Engineering, Trondheim, Norway. Society of Petroleum Engineers.

Bramham, E. K. (2014). LiDAR and InSAR analysis of deformation in the Krafla rift zone, NE Iceland (Ph.D. thesis). University of Leeds. https://etheses.whiterose.ac.uk/7289/

Brandsdóttir, B., Menke, W., Einarsson, P., White, R. S., and Staples, R. K. (1997). Färoe-Iceland Ridge Experiment 2. Crustal structure of the Krafla central volcano. Journal of Geophysical Research: Solid Earth, 102(B4), 7867–7886. https://doi.org/10.1029/96JB03799

Brouwer, W. S., and Hanssen, R. F. (2024). Estimating three-dimensional displacements with InSAR: The strapdown approach. Journal of Geodesy, 98, 110. https://doi.org/10.1007/s00190-024-01918-2

Buck, W. R., Einarsson, P., and Brandsdóttir, B. (2006). Tectonic stress and magma chamber size as controls on dike propagation: Constraints from the 1975–1984 Krafla rifting episode. Journal of Geophysical Research: Solid Earth, 111, B12404. https://doi.org/10.1029/2005JB003879

Cao, Y., Jónsson, S., and Hreinsdóttir, S. (2023). Iceland kinematics from InSAR. Journal of Geophysical Research: Solid Earth, 128, e2022JB025546. https://doi.org/10.1029/2022JB025546

Cashman, K. V., Sparks, R. S. J., and Blundy, J. D. (2017). Vertically extensive and unstable magmatic systems: A unified view of igneous processes. Science, 355(6331). https://doi.org/10.1126/science.aag3055

Chadwick, W. W., and Dieterich, J. H. (1995). Mechanical modeling of circumferential and radial dike intrusion on Galapagos volcanoes. Journal of Volcanology and Geothermal Research, 66(1–4), 37–52. https://doi.org/10.1016/0377-0273(94)00060-T

Corti, N., Bonali, F. L., Pasquaré Mariotto, F., Tibaldi, A., Russo, E., Hjartardóttir, Á. R., Einarsson, P., Rigoni, V., and Bressan, S. (2021). Fracture Kinematics and Holocene Stress Field at the Krafla Rift, Northern Iceland. Geosciences, 11(2), 101. https://doi.org/10.3390/geosciences11020101

Currenti, G., and Williams, C. A. (2014). Numerical modeling of deformation and stress fields around a magma chamber: Constraints on failure conditions and rheology. Physics of the Earth and Planetary Interiors, 226, 14–27. https://doi.org/10.1016/j.pepi.2013.11.003

Dahm, T. (2002). Numerical simulations of the propagation path and the arrest of fluid-filled fractures in the Earth. Geophysical Journal International, 141, 623–638. https://doi.org/10.1046/j.1365-246x.2000.00102

Daniels, K. A., and Menand, T. (2015). An experimental investigation of dyke injection under regional extensional stress. Journal of Geophysical Research: Solid Earth, 120, 2014–2035. https://doi.org/10.1002/2014JB011627

Davis, J. L., Wernicke, B. P., Bisnath, S., Niemi, N. A., and Elósegui, P. (2006). Subcontinental-scale crustal velocity changes along the Pacific-North America plate boundary. Nature, 441(29), 1131–1134. https://doi.org/10.1038/nature04781

De Wit, J. J. M., Cox, P. B., and Bosma, D. A. (2024). Quality-of-service based radar resource management for concurrent SAR imaging modes. In 2024 International Radar Conference (RADAR) (pp. 1–6). IEEE. https://doi.org/10.1109/RADAR58436.2024.10993892

de Zeeuw-van Dalfsen, E., Pedersen, R., Sigmundsson, F. and Pagli, C. (2004). Satellite radar interferometry 1993–1999 suggests deep accumulation of magma near the crust-mantle boundary at the Krafla volcanic system, Iceland. Geophysical Research Letters, 31, L13611. https://doi.org/10.1029/2004GL020059

Del Negro, C., Currenti, G., and Scandura, D. (2009). Temperature-dependent viscoelastic modeling of ground deformation: Application to Etna volcano during the 1993–1997 inflation period. Physics of the Earth and Planetary Interiors, 172(3–4), 299–309. https://doi.org/10.1016/j.pepi.2008.10.019

DeMets, C., Gordon, R. G., and Argus, D. F. (2010). Geologically current plate motions. Geophysical Journal International, 181, 1–80. https://doi.org/10.1111/j.1365-246X.2009.04491.x

DeMets, C., Gordon, R. G., Argus, D. F., and Stein, S. (1990). Current plate motions. Geophysical Journal International, 101(2), 425–478. https://doi.org/10.1111/j.1365-246X.1990.tb06579.x

DeMets, C., Gordon, R. G., Argus, D. F., and Stein, S. (1994). Effect of recent revisions to the geomagnetic reversal time scale on estimates of current plate motions. Geophysical Research Letters, 21(20), 2191–2194. https://doi.org/10.1029/94GL02118

Deng, L., Xiao, Y., Chen, Q., Peng, W., Li, Z., Chen, H., and Wu, Z. (2025). Detection and interpretation of the time-varying seasonal signals in China with multi-geodetic

measurements. Geodesy and Geodynamics, 16(1), 42–54. https://doi.org/10.1016/j.geog.2024.05.005
Didova, O., Gunter, B., Riva, R., and Roese-Koerner, L. (2016). An approach for estimating time-variable rates from geodetic time series. Journal of Geodesy, 90(11), 1207–1221. https://doi.org/10.1007/s00190-016-0918-5
Dinçer, I., Acar, A., Çobanoğlu, I., and Uras, Y. (2004). Correlation between Schmidt hardness, uniaxial compressive strength and Young's modulus for andesites, basalts and tuffs. Bulletin of Engineering Geology and the Environment, 63(2), 141–148. https://doi.org/10.1007/s10064-004-0230-0
Dorndorf, A., Kargoll, B., Paffenholz, J.-A., and Alkhatib, H. (2021). Bayesian Robust Multivariate Time Series Analysis in Nonlinear Models with Autoregressive and t-Distributed Errors. Engineering Proceedings, 5(1), 20. https://doi.org/10.3390/engproc2021005020
Dragert, H., Wang, K. and James, T. S. (2001). A silent slip event on the deeper Cascadia subduction interface. Science, 292(5521), 1525–1528. https://doi.org/10.1126/science.1060152
Dragoni, M., and Magnanensi, C. (1989). Displacement and stress produced by a pressurized, spherical magma chamber, surrounded by a viscoelastic shell. Physics of the Earth and Planetary Interiors, 56(3–4), 316–328. https://doi.org/10.1016/0031-9201(89)90166-0
Drewes, H. (1998). Combination of VLBI, SLR, and GPS determined station velocities for actual plate kinematic and crustal deformation models. In Geodynamics (pp. 254–259). Springer. https://doi.org/10.1007/978-3-642-72245-5_59
Drewes, H. (2009). The Actual Plate Kinematic and Crustal Deformation Model APKIM2005 as basis for a non-rotating ITRF. In Geodetic Reference Frames (Vol. 134, pp. 95–99). Springer. https://doi.org/10.1007/978-3-642-00860-3_15
Drouin, V. (2024). InSAR monitoring of Krafla, Bjarnarflag and Þeistareykir geothermal areas (2024 update). Landsvirkjun, Reykjavík. Retrieved from https://gogn.lv.is/files/2024/2024-085.pdf
Drouin, V., and Sigmundsson, F. (2019). Countrywide observations of plate spreading and glacial isostatic adjustment in Iceland inferred by Sentinel-1 radar interferometry, 2015–2018. Geophysical Research Letters, 46, 8046–8055. https://doi.org/10.1029/2019GL082629
Drouin, V., Sigmundsson, F., Ófeigsson, B. G., Hreinsdóttir, S., Sturkell, E., and Einarsson, P. (2017a). Deformation in the Northern Volcanic Zone of Iceland 2008–2014: An interplay of tectonic, magmatic, and glacial isostatic deformation. Journal of Geophysical Research: Solid Earth, 122(4), 3158–3178. https://doi.org/10.1002/2016JB013206
Drouin, V., Sigmundsson, F., Verhagen, S., Ófeigsson, B. G., Spaans, K., and Hreinsdóttir, S. (2017b). Deformation at Krafla and Bjarnarflag geothermal areas, Northern Volcanic Zone of Iceland, 1993–2015. Journal of Volcanology and Geothermal Research, 344, 92–105. https://doi.org/10.1016/j.jvolgeores.2017.06.013
Dvorak, J. J., and Dzurisin, D. (1997). Volcano geodesy: The search for magma reservoirs and the formation of eruptive vents. Reviews of Geophysics, 35(3), 343–384. https://doi.org/10.1029/97RG00070
Dzurisin, D. (2003). A comprehensive approach to monitoring volcano deformation as a window on the eruption cycle. Reviews of Geophysics, 41(1), 1001. https://doi.org/10.1029/2001RG000107
Ebmeier, S. K., Andrews, B. J., Araya, M. C., Arnold, D. W. D., Biggs, J., Cooper, C., et al. (2018). Synthesis of global satellite observations of magmatic and volcanic

deformation: Implications for volcano monitoring and the lateral extent of magmatic domains. Journal of Applied Volcanology, 7, 2. https://doi.org/10.1186/s13617-018-0071-3

Edmonds, M., Cashman, K. V., Holness, M., and Jackson, M. (2019). Architecture and dynamics of magma reservoirs. Philosophical Transactions of the Royal Society A: Mathematical, Physical and Engineering Sciences, 377(2139), 20180298. https://doi.org/10.1098/rsta.2018.0298

Einarsson, P. (1978). S-wave shadows in the Krafla Caldera in NE-Iceland, evidence for a magma chamber in the crust. Bulletin of Volcanology, 41, 187–195. https://doi.org/10.1007/BF02597222

Einarsson, P. (1991). Umbrotin við Kröflu 1975–89. In Garðarsson, A. and Einarsson, Á. (Eds.), Náttúra Mývatns (pp. 97–139). Hið íslenska náttúrufræðifélag, Reykjavík.

Eskandari, R. and Scaioni, M. (2024). Spatiotemporal pattern detection of ground deformations induced by extreme rainfall using InSAR EGMS: The case of Cortina d'Ampezzo after Vaia Storm. ISPRS Annals of the Photogrammetry, Remote Sensing and Spatial Information Sciences, X-3-2024, 131–138. https://doi.org/10.5194/isprs-annals-X-3-2024-131-2024

Euler, L. (1765). Theoria motus corporum solidorum seu rigidorum [Theory of the motion of solid or rigid bodies]. A. F. Röse (Ed.), Opera Omnia, Series 2, Vol. 1.

Ewart, J. A., Voight, B., and Björnsson, A. (1991). Elastic deformation models of Krafla Volcano, Iceland, for the decade 1975 through 1985. Bulletin of Volcanology, 53, 436–459. https://doi.org/10.1007/BF00258184

Fattahi, H., and Amelung, F. (2014). InSAR uncertainty due to orbital errors. Geophysical Journal International, 199(1), 549–560. https://doi.org/10.1093/gji/ggu276

Fattahi, H., and Amelung, F. (2015). InSAR bias and uncertainty due to the systematic and stochastic tropospheric delay. Journal of Geophysical Research: Solid Earth, 120, 8758–8773. https://doi.org/10.1002/2015JB012419

Fattahi, H., Simons, M., and Agram, P. (2017). InSAR time-series estimation of the ionospheric phase delay: An extension of the split range-spectrum technique. IEEE Transactions on Geoscience and Remote Sensing, 55(10), 5984–5996. https://doi.org/10.1109/TGRS.2017.2718566

Feng, S., Bo, W., Ma, Q., Li, M., and Liu, J. (2017). Spectral analysis for GNSS coordinate time series using chirp Fourier transform. Acta Geophysica, 65, 1111–1118. https://doi.org/10.1007/s11600-017-0090-1

Fernández, J., Pepe, A., Poland, M. P., and Sigmundsson, F. (2017). Volcano geodesy: Recent developments and future challenges. Journal of Volcanology and Geothermal Research, 344, 1–12. https://doi.org/10.1016/j.jvolgeores.2017.08.006

Ferretti, A., Monti-Guarnieri, A., Prati, C., Rocca, F., and Massonnet, D. (2007). InSAR Principles: Guidelines for SAR Interferometry Processing and Interpretation (TM-19, February 2007) (J. Lichtenegger, Tech. Coord.; K. Fletcher, Ed.). European Space Agency, ESA Publications, ESTEC, Noordwijk, The Netherlands. ISBN: 92-9092-233-8.

Ferretti, A., Prati, C., and Rocca, F. (2001). Permanent scatterers in SAR interferometry. IEEE Transactions on Geoscience and Remote Sensing, 39(1), 8–20. https://doi.org/10.1109/36.898661

Foulger, G. R., Beutler, G., Bilham, R., Einarsson, P., Fankhauser, S., Gurtner, W., et al. (1993). The Iceland 1986 GPS geodetic survey: Tectonic goals and data processing results. Bulletin Géodésique, 67, 148–172. https://doi.org/10.1007/BF00806254

Foulger, G., Jahn, C. H., Seeber, G., Einarsson, P., Julian, B. R., Heki, K. (1992). Post-rifting stress relaxation at the divergent plate boundary in Northeast Iceland. Nature, 358, 488–490. https://doi.org/10.1038/358488a0

Freed, A. M. and Bürgmann, R. (2004). Evidence of power-law flow in the Mojave desert mantle. Nature, 430, 548–551. https://doi.org/10.1038/nature02784

Freire, S., Florczyk, A. J., Pesaresi, M., and Sliuzas, R. (2019). An Improved Global Analysis of Population Distribution in Proximity to Active Volcanoes, 1975–2015. ISPRS International Journal of Geo-Information, 8(8), 341. https://doi.org/10.3390/ijgi8080341

Fuhrmann, T., and Garthwaite, M. C. (2019). Resolving Three-Dimensional Surface Motion with InSAR: Constraints from Multi-Geometry Data Fusion. Remote Sensing, 11(3), 241. https://doi.org/10.3390/rs11030241

Gambino, S., Falzone, G., Ferro, A., and Laudani, G. (2014). Volcanic processes detected by tiltmeters: A review of experience on Sicilian volcanoes. Journal of Volcanology and Geothermal Research, 271, 43–54. https://doi.org/10.1016/j.jvolgeores.2013.11.007

Gazeaux, J., Williams, S., King, M., Bos, M., Dach, R., Deo, M., et al. (2013). Detecting offsets in GPS time series: First results from the Detection of Offsets in GPS Experiment. Journal of Geophysical Research: Solid Earth, 118, 2397–2407. https://doi.org/10.1002/jgrb.50152

Geirsson, H., Árnadóttir, T., Hreinsdóttir, S., Decriem, J., Lafemina, P. C., Jónsson, S., et al. (2010). Overview of results from continuous GPS observations in Iceland from 1995 to 2010. Jökull, 2010(60), 3–22. https://doi.org/10.33799/jokull2010.60.003

Geirsson, H., Árnadóttir, T., Völksen, C., Jiang, W., Sturkell, E., Villemin, T., et al. (2006). Current plate movements across the Mid-Atlantic Ridge determined from 5 years of continuous GPS measurements in Iceland. Journal of Geophysical Research: Solid Earth, 111, B09407. https://doi.org/10.1029/2005JB003717

Geirsson, H., LaFemina, P., Árnadóttir, T., Sturkell, E., Sigmundsson, F., Travis, M., Schmidt, P., Lund, B., Hreinsdóttir, S., and Bennett, R. (2012). Volcano deformation at active plate boundaries: Deep magma accumulation at Hekla volcano and plate boundary deformation in south Iceland. Journal of Geophysical Research: Solid Earth, 117(B11), B11409. https://doi.org/10.1029/2012JB009400

Geng, J., Chen, X., Pan, Y., Mao, S., Li, C., Zhou, J., and Zhang, K. (2019). PRIDE PPP-AR: An open-source software for GPS PPP ambiguity resolution. GPS Solutions, 23(1), 91. https://doi.org/10.1007/s10291-019-0888-1

Geng, J., Shi, C., and Ge, M., Dodson, A. H., Lou, Y., Zhao, Q., Liu, J. (2012). Improving the estimation of fractional-cycle biases for ambiguity resolution in precise point positioning. Journal of Geodesy, 86, 579–589. https://doi.org/10.1007/s00190-011-0537-0

Gerbault, M., Cappa, F., and Hassani, R. (2012). Elasto-plastic and hydromechanical models of failure around an infinitely long magma chamber. Geochemistry, Geophysics, Geosystems, 13, Q03009. https://doi.org/10.1029/2011GC003917

Gerke, K. (1974). Crustal movements in the Myvatn and in the Thingvallavatn area, both horizontal and vertical. In L. Kristjansson (Ed.), Geodynamics of Iceland and the North Atlantic Area (pp. 263–275). Dordrecht, Netherlands: D. Reidel Publishing Company.

Grandin, R., Socquet, A., Binet, R., Klinger, Y., Jacques, E., de Chabalier, J.-B., et al. (2009). September 2005 Manda Hararo-Dabbahu rifting event, Afar (Ethiopia): Constraints provided by geodetic data. Journal of Geophysical Research: Solid Earth, 114(B8), B08404. https://doi.org/10.1029/2008JB005843

Grandin, R., Socquet, A., Jacques, E., Mazzoni, N., de Chabalier, J.-B., and King, G. C. P. (2010). Sequence of rifting in Afar, Manda-Hararo rift, Ethiopia, 2005–2009: Time-space evolution and interactions between dikes from interferometric synthetic aperture radar and static stress change modeling. Journal of Geophysical Research: Solid Earth, 115, B10413. https://doi.org/10.1029/2009JB000815

Grandin, R., Socquet, A., Doubre, C., Jacques, E., and King, G. C. P. (2012). Elastic thickness control of lateral dyke intrusion at mid-ocean ridges. Earth and Planetary Science Letters, 319–320, 83–95. https://doi.org/10.1016/j.epsl.2011.12.011

Gregg, P. M., Zhan, Y., Amelung, F., Geist, D., Mothes, P., Koric, S., et al. (2022). Forecasting mechanical failure and the 26 June 2018 eruption of Sierra Negra Volcano, Galápagos, Ecuador. Science Advances, 8(22), eabm4261. https://doi.org/10.1126/sciadv.abm4261

Greiner, S. H. M., and Geirsson, H. (2024). Including a pressure dependent relation between static and dynamic elastic moduli in a Finite Element deformation model of Grímsvötn Volcano, Iceland. Volcanica, 7(2), 907–924. https://doi.org/10.30909/vol.07.02.907924

Greiner, S. H. M., Sigmundsson, F., Geirsson, H., Burchardt, S., and Galland, O. (2025). Tectonic stress as the driving mechanism for dike opening in an oblique rift setting: A deformation model of the 2021 Fagradalsfjall dike, Iceland. Geophysical Research Letters, 52, e2024GL113970. https://doi.org/10.1029/2024GL113970

Gripp, A. E., and Gordon, R. G. (1990). Current plate velocities relative to the hotspots incorporating the NUVEL-1 global plate motion model. Geophysical Research Letters, 17(8), 1109–1112. https://doi.org/10.1029/GL017i008p01109

Gripp, A. E., and Gordon, R. G. (2002). Young tracks of hotspots and current plate velocities. Geophysical Journal International, 150(2), 321–361. https://doi.org/10.1046/j.1365-246X.2002.01627.x

Grönvold, K. (1984). Myvatn Fires 1724–1729: Chemical composition of the lava. Nordic Volcanological Institute Report, Reykjavík, Iceland.

Grönvold, K., and Mäkipää, H. (1978). Chemical composition of Krafla lavas 1975–1977. Nordic Volcanological Institute Report No. 78–16, Reykjavík, Iceland.

Gudmundsson, B. Þ., and Arnórsson, S. (2002). Geochemical monitoring of the Krafla and Námafjall geothermal areas, N-Iceland. Geothermics, 31(2), 195–243. https://doi.org/10.1016/S0375-6505(01)00022-0

Guðmundsson, G., Pálmason, G., Grönvold, K., Ragnarsson, K., Sæmundsson, K., and Arnórsson, S. (1971). Námafjall–Krafla: áfangaskýrsla um rannsókn jarðhitasvæðanna. Orkustofnun Report, Reykjavík, Iceland.

Gudnason, E. Á., Drouin, V., Yang, Y., Sigmundsson, F., Ágústsdóttir, T., and Mortensen, A. K. (2024). Changes in seismicity and observed deformation related to inflation at the Theistareykir high-temperature geothermal field, NE Iceland, in 2023–2024. EGU General Assembly 2024, Vienna, Austria, 14–19 April 2024 (EGU24-19913). https://doi.org/10.5194/egusphere-egu24-19913

Hampton, R. L., Bindeman, I. N., Stern, R. A., Coble, M. A., and Rooyakkers, S. M. (2021). A microanalytical oxygen isotopic and U–Th geochronologic investigation and modeling of rhyolite petrogenesis at the Krafla Central Volcano, Iceland. Journal of Volcanology and Geothermal Research, 414, 107229. https://doi.org/10.1016/j.jvolgeores.2021.107229

Hanssen, R. F. (2002). Radar system theory and interferometric processing. In Radar Interferometry (pp. 9–43). Springer, Dordrecht. https://doi.org/10.1007/0-306-47633-9_2

Hautmann, S., Gottsmann, J., Sparks, R. S. J., Mattioli, G. S., Sacks, I. S., and Strutt, M. H. (2010). Effect of mechanical heterogeneity in arc crust on volcano deformation with application to Soufrière Hills Volcano, Montserrat, West Indies. Journal of Geophysical Research: Solid Earth, 115, B09203. https://doi.org/10.1029/2009JB006909

He, X., Bos, M. S., Montillet, J. P., and Fernandes, R. M. S. (2019). Investigation of the noise properties at low frequencies in long GNSS time series. Journal of Geodesy, 93, 1271–1282. https://doi.org/10.1007/s00190-019-01244-y

Head, M., Hickey, J., Gottsmann, J., and Fournier, N. (2021). Exploring the impact of thermally controlled crustal viscosity on volcanic ground deformation. Journal of Geophysical Research: Solid Earth, 126, e2020JB020724. https://doi.org/10.1029/2020JB020724

Heimisson, E. R., Einarsson, P., Sigmundsson, F., and Brandsdóttir, B. (2015). Kilometer-scale Kaiser effect identified in Krafla volcano, Iceland. Geophysical Research Letters, 42(19), 7958–7965. https://doi.org/10.1002/2015GL065680

Heki, K., Foulger, G. R., Julian, B. R., and Jahn, C.-H. (1993). Plate dynamics near divergent boundaries: Geophysical implications of postrifting crustal deformation in NE Iceland. Journal of Geophysical Research, 98(B8), 14279–14297. https://doi.org/10.1029/93JB00781

Henriot, O., and Villemin, T. (2005). Deformation at the northern end of the Icelandic rift mapped by InSAR (1992-2000), a decade after the Krafla Rifting Episode. Geodinamica Acta, 18(1), 43–57. https://doi.org/10.3166/ga.18.43-57

Herring, T. A., King, R. W., Floyd, M. A., and McClusky, S. C. (2018). Introduction to GAMIT/GLOBK. Massachusetts Institute of Technology. Retrieved from http://geoweb.mit.edu/gg/Intro_GG.pdf

Hersir, G. P., Sigmundsson, F., Ágústsson, K., Magnússon, I. Þ., Drouin, V., Vilhjálmsson, A. M., et al. (2020). Geodetic observation and surface deformation at Krafla in late 2019–2020. Landsvirkjun Report No. LV-2020-036, Reykjavík, Iceland.

Himematsu, Y., Ozawa, T., and Aoki, Y. (2024). Precursory crater contraction associated with the 2017 eruption of Shinmoe-dake volcano (Japan) detected by PALSAR-2 and Sentinel-1 InSAR. Earth, Planets and Space, 76, 141. https://doi.org/10.1186/s40623-024-02083-8

Hjartardóttir, Á. R., Einarsson, P., Bramham, E., and Wright, T. (2012). The Krafla fissure swarm, Iceland, and its formation by rifting events. Bulletin of Volcanology, 74, 2139–2153. https://doi.org/10.100.1007/s00445-012-0659-0

Hjartardóttir, Á. R., Einarsson, P., Magnúsdóttir, S., Björnsdóttir, Þ., and Brandsdóttir, B. (2016). Fracture systems of the Northern Volcanic Rift Zone, Iceland: An onshore part of the Mid-Atlantic plate boundary. Geological Society, London, Special Publications, 420(1), 297–314. https://doi.org/10.1144/SP420.1

Hoek, E. (1990). Estimating Mohr–Coulomb friction and cohesion values from the Hoek–Brown failure criterion. International Journal of Rock Mechanics and Mining Sciences and Geomechanics Abstracts, 12, 227–229. https://doi.org/10.1016/0148-9062(90)94333-O

Hofmann-Wellenhof, B., Lichtenegger, H., and Wasle, E. (2007). GNSS—global navigation satellite systems: GPS, GLONASS, Galileo, and more. Vienna, Austria: Springer Science and Business Media.

Hofton, M. A., and Foulger, G. R. (1996). Postrifting anelastic deformation around the spreading plate boundary, north Iceland: 1. Modeling of the 1987–1992 deformation

field using a viscoelastic Earth structure. Journal of Geophysical Research, 101(B11), 25403–25421. https://doi.org/10.1029/96JB02466

Hohensinn, R., Ruttner, P., and Bock, Y. (2024). Sensitivity of GNSS to vertical land motion over Europe: Effects of geophysical loadings and common-mode errors. Journal of Geodesy, 98, 68. https://doi.org/10.1007/s00190-024-01856-z

Hollingsworth, J., Leprince, S., Ayoub, F., and Avouac, J.-P. (2012). Deformation during the 1975–1984 Krafla rifting crisis, NE Iceland, measured from historical optical imagery. Journal of Geophysical Research: Solid Earth, 117, B11407. https://doi.org/10.1029/2012JB009140

Hollingsworth, J., Leprince, S., Ayoub, F., and Avouac, J.-P. (2013). New constraints on dike injection and fault slip during the 1975–1984 Krafla rift crisis, NE Iceland. Journal of Geophysical Research: Solid Earth, 118, 3707–3727. https://doi.org/10.1002/jgrb.50223

Hooper, A., Zebker, H., Segall, P., and Kampes, B. (2004). A new method for measuring deformation on volcanoes and other natural terrains using InSAR persistent scatterers. Geophysical Research Letters, 31, L23611. https://doi.org/10.1029/2004GL021737

Hreinsdóttir, S., Sigmundsson, F., Roberts, M. J., Björnsson, H., Grapenthin, R., Arason, T., Árnadóttir, T., et al. (2014). Volcanic plume height correlated with magma-pressure change at Grímsvötn Volcano, Iceland. Nature Geoscience, 7, 214–218. https://doi.org/10.1038/ngeo2044

Islam, M., and Sturkell, E. (2015). Temperature-dependent Newtonian rheology in advection-convection geodynamical model for plate spreading in Eastern Volcanic Zone, Iceland. Journal of Geoscience and Environment Protection, 3(5), 14–26. https://doi.org/10.4236/gep.2015.35003

Jaeger, J. C., Cook, N. G. W., and Zimmerman, R. W. (2007). Fundamentals of rock mechanics (4th ed.). Malden, MA: Blackwell Publishing.

Jahn, C. H., Seeber, G., Foulger, G., and Björnsson, A. (1990). A GPS survey in the North-East Volcanic Zone of Iceland 1987: First results. In P. Vyskocil, C. Reigber, and P. A. Cross (Eds.), Global and Regional Geodynamics (Vol. 101). New York, NY: Springer. https://doi.org/10.1007/978-1-4615-7109-4_21

Jóhannesson, H., and Sæmundsson, K. (2009). Jarðfræðikort af Íslandi 1:600,000, höggun: Geological map of Iceland 1:600,000 – Tectonics. Icelandic Institute of Natural History.

Johnsen, G., Björnsson, A., and Sigurdsson, S. (1980). Gravity and elevation changes caused by magma movement beneath the Krafla Caldera, Northeast Iceland. Journal of Geophysics, 47(1), 132–140. Retrieved from https://journal.geophysicsjournal.com/JofG/article/view/99

Johnson, D. J., Sigmundsson, F., and Delaney, P. T. (2000). Comment on 'Volume of magma accumulation or withdrawal estimated from surface uplift or subsidence' by Delaney and McTigue. Bulletin of Volcanology, 61, 491–493. https://doi.org/10.1007/s004450050006

Jónasson, K. (1994). Rhyolite volcanism in the Krafla central volcano, north-east Iceland. Bulletin of Volcanology, 56(6), 516–528. https://doi.org/10.1007/BF00302832

Jónsson, S. (2012). Tensile rock mass strength estimated using InSAR. Geophysical Research Letters, 39, L21305. https://doi.org/10.1029/2012GL053309

Kebede, B. A., Pagli, C., Keir, D., Sigmundsson, F., La Rosa, A., Wang, H., et al. (2025). Continuous subsidence of Dallol volcano caused by magmatic, hydrothermal, and salt dissolution processes: Insights from InSAR observations. Geochemistry, Geophysics, Geosystems, 26, e2024GC012048. https://doi.org/10.1029/2024GC012048

Kim, D., Brown, L. D., Árnason, K., Gudmundsson, Ó., Águstsson, K., and Flóvenz, Ó. G. (2020). Magma "bright spots" mapped beneath Krafla, Iceland, using RVSP imaging of reflected waves from microearthquakes. Journal of Volcanology and Geothermal Research, 391, 106365. https://doi.org/10.1016/j.jvolgeores.2018.04.022

Kjøll, H. J., Galland, O., Labrousse, L., and Andersen, T. B. (2019). Emplacement mechanisms of a dyke swarm across the brittle-ductile transition and the geodynamic implications for magma-rich margins. Earth and Planetary Science Letters, 518, 223–235. https://doi.org/10.1016/j.epsl.2019.04.016

Klos, A., Bogusz, J., Figurski, M., and Kosek, W. (2015). On the handling of outliers in the GNSS time series by means of the noise and probability analysis. In C. Rizos and P. Willis (Eds.), IAG 150 Years. International Association of Geodesy Symposia (Vol. 143). Springer, Cham. https://doi.org/10.1007/1345_2015_78

Klos, A., Bos, M. S., and Bogusz, J. (2018). Detecting time-varying seasonal signal in GPS position time series with different noise levels. GPS Solutions, 22, 21. https://doi.org/10.1007/s10291-017-0686-6

Kreemer, C., Blewitt, G., and Klein, E. C. (2014). A geodetic plate motion and global strain rate model. Geochemistry, Geophysics, Geosystems, 15(10), 3849–3889. https://doi.org/10.1002/2014GC005407

Kreemer, C., Holt, W. E., and Haines, A. J. (2003). An integrated global model of present-day plate motions and plate boundary deformation. Geophysical Journal International, 154(1), 8–34. https://doi.org/10.1046/j.1365-246X.2003.01917.x

La Rosa, A., Pagli, C., Wang, H., Cavallaro, D., Keir, D., Wright, T. J., and Ruch, J. (2024). Simultaneous rift-scale inflation of a deep crustal sill network in Afar, East Africa. Nature Communications, 15, 4287. https://doi.org/10.1038/s41467-024-47136-4

LaFemina, P. C., Dixon, T. H., Malservisi, R., Árnadóttir, T., Sturkell, E., Sigmundsson, F., and Einarsson, P. (2005). Geodetic GPS measurements in south Iceland: Strain accumulation and partitioning in a propagating ridge system. Journal of Geophysical Research: Solid Earth, 110, B11405. https://doi.org/10.1029/2005JB003675

Lanari, R., Casu, F., Manzo, M., Zeni, G., Berardino, P., Manunta, M., and Pepe, A. (2007). An overview of the Small BAseline Subset algorithm: A DInSAR technique for surface deformation analysis. Pure and Applied Geophysics, 164, 637–661. https://doi.org/10.1007/s00024-007-0192-9

Landmælingar Íslands (LMÍ). (2020). ÍslandsDEM útgáfa 1.0 [Digital elevation model]. https://gatt.natt.is/geonetwork/srv/api/records/e6712430-a63c-4ae5-9158-c89d16da6361

Langbein, J. (2012). Estimating rate uncertainty with maximum likelihood: Differences between power-law and flicker–random-walk models. Journal of Geodesy, 86, 775–783. https://doi.org/10.1007/s00190-012-0556-5

Lanzi, C., Drouin, V., Sigmundsson, F., Geirsson, H., Hersir, G. P., Ágústsson, K., Parks, M. M., et al. (2023). Pressure increase at the magma-hydrothermal interface at Krafla caldera, North-Iceland, 2018–2020: Magmatic processes or hydrothermal changes? Journal of Volcanology and Geothermal Research, 440, 107849. https://doi.org/10.1016/j.jvolgeores.2023.107849

Lanzi, C., Sigmundsson, F., Geirsson, H., and Hreinsdóttir, S. (2022). 2021 GNSS surveying and surface deformation at Krafla, Námafjall and Þeistareykir: Status report, February 2022. Landsvirkjun Report No. LV-2022-027, Reykjavík, Iceland. Retrieved from https://gogn.lv.is/files/2022/2022-027.pdf

Lanzi, C., Sigmundsson, F., Parks, M. M., Geirsson, H., and Drouin, V. (2024). Strain localization at volcanoes undergoing extension: Investigation of long-term

deformation at Krafla and Askja volcanic systems in North Iceland. Geophysical Research Letters, 51, e2024GL110299. https://doi.org/10.1029/2024GL110299

Lazecký, M., Spaans, K., González, P. J., Maghsoudi, Y., Morishita, Y., Albino, F., Elliott, J., Greenall, N., Hatton, E., Hooper, A., Juncu, D., McDougall, A., Walters, R. J., Watson, C. S., Weiss, J. R., and Wright, T. J. (2020). LiCSAR: An Automatic InSAR Tool for Measuring and Monitoring Tectonic and Volcanic Activity. Remote Sensing, 12(15), 2430. https://doi.org/10.3390/rs12152430

Le Mével, H., Córdova, L., Cardona, C., Lundgren, P., Dzurisin, D., Pritchard, M. E., and Feigl, K. L. (2021). Unrest at the Laguna del Maule volcanic field 2005–2020: Renewed acceleration of deformation. Bulletin of Volcanology, 83, 39. https://doi.org/10.1007/s00445-021-01457-0

Lee, S., Choi, E., Son, M., Song, S. G. and Gómez, D. D. (2025). Viscoelastic modelling reveals correlation between GNSS-derived deformation rates after the 2011 Tohoku-Oki earthquake and lithospheric thickness in the southern Korean Peninsula. Geophysical Journal International, 242(1), ggaf182. https://doi.org/10.1093/gji/ggaf182

Lengliné, O., Marsan, D., Got, J.-L., Pinel, V., Ferrazzini, V., and Okubo, P. G. (2008). Seismicity and deformation induced by magma accumulation at three basaltic volcanoes. Journal of Geophysical Research: Solid Earth, 113, B12305. https://doi.org/10.1029/2008JB005937

Li, J., Jin, G., Xiong, X., Zhou, L., Ye, H., Shi, Q. and Yang, H. (2024). Surface time series response and deformation cause analysis in 2021 Zhengzhou extreme weather, China. Earth and Space Science, 11, e2024EA003643. https://doi.org/10.1029/2024EA003643

Li, S., Grapenthin, R., Sigmundsson, F., Drouin, V., Hreinsdóttir, S., and Ófeigsson, B. G. (2022). Post-rifting relaxation during 2015–2020 following the Bárðarbunga-Holuhraun dike intrusion and eruption in Iceland. Geophysical Research Letters, 49, e2022GL098977. https://doi.org/10.1029/2022GL098977

Li, Z., Jiang, W., van Dam, T., Zou, X., Chen, Q. and Chen, H. (2025). A review on modeling environmental loading effects and their contributions to nonlinear variations of Global Navigation Satellite System coordinate time series. Engineering, 47, 26–37. https://doi.org/10.1016/j.eng.2024.09.001

Lister, J. R., and Kerr, R. C. (1991). Fluid-mechanical models of crack propagation and their application to magma transport in dykes. Journal of Geophysical Research, 96(B6), 10049–10077. https://doi.org/10.1029/91JB00600

Liu, F., Elliott, J. R., Ebmeier, S. K., Craig, T. J., Hooper, A., Novoa Lizama, C., and Delgado, F. (2023). First onset of unrest captured at Socompa: A recent geodetic survey at Central Andean volcanoes in Northern Chile. Geophysical Research Letters, 50, e2022GL102480. https://doi.org/10.1029/2022GL102480

Liu, X., Xia, T., Liu-Zeng, J., Deng, D., Jia, Z., Wang, P., Yu, P., and Wang, W. (2023). Coseismic and early postseismic deformation of the 2020 Nima Mw 6.4 earthquake, central Tibet, from InSAR and GNSS observations. Frontiers in Earth Science, 10, 1012773. https://doi.org/10.3389/feart.2022.1012773

Lundgren, P., Casu, F., Manzo, M., Pepe, A., Berardino, P., Sansosti, E., and Lanari, R. (2004). Gravity and magma induced spreading of Mount Etna volcano revealed by satellite radar interferometry. Geophysical Research Letters, 31, L04602. https://doi.org/10.1029/2003GL018736

Lyon, T. J., Filmer, M. S., and Featherstone, W. E. (2018). On the use of repeat leveling for the determination of vertical land motion: Artifacts, aliasing, and extrapolation errors.

Journal of Geophysical Research: Solid Earth, 123, 7021–7039. https://doi.org/10.1029/2018JB015705

Ma, Y., Yang, Y., Zhou, X., Hu, L., and Liu, W. (2025). Stochastic properties of GNSS height time series caused by aperiodic part of environmental loading deformations: Case study in Beijing and its surrounding areas. Advances in Space Research, 76(2), 734–749. https://doi.org/10.1016/j.asr.2025.05.029

Maccaferri, F., Bonafede, M., and Rivalta, E. (2010). A numerical model of dyke propagation in layered elastic media. Geophysical Journal International, 180(3), 1107–1123. https://doi.org/10.1111/j.1365-246X.2009.04495.x

Manconi, A., Walter, T. R., and Amelung, F. (2007). Effects of mechanical layering on volcano deformation. Geophysical Journal International, 170, 952–958. https://doi.org/10.1111/j.1365-246X.2007.03449.x

Massonnet, D., Rossi, M., Carmona, C., Adragna, F., Peltzer, G., Feigl, K., and Rabaute, T. (1993). The displacement field of the Landers earthquake mapped by radar interferometry. Nature, 364, 138–142. https://doi.org/10.1038/364138a0

Matthews, S. W., Caracciolo, A., Bali, E., Halldórsson, S. A., Sigmarsson, O., Guðfinnsson, G. H., et al. (2024). A dynamic mid-crustal magma domain revealed by the 2023 to 2024 Sundhnúksgígar eruptions in Iceland. Science, 386(6719), 309–314. https://doi.org/10.1126/science.adp8778

McCaffrey, R., Long, M. D., Goldfinger, C., Zwick, P. C., Nabelek, J. L., Johnson, C. K., and Smith, C. (2000). Rotation and plate locking at the southern Cascadia subduction zone. Geophysical Research Letters, 27(19), 3117–3120. https://doi.org/10.1029/2000GL011768

McTigue, D. F. (1987). Elastic stress and deformation near a finite spherical magma body: Resolution of the point source paradox. Journal of Geophysical Research: Solid Earth, 92(B12), 12931–12940. https://doi.org/10.1029/JB092iB12p12931

Meertens, C. M., and Smith, R. B. (1991). Crustal deformation of the Yellowstone Caldera from first GPS measurements: 1987–1989. Geophysical Research Letters, 18(9), 1763–1766. https://doi.org/10.1029/91GL01470

Mériaux, C., and Jaupart, C. (1995). Simple fluid dynamic models of volcanic rift zones. Earth and Planetary Science Letters, 136(3–4), 223–240. https://doi.org/10.1016/0012-821X(95)00170-H

Metzger, S., and Jónsson, S. (2014). Plate boundary deformation in North Iceland during 1992–2009 revealed by InSAR time-series analysis and GPS. Tectonophysics, 634, 127–138. https://doi.org/10.1016/j.tecto.2014.07.027

Metzger, S., Jónsson, S., and Geirsson, H. (2011). Locking depth and slip-rate of the Húsavík Flatey fault, North Iceland, derived from continuous GPS data 2006–2010. Geophysical Journal International, 187(2), 564–576. https://doi.org/10.1111/j.1365-246X.2011.05176.x

Metzger, S., Jónsson, S., Danielsen, G., Hreinsdóttir, S., Jouanne, F., Giardini, D., et al. (2013). Present kinematics of the Tjörnes Fracture Zone, North Iceland, from campaign and continuous GPS measurements. Geophysical Journal International, 192, 441–455. https://doi.org/10.1093/gji/ggs032

Mogi, K. (1958). Relations between the eruptions of various volcanoes and the deformations of the ground surface around them. Bulletin of the Earthquake Research Institute, University of Tokyo, 36, 99–134.

Moller, D., and Ritter, B. (1980). Geodetic measurements and horizontal crustal movements in the rift zone of NE-Iceland. Journal of Geophysics, 47(1), 110–119. https://journal.geophysicsjournal.com/JofG/article/view/115

Montanaro, C., Mortensen, A. K., Weisenberger, T. B., Hannington, M., Óladóttir, B. A., and Thordarson, T. (2021). Stratigraphic reconstruction of the Víti breccia at Krafla volcano (Iceland): Insights into pre-eruptive conditions priming explosive eruptions in geothermal areas. Bulletin of Volcanology, 83, 81. https://doi.org/10.1007/s00445-021-01502-y

Montgomery-Brown, E. K., and Miklius, A. (2021). Periodic dike intrusions at Kīlauea volcano, Hawai'i. Geology, 49(4), 397–401. https://doi.org/10.1130/G47970.1

Morishita, Y., Lazecky, M., Wright, T. J., Weiss, J. R., Elliott, J. R., and Hooper, A. (2020). LiCSBAS: An Open-Source InSAR Time Series Analysis Package Integrated with the LiCSAR Automated Sentinel-1 InSAR Processor. Remote Sensing, 12(3), 424. https://doi.org/10.3390/rs12030424

Mortensen, A. K., Egilson, Þ., Gautason, B., Árnadóttir, S., and Guðmundsson, Á. (2014). Stratigraphy, alteration mineralogy, permeability and temperature conditions of well IDDP-1, Krafla, NE-Iceland. Geothermics, 49, 31–41. https://doi.org/10.1016/j.geothermics.2013.09.013

Mortensen, A., Grönvold, K., Gudmundsson, Á., Steingrímsson, B., and Egilson, T. (2010). Quenched silicic glass from well KJ-39 in Krafla, North-Eastern Iceland. In World Geothermal Congress 2010.

Mortensen, A., Guðmundsson, Á., Steingrímsson, B., Sigmundsson, F., Axelsson, G., Ármannsson, H., et al. (2015). The Krafla geothermal system research summary and conceptual model revision. Landsvirkjun Report No. LV-2015-098, Reykjavík, Iceland.

Motagh, M., Shamshiri, R., Haghshenas Haghighi, M., Wetzel, H.-U., Akbari, B., Nahavandchi, H., Roessner, S., and Arabi, S. (2017). Quantifying groundwater exploitation induced subsidence in the Rafsanjan plain, southeastern Iran, using InSAR time-series and in situ measurements. Engineering Geology, 218, 134–151. https://doi.org/10.1016/j.enggeo.2017.01.011

Müller, R. D., Sdrolias, M., Gaina, C., and Roest, W. R. (2008). Age, spreading rates, and spreading asymmetry of the world's ocean crust. Geochemistry, Geophysics, Geosystems, 9(4), Q04006. https://doi.org/10.1029/2007GC001743

Muirhead, J. D., Wright, L. J. M., and Scholz, C. A. (2019). Rift evolution in regions of low magma input in East Africa. Earth and Planetary Science Letters, 506, 332–346. https://doi.org/10.1016/j.epsl.2018.11.004

Natashima, Y. (1993). Static stability and propagation of a fluid–filled crack in rock: Implication for fluid transport in magmatism and metamorphism. Journal of Physics of the Earth, 41(3), 189–202.

National Oceanic and Atmospheric Administration (NOAA). (2017). What is geodetic leveling? National Oceanic and Atmospheric Administration Web Page. Retrieved July 2, 2025, from https://www.ngs.noaa.gov/heightmod/Leveling/

Niemczyk, O. (1943). Splaten auf Island. Stuttgart, Germany: Konrad Wittwer Verlag.

Nikolaidis, R. (2002). Observation of geodetic and seismic deformation with the Global Positioning System. Ph.D. dissertation, University of California, San Diego.

Nishimura, T., Ozawa, S., Murakami, M., Sagiya, T., Tada, T., Kaidzu, M., and Ukawa, M. (2001). Crustal deformation caused by magma migration in the northern Izu Islands, Japan. Geophysical Research Letters, 28(19), 3745–3748. https://doi.org/10.1029/2001GL013051

Niu, Y., Rebischung, P., Li, M., Wei, N., Shi, C., and Altamimi, Z. (2023). Temporal spectrum of spatial correlations between GNSS station position time series. Journal of Geodesy, 97, 12. https://doi.org/10.1007/s00190-023-01703-7

Noll, M. L., and Rydlund, P. H. (2020). Procedures and best practices for trigonometric leveling in the U.S. Geological Survey. U.S. Geological Survey Techniques and Methods, Book 11, Chapter D3. https://doi.org/10.3133/tm11D3

Novoa, C., Remy, D., Gerbault, M., Baez, J. C., Tassara, A., Cordova, L., Cardona, C., et al. (2019). Viscoelastic relaxation: A mechanism to explain the decennial large surface displacements at the Laguna del Maule silicic volcanic complex. Earth and Planetary Science Letters, 521, 46–59. https://doi.org/10.1016/j.epsl.2019.06.005

Oelsmann, J., Passaro, M., Sánchez, L., Dettmering, D., Schwatke, C., and Seitz, F. (2022). Bayesian modelling of piecewise trends and discontinuities to improve the estimation of coastal vertical land motion. Journal of Geodesy, 96, 62. https://doi.org/10.1007/s00190-022-01645-6

Okada, Y. (1992). Internal deformation due to shear and tensile faults in a half-space. Bulletin of the Seismological Society of America, 82(2), 1018–1040. https://doi.org/10.1785/BSSA0820021018

Opheim, J. A., and Gudmundsson, A. (1989). Formation and geometry of fractures, and related volcanism, of the Krafla fissure swarm, northeast Iceland. Geological Society of America Bulletin, 101(12), 1608–1622. https://doi.org/10.1130/0016-7606(1989)101<1608:FAGOFA>2.3.CO;2

Owen, S., Segall, P., Lisowski, M., Miklius, A., Murray, M., Bevis, M., and Foster, J. (2000). January 30, 1997 eruptive event on Kilauea Volcano, Hawaii, as monitored by continuous GPS. Geophysical Research Letters, 27(17), 2757–2760. https://doi.org/10.1029/1999GL008454

Paquet, F., Dauteuil, O., Hallot, E., and Moreau, F. (2007). Tectonics and magma dynamics coupling in a dyke swarm of Iceland. Journal of Structural Geology, 29(9), 1477–1493. https://doi.org/10.1016/j.jsg.2007.06.001

Parks, M., Drouin, V., Sigmundsson, F., Hjartardóttir, Á. R., Geirsson, H., Pedersen, G. B. M., et al. (2025). 2023–2024 inflation–deflation cycles at Svartsengi and repeated dike injections and eruptions at the Sundhnúkur crater row, Reykjanes Peninsula, Iceland. Earth and Planetary Science Letters, 658, 119324. https://doi.org/10.1016/j.epsl.2025.119324

Parks, M., Sigmundsson, F., Drouin, V., Hjartardóttir, Á. R., Geirsson, H., and Hooper, A. (2023). Deformation, seismicity, and monitoring response preceding and during the 2022 Fagradalsfjall eruption, Iceland. Bulletin of Volcanology, 85, 60. https://doi.org/10.1007/s00445-023-01671-y

Parks, M. M., Sigmundsson, F., Drouin, V., Hreinsdóttir, S., Hooper, A., Yang, Y., et al. (2024). 2021–2023 unrest and geodetic observations at Askja volcano, Iceland. Geophysical Research Letters, 51, e2023GL106730. https://doi.org/10.1029/2023GL106730

Pedicini, M., Bonali, F. L., Corti, N., and Tibaldi, A. (2025). Rift structure and development: The Krafla Fissure Swarm (Northern Iceland). Journal of Structural Geology, 191, 105332. https://doi.org/10.1016/j.jsg.2024.105332

Penna, N. T., King, M. A., and Stewart, M. P. (2007). GPS height time series: Short-period origins of spurious long-period signals. Journal of Geophysical Research: Solid Earth, 112, B02402. https://doi.org/10.1029/2005JB004047

Poland, M. P., Miklius, A., and Montgomery-Brown, E. (2014). Magma supply, storage, and transport at shield-stage Hawaiian volcanoes. In M. P. Poland, T. J. Takahashi, and C. Landowski (Eds.), Characteristics of Hawaiian volcanoes (pp. 179–234). U.S. Geological Survey Professional Paper 1801. U.S. Geological Survey. https://doi.org/10.3133/pp18015

Prawirodirdjo, L., and Bock, Y. (2004). Instantaneous global plate motion model from 12 years of continuous GPS observations. Journal of Geophysical Research: Solid Earth, 109, B08405. https://doi.org/10.1029/2003JB002944

Qianqian, Z., and Qingming, G. (2013). Bayesian methods for outliers detection in GNSS time series. Journal of Geodesy, 87, 609–627. https://doi.org/10.1007/s00190-013-0640-5

Qin, R., and Buck, W. R. (2008). Why meter-wide dikes at oceanic spreading centers? Earth and Planetary Science Letters, 265(3–4), 466–474. https://doi.org/10.1016/j.epsl.2007.10.044

Ray, J., Altamimi, Z., Collilieux, X., and van Dam, T. (2008). Anomalous harmonics in the spectra of GPS position estimates. GPS Solutions, 12(1), 55–64. https://doi.org/10.1007/s10291-007-0067-7

Ripepe, M., Lacanna, G., Pistolesi, M., De Angelis, S., Genco, R., Marchetti, E., et al. (2021). Ground deformation reveals the scale-invariant conduit dynamics driving explosive basaltic eruptions. Nature Communications, 12, 1683. https://doi.org/10.1038/s41467-021-21722-2

Rivalta, E. (2010). Evidence that coupling to magma chambers controls the volume history and velocity of laterally propagating intrusions. Journal of Geophysical Research: Solid Earth, 115, B07203. https://doi.org/10.1029/2009JB006922

Rivalta, E., Taisne, B., Bunger, A. P., and Katz, R. F. (2015). A review of mechanical models of dike propagation: Schools of thought, results and future directions. Tectonophysics, 638, 1–42. https://doi.org/10.1016/j.tecto.2014.10.003

Rooyakkers, S. M., Carroll, K. J., Gutai, A. F., Winpenny, B., Bali, E., Guðfinnsson, G. H., et al. (2024). Hydraulically linked reservoirs simultaneously fed the 1975–1984 Krafla Fires eruptions: Insights from petrochemistry. Earth and Planetary Science Letters, 646, 118960. https://doi.org/10.1016/j.epsl.2024.118960

Rooyakkers, S. M., Stix, J., Berlo, K., Petrelli, M., Hampton, R. L., Barker, S. J., and Morgavi, D. (2021). The origin of rhyolitic magmas at Krafla Central Volcano (Iceland). Journal of Petrology, 62(8), egab064. https://doi.org/10.1093/petrology/egab064

Rooyakkers, S. M., Stix, J., Berlo, K., Petrelli, M., Hampton, R. L., Morgavi, D., and Barker, S. J. (2022). Rifting and recharge as triggers of the mixed basalt–rhyolite Halarauður ignimbrite eruption (Krafla, Iceland). Contributions to Mineralogy and Petrology, 177(3), 32. https://doi.org/10.1007/s00410-021-01881-7

Roper, S. M., and Lister, J. R. (2007). Buoyancy-driven crack propagation: The limit of large fracture toughness. Journal of Fluid Mechanics, 580, 359–380. https://doi.org/10.1017/S0022112007005472

Rüeger, J. M. (2012). Electronic distance measurement: An introduction (4th ed.). Springer Science and Business Media.

Rule, G. (2020). The origin of magma encountered during drilling of geothermal well KJ-39, Krafla, Iceland and the relationship with the nearby IDDP-1 magma (Master's thesis). University of Canterbury. https://ir.canterbury.ac.nz/server/api/core/bitstreams/ff382d6d-ca13-4493-9012-8fd9007bcdc5/content

Sæmundsson, K. (1991). Jarðfræði Kröflukerfisins. In A. Gardarsson and A. Einarsson (Eds.), Náttúra Mývatns (pp. 24–95). Reykjavík: Hið íslenska náttúrufræðifélag.

Samsonov, S. V., Feng, W., Peltier, A., Geirsson, H., d'Oreye, N., and Tiampo, K. F. (2017). Multidimensional Small Baseline Subset (MSBAS) for volcano monitoring in two dimensions: Opportunities and challenges. Case study Piton de la Fournaise volcano.

Journal of Volcanology and Geothermal Research, 344, 121–138. https://doi.org/10.1016/j.jvolgeores.2017.04.017
Savage, J. C., and Burford, R. O. (1973). Geodetic determination of relative plate motion in central California. Journal of Geophysical Research, 78(5), 832–845. https://doi.org/10.1029/JB078i005p00832
Savage, J. C., and Prescott, W. H. (1978). Asthenosphere readjustment and the earthquake cycle. Journal of Geophysical Research, 83(B7), 3369–3376. https://doi.org/10.1029/JB083iB07p03369
Savitzky, A., and Golay, M. J. E. (1964). Smoothing and differentiation of data by simplified least squares procedures. Analytical Chemistry, 36(8), 1627–1639. https://doi.org/10.1021/ac60214a047
Schmandt, M. (n.d.). Chapter 2: Input. In GIS Commons. Retrieved July 4, 2025, from https://giscommons.org/chapter-2-input/
Schuler, J., Greenfield, T., White, R. S., Roecker, S. W., Brandsdóttir, B., Stock, J. M., et al. (2015). Seismic imaging of the shallow crust beneath the Krafla central volcano, NE Iceland. Journal of Geophysical Research: Solid Earth, 120(10), 7156–7173. https://doi.org/10.1002/2015JB012350
Segall, P., Anderson, K. R., Pulvirenti, F., Wang, T., and Johanson, I. (2020). Caldera collapse geometry revealed by near-field GPS displacements at Kīlauea Volcano in 2018. Geophysical Research Letters, 47, e2020GL088867. https://doi.org/10.1029/2020GL088867
Segall, P., Cervelli, P., Owen, S., Lisowski, M., and Miklius, A. (2001). Constraints on dike propagation from continuous GPS measurements. Journal of Geophysical Research: Solid Earth, 106(B9), 19301–19317. https://doi.org/10.1029/2001JB000229
Sella, G. F., Dixon, T. H., and Mao, A. (2002). REVEL: A model for recent plate velocities from space geodesy. Journal of Geophysical Research: Solid Earth, 107(B4), ETG 11-1–ETG 11-30. https://doi.org/10.1029/2000JB000033
Shen, Y., Li, W., Xu, G., and Li, B. (2014). Spatiotemporal filtering of regional GNSS network's position time series with missing data using principal component analysis. Journal of Geodesy, 88, 1–12. https://doi.org/10.1007/s00190-013-0663-y
Shi, K., Chen, X., Sun, H., Ding, H., Guo, R., and Fan, X. (2025). Fine detection of transient signals in GNSS time series using multi-station Hankel Spectrum Analysis. Journal of Geophysical Research: Solid Earth, 130, e2024JB030672. https://doi.org/10.1029/2024JB030672
Shreve, T., Grandin, R., Smittarello, D., Cayol, V., Pinel, V., Boichu, M., and Morishita, Y. (2021). What triggers caldera ring-fault subsidence at Ambrym volcano? Insights from the 2015 dike intrusion and eruption. Journal of Geophysical Research: Solid Earth, 126, e2020JB020277. https://doi.org/10.1029/2020JB020277
Sigmundsson, F., Hooper, A., Hreinsdóttir, S., Vogfjörd, K. S., Ófeigsson, B. G., Heimisson, E. R., et al. (2015). Segmented lateral dyke growth in a rifting event at Bárðarbunga volcanic system, Iceland. Nature, 517(7533), 191–195. https://doi.org/10.1038/nature14111
Sigmundsson, F., Parks, M., Geirsson, H., Hooper, A., Drouin, V., Vogfjörd, K. S., et al. (2024). Fracturing and tectonic stress drive ultrarapid magma flow into dikes. Science, 383(6688), 1228–1235. https://doi.org/10.1126/science.adn2838
Sigmundsson, F., Parks, M., Pedersen, R., Jónsdóttir, K., Ófeigsson, B. G., Grapenthin, R., et al. (2018). Magma movements in volcanic plumbing systems and their associated ground deformation and seismic patterns. In K. Cashman, J. Sparks, and H. Blundy

(Eds.), Volcanic and igneous plumbing systems (pp. 285–322). Elsevier. https://doi.org/10.1016/B978-0-12-809749-6.00011-X

Sigmundsson, F., Pinel, V., Grapenthin, R., Hooper, A., Halldórsson, S. A., Einarsson, P., Ófeigsson, B. G., et al. (2020). Unexpected large eruptions from buoyant magma bodies within viscoelastic crust. Nature Communications, 11, 2403. https://doi.org/10.1038/s41467-020-16054-6

Sigmundsson, F., Vadon, H., and Massonnet, D. (1997). Readjustment of the Krafla spreading segment to crustal rifting measured by satellite radar interferometry. Geophysical Research Letters, 24(15), 1843–1846. https://doi.org/10.1029/97GL01934

Simakin, A. G., and Ghassemi, A. (2010). The role of magma chamber–fault interaction in caldera forming eruptions. Bulletin of Volcanology, 72, 85–101. https://doi.org/10.1007/s00445-009-0306-6

Small, C., and Naumann, T. (2001). The global distribution of human population and recent volcanism. Global Environmental Change Part B: Environmental Hazards, 3(3), 93–109. https://doi.org/10.3763/ehaz.2001.0309

Sobrero, F. S., Bevis, M., Gómez, D. D. and Wang, F. (2020). Logarithmic and exponential transients in GNSS trajectory models as indicators of dominant processes in postseismic deformation. Journal of Geodesy, 94, 84. https://doi.org/10.1007/s00190-020-01413-4

Spera, F. J. (2000). Physical properties of magma. In H. Sigurdsson (Ed.), Encyclopedia of volcanoes (pp. 171–190). Academic Press.

Spickernagel, H. (1966). Höhenänderungen in Nordost-Island [Height changes in Northeast Iceland]. Technical report, University of Leoben, Austria.

Stelling, P., Shevenell, L., Hinz, N., Coolbaugh, M., Melosh, G., and Cumming, W. (2016). Geothermal systems in volcanic arcs: Volcanic characteristics and surface manifestations as indicators of geothermal potential and favorability worldwide. Journal of Volcanology and Geothermal Research, 324, 57–72. https://doi.org/10.1016/j.jvolgeores.2016.05.018

Sturkell, E., Sigmundsson, F., Geirsson, H., Ólafsson, H., and Theodórsson, T. (2008). Multiple volcano deformation sources in a post-rifting period: 1989–2005 behaviour of Krafla, Iceland constrained by levelling, tilt and GPS observations. Journal of Volcanology and Geothermal Research, 177(2), 405–417. https://doi.org/10.1016/j.jvolgeores.2008.06.013

Suito, H. (2017). Importance of rheological heterogeneity for interpreting viscoelastic relaxation caused by the 2011 Tohoku-Oki earthquake. Earth, Planets and Space, 69, 21. https://doi.org/10.1186/s40623-017-0611-9

Sumita, I., and Ota, Y. (2011). Experiments on buoyancy–driven crack around the brittle–ductile transition. Earth and Planetary Science Letters, 304, 337–346. https://doi.org/10.1016/j.epsl.2011.01.032

Tadono, T., Ohki, M., Motohka, T., Rosenqvist, A., and Sobue, S. (2025). Advanced Land Observing Satellite-2 “DAICHI-2” (ALOS-2): Overview and operational status. IEEE Geoscience and Remote Sensing Magazine, Early Access, 2–10. https://doi.org/10.1109/MGRS.2025.3535720

Taisne, B., and Jaupart, C. (2009). Dike propagation through layered rocks. Journal of Geophysical Research: Solid Earth, 114, B09203. https://doi.org/10.1029/2008JB006228

Theodórsson, T., and Búi, J. (2011). Krafla, Mývatn, fínhæðarmælingar 2010. Landsvirkjun Report No. LV-2011/048, Reykjavík, Iceland.

Theodórsson, Þ., and Jónsson, B. (2006). Krafla, Mývatn og Laxá: Fínhæðarmælingar sumarið 2005. Landsvirkjun Report No. LV-2006/050, Reykajvík, Iceland.
Thorarinsson, S. (1979). The postglacial history of the Mývatn area. Oikos, 32(1/2), 16–28. https://www.jstor.org/stable/3544218
Tibaldi, A., Bonali, F. L., Pasquaré Mariotto, F., Corti, N., Russo, E., Einarsson, P., and Hjartardóttir, Á. R. (2020). Rifting kinematics produced by magmatic and tectonic stresses in the North Volcanic Zone of Iceland. Frontiers in Earth Science, 8, 174. https://doi.org/10.3389/feart.2020.00174
Tizzani, P., Manconi, A., Zeni, G., Pepe, A., Manzo, M., Camacho, A., and Fernández, J. (2010). Long-term versus short-term deformation processes at Tenerife (Canary Islands). Journal of Geophysical Research: Solid Earth, 115(B12), B12412. https://doi.org/10.1029/2010JB007735
Tobita, M. (2016). Combined logarithmic and exponential function model for fitting postseismic GNSS time series after 2011 Tohoku-Oki earthquake. Earth, Planets and Space, 68, 41. https://doi.org/10.1186/s40623-016-0422-4
Townsend, M., and Huber, C. (2020). A critical magma chamber size for volcanic eruptions. Geology, 48(5), 431–435. https://doi.org/10.1130/G47045.1
Tregoning, P. and van Dam, T. (2005). Atmospheric pressure loading corrections applied to GPS data at the observation level. Geophysical Research Letters, 32, L22310. https://doi.org/10.1029/2005GL024104
Tryggvason, E. (1978). Tilt observations in the Krafla-Myvatn area, 1976–1977. Nordic Volcanological Institute Report No. 7802, Reykjavík, Iceland.
Tryggvason, E. (1979). Tilt observations in the Krafla-Myvatn area. Nordic Volcanological Institute Report No. 7907, Reykjavík, Iceland.
Tryggvason, E. (1980). Subsidence events in the Krafla area, North Iceland, 1975–1979. Journal of Geophysics, 41(1), 141–153. Retrieved from https://journal.geophysicsjournal.com/JofG/article/view/76
Tryggvason, E. (1984). Widening of the Krafla fissure swarm during the 1975–1981 volcano-tectonic episode. Bulletin of Volcanology, 47, 47–69. https://doi.org/10.1007/BF01960540
Tryggvason, E. (1986). Multiple magma reservoirs in a rift zone volcano: Ground deformation and magma transport during the September 1984 eruption of Krafla, Iceland. Journal of Volcanology and Geothermal Research, 28(1–2), 1–44. https://doi.org/10.1016/0377-0273(86)90003-X
Tryggvason, E. (1994). Surface deformation at the Krafla volcano, North Iceland, 1982–1992. Bulletin of Volcanology, 56, 98–107. https://doi.org/10.1007/BF00304105
Tryggvason, E. (1995). Optical levelling tilt stations in the vicinity of Krafla and the Krafla fissure swarm: Observations 1976 to 1994 (NVI Report No. 9505). University of Iceland, Nordic Volcanological Institute. https://nordvulk.hi.is/sites/nordvulk.hi.is/files/NVI_Reports_pdf/nvi_report_9505_low_text.pdf
Urbani, S., Acocella, V., and Rivalta, E. (2018). What drives the lateral versus vertical propagation of dikes? Insights from analogue models. Journal of Geophysical Research: Solid Earth, 123, 3680–3697. https://doi.org/10.1029/2017JB015376
Vanicek, P., Castle, R. O., and Balazs, E. I. (1980). Geodetic leveling and its applications. Reviews of Geophysics, 18(2), 505–524. https://doi.org/10.1029/RG018i002p00505
Vitti, A. (2012). Sigseg: a tool for the detection of position and velocity discontinuities in geodetic time-series. GPS Solutions, 16, 405-410. https://doi.org/10.1007/s10291-012-0257-9

Wallace, L. M. and Rollins, C. (2024). Chapter 5 – GNSS observations of transient deformation in plate boundary zones. In Aoki, Y. and Kreemer, C. (Eds.), GNSS Monitoring of the Terrestrial Environment (pp. 83–110). Elsevier. https://doi.org/10.1016/B978-0-323-95507-2.00009-8

Wang, L., Wu, Q., Wu, F., and He, X. (2022). Noise content assessment in GNSS coordinate time-series with autoregressive and heteroscedastic random errors. Geophysical Journal International, 231(2), 856–876. https://doi.org/10.1093/gji/ggac228

Wang, X., Aoki, Y., and Chen, J. (2019). Surface deformation of Asama volcano, Japan, detected by time series InSAR combining persistent and distributed scatterers, 2014–2018. Earth, Planets and Space, 71, 121. https://doi.org/10.1186/s40623-019-1104-9

Wang, X., Cheng, Y., Wu, S., and Zhang, K. (2016). An enhanced singular spectrum analysis method for constructing nonsecular model of GPS site movement. Journal of Geophysical Research: Solid Earth, 121, 2193-2211. https://doi.org/10.1002/2015JB012573

Wdowinski, S., Bock, Y., Zhang, J., Fang, P., and Genrich, J. (1997). Southern California permanent GPS geodetic array: Spatial filtering of daily positions for estimating coseismic and postseismic displacements induced by the 1992 Landers earthquake. Journal of Geophysical Research: Solid Earth, 102(B8), 18057–18070. https://doi.org/10.1029/97JB01378

Weber, G., Biggs, J., and Annen, C. (2025). Distinct patterns of volcano deformation for hot and cold magmatic systems. Nature Communications, 16, 532. https://doi.org/10.1038/s41467-024-55443-z

Weertman, J. (1971). Theory of water-filled crevasses in glaciers applied to vertical magma transport beneath oceanic ridges. Journal of Geophysical Research, 76(5), 1171–1183. https://doi.org/10.1029/JB076i005p01171

Weertman, J. (1973). Can a water–filled crevasse reach the bottom surface of a glacier? Symposium on the Hydrology of Glaciers, Cambridge, England.

Wendt, K., Möller, D., and Ritter, B. (1985). Geodetic measurements of surface deformations during the present rifting episode in NE Iceland. Journal of Geophysical Research, 90(B12), 10163–10172. https://doi.org/10.1029/JB090iB12p10163

Williams, S. D. P. (2003). The effect of coloured noise on the uncertainties of rates estimated from geodetic time series. Journal of Geodesy, 76, 483–494. https://doi.org/10.1007/s00190-002-0283-4

Wright, T. J., Ebinger, C., Biggs, J., Ayele, A., Yirgu, G., Keir, D., and Stork, A. (2006). Magma-maintained rift segmentation at continental rupture in the 2005 Afar dyking episode. Nature, 442, 291–294. https://doi.org/10.1038/nature04978

Wright, T. J., Parsons, B. E., and Lu, Z. (2004). Toward mapping surface deformation in three dimensions using InSAR. Geophysical Research Letters, 31, L01607. https://doi.org/10.1029/2003GL018827

Wright, T. J., Sigmundsson, F., Pagli, C., Belachew, M., Hamling, I. J., Brandsdóttir, B., et al. (2012). Geophysical constraints on the dynamics of spreading centres from rifting episodes on land. Nature Geoscience, 5, 242–250. https://doi.org/10.1038/ngeo1428

Wu, D., Yan, H. and Yuan, S. (2018). L1 regularization for detecting offsets and trend change points in GNSS time series. GPS Solutions, 22, 88. https://doi.org/10.1007/s10291-018-0756-4

Wu, S., Liu, Z., Zhou, T., Chen, J., and Wang, Q. (2023). Detection of periodic signals with time-varying coefficients from CMONOC stations in China by singular spectrum analysis. IEEE Transactions on Geoscience and Remote Sensing, 61, 5802812. https://doi.org/10.1109/TGRS.2023.3315336

Yan, H., Chen, W., Zhu, Y., Zhang, W., and Zhong, M. (2009). Contributions of thermal expansion of monuments and nearby bedrock to observed GPS height changes. Geophysical Research Letters, 36, L13301. https://doi.org/10.1029/2009GL038152

Yang, Y., Lanzi, C., Sigmundsson, F., Geirsson, H., and Hreinsdóttir, S. (2023). GNSS surveying and ground deformation at Krafla, Námafjall and Þeistareykir: Status report, May 2023. Landsvirkjun Report No. LV-2022-034, Reykjavík, Iceland.

Yang, Y., Sigmundsson, F., Drouin, V., Geirsson, H. (2025). 2002–2023 ground displacements and strain in the Þeistareykir and Krafla areas based on GNSS and InSAR. Landsvirkjun Report, LV-2025-006, Reykjavík, Iceland.

Yuan, P., Jiang, W., Wang, K., and Sneeuw, N. (2018). Effects of Spatiotemporal Filtering on the Periodic Signals and Noise in the GPS Position Time Series of the Crustal Movement Observation Network of China. Remote Sensing, 10(9), 1472. https://doi.org/10.3390/rs10091472

Zebker, H. A., and Villasenor, J. (1992). Decorrelation in interferometric radar echoes. IEEE Transactions on Geoscience and Remote Sensing, 30(5), 950–959. https://doi.org/10.1109/36.175330

Zhan, Y., and Gregg, P. M. (2019). How accurately can we model magma reservoir failure with uncertainties in host rock rheology? Journal of Geophysical Research: Solid Earth, 124, 8030–8042. https://doi.org/10.1029/2019JB018178

Zhou, X., Yang, Y., Chen, H., Ouyang, W., and Fan, W. (2019). A modified Least Square harmonics estimation method and comparative analysis of established full periodicity models. Earth and Space Science, 6, 2160–2179. https://doi.org/10.1029/2019EA000750

Zierenberg, R. A., Schiffman, P., Barfod, G. H., Lesher, C. E., Marks, N. E., Mortensen, A. K., and Fridleifsson, G. O. (2013). Composition and origin of rhyolite melt intersected by drilling in the Krafla geothermal field, Iceland. Contributions to Mineralogy and Petrology, 165(2), 327–347. https://doi.org/10.1007/s00410-012-0811-z

Paper I

Joint Bayesian Modeling of Velocity Break Points, Noise Characteristics, and Their Uncertainties in GNSS Time Series: Far-Field Velocity Anomalies Concurrent with Magmatic Activity in Iceland

Check for updates

AGU ADVANCING EARTH AND SPACE SCIENCES

Geophysical Research Letters®

RESEARCH LETTER
10.1029/2023GL103432

Key Points:

- The lower limit of velocity change values, where reliable estimates can be derived, depends on noise characteristics of Global Navigation Satellite System time series
- Increased rift-perpendicular movement before the 2014 Bárðarbunga dike intrusion is inferred with 95% confidence, 120 km north of it
- Concurrent far-field velocity anomalies and near-field precursors may indicate coupling between distant volcanic systems at a plate boundary

Supporting Information:

Supporting Information may be found in the online version of this article.

Correspondence to:

Y. Yang,
yiy1@hi.is

Citation:

Yang, Y., Sigmundsson, F., & Geirsson, H. (2023). Joint Bayesian modeling of velocity break points, noise characteristics, and their uncertainties in GNSS time series: Far-field velocity anomalies concurrent with magmatic activity in Iceland. *Geophysical Research Letters*, *50*, e2023GL103432. https://doi.org/10.1029/2023GL103432

Received 24 MAR 2023
Accepted 29 JUN 2023

© 2023 The Authors.
This is an open access article under the terms of the Creative Commons Attribution-NonCommercial License, which permits use, distribution and reproduction in any medium, provided the original work is properly cited and is not used for commercial purposes.

Joint Bayesian Modeling of Velocity Break Points, Noise Characteristics, and Their Uncertainties in GNSS Time Series: Far-Field Velocity Anomalies Concurrent With Magmatic Activity in Iceland

Yilin Yang[1], Freysteinn Sigmundsson[1], and Halldór Geirsson[1]

[1]Nordic Volcanological Center, Institute of Earth Sciences, University of Iceland, Reykjavík, Iceland

Abstract Estimating the timing of velocity changes (break points) in Global Navigation Satellite System (GNSS) coordinate time series is required for understanding various Earth processes and how they may couple with each other. We jointly estimate break points, noise parameters and their uncertainties in GNSS time series using Bayesian interference. Synthetic data experiments demonstrate that time-correlated noise can cause spurious estimates of break points for small velocity change and suggest the lower limits of velocity change for reliable estimates. A case study at the Krafla volcanic system shows increased rift-perpendicular movementof 7.6–9.8 mm/yr, preceding by 23–77 days the 2014 Bárðarbunga rifting episode that occurred ∼120 km to the south (maximum likelihood estimates). These far-field velocity anomalies occur in the same period as enhanced near-field seismicity and deformation before the dike intrusion at Bárðarbunga, possibly indicating the coupling between the two volcanic systems through a deep partial melt zone.

Plain Language Summary The velocity of ground movements can change due to Earth's activities. Satellite positioning techniques record these changes, while noise in the records may obscure their analyses. We developed a statistical method to detect velocity changes from these noisy records and give an estimate of uncertainty. Simulated data is used to examine the method, revealing the lower limits of velocity change for reliable estimates. Then the method is applied to detect velocity changes in the records at the Krafla volcanic system, Iceland. With maximum likelihood estimates, it is inferred that the ground moves 7.6–9.8 mm/yr faster, in rift-perpendicular direction, before the start of the 2014 Bárðarbunga dike intrusion that occurred ∼120 km to the south. The ground movements resume to approximately the original velocities by a second velocity change in late 2014 or early 2015. The onset of the far-field velocity anomalies occurs in the same period as enhanced near-field seismicity and deformation rate before the dike intrusion at Bárðarbunga. In the context of enhanced seismicity at the Bárðarbunga volcano and rapid inflation at the Askja volcano before the Krafla rifting episode in 1975–1984, our result may again indicate coupling among the volcanic systems in Iceland.

1. Introduction

Velocity changes of ground deformation, recorded with Global Navigation Satellite System (GNSS) coordinate time series, can manifest various geophysical processes, for example, volcanic-hydrothermal processes, tectonics, and the variation in groundwater level (Borsa et al., 2014; Davis et al., 2006; Geirsson et al., 2010). Break points in GNSS time series, defined as the timing of velocity changes, may signal the changes of causative processes. Together with velocity change values, they provide valuable information for many applications. In this study, a method is developed for the joint estimation of break points, velocity change values and their associated uncertainties. We applied the method to study the transient deformation in the Northern Volcanic Zone (NVZ) of Iceland during 2014–2015.

Previous studies have applied advanced methods to model velocity changes with continuous curves, for example, polynomials, wavelets, singular spectrum analysis, and Kalman filter (Borghi et al., 2012; Bos et al., 2020; Didova et al., 2016; Wang et al., 2016). However, such approach obstructs the finding of break points. In contrast, piecewise functions are transparent for estimating both break points and velocity change values (e.g., Davis et al., 2006; Ducrocq et al., 2021). Detecting break points for piecewise functions is a non-linear problem because the location of a break point affects velocity estimation.

19448007, 2023, 14, Downloaded from https://agupubs.onlinelibrary.wiley.com/doi/10.1029/2023GL103432 by RH-net, Wiley Online Library on [18/07/2023]. See the Terms and Conditions (https://onlinelibrary.wiley.com/terms-and-conditions) on Wiley Online Library for rules of use; OA articles are governed by the applicable Creative Commons License

Statistical criteria considering fitting error have been applied to detect break points for piecewise functions (Benciolini et al., 2012; Bos et al., 2018; Vitti, 2012; Wu et al., 2018). These methods usually report the optimal break points but without uncertainties. Another approach to detect break points is Bayesian modeling, with a Markov Chain Monte Carlo method, inferring the posterior distribution of parameters, and thereby obtaining parameter estimates and uncertainties jointly. This approach has been widely used in some aspects of GNSS time series analysis (Baragatti et al., 2019; Borghi et al., 2012; Koulali & Clarke, 2021; Olivare-Pulido et al., 2020; Olivares & Teferle, 2013; Qianqian & Qingming, 2013). With Bayesian modeling, Liu et al. (2023) determined the onset time of unrest at Socompa volcano, assuming white noise (WN) in GNSS time series. Oelsmann et al. (2022) detected velocity changes accompanied with steps, considering the noise as the first-order autoregressive process, or AR(1). However, more realistic noise model is required as the noise conforms to AR(1) only when sufficient signals are subtracted (Amiri-Simkooei et al., 2007), and velocity changes without simultaneous steps need further examination with the Bayesian approach.

The noise in GNSS time series is usually described using power-law noise (PLN), of which the power spectrum follows:

$$P(f) = P_0\left(\frac{f}{f_0}\right)^{\kappa} \tag{1}$$

where $P(f)$ is the power at frequency f of the noise, P_0 and f_0 are constants, and κ is the spectral index (Williams, 2003). κ for GNSS time series ranges from -2 to 0 and is usually estimated individually for each station and coordinate component. When κ is 0, -1 and -2, the noise behaves as WN, flicker noise (FLN) and random-walk noise, respectively. PLN is caused by the complexity of signals in GNSS time series and the simplified models in data processing (Amiri-Simkooei et al., 2017; Dmitrieva et al., 2017; Dong et al., 2002; Klos et al., 2018; Langbein & Johnson, 1997; Wang & Herring, 2019; Zhou et al., 2019). Neglecting PLN oversimplifies the temporal relationship among observations in the time series and causes underestimation of uncertainties (Mao et al., 1999). Thus, the joint estimation of velocity changes and PLN parameters will enhance the reliability of results.

Therefore, we implement Bayesian modeling to jointly estimate break points, velocity change values, PLN parameters and their uncertainties. We examine the performance of the method with synthetic data and apply it to infer the timing of transient deformation in the NVZ of Iceland during 2014–2015.

2. Methods

We start with a common function model of GNSS time series. It is subsequently simplified with data pre-processing to reduce calculation cost. Then Bayesian modeling of velocity changes is implemented based on the Geodetic Bayesian Inversion Software (GBIS; Bagnardi & Hooper, 2018) using MATLAB.

A function model for a GNSS time series considering steps and velocity changes is (Nikolaidis, 2002):

$$\begin{aligned} y &= a + bt + \sum_{i=1}^{2}[c_i \sin(2\pi i t) + d_i \cos(2\pi i t)] \\ &\quad + \sum_{j=1}^{m} e_j \mathrm{H}(t - t_j) + \sum_{k=1}^{n} g_k (t - t_k)\mathrm{H}(t - t_k) + \varepsilon \end{aligned} \tag{2}$$

where y is the coordinate at time t, a and b are initial station position and velocity, c_i and d_i are the amplitudes of annual and semi-annual signals, and m is the number of steps with e_j and t_j being their magnitudes and timing, respectively. n is the number of velocity changes with t_k and g_i being corresponding timing (break points) and values. H( ) is the Heaviside function. ε is residual, the difference between the observation and the model. The noise is usually assessed from residuals, of which the covariance matrix $\mathbf{C}$ is a combination of WN and PLN (Amiri-Simkooei et al., 2007; Langbein, 2012; Williams, 2003):

$$\mathbf{C} = \alpha^2\mathbf{I} + \beta^2\mathbf{J}_{\kappa} \tag{3}$$

here α and β represent the amplitudes of WN and PLN, respectively. $\mathbf{I}$ indicates the identity matrix and the calculation of $\mathbf{J}_{\kappa}$ is described in Text S1 in Supporting Information S1.

19448007, 2023, 14, Downloaded from https://agupubs.onlinelibrary.wiley.com/doi/10.1029/2023GL103432 by RH-net, Wiley Online Library on [18/07/2023]. See the Terms and Conditions (https://onlinelibrary.wiley.com/terms-and-conditions) on Wiley Online Library for rules of use; OA articles are governed by the applicable Creative Commons License

Pre-processing of the time series preliminarily estimates all parameters, retains the velocity changes, and removes other signals. The procedure (Table S1 in Supporting Information S1) includes: (a) removing outliers, (b) visually detecting steps and approximate break points, (c) preliminarily estimating a, b, c_i, d_i, e_j and g_k; (d) evaluating α, β, and κ from residuals, and (e) subtracting a, steps, and seasonal signals from the time series. Our pre-processing partially uses the HECTOR software (Bos et al., 2013). After pre-processing, the function model is simplified as:

$$y = a' + bt + \sum_{k=1}^{n} g_k(t - t_k)\mathrm{H}(t - t_k) + \varepsilon \tag{4}$$

where a' is the residual intercept with its value approaching zero. The data and residual vectors can be denoted as $\mathbf{y}$ and ε, respectively. By fixing WN amplitude as the estimate $\hat{\alpha}$ from pre-processing, Equation 3 is simplified as:

$$\mathbf{C} = \hat{\alpha}^2\mathbf{I} + \beta^2\mathbf{J}_\kappa \tag{5}$$

This is justified based on the relatively small effect of WN on uncertainties (Hackl et al., 2011).

We estimate the remaining parameters in Equations 4 and 5 simultaneously with Bayesian interference. The parameter vector is

$$\mathbf{m} = \left[a'\, b\, t_1 \cdots t_n\, g_1 \cdots g_n\, \kappa\, \beta\right] \tag{6}$$

where $t_1 \cdots t_n$ represent break points and $g_1 \cdots g_n$ represent velocity change values. The joint conditional probability distribution (PD) of $\mathbf{m}$ given observations $\mathbf{y}$ can be derived with Bayesian theorem:

$$\mathrm{p}(\mathbf{m}|\mathbf{y}) = \frac{\mathrm{p}(\mathbf{y}|\mathbf{m})\mathrm{p}(\mathbf{m})}{\mathrm{p}(\mathbf{y})} \tag{7}$$

where $\mathrm{p}(\mathbf{m}|\mathbf{y})$ is the targeted PD and $\mathrm{p}(\mathbf{y}|\mathbf{m})$ indicates the PD of $\mathbf{y}$ given $\mathbf{m}$. $\mathrm{P}(\mathbf{m})$ is the a priori PD of $\mathbf{m}$, which we assume to follow uniform distribution within the search range of $\mathbf{m}$. The search range is set according to the pre-processing results. The logarithm of $\mathrm{p}(\mathbf{y}|\mathbf{m})$ can be calculated assuming Gaussian distribution of the parameters (Koulali & Clarke, 2021; Langbein, 2004):

$$\ln(\mathrm{p}(\mathbf{y}|\mathbf{m})) = -\frac{1}{2}\left(N\ln(2\pi) + \ln(\det(\mathbf{C})) + \varepsilon^{\mathrm{T}}\mathbf{C}^{-1}\varepsilon\right) \tag{8}$$

where N is the number of data points. Iterated sampling of $\mathbf{m}$ with Metropolis-Hastings algorithm (Bagnardi & Hooper, 2018; Hastings, 1970; Metropolis et al., 1953) gives an estimate of the posterior joint distribution of parameters, denoted as $\hat{\mathrm{p}}(\mathbf{m}|\mathbf{y})$. With $\hat{\mathrm{p}}(\mathbf{m}|\mathbf{y})$, one has all statistical information of the parameter estimates, including a parameter combination with the maximum likelihood (denoted as the optimal estimates) and the individual mean values of the marginal PDs (denoted as the mean estimates). The 95% confidence interval of $\hat{\mathrm{p}}(\mathbf{m}|\mathbf{y})$ is denoted as uncertainty hereinafter.

3. The Validation of Bayesian Modeling With Synthetic Time Series

We validate the method with synthetic time series generated with Equation 4 and pre-processing results of observed data (Table S2 in Supporting Information S1). For clearer comparison of the results, we added WN and FLN. The WN amplitude is set to 1 mm, and the FLN amplitude varies among 3, 4, and 5 mm/yr$^{0.25}$. The time series spans 5 yr, from 2019 to 2024. The initial velocity is 5 mm/yr, and one break point is simulated at the middle of the time series (2.5 yr). The velocity change is set to −1.0, −2.5, −5.0, −7.5, −10.0, −15.0, −20.0 mm/yr. Pre-processing follows Section 2, but the seasonal signals are not estimated nor removed. The preliminary estimate of break point is set to 2.55 yr. We run 120,000 sampling iterations for the synthetic series. The search range of the parameters is in Table S3 in Supporting Information S1 and the synthetic time series are displayed in Figure S1 in Supporting Information S1.

Figures 1a–1c show the synthetic data and inferred models. For g of −20 mm/yr (Figure 1a), the model fits the time series well, with the estimation error of break point smaller than 10 d and its uncertainty of 60 d, illustrating the effectiveness of the method. For g of −5 mm/yr (Figure 1b), the simulated break point is masked by the noise. The estimation error is larger than 1 yr, although the 95% confidence interval includes the true break point. Thus,

19448007, 2023, 14, Downloaded from https://agupubs.onlinelibrary.wiley.com/doi/10.1029/2023GL103432 by RHI-net, Wiley Online Library on [18/07/2023]. See the Terms and Conditions (https://onlinelibrary.wiley.com/terms-and-conditions) on Wiley Online Library for rules of use; OA articles are governed by the applicable Creative Commons License

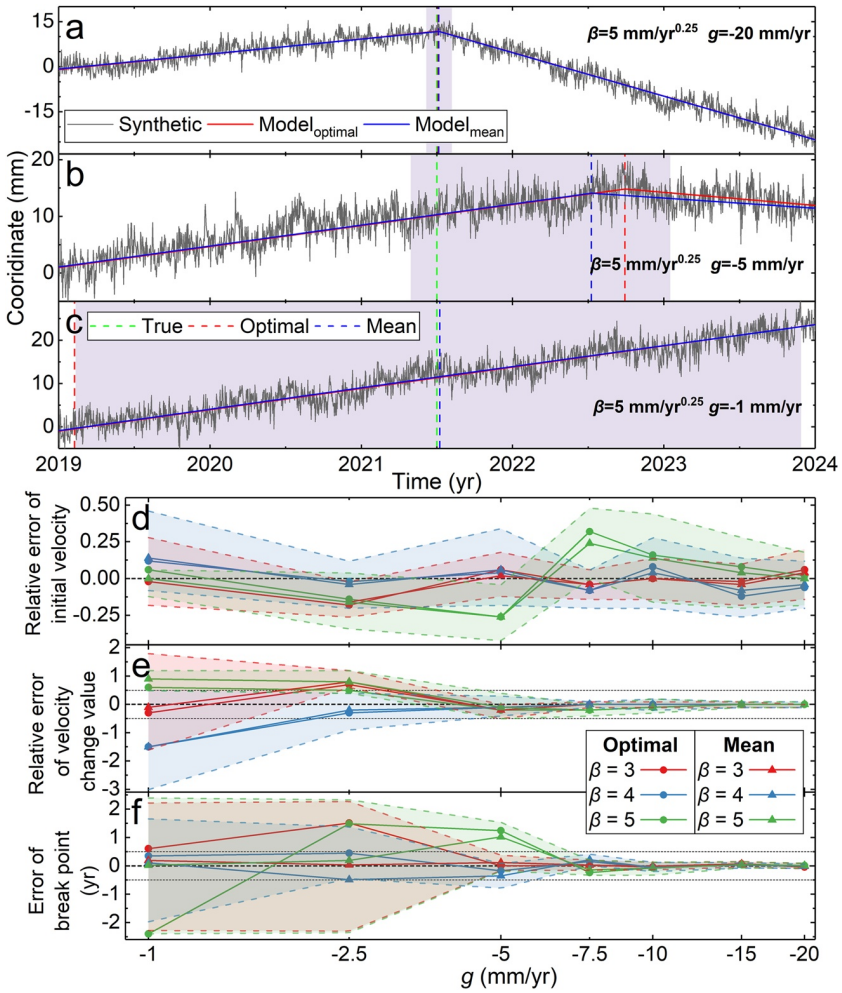


Figure 1. Synthetic data experiments with a single break point, different noise levels and velocity change values. (a–c) Synthetic time series and the established models with FLN amplitude (β) of 5 mm/yr$^{0.25}$ and velocity changes (g) of −20, −5, and −1 mm/yr, respectively. The purple shaded area indicates the 95% confidence interval of break points. (d–f) The estimation errors and uncertainties of synthetic experiments. The relative errors are the differences between the estimates and true values, divided by the true values. The horizontal axes are with a logarithmic scale.

the estimates of break points with small velocity changes can be offset by PLN. g of −1 mm/yr yields break point uncertainty similar to the search range. In this case the Markov chain (Figure S2 in Supporting Information S1) fails to converge, inducing random values within the search range taken as an estimate, which should not be accepted. We study the general variations of estimation for different g, aiming at break point uncertainty smaller than half a year (Figures 1d–1f and Table S4 in Supporting Information S1). In a 5-yr-length time series, we suggest the velocity change value be larger than −7.5, −10, and −15 mm/yr for FLN amplitude of 3, 4, and 5 mm/yr$^{0.25}$ for a reliable break point estimate.

The temporal characteristics of individual noise series can vary notably even with the same parameters. We do run the experiments again with another set of noise (Figure S3 in Supporting Information S1) and derive the same lower limits as above.

4. Far-Field Velocity Anomalies Concurrent With Magma Unrest

4.1. Northern Volcanic Zone of Iceland

The NVZ is a part of the Mid-Atlantic plate boundary in Iceland (Einarsson, 2008). It is divided into several volcanic systems, including Þeistareykir, Krafla, Fremrinámar, Askja and Bárðarbunga (Figure 2). Relatively

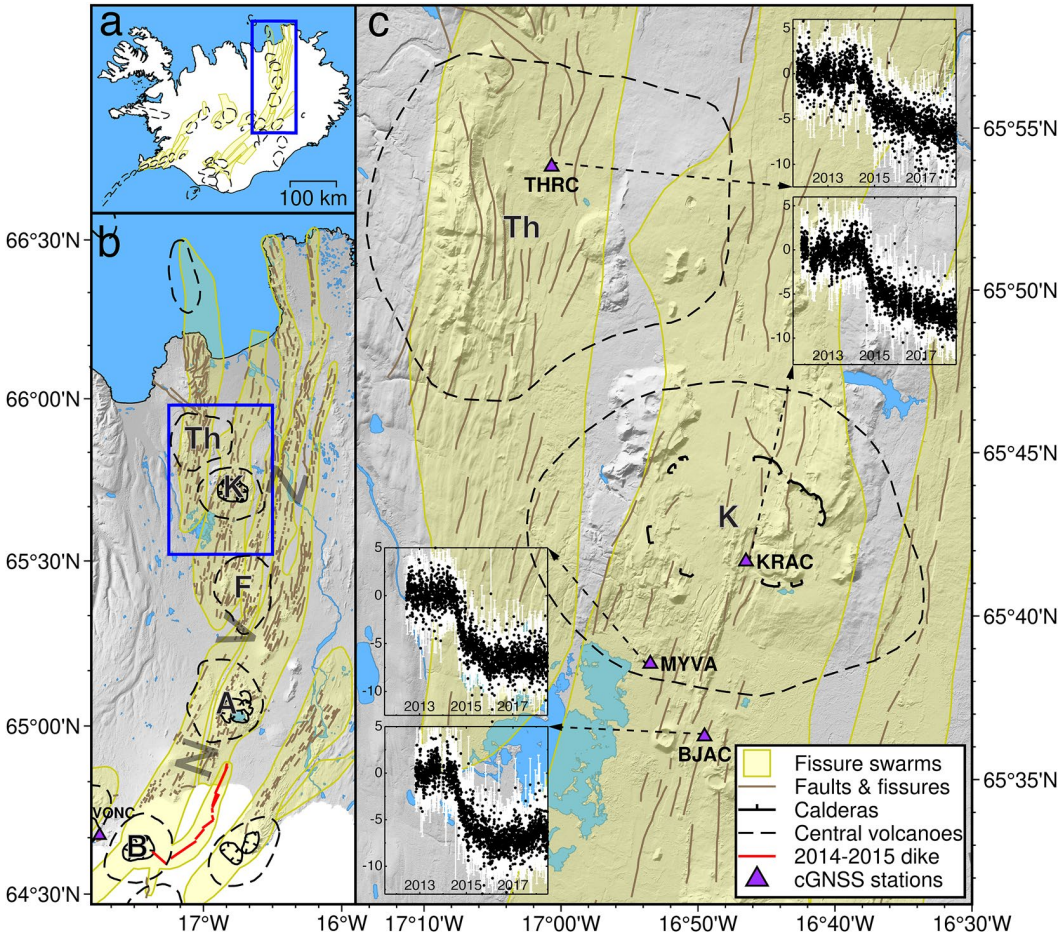


Figure 2. (a) A map of Iceland with the blue rectangle indicating the Northern Volcanic Zone (NVZ). (b) A map of NVZ with volcanic systems: B: Bárðarbunga. A: Askja. F: Fremrinámar. K: Krafla. Th: Þeistareykir (Saemundsson, 1979; Sigmundsson, Einarsson, et al., 2020). Faults and fissures swarms (brown) are from Jóhannesson and Sæmundsson (2009). Blue rectangle indicates the area shown in panel c. (c) Locations of cGNSS stations with their detrended east-component time series. The dashed lines with arrows point from the stations to their time series, where the black dots and white lines indicate the coordinates and their uncertainties, respectively (unit: mm), and the horizontal axes indicate time (unit: yr).

homogeneous mantle, consistent mantle forming conditions and similar melt fractions along the NVZ compared to the whole Iceland have been inferred with radiogenic isotopes (Harðardóttir et al., 2022). The latest rifting episode at Krafla during 1975–1984 included ~20 dike intrusions and nine eruptions, with earthquakes, faulting and accumulated widening of 4–5 m on average in the volcanic system (e.g., Björnsson et al., 1977; Wright et al., 2012). Since late 2011, ground deformation has been monitored with continuous GNSS (cGNSS) stations KRAC, MYVA and BJAC at Krafla, and THRC at Þeistareykir. In August 2014, a dike intrusion occurred at Bárðarbunga, ~120 km south of the Krafla area (Parks et al., 2017; Sigmundsson et al., 2014), which propagated 48 km and fed the 6-month-long Holuhraun eruption at its northern end. At a similar period, four cGNSS stations at Krafla and Þeistareykir show faster movements to the west (Figure 2c and Figure S4 in Supporting Information S1; Lanzi et al., 2023).

4.2. Bayesian Modeling Results

The daily coordinate time series at the four stations were derived with GAMIT/GLOBK 10.75 (Figure S4 and Text S2 in Supporting Information S1; Herring et al., 2018). Pre-processing infers velocity anomalies characterized by two break points during 2014–2015 (Figure 3 and Table S2 in Supporting Information S1). Bayesian modeling is only implemented to the east component as only its velocity changes allow reliable estimates (8 mm/yr vs. the FLN amplitude of 3.0–3.4 mm/yr$^{0.25}$ from pre-processing). We run 500,000 sampling iterations to better realize the PDs.

19448007, 2023, 14, Downloaded from https://agupubs.onlinelibrary.wiley.com/doi/10.1029/2023GL103432 by RH-net, Wiley Online Library on [18/07/2023]. See the Terms and Conditions (https://onlinelibrary.wiley.com/terms-and-conditions) on Wiley Online Library for rules of use; OA articles are governed by the applicable Creative Commons License

19448007, 2023, 14, Downloaded from https://agupubs.onlinelibrary.wiley.com/doi/10.1029/2023GL103432 by RH-net, Wiley Online Library on [18/07/2023]. See the Terms and Conditions (https://onlinelibrary.wiley.com/terms-and-conditions) on Wiley Online Library for rules of use; OA articles are governed by the applicable Creative Commons License

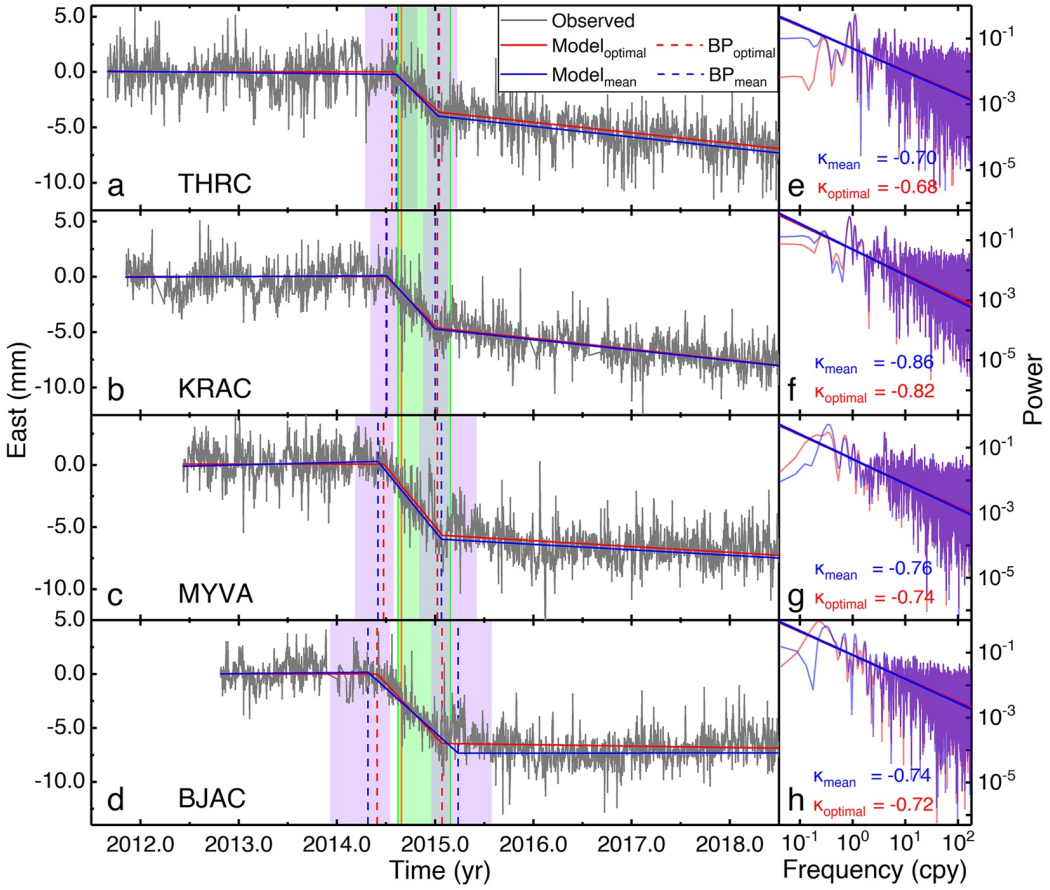


Figure 3. Bayesian modeling results for the four time series at Krafla and Þeistareykir. (a–d) Preprocessed time series in east component with the established models. The time series are detrended with the optimal initial velocities. The purple shaded area indicates the 95% confidence interval of break points. The green shaded area indicates the period of the Bárðarbunga diking and eruption (Sigmundsson et al., 2014), with the start of dike intrusion on 16 August 2014 (2014.6260) and the end of eruption on 27 February 2015 (2015.1603). The vertical orange line indicates the start of the eruption on 29 August 2014 (2014.6575). (e–h) The power spectrums of residuals and the obtained spectrum indices (κ).

Results are shown in Figures 3 and 4a, Figures S5, S6, and Table S5 in Supporting Information S1. Generally, the established models fit the time series well. For the first velocity change, the optimal estimates derive break points at 2014.4114, 2014.4758, 2014.5018, and 2014.5601 at station BJAC, MYVA, KRAC and THRC, respectively. Corresponding velocity change values are −9.8, −9.6, −8.9, and −7.6 mm/yr. The largest break point uncertainty is 227 d at BJAC, which is mainly caused by missing data, and the smallest is 102 d at KRAC. Accounting for all the stations at Krafla, the 95% confidence interval of the break points ranges from 2014.1860 to 2014.6166 (9 March to 14 August 2014). The second velocity changes have similar magnitude as the first ones, however with opposite sign. The root mean square of the differences between their absolute values is 0.7 mm/yr. The uncertainties of the second break points all overlap with the end of the Holuhraun eruption (29 August 2014).

Therefore, we infer that the westward-accelerated movements at Krafla (9 March to 14 August 2014) precede the Bárðarbunga dike intrusion (16 August 2014) with 95% confidence interval (±83 d on average). At the second break points the station velocities resume similar velocities as before the movement anomalies. The optimal estimates suggest the resumption occurs before the end of Holuhraun eruption but uncertainties allow no solid conclusion.

5. Discussion

The span of the time series affects the parameter estimations. Additional synthetic data experiments (Text S3 and Figure S7 in Supporting Information S1) indicate longer span before a break point generally reduces the uncertainties of the initial velocity and break point but has less effect on errors. For a fixed span of time series, shorter

19448007, 2023, 14, Downloaded from https://agupubs.onlinelibrary.wiley.com/doi/10.1029/2023GL103432 by RH-net, Wiley Online Library on [18/07/2023]. See the Terms and Conditions (https://onlinelibrary.wiley.com/terms-and-conditions) on Wiley Online Library for rules of use; OA articles are governed by the applicable Creative Commons License

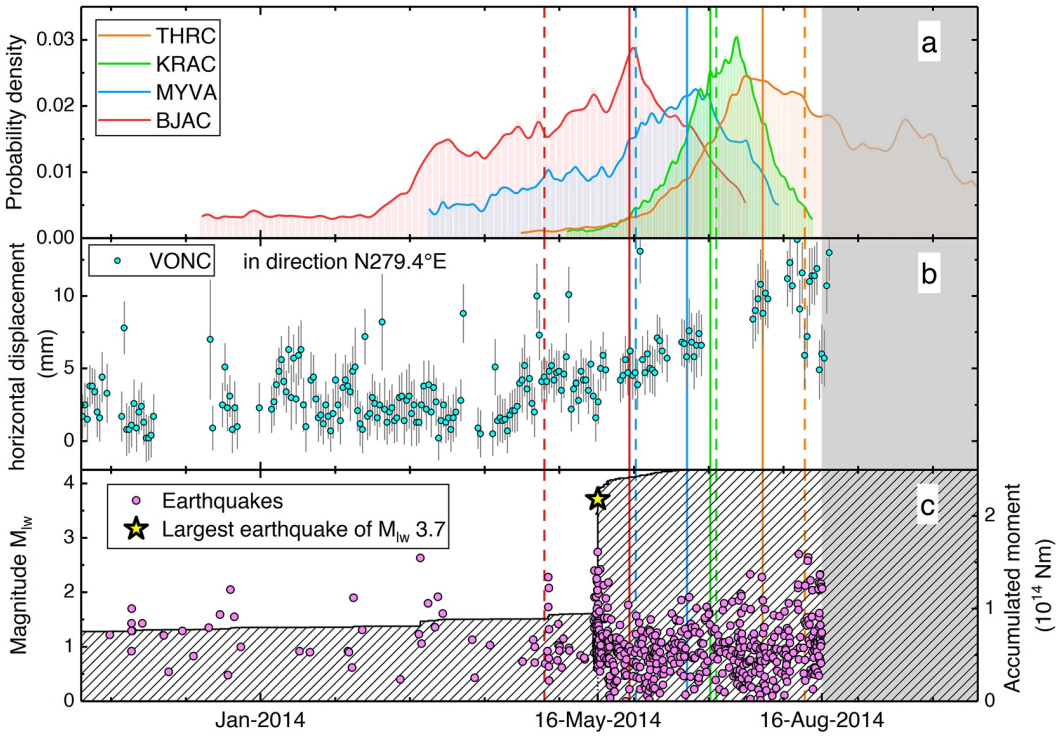


Figure 4. Comparison between the far-field velocity anomalies and near-field precursors of the Bárðarbunga rifting episode. (a) Marginal posterior probability distributions of the first break points within 95% confidence intervals. The color-shaded areas start and end at the lower and higher limit of the 95% confidence intervals, respectively. The vertical solid and dashed lines indicate the optimal and mean estimates, respectively. The gray area indicates the period after the onset of the Bárðarbunga dike intrusion. (b) The horizontal displacement in direction N279.4°E (the azimuth of maximum horizontal motion) at VONC station (11 km west of the Bárðarbunga) from detrended GNSS time series. (c) Seismicity at Bárðarbunga versus time (left axis) and accumulated seismic moment (right axis) before the dike intrusion. The data in panels b and c are from Sigmundsson, Pinel, et al. (2020).

span before the break point hampers the precision of the initial velocity while shorter span after the break point hinders the velocity change estimation. Consequently, they both raise the uncertainty of velocity change. The relatively large uncertainties of the second break points at Krafla are partially attributed to the short span (less than 1 year) between the two break points (Figure 3). The difference in the total time span of the four cGNSS time series is less than 1 yr, with minimal influence on the results.

The joint parameter distributions (Figure S6 in Supporting Information S1) indicate strong anti-correlation between the two velocity change values, and between the two noise parameters. The anti-correlation between the velocity change values is because the second one is referenced to the first one. The anti-correlation of noise parameters has been observed in previous research (e.g., Chen et al., 2018; Gobron et al., 2021). The unit of PLN amplitude varies with the spectral index in Equation 1, making their amplitudes not directly comparable. Thus, we compare the PDs of noise amplitude with the preliminary results after unit normalization (Gobron et al., 2021; Text S5 and Figure S8 in Supporting Information S1) and find that the preliminary estimates of noise amplitude are within 95% confidence intervals of Bayesian results, validating the method on noise assessment.

Magmatic processes can cause gradual velocity changes, for example, exponential-logarithmic functions (Bevis & Brown, 2014), instead of sudden changes at specific epochs as modeled in Equation 2. Our method can be generalized with different functions. However, when applying Equation 2 to gradual velocity changes, the break point uncertainty can be expected to provide an estimate of the duration of the varying velocity.

Near-field precursors prior to the onset of the Bárðarbunga dike include enhanced ground deformation and seismicity (Sigmundsson, Pinel, et al., 2020), which can be compared with the velocity anomalies at Krafla (Figure 4). The probability density of the beginning of far-field velocity anomalies is higher in the period when the near-field station, VONC (Figure 2b), moves faster away from the Bárðarbunga caldera (Figure 4b) and when

19448007, 2023, 14, Downloaded from https://agupubs.onlinelibrary.wiley.com/doi/10.1029/2023GL103432 by RH-net, Wiley Online Library on [18/07/2023]. See the Terms and Conditions (https://onlinelibrary.wiley.com/terms-and-conditions) on Wiley Online Library for rules of use; OA articles are governed by the applicable Creative Commons License

an M_{lw} 3.7 earthquake occurs at Bárðarbunga (Figure 4c), marking a period of increased seismicity lasting until the diking onset. A comparable velocity anomaly is observed at another near-field station before the dike intrusion (Figure S9b in Supporting Information S1). Therefore, the far-field velocity anomalies at Krafla occur in the same period as the near-field precursors at Bárðarbunga. These far-field velocity anomalies localize at the NVZ as the time series at other four far-field cGNSS stations at distances of 110–150 km from Bárðarbunga show no similar pattern of deformation (Figure S9c in Supporting Information S1).

The concurrent activities at Krafla and Bárðarbunga may indicate a coupling relationship between the two volcanic systems along the NVZ. During 25 October 2013–31 October 2014, five minor seismic swarms are clustered in the Krafla region (Blanck et al., 2014). Three correlate with reduced reinjection rate at two geothermal boreholes and two occur in areas of previous seismicity in 2009–2012 relating to the rift axis activities (Schuler et al., 2016). Thus, these seismic swarms cannot be taken as unusual activity relating to the velocity anomalies. The absence of unusual seismicity with the velocity anomalies may indicate the involvement of ductile processes, aseismic faulting, or insufficient strain change to cause seismicity.

Volcanic systems at NVZ may be coupled, eventually through a partial melt zone that can channel pressure variations. Pressure pulse propagation in a partial melt zone has been suggested in the past to cause coupled activity at volcanoes in the NVZ. Leveling and lake level measurements at Askja indicate rapid inflation of >20 cm/yr during 1970–1972 above a pressurized magma source, which reverses to deflation probably after 1974 (Tryggvason, 1989). At the Bárðarbunga volcano, the onset of long-lasting sequence of M5-5.5 earthquakes in 1974, signifying pressure changes in its roots, was concurrent with the magma inflow at Krafla (Einarsson, 1987, 1991). Suggested explanation was that magma flow into the roots of the Krafla volcano reduced the pressure under Bárðarbunga and Askja, causing deflation at both. The partial melt zone in the NVZ is described as a magmatic axis by Marquart and Jacoby (1985) and Jocoby et al. (1989). We envision no material flow between volcanic systems below the brittle-ductile boundary, only mechanical coupling.

Possibilities for further examination of the geodetic signals at the cGNSS sites studied here are limited, but campaign GNSS and Interferometric Synthetic Aperture Radar (InSAR) observations (Drouin et al., 2017) provide some constraints. The campaign GNSS stations nearest to the continuous ones, measured yearly, show general decrease in eastward movement consistent with cGNSS results, while the InSAR times series analysis at ground pixels close to the cGNSS stations are less conclusive (Figure S10 in Supporting Information S1).

A few studies have addressed the coupling between volcanoes and/or magma bodies. Lower crust earthquakes at 12–25 km depth at Askja during 2005–2010 implies melt injected by multiple pulses from a deep magma source (Key et al., 2011). Deep magma bodies may offset from shallow ones within the same volcanic system (Cordell et al., 2018), for example, earthquakes at 7–22 km depth and ∼12 km southeast of the Bárðarbunga caldera before the dike intrusion in 2014 can indicate a laterally offset magma feeding source (Hudson et al., 2017). At the Grímsvötn volcano, ∼27 km southeast of Bárðarbunga, velocity anomalies of ground deformation are observed ten months before the 2014 Bárðarbunga diking, indicating the decrease of magma inflow (Bato et al., 2018). Biggs et al. (2016) summarizes possible mechanisms for the coupling between volcanoes, where Campi Flegrei and Vesuvius in Italy and Mauna Loa and Kīlauea in Hawaii are also suggested to be linked with an asthenospheric source. However, the distances between these interacted volcanoes are only 25–35 km. Our finding suggests coupling over ∼120 km distance, eventually related to the mantle plume under Iceland. Future research on the spatial evolution of the velocity anomalies (e.g., with a dense cGNSS network) may provide better insight into the causative processes of long-distance volcano coupling.

6. Conclusions

Bayesian modeling is implemented to jointly estimate velocity break points, velocity change values and power-law noise in GNSS time series, together with their probability density distributions. Synthetic data experiments validate the method and suggest velocity change value exceeding 7.5, 10, and 15 mm/yr for flicker noise amplitude of 3, 4, and 5 mm/yr$^{0.25}$, respectively, can be satisfactorily detected in 5-yr-length time series. Applying the method to observed data during 2014–2015 at Krafla and Þeistareykir, we infer that a velocity change in the east component at Krafla precedes the 2014 Bárðarbunga dike intrusion by 23–77 days, with a 95% confidence level of ±83 d on average. The amount of the velocity changes is 7.6–9.8 mm/yr and the velocities resume to approximately the original level with another velocity change in late 2014 or early 2015. The onset of the velocity

anomalies occurs in the same period as enhanced seismicity and deformation rate before the dike intrusion at Bárðarbunga, possible providing evidence for large-scale coupling among the volcanic systems in the Northern Volcanic Zone of Iceland.

Data Availability Statement

The coordinate time series at the four stations are available at https://doi.org/10.17605/OSF.IO/4JDHV. The modified GBIS scripts for detecting break points in time series (GBIS4TS) are available at https://doi.org/10.17605/OSF.IO/Q35TW with a synthetic time series for verifying installation provided. The original version of the GBIS software is available at https://comet.nerc.ac.uk/gbis/ and the HECTOR software is available at http://segal.ubi.pt/web-services/whatishector/.

Acknowledgments
The authors are grateful to Nico Fournier and an anonymous referee for their important comments. This study received funding from the European Union's Horizon 2020 research and innovation programme No. 858092 (IMPROVE project) and partially from Icelandic Research Fund No. 239615-051 (ISVOLC project). We acknowledge Marco Bagnardi and Andrew Hooper (AH) for GBIS software, and AH for discussions. We thank Chiara Lanzi and Sigrún Hreinsdóttir for supporting GNSS data processing. The cGNSS stations are operated jointly with the National Power Company of Iceland. We thank Vincent Drouin for providing InSAR time series and discussions. We thank Páll Einarsson, Juliet Biggs, Fei Liu, Sæmundur A. Halldórsson, Tim J. Craig, John Maclennan, Joachim Gottsmann, Sonja Greiner, Patricia Fehrentz, Xiaohui Zhou, Yifang Ma and Alberto Caracciolo for discussions. We acknowledge International GNSS Services for data support and Space & Earth Geodetic Analysis Laboratory, Portugal, for HECTOR software. The maps are plotted with the Generic Mapping Tools (Wessel et al., 2019).

References

Amiri-Simkooei, A. R., Mohammadloo, T. H., & Argus, D. F. (2017). Multivariate analysis of GPS position time series of JPL second reprocessing campaign. *Journal of Geodesy*, *91*(6), 685–704. https://doi.org/10.1007/s00190-016-0991-9

Amiri-Simkooei, A. R., Tiberius, C. C. J. M., & Teunissen, P. J. G. (2007). Assessment of noise in GPS coordinate time series: Methodology and results. *Journal of Geophysical Research*, *112*(B7), B07413. https://doi.org/10.1029/2006JB004913

Bagnardi, M., & Hooper, A. (2018). Inversion of surface deformation data for rapid estimates of source parameters and uncertainties: A Bayesian approach. *Geochemistry, Geophysics, Geosystems*, *19*(7), 2194–2211. https://doi.org/10.1029/2018GC007585

Baragatti, M., Bertin, K., Lebarbier, E., & Meza, C. (2019). A Bayesian approach for the segmentation of series with a functional effect. *Statistical Modelling*, *19*(2), 194–220. https://doi.org/10.1177/1471082X18755539

Bato, M. G., Pinel, V., Yan, Y., Jouanne, F., & Vandemeulebrouckm, J. (2018). Possible deep connection between volcanic systems evidenced by sequential assimilation of geodetic data. *Scientific Reports*, *8*(1), 11702. https://doi.org/10.1038/s41598-018-29811-x

Benciolini, B., Reguzzoni, M., Venuti, G., & Vitti, A. (2012). Bayesian and variational methods for discontinuity detection: Theory overview and performance comparison. In N. Sneeuw, P. Novák, M. Crespi, &, F. Sansò (Eds.), *VII Hotine-Marussi Symposium on Mathematical Geodesy*. Springer.

Bevis, M., & Brown, A. (2014). Trajectory models and reference frames for crustal motion geodesy. *Journal of Geodesy*, *88*(3), 283–311. https://doi.org/10.1007/s00190-013-0685-5

Biggs, J., Robertson, E., & Cashman, K. (2016). The lateral extent of volcanic interactions during unrest and eruption. *Nature Geoscience*, *9*(4), 301–311. https://doi.org/10.1038/ngeo2658

Björnsson, A., Saemundsson, K., Einarsson, P., Tryggvason, E., & Grönvold, K. (1977). Current rifting episode in north Iceland. *Nature*, *266*(5600), 318–323. https://doi.org/10.1038/266318a0

Blanck, H., Ágústsson, K., & Gunnarsson, K. (2014). Seismic monitoring of Krafla. For the period October 2013 to October 2014. Retrieved from http://gogn.lv.is/files/2014/2014-136.pdf

Borghi, A., Cannizzaro, L., & Vitti, A. (2012). Advanced techniques for discontinuity detection in GNSS coordinate time-series. An Italian case study. In S. Kenyon, M. Pacino, & U. Marti (Eds.), *Geodesy for Planet Earth*. Springer.

Borsa, A. A., Agnew, D. C., & Cayan, D. R. (2014). Ongoing drought-induced uplift in the western United States. *Science*, *345*(6204), 1587–1590. https://doi.org/10.1126/science.1260279

Bos, M. S., Fernandes, R. M. S., & Karegar, M. (2018). The effect of colored noise on automatic offset detection in GNSS time series. In *Abstract presented at international GNSS service Wuhan workshop 2018*. Retrieved from http://acc.igs.org/workshop2018.html

Bos, M. S., Fernandes, R. M. S., Montillet, J. P., & Williams, S. D. P. (2020). Introduction to geodetic time series analysis. In J. P. Montillet & M. Bos (Eds.), *Geodetic time series analysis in Earth sciences*. Springer.

Bos, M. S., Fernandes, R. M. S., Williams, S. D. P., & Bastos, L. (2013). Fast error analysis of continuous GNSS observations with missing data. *Journal of Geodesy*, *87*(4), 351–360. https://doi.org/10.1007/s00190-012-0605-0

Chen, G., Zhao, Q., Wei, N., & Liu, J. (2018). Impacts on noise analyses of GNSS position time series caused by seasonal signal, weight matrix, offset, and helmert transformation parameters. *Remote Sensing*, *10*, 1584. https://doi.org/10.3390/rs10101584

Cordell, D., Unsworth, M. J., & Díaz, D. (2018). Imaging the Laguna del Maule volcanic field, central Chile using magnetotellurics: Evidence for crustal melt regions laterally-offset from surface vents and lava flows. *Earth and Planetary Science Letters*, *488*, 168–180. https://doi.org/10.1016/j.epsl.2018.01.007

Davis, J. L., Wernicke, B. P., Bisnath, S., Niemi, N. A., & Elósegui, P. (2006). Subcontinental-scale crustal velocity changes along the Pacific-North America plate boundary. *Nature*, *441*(29), 1131–1134. https://doi.org/10.1038/nature04781

Didova, O., Gunter, B., Riva, R., & Roese-Koerner, L. (2016). An approach for estimating time-variable rates from geodetic time series. *Journal of Geodesy*, *90*(11), 1207–1221. https://doi.org/10.1007/s00190-016-0918-5

Dmitrieva, K., Segall, P., & Bradley, A. M. (2017). Effects of linear trends on estimation of noise in GNSS position time-series. *Geophysical Journal International*, *208*(1), 281–288. https://doi.org/10.1093/gji/ggw391

Dong, D., Fang, P., Bock, Y., Cheng, M. K., & Miyazaki, S. (2002). Anatomy of apparent seasonal variations from GPS-derived site position time series. *Journal of Geophysical Research*, *107*(B4), ETG9-1.–ETG9-16. https://doi.org/10.1029/2001JB000573

Drouin, V., Sigmundsson, F., Verhagen, S., Ófeigsson, B. G., Spaans, K., & Hreinsdóttir, S. (2017). Deformation at Krafla and Bjarnarflag geothermal areas, northern volcanic zone of Iceland, 1993–2015. *Journal of Volcanology and Geothermal Research*, *344*, 92–105. https://doi.org/10.1016/j.jvolgeores.2017.06.013

Ducrocq, C., Geirsson, H., Árnadóttir, T., Juncu, D., Drouin, V., Gunnarsson, G., et al. (2021). Inflation-deflation episodes in the Hengill and Hrómundartindur volcanic complexes, SW Iceland. *Frontiers in Earth Science*, *9*, 725109. https://doi.org/10.3389/feart.2021.725109

Einarsson, P. (1987). The anomalous mantle beneath Iceland and possible pressure connection between volcanoes. In *Abstract presented at symposium on how volcanoes work*. Hilo.

Einarsson, P. (1991). Earthquakes and present-day tectonism in Iceland. *Tectonophysics*, *189*(1–4), 261–279. https://doi.org/10.1016/0040-1951(91)90501-I

Einarsson, P. (2008). Plate boundaries, rifts and transforms in Iceland. *Jökull*, *58*(12), 35–58. https://doi.org/10.33799/jokull2008.58.035

19448007, 2023, 14, Downloaded from https://agupubs.onlinelibrary.wiley.com/doi/10.1029/2023GL103432 by RH-net, Wiley Online Library on [18/07/2023]. See the Terms and Conditions (https://onlinelibrary.wiley.com/terms-and-conditions) on Wiley Online Library for rules of use; OA articles are governed by the applicable Creative Commons License

Geirsson, H., Árnadóttir, T., Hreinsdóttir, S., Decriem, J., Lafemina, P. C., Jónsson, S., et al. (2010). Overview of results from continuous GPS observations in Iceland from 1995 to 2010. *Jökull*, *2010*(60), 3–22. https://doi.org/10.33799/jokull2010.60.003

Gobron, K., Rebischung, P., Van Camp, M., Demoulin, A., & de Viron, O. (2021). Influence of aperiodic non-tidal atmospheric and oceanic loading deformations on the stochastic properties of global GNSS vertical land motion time series. *Journal of Geophysical Research: Solid Earth*, *126*(9), e2021JB022370. https://doi.org/10.1029/2021JB022370

Hackl, M., Malservisi, R., Hugentobler, U., & Wonnacott, R. (2011). Estimation of velocity uncertainties from GPS time series: Examples from the analysis of the South African TrigNet network. *Journal of Geophysical Research*, *116*(B11), B11404. https://doi.org/10.1029/2010JB008142

Harðardóttir, S., Mattews, S., Halldórsson, S. A., & Jackson, M. G. (2022). Spatial distribution and geochemical characterization of Icelandic mantle end-members: Implications for plume geometry and melting processes. *Chemical Geology*, *604*, 120930. https://doi.org/10.1016/j.chemgeo.2022.120930

Hastings, W. K. (1970). Monte Carlo sampling methods using Markov chains and their applications. *Biometrika*, *57*(1), 97–109. https://doi.org/10.1093/biomet/57.1.97

Herring, T. A., King, R. W., Floyd, M. A., & McClusky, S. C. (2018). *Introduction to GAMIT/GLOBK*. Massachusetts Institute of Technology. Retrieved from http://geoweb.mit.edu/gg/Intro_GG.pdf

Hudson, T. S., White, R. S., Greenfield, T., Ágústsdóttir, T., Brisbourne, A., & Green, R. G. (2017). Deep crustal melt plumbing of Bárðarbunga volcano, Iceland. *Geophysical Research Letters*, *44*(17), 8785–8794. https://doi.org/10.1002/2017GL074749

Jocoby, W. R., Zdarsky, H., & Altmann, U. (1989). Geodetic and geophysical evidence for magma movement and dyke injection during the Krafla rifting episode in North Iceland. In (Ed.), J. M. Sinton (Ed.), *Evolution of mid ocean ridges*. https://doi.org/10.1029/GM057p0065

Jóhannesson, H., & Sæmundsson, K. (2009). Geological map of Iceland - Tectonics - 1:600.000 [Dataset]. Icelandic Institute of Natural History. https://gatt.lmi.is/geonetwork/srv/eng/catalog.search#/metadata/%7B005FFDAD-69A1-4385-B16F-FD31B960FE33%7D/formatters/xsl-view?root=div&view=advanced

Key, J., White, R. S., Soosalu, H., & Jakobsdóttir, S. S. (2011). Multiple melt injection along a spreading segment at Askja, Iceland. *Geophysical Research Letters*, *38*(5), L05301. https://doi.org/10.1029/2010GL046264

Klos, A., Bos, M. S., & Bogusz, J. (2018). Detecting time-varying seasonal signal in GPS position time series with different noise levels. *GPS Solutions*, *22*(1), 21. https://doi.org/10.1007/s10291-017-0686-6

Koulali, A., & Clarke, P. J. (2021). Modelling quasi-periodic signals in geodetic time-series using Gaussian processes. *Geophysical Journal International*, *226*(3), 1705–1714. https://doi.org/10.1093/gji/ggab168

Langbein, J. (2004). Noise in two-color electronic distance meter measurements revisited. *Journal of Geophysical Research*, *109*(B4), B04406. https://doi.org/10.1029/2003JB002819

Langbein, J. (2012). Estimating rate uncertainty with maximum likelihood: Differences between power-law and flicker-random-walk models. *Journal of Geodesy*, *86*(9), 775–783. https://doi.org/10.1007/s00190-012-0556-5

Langbein, J., & Johnson, H. (1997). Correlated errors in geodetic time series: Implications for time-dependent deformation. *Journal of Geophysical Research*, *102*(B1), 591–603. https://doi.org/10.1029/96JB02945

Lanzi, C., Drouin, V., Sigmundsson, F., Geirsson, H., Hersir, G. P., Ágústsson, K., et al. (2023). Pressure increase at the magma-hydrothermal interface at Krafla caldera, North-Iceland, 2018–2020: Magmatic processes or hydrothermal changes? *Journal of Volcanology and Geothermal Research*, *440*, 107849. https://doi.org/10.1016/j.jvolgeores.2023.107849

Liu, F., Elliott, J. R., Ebmeier, S. K., Craig, T. J., Hooper, A., Novoa Lizama, C., & Delgado, F. (2023). First onset of unrest captured at Socompa: A recent geodetic survey at central Andean volcanoes in northern Chile. *Geophysical Research Letters*, *50*(10), e2022GL102480. https://doi.org/10.1029/2022GL102480

Mao, A., Harrison, C., & Dixon, T. H. (1999). Noise in GPS coordinate time series. *Journal of Geophysical Research*, *104*(B2), 2797–2816. https://doi.org/10.1029/1998JB900033

Marquart, G., & Jacoby, W. (1985). On the mechanism of magma injection and plate divergence during the Krafla Rifting Episode in NE Iceland. *Journal of Geophysical Research*, *90*(B12), 10178–10192. https://doi.org/10.1029/JB090iB12p10178

Metropolis, N., Rosenbluth, A. W., Rosenbluth, M. N., Teller, A. H., & Teller, E. (1953). Equation of state calculations by fast computing machines. *The Journal of Chemical Physics*, *21*(6), 1087–1092. https://doi.org/10.1063/1.1699114

Nikolaidis, R. (2002). *Observation of geodetic and seismic deformation with the global positioning system, (Doctoral dissertation)*. University of California. Retrieved from Scripps Orbit and Permanent Array Center Retrieved from http://sopac.ucsd.edu/input/processing/pubs/nikoThesis.pdf

Oelsmann, J., Passaro, M., Sánchez, L., Dettmering, D., Schwatke, C., & Seitz, F. (2022). Bayesian modelling of piecewise trends and discontinuities to improve the estimation of coastal vertical land motion. *Journal of Geodesy*, *96*(9), 62. https://doi.org/10.1007/s00190-022-01645-6

Olivare-Pulido, G., Teferle, F. N., & Hunegnaw, A. (2020). Markov chain Monte Carlo and the application to geodetic time series analysis. In J. P. Montillet & M. Bos (Eds.), *Geodetic time series analysis in Earth sciences*. Springer.

Olivares, G., & Teferle, F. N. (2013). A Bayesian Monte Carlo Markov chain method for parameter estimation of fractional differenced Gaussian processes. *IEEE Transactions on Signal Processing*, *61*(9), 2405–2412. https://doi.org/10.1109/TSP.2013.2245658

Parks, M. M., Heimisson, E. R., Sigmundsson, F., Hooper, A., Vogfjörd, K. S., Árnadóttir, T., et al. (2017). Evolution of deformation and stress changes during the caldera collapse and dyking at Bárdarbunga, 2014-2015: Implication for triggering of seismicity at nearby Tungnafellsjökull volcano. *Earth and Planetary Science Letters*, *462*, 212–223. https://doi.org/10.1016/j.epsl.2017.01.020

Qianqian, Z., & Qingming, Q. (2013). Bayesian methods for outliers detection in GNSS time series. *Journal of Geodesy*, *87*(7), 609–627. https://doi.org/10.1007/s00190-013-0640-5

Saemundsson, K. (1979). Outline of the geology of Iceland. *Jökull*, *29*(1), 7–28. https://doi.org/10.33799/jokull1979.29.007

Schuler, J., Pugh, D. J., Hauksson, E., White, R. S., Stock, J. M., & Brandsdóttir, B. (2016). Focal mechanisms and size distribution of earthquakes beneath the Krafla central volcano, NE Iceland. *Journal of Geophysical Research: Solid Earth*, *121*(7), 5152–5168. https://doi.org/10.1002/2016JB013213

Sigmundsson, F., Einarsson, P., Hjartardóttir, A. R., Drouin, V., Jónsdóttir, K., Árnadóttir, T., et al. (2020). Geodynamics of Iceland and the signatures of plate spreading. *Journal of Volcanology and Geothermal Research*, *391*, 106436. https://doi.org/10.1016/j.jvolgeores.2018.08.014

Sigmundsson, F., Hooper, A., Hreinsdóttir, S., Vogfjörd, K. S., Ófeigsson, B. G., Heimisson, E. R., et al. (2014). Segmented lateral dyke growth in a rifting event at Bárðarbunga volcanic system, Iceland. *Nature*, *517*(7533), 191–195. https://doi.org/10.1038/nature14111

Sigmundsson, F., Pinel, V., Grapenthin, R., Hooper, A., Halldórsson, S. A., Einarsson, P., et al. (2020). Unexpected large eruptions from buoyant magma bodies within viscoelastic crust. *Nature Communications*, *11*(1), 2403. https://doi.org/10.1038/s41467-020-16054-6

Tryggvason, E. (1989). Ground deformation in Askja, Iceland: Its source and possible relation to flow of the mantle plume. *Journal of Volcanology and Geothermal Research*, *39*(1), 61–67. https://doi.org/10.1016/0377-0273(89)90021-8

Vitti, A. (2012). Sigseg: A tool for the detection of position and velocity discontinuities in geodetic time-series. *GPS Solutions*, *16*(3), 405–410. https://doi.org/10.1007/s10291-012-0257-9

19448007, 2023, 14, Downloaded from https://agupubs.onlinelibrary.wiley.com/doi/10.1029/2023GL103432 by RHI-net, Wiley Online Library on [18/07/2023]. See the Terms and Conditions (https://onlinelibrary.wiley.com/terms-and-conditions) on Wiley Online Library for rules of use; OA articles are governed by the applicable Creative Commons License

Wang, L., & Herring, T. (2019). Impact of estimating position offsets on the uncertainties of GNSS site velocity estimates. *Journal of Geophysical Research: Solid Earth*, *124*(12), 13452–13467. https://doi.org/10.1029/2019JB017705

Wang, X., Cheng, Y., Wu, S., & Zhang, K. (2016). An enhanced singular spectrum analysis method for constructing nonsecular model of GPS site movement. *Journal of Geophysical Research: Solid Earth*, *121*(3), 2193–2211. https://doi.org/10.1002/2015JB012573

Wessel, P., Luis, J. F., Uieda, L., Scharroo, R., Wobbe, F., Smith, W. H. F., & Tian, D. (2019). The generic mapping tools version 6. *Geochemistry, Geophysics, Geosystems*, *20*(11), 5556–5564. https://doi.org/10.1029/2019GC008515

Williams, S. D. P. (2003). The effect of coloured noise on the uncertainties of rates estimated from geodetic time series. *Journal of Geodesy*, *76*(9–10), 483–494. https://doi.org/10.1007/s00190-002-0283-4

Wright, T., Sigmundsson, F., Pagli, C., Belachew, M., Hamling, I. J., Brandsdóttir, B., et al. (2012). Geophysical constraints on the dynamics of spreading centres from rifting episodes on land. *Nature Geoscience*, *5*(4), 242–250. https://doi.org/10.1038/ngeo1428

Wu, D., Yan, H., & Yuan, S. (2018). L1 regularization for detecting offsets and trend change points in GNSS time series. *GPS Solutions*, *22*(3), 88. https://doi.org/10.1007/s10291-018-0756-4

Zhou, X., Yang, Y., Chen, H., Ouyang, W., & Fan, W. (2019). A modified Least Square harmonics estimation method and comparative analysis of established full periodicity models. *Earth and Space Science*, *6*(11), 2160–2179. https://doi.org/10.1029/2019EA000750

References From the Supporting Information

Altamimi, Z., Rebischung, P., Métivier, L., & Collilieux, X. (2016). ITRF2014: A new release of the international terrestrial reference frame modeling nonlinear station motions. *Journal of Geophysical Research: Solid Earth*, *121*(8), 6109–6131. https://doi.org/10.1002/2016JB013098

Boehm, J., Werl, B., & Schuh, H. (2006). Troposphere mapping functions for GPS and very long baseline interferometry from European centre for medium-range weather forecasts operational analysis data. *Journal of Geophysical Research*, *111*(B2), B02406. https://doi.org/10.1029/2005JB003629

Gazeaux, J., Williams, S., King, M., Bos, M., Dach, R., Deo, M., et al. (2013). Detecting offsets in GPS time series: First results from the detection of offsets in GPS experiment. *Journal of Geophysical Research: Solid Earth*, *118*(5), 2397–2407. https://doi.org/10.1002/jgrb.50152

Leys, C., Ley, C., Klein, O., Bernard, P., & Licata, L. (2013). Detecting outliers: Do not use standard deviation around the mean, use absolute deviation around the median. *Journal of Experimental Social Psychology*, *49*(4), 764–766. https://doi.org/10.1016/j.jesp.2013.03.013

Lyard, F., Lefevre, F., Letellier, T., & Francis, O. (2006). Modelling the global ocean tides: Modern insights from FES2004. *Ocean Dynamics*, *56*(5–6), 394–415. https://doi.org/10.1007/s10236-006-0086-x

19448007, 2023, 14, Downloaded from https://agupubs.onlinelibrary.wiley.com/doi/10.1029/2023GL103432 by RH-net, Wiley Online Library on [18/07/2023]. See the Terms and Conditions (https://onlinelibrary.wiley.com/terms-and-conditions) on Wiley Online Library for rules of use; OA articles are governed by the applicable Creative Commons License

Geophysical Research Letters

Supporting Information for

Joint Bayesian Modeling of Velocity Break Points, Noise Characteristics, and Their Uncertainties in GNSS Time Series: Far-Field Velocity Anomalies Concurrent with Magmatic Activity in Iceland

Yilin Yang[1], Freysteinn Sigmundsson[1], Halldór Geirsson[1]

[1]Nordic Volcanological Center, Institute of Earth Sciences, University of Iceland, Reykjavík, Iceland

Contents of this file

Texts S1 to S4
Figures S1 to S10
Tables S1 to S5

Introduction

This supporting information provides four texts on calculating the covariance matrix of time-correlated noise, the GNSS solution strategies, the scheme of additional synthetic data experiments and the unit normalization of power-law noise amplitudes, respectively. Figure S1 displays the simulated time series for synthetic data experiments. Figure S2, S3 and S7 give additional results of the synthetic data experiments. Figure S4 displays the raw GNSS time series at the four stations at Krafla and Þeistareykir. Figure S5 to S6 provide additional results for the real-data experiment. Figure S8 compares the posteriori distributions of noise amplitude with the preliminary estimates. Figure S9 inspects time series from other five cGNSS stations in Iceland for studying eventual velocity anomalies. Figure S10 inspects the velocity anomalies with campaign GNSS and Interferometric Synthetic Aperture Radar (InSAR) data. Tables S1 and S3 give technical details for data pre-processing and setting up Bayesian modeling. Table S2 provides the pre-processing results of the observed data. Table S4 and S5 list the Bayesian results from synthetics data experiments and with observed GNSS time series, respectively.

Text S1. Calculating the covariance matrix of PLN

The covariance matrix of PLN, $\mathbf{J}_\kappa$, is here calculated using the transform matrix $\mathbf{T}$, where

$$\mathbf{J}_\kappa = \mathbf{T}\mathbf{T}^T \tag{1}$$

$$\mathbf{T} = \Delta T^{-\kappa/4} \begin{bmatrix} \psi_0 & 0 & 0 & \cdots & 0 \\ \psi_1 & \psi_0 & 0 & \cdots & 0 \\ \psi_2 & \psi_1 & \psi_0 & \cdots & 0 \\ \vdots & \vdots & \vdots & \ddots & \vdots \\ \psi_n & \psi_{n-1} & \psi_{n-2} & \cdots & \psi_0 \end{bmatrix} \tag{2}$$

$$\psi_n = \frac{-\frac{\kappa}{2}\left(1-\frac{\kappa}{2}\right)\cdots\left(n-1-\frac{\kappa}{2}\right)}{n!} \tag{3}$$

and ΔT in the scaling factor is the sampling interval of the time series, following Williams (2003).

Text S2. GNSS solution strategies

The GNSS data processing was conducted at University of Iceland with the GAMIT/GLOBK 10.75 software (Herring et al., 2018). We only analyze the observations from Global Positioning System (GPS) data. The IGS final orbit, ocean tide model FES2004 (Lyard et al., 2006), and IGS ionosphere products were applied. The wet zenith tropospheric delays are corrected with Vienna Mapping Function (VMF1; Boehm et al., 2006). The corrections for solid and pole tides are applied. The elevation mask angle is set to 10°. The time series were derived in the IGb14/ITRF2014 reference frame (X, Y, Z; Altamimi et al., 2016), where global International GNSS Services (IGS) stations are referenced for the calculation of transformation parameters. Then the coordinates are converted to topocentric coordinate system (north, east, up). Although MYVA stations started recording in 2006, there are several data gaps more than half year and consequently the segment before epoch 2012.4358 at MYVA station are removed to avoid influence of data gaps.

Text S3. Synthetic data experiments on the effect of time span

The effect of time series span on the parameter estimations is discussed in the first paragraph in section 5 of the main text. This text describes the schemes for additional synthetic data experiments exploring this effect. The synthetic time series are generated with equation 4 in the main text. Here we adopt WN and FLN of 1 mm and 4 mm/yr$^{0.25}$, respectively, and velocity change value of -10 mm/yr, namely the low limit of velocity change for satisfactory results in section 3 of the main text. The synthetic time series spans 5 yr, from 2019 to 2024. The epoch of the break points is varied from 2020.25 to 2022.75 with an interval of 0.25 yr. The epochs before 2020.25 and after 2022.75 are not considered as their corresponding searching range would exceed the time series length. The preliminary estimate of break point is set to the true value plus 0.05 yr, similar to what done in section 3. We run 120,000 iterations for the synthetic series.

Text S4. Unit normalization of power-law noise amplitude

One can directly compare the noise amplitude estimates only if they are in the same unit, e.g., mm/yr$^{0.25}$ for flicker noise. However, as we keep the spectral index (κ) flexible in Bayesian modeling, the unit of power-law noise (PLN) amplitude (mm/yr$^{\kappa/4}$) changes with κ, making the amplitudes not directly comparable if the units change. Therefore, a modification for unit normalization is applied, following Gobron et al. (2021), before the comparison in Figure S6:

$$\beta' = \beta \sqrt{\frac{1}{L}\mathrm{tr}(\mathbf{J}_\kappa) - \frac{1}{L^2}\mathbf{u}^T\mathbf{J}_\kappa\mathbf{u}} \tag{4}$$

where β' represents the modified amplitude. L is the number of epochs in the time series and $\mathbf{u}$ is a column vector with all the elements being 1. $\mathrm{tr}(\mathbf{J}_\kappa)$ indicates the trace of covariance matrix $\mathbf{J}_\kappa$. The unit of modified amplitude is normalized to mm.

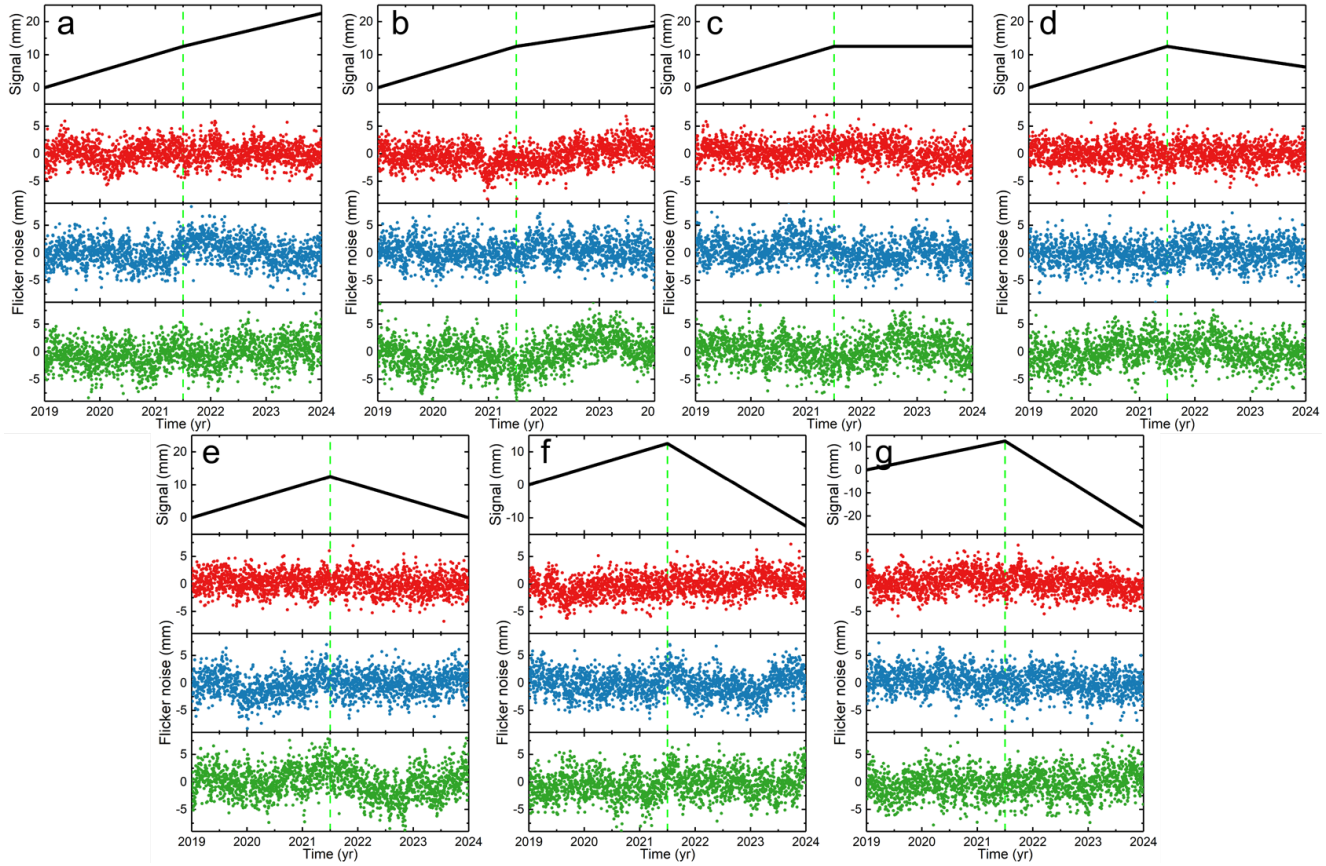
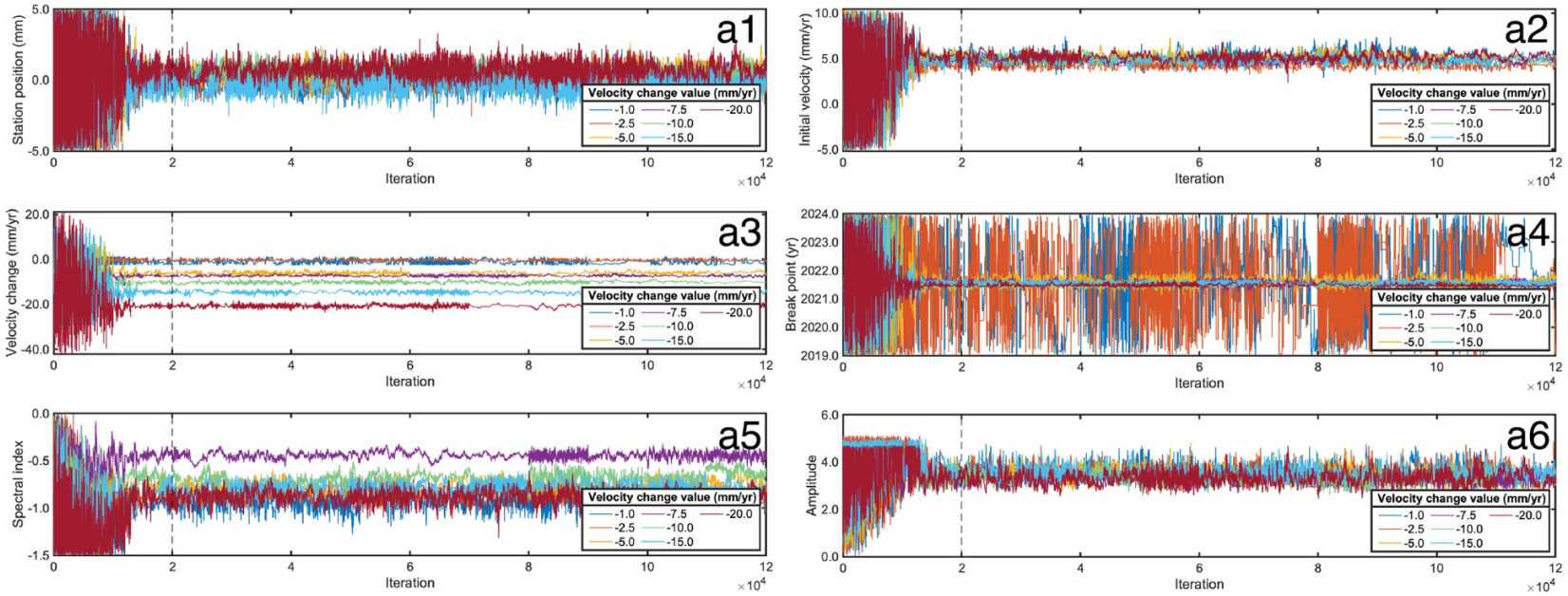
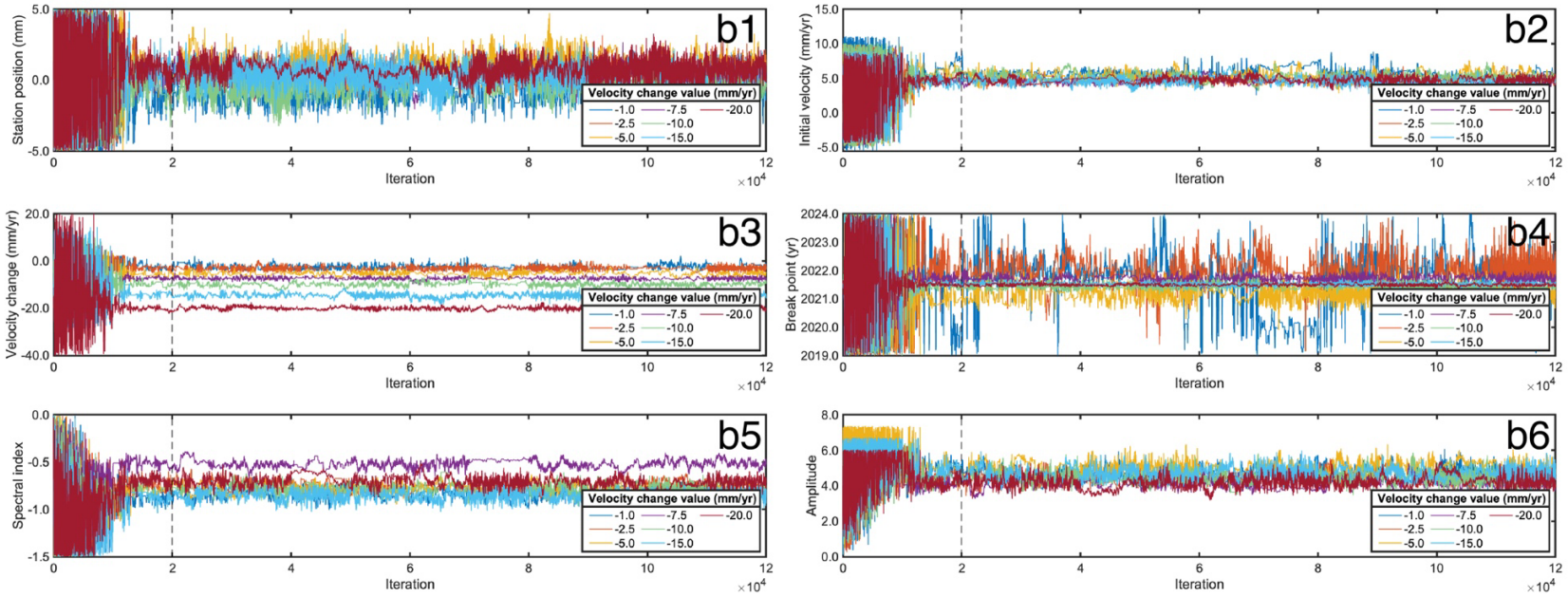


Figure S1. Simulated time series with velocity change (signal) and flicker noise series in the synthetic data experiments. Figure S1a to S1g correspond to velocity change value of -1.0, -2.5, -5.0, -7.5, -10.0, -15.0, and -20.0 mm/yr, respectively. The red, blue and green dots correspond to the flicker noise with amplitudes of 3.0, 4.0, and 5.0 mm/yr$^{0.25}$, that is added to the simulated signals (black dots). The flicker noise series are generated by multiplying the covariance matrix in equation 3 and a white noise series with amplitude of 1 mm. The light-green vertical dashed line indicates the true break point. All the noise series include a white noise series with amplitude of 1 mm.


a1
Station position (mm)
Iteration
×10^4
a2
Initial velocity (mm/yr)
Iteration
×10^4
a3
Velocity change (mm/yr)
Iteration
×10^4
a4
Break point (yr)
Iteration
×10^4
a5
Spectral index
Iteration
×10^4
a6
Amplitude
Iteration
×10^4
Velocity change value (mm/yr)
-1.0
-2.5
-5.0
-7.5
-10.0
-15.0
-20.0


b1
Station position (mm)
Iteration
b2
Initial velocity (mm/yr)
Iteration
b3
Velocity change (mm/yr)
Iteration
b4
Break point (yr)
Iteration
b5
Spectral index
Iteration
b6
Amplitude
Iteration
Velocity change value (mm/yr)
-1.0
-2.5
-5.0
-7.5
-10.0
-15.0
-20.0
×10^4

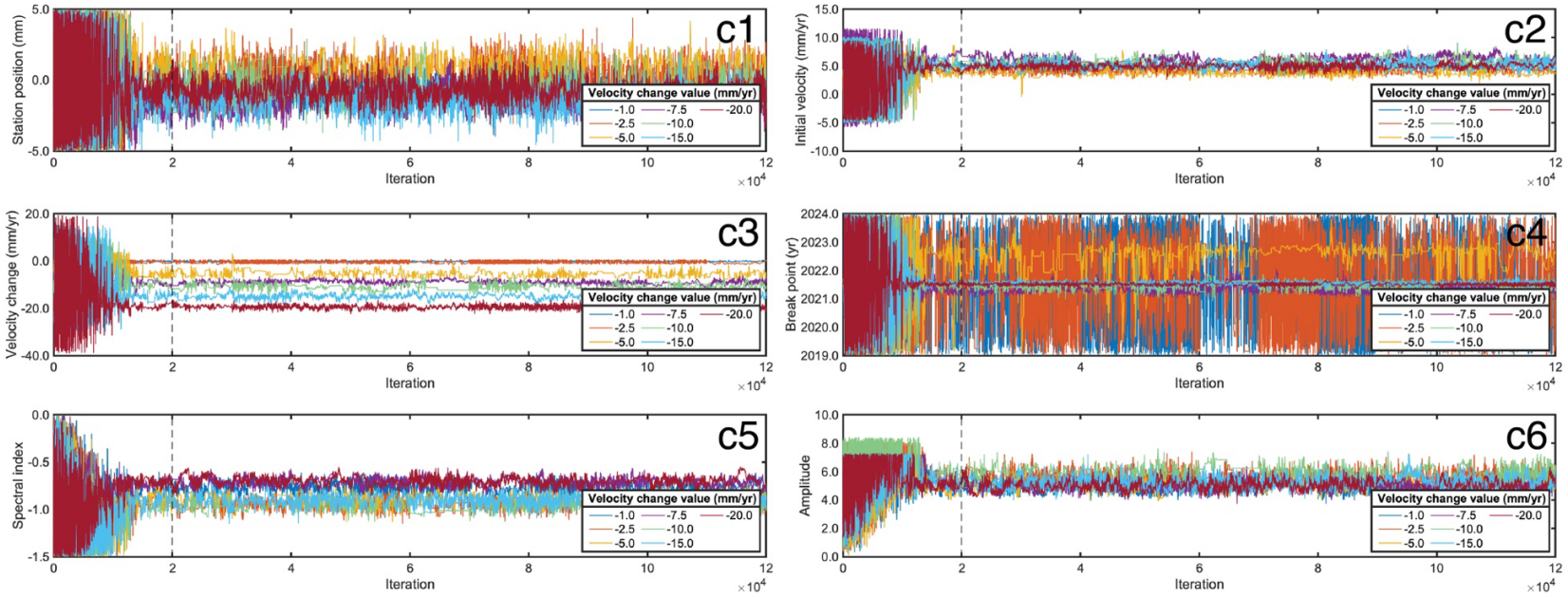


Figure S2. The convergence of Markov chain (trace plots) for the parameters in synthetic data experiments. (a1)-(a6), (b1)-(b6) and (c1)-(c6) show the trace plots when flicker noise amplitude equals 3, 4 and 5 mm/yr$^{0.25}$, respectively. (a1), (b1) and (c1) show the trace plots for station position (the residual intercept in equation 4). (a2), (b2) and (c2) show the trace plots for initial velocity. (a3), (b3) and (c3) show the trace plots for velocity change. (a4), (b4) and (c4) show the trace plots for break point. (a5), (b5) and (c5) show the trace plots for spectral index. (a6), (b6) and (c6) show the trace plots for power-law noise amplitude (unit: mm/yr$^{\kappa/4}$, dependent on the spectral index κ). The vertical dashed line is the suggested iterations before convergence (burn-in period), which is 20000 iterations in this study.

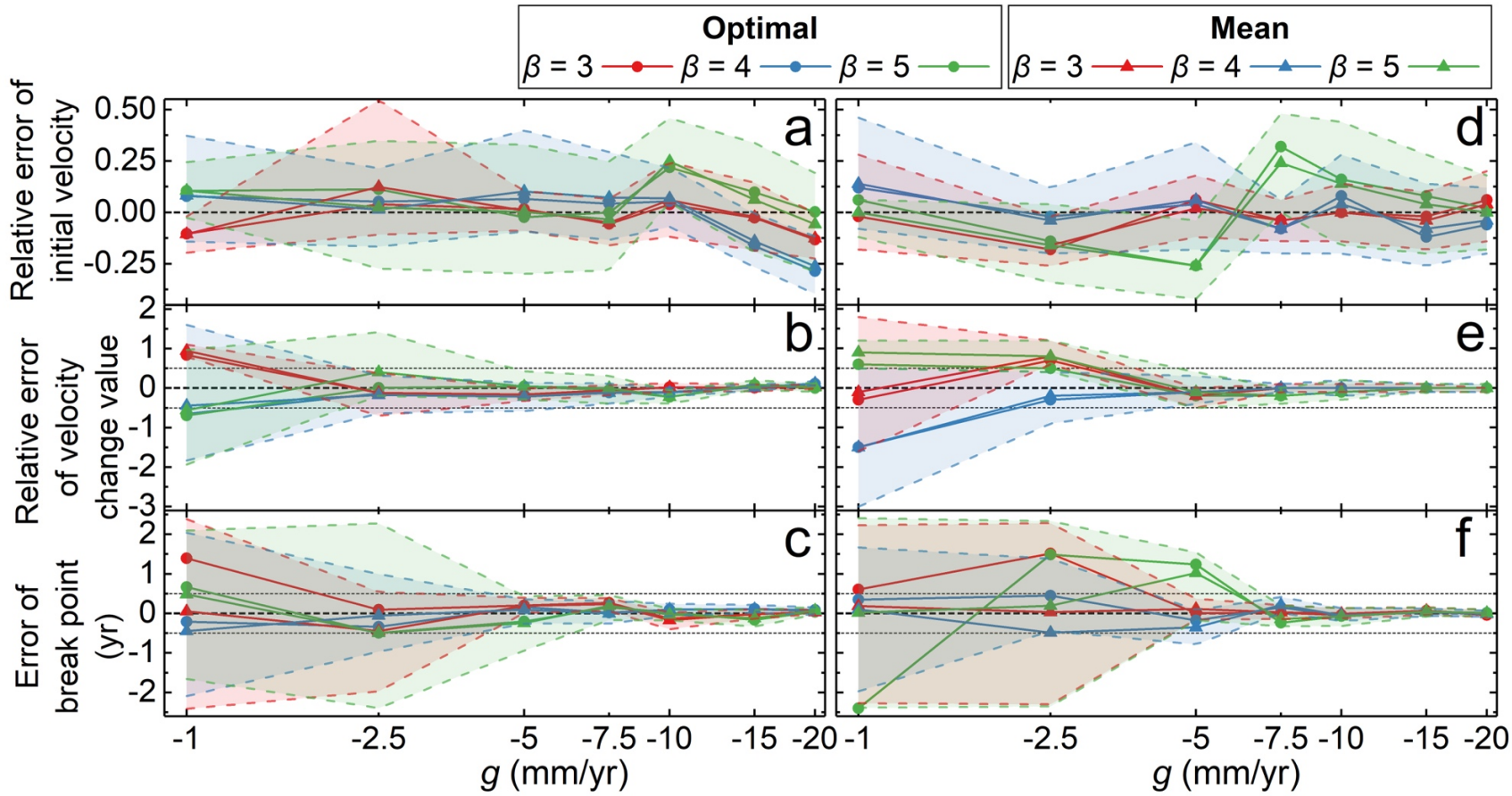
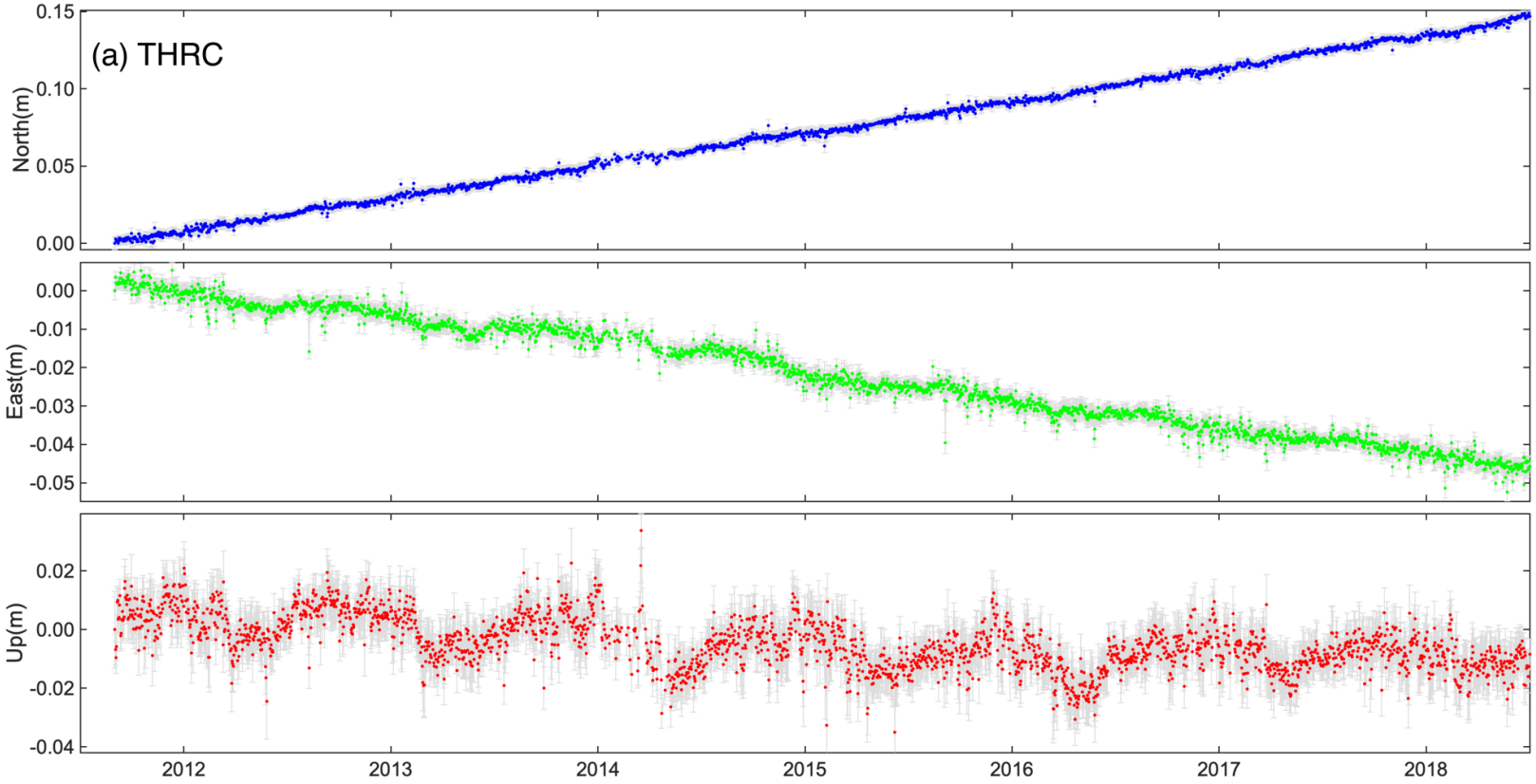
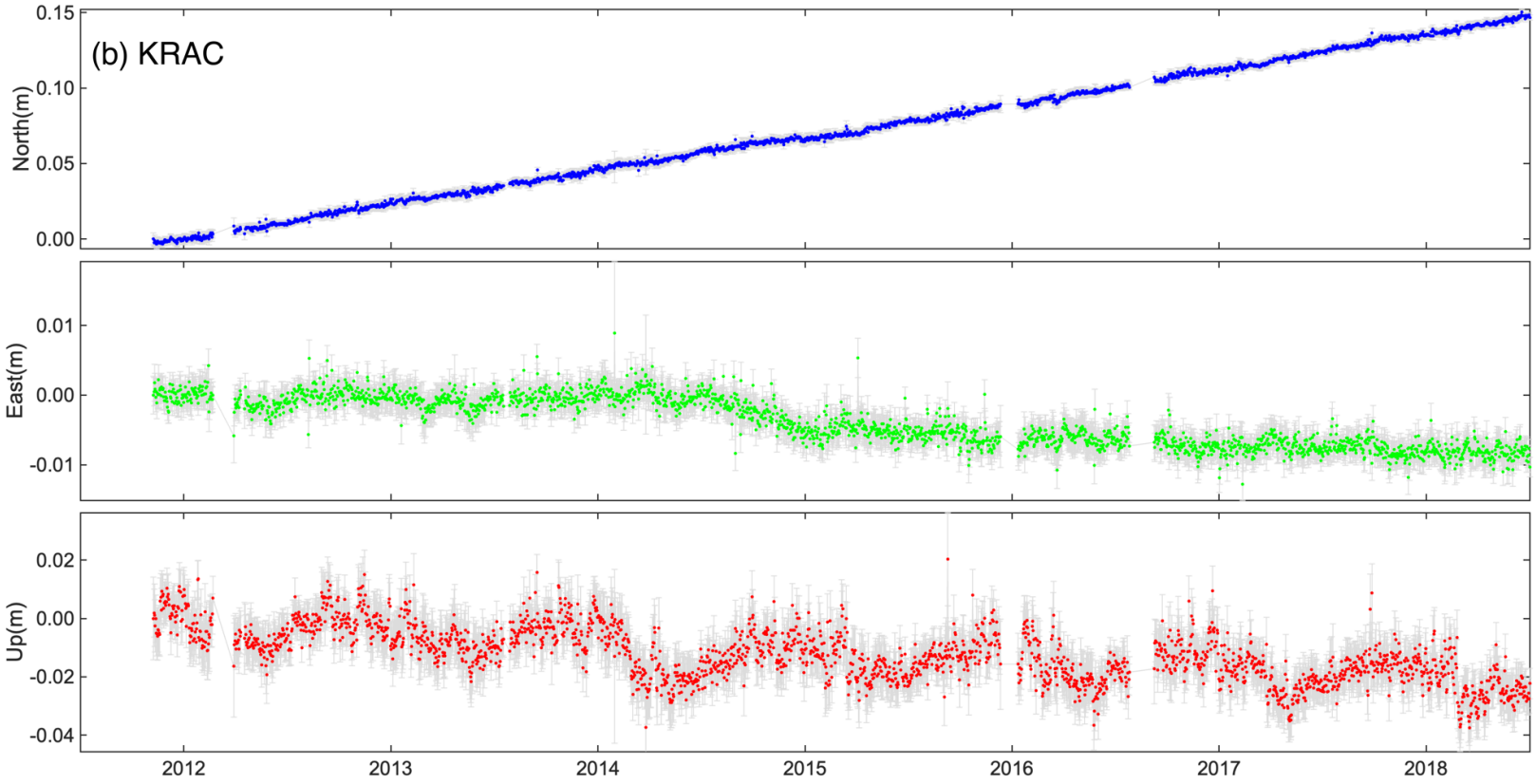
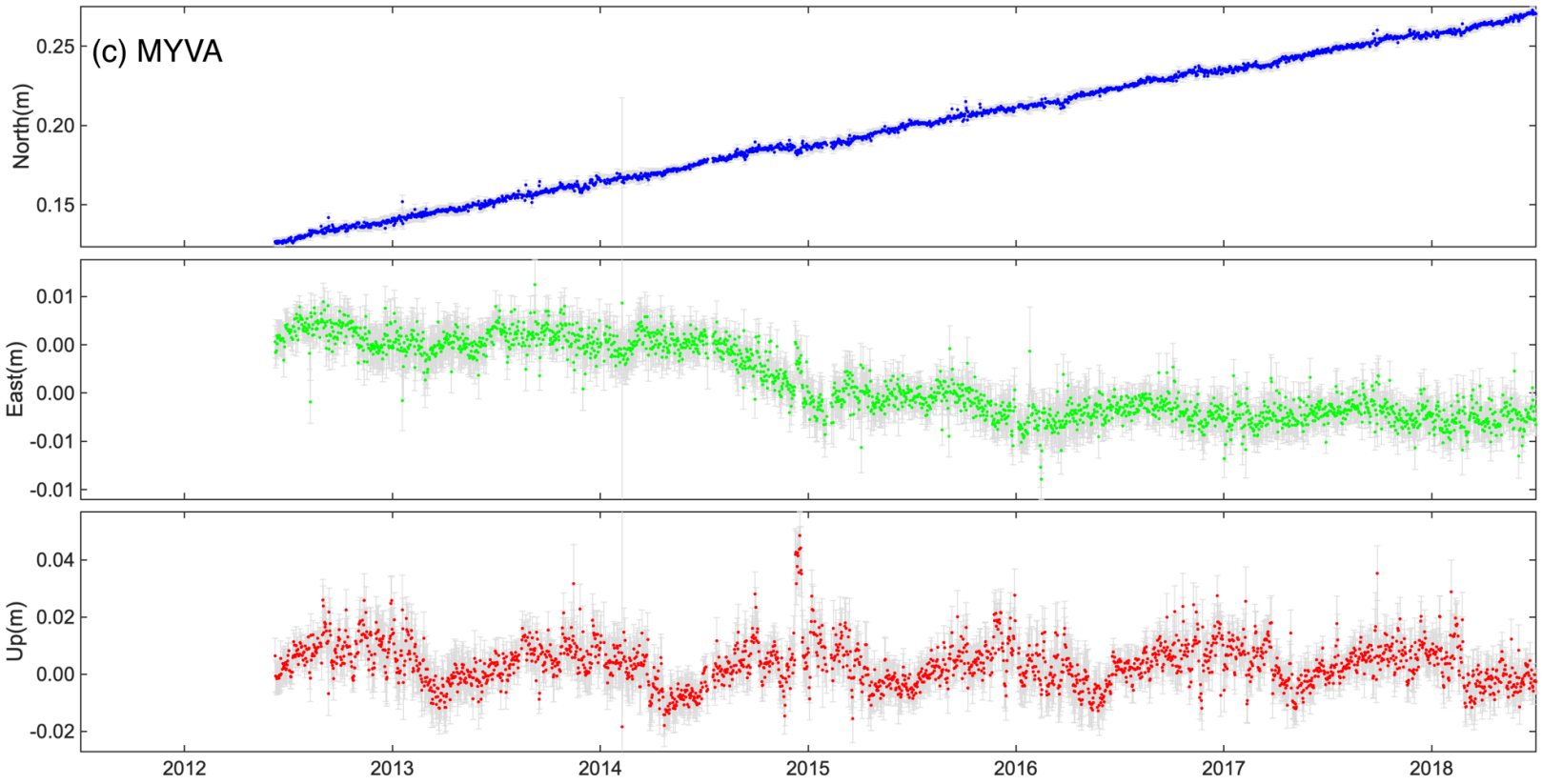


Figure S3. The estimation errors and uncertainties of synthetic data experiments. (a)-(c) the results from the synthetic data experiments with another set of noise series than Figure 3d-3f. (d)-(f) Same as Figure 3d-3f. The errors are usually the difference between the estimates and the true values, while the relative errors are the differences between the estimates and true values divided by the true values. The horizontal axes are with a logarithmic scale. The small uncertainty of the leftmost red data points in Figure S3b is caused by the rather narrow searching range, where a similarly large uncertainty as Figure S3e should be obtained after adjusting the search range.


(a) THRC
North(m)
East(m)
Up(m)
0.15
0.10
0.05
0.00
-0.01
-0.02
-0.03
-0.04
-0.05
0.02
2012
2013
2014
2015
2016
2017
2018


(b) KRAC
North(m)
East(m)
Up(m)
0.15
0.10
0.05
0.00
0.01
0.00
-0.01
0.02
0.00
-0.02
-0.04
2012
2013
2014
2015
2016
2017
2018


(c) MYVA
North(m)
0.25
0.20
0.15
East(m)
0.01
0.00
0.00
-0.01
-0.01
Up(m)
0.04
0.02
0.00
-0.02
2012
2013
2014
2015
2016
2017
2018

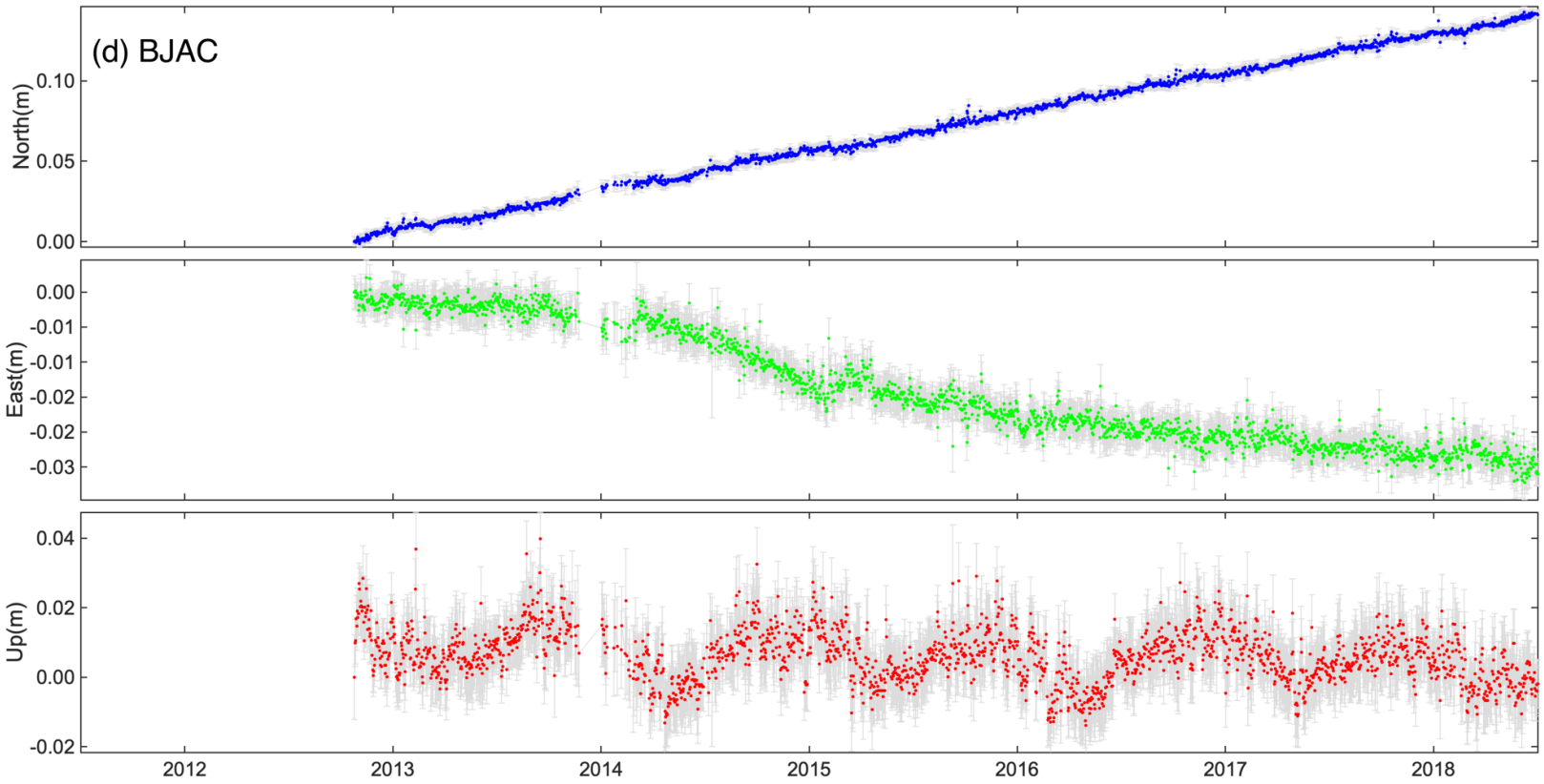
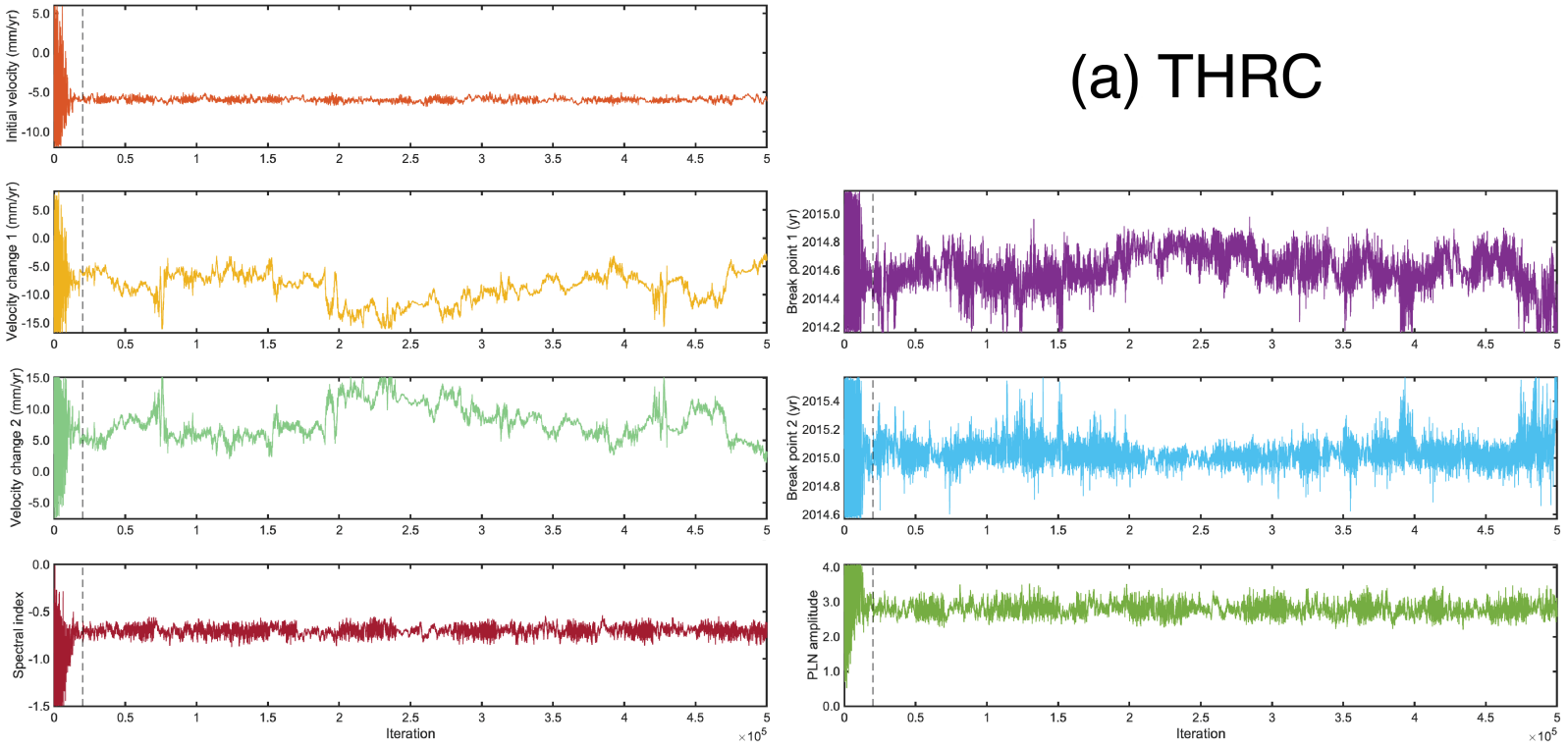
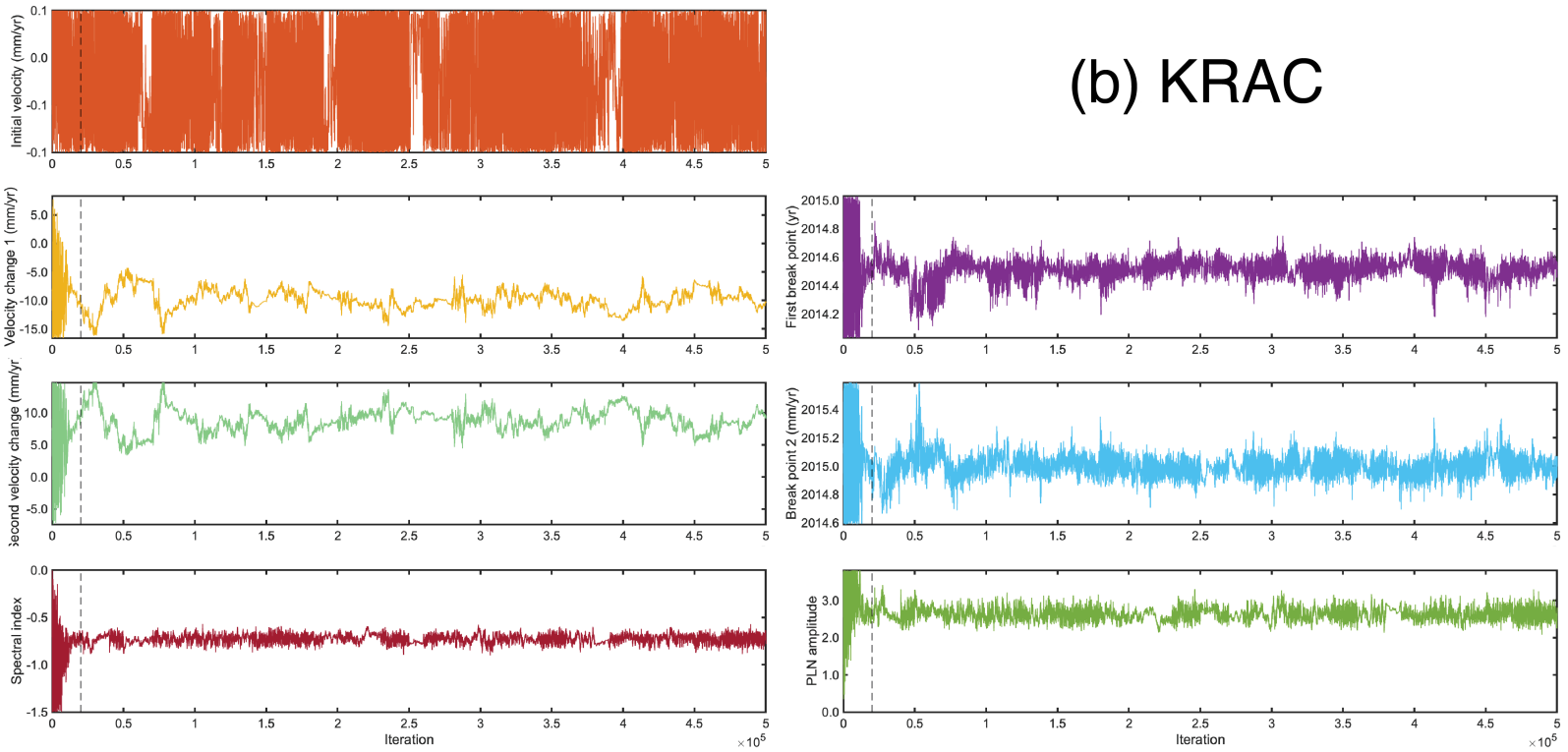


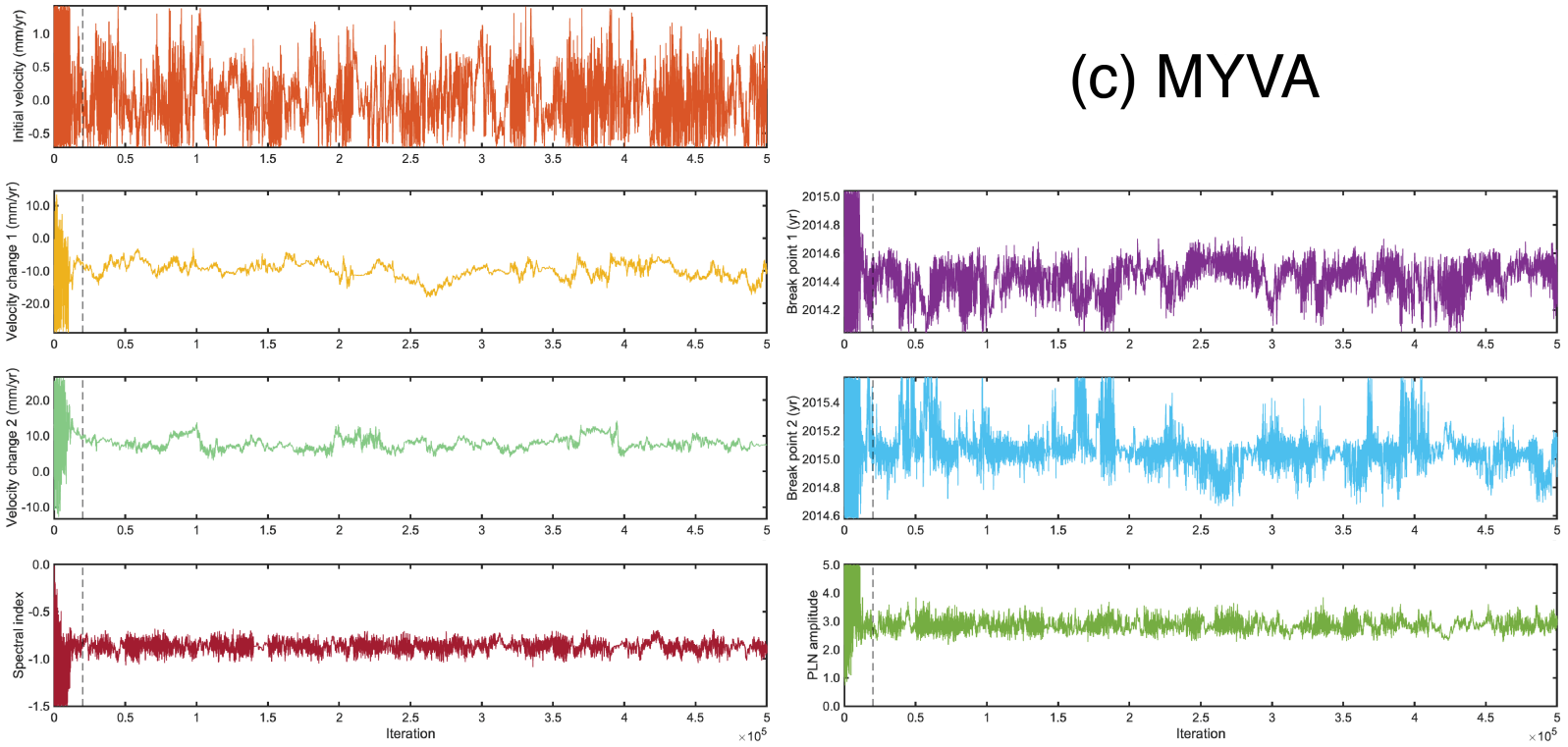
Figure S4. Raw GNSS coordinate time series at the four cGNSS stations at Krafla and Þeistareykir. The dots indicate the coordinates and the gray lines indicate their uncertainties. The GNSS time series are relative to ITRF2014/IGb14 (Altammimi et al., 2016). The subplots show the raw GNSS time series from THRC (a), KRAC (b), MYVA (c) and BJAC (d) stations. The three panels in each subplot display raw GNSS time series in north (blue), east (green) and up (red) components from top to bottom, respectively.


Initial velocity (mm/yr)
Velocity change 1 (mm/yr)
Velocity change 2 (mm/yr)
Spectral index
Break point 1 (yr)
Break point 2 (yr)
PLN amplitude
Iteration
×10^5

(a) THRC


Initial velocity (mm/yr)
Velocity change 1 (mm/yr)
First break point (yr)
Second velocity change (mm/yr
Break point 2 (mm/yr)
Spectral index
PLN amplitude
Iteration
Iteration
×10^5
×10^5

(b) KRAC


Initial velocity (mm/yr)
Velocity change 1 (mm/yr)
Velocity change 2 (mm/yr)
Spectral index
Break point 1 (yr)
Break point 2 (yr)
PLN amplitude
Iteration
×10^5

(c) MYVA

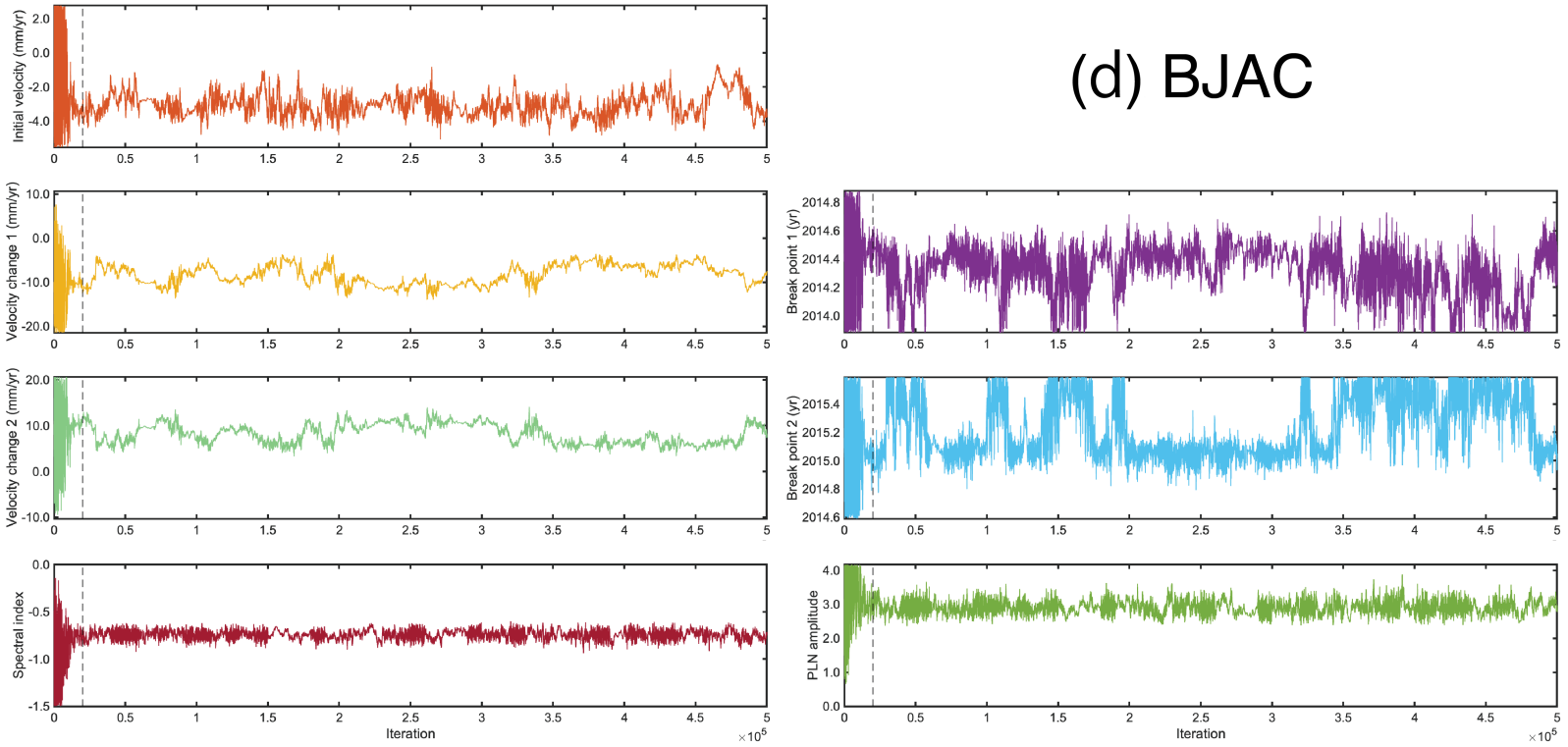
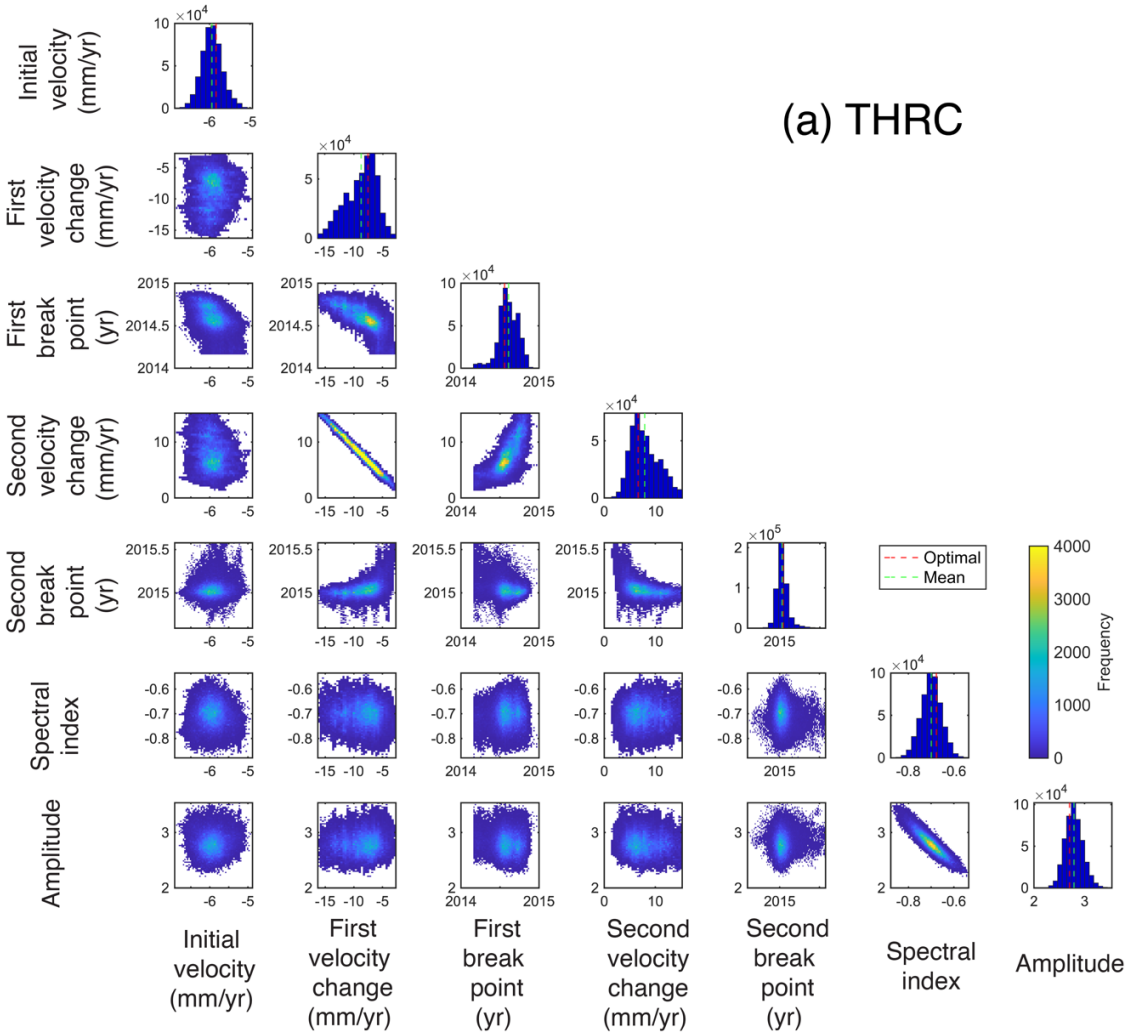
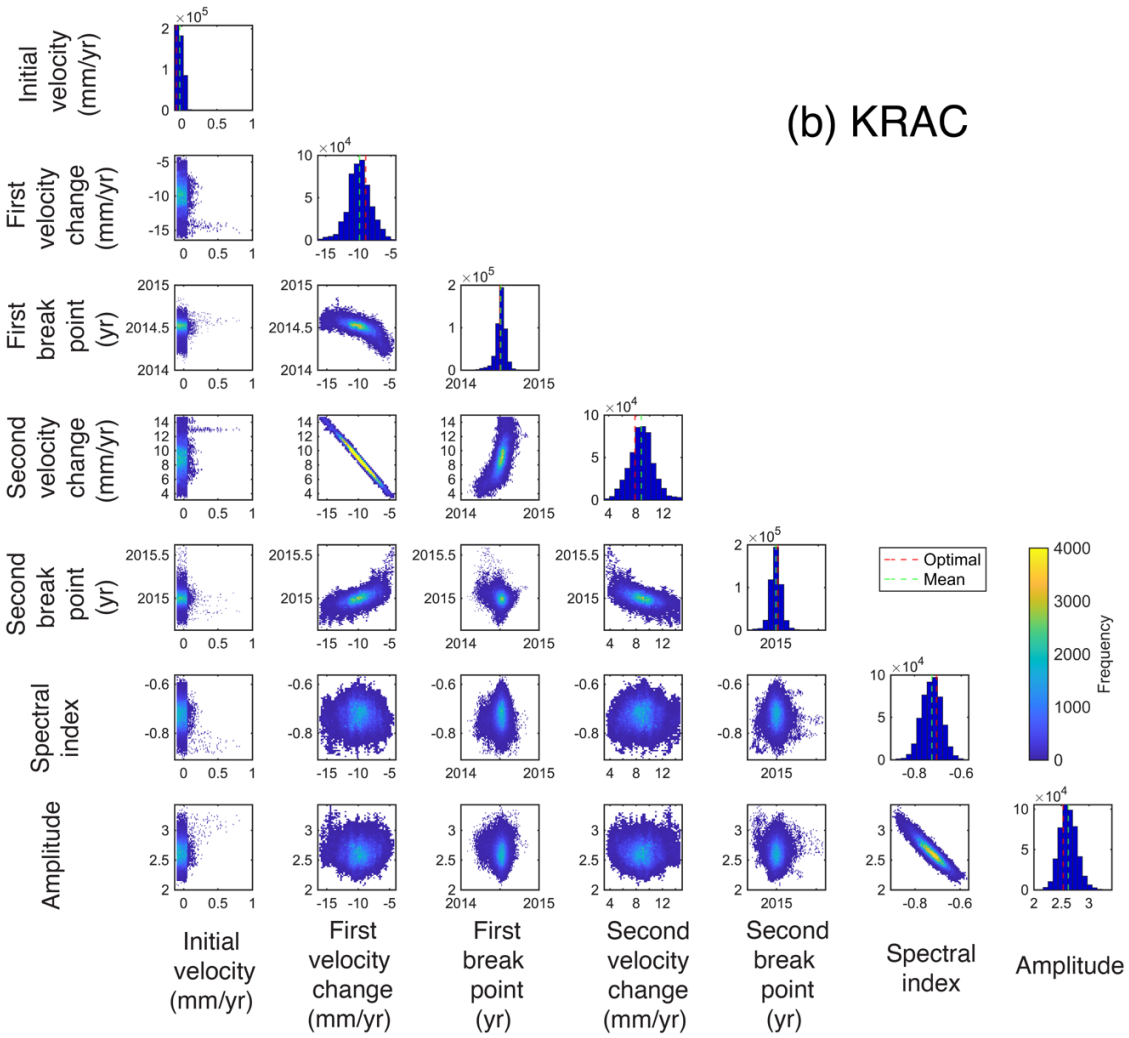
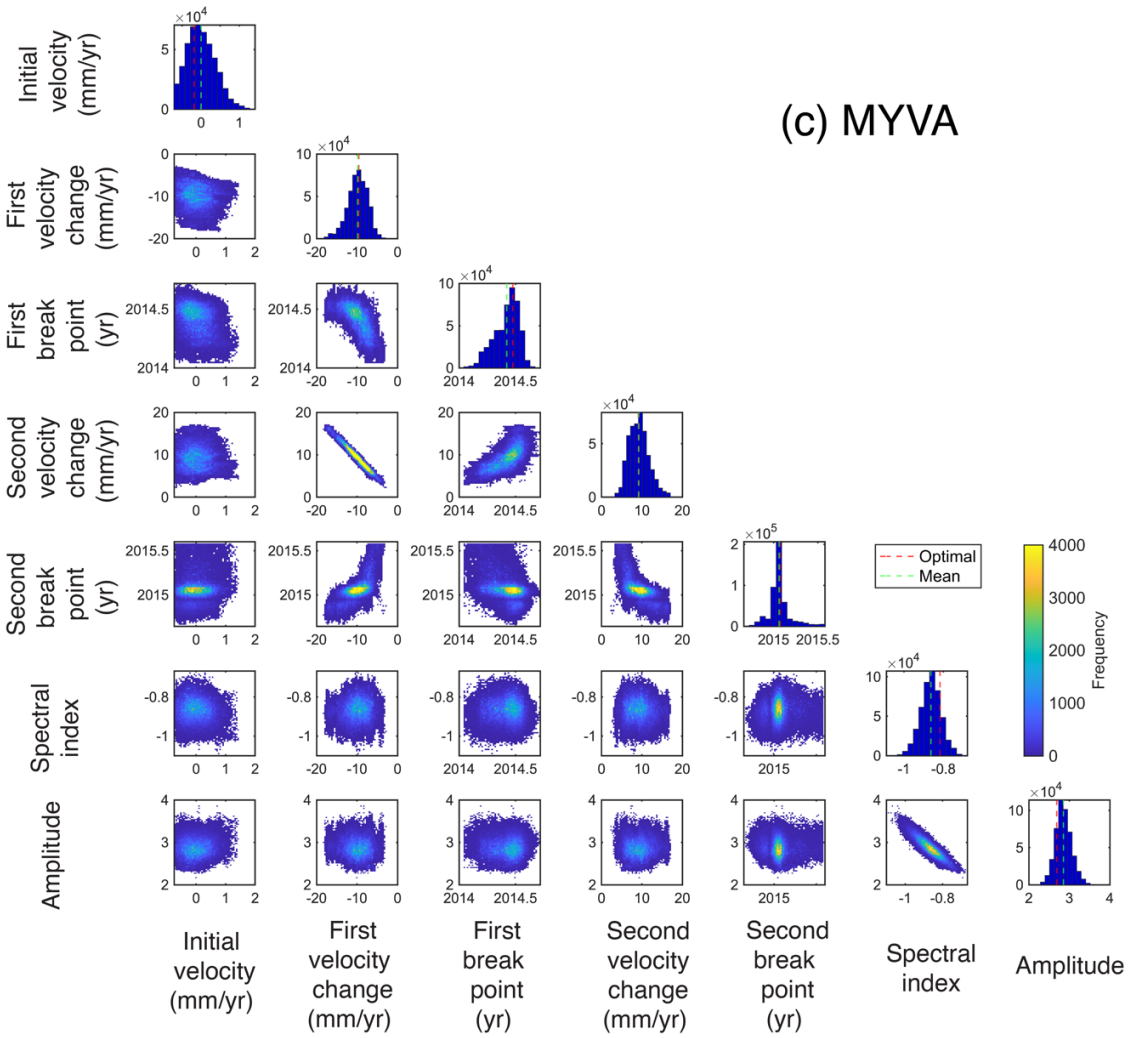


Figure S5. Trace plots of inferred model parameters from observed time series in the Krafla and Þeistareykir area. The left panels in each subplot display the trace plots of initial velocity, first velocity change, second velocity change and spectral index, from top to bottom, respectively. The right panels in each subplot display the trace plots of first break point, second break point, and power-law noise (PLN) amplitude from top to bottom, respectively. The unit of the PLN amplitude is mm/yr$^{\kappa/4}$, dependent on the spectral index κ. The vertical grey dashed lines indicate the suggested iteration number before convergence (burn-in period) and the parameters from the burn-in period are excluded in further results. In Figure S3c, although the trace plot of initial velocity does not convergence in the searching range, it should be noted that the initial velocity is rather close to zero and the search range is only 0.2 mm/yr. The results converge according to other trace plots.


(a) THRC
Initial velocity (mm/yr)
First velocity change (mm/yr)
First break point (yr)
Second velocity change (mm/yr)
Second break point (yr)
Spectral index
Amplitude
Optimal
Mean
Frequency
4000
3000
2000
1000
0


(b) KRAC
Initial velocity (mm/yr)
First velocity change (mm/yr)
First break point (yr)
Second velocity change (mm/yr)
Second break point (yr)
Spectral index
Amplitude
Optimal
Mean
Frequency
Initial velocity (mm/yr)
First velocity change (mm/yr)
First break point (yr)
Second velocity change (mm/yr)
Second break point (yr)
Spectral index
Amplitude


(c) MYVA
Initial velocity (mm/yr)
First velocity change (mm/yr)
First break point (yr)
Second velocity change (mm/yr)
Second break point (yr)
Spectral index
Amplitude
Optimal
Mean
Frequency

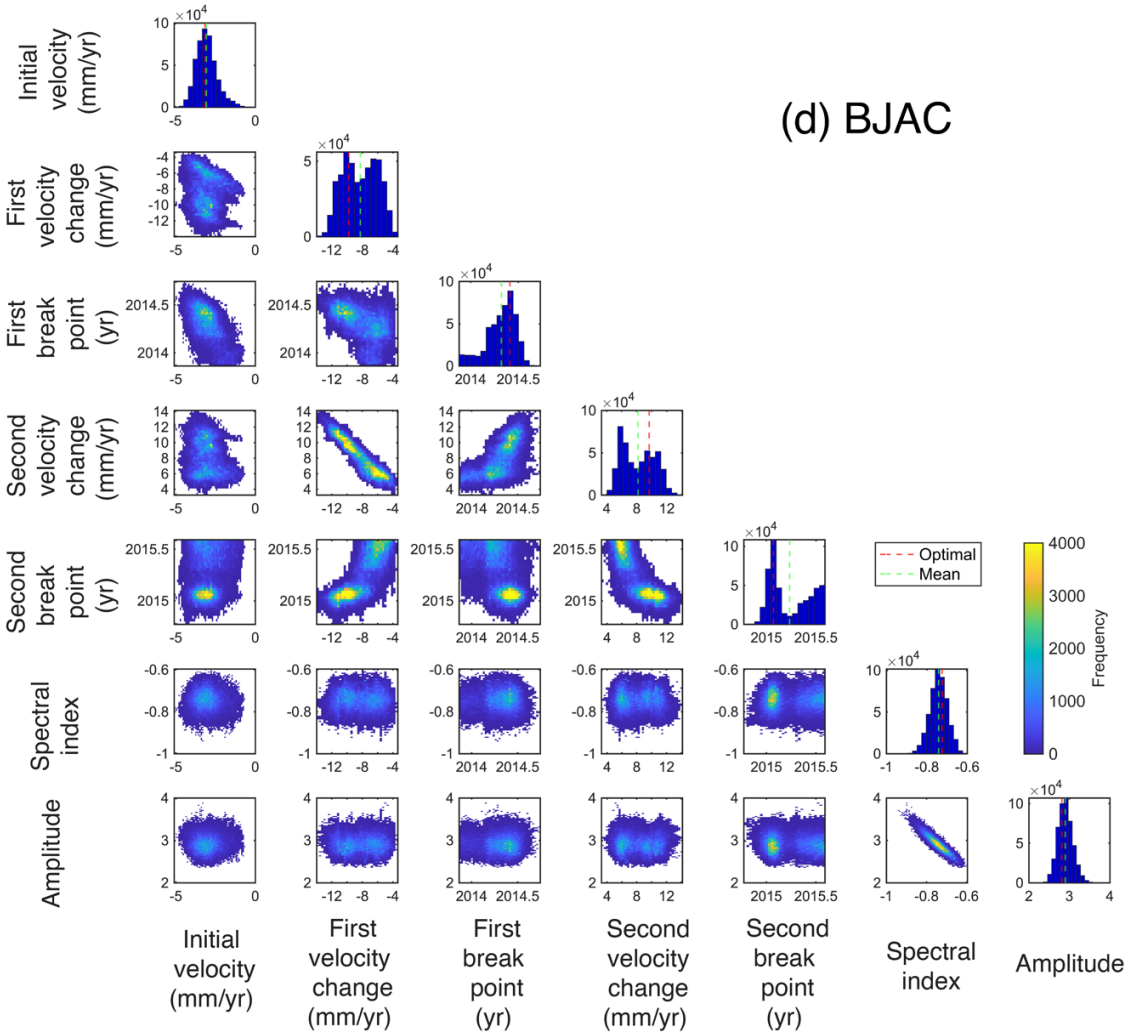


Figure S6. Marginal posterior probability distributions (PDs) of the parameters from observed time series in the Krafla and Þeistareykir area. The diagonal subplots show the PDs of single parameter, and the non-diagonal ones show the joint PDs of two parameters. The color contours indicate the frequency. Amplitude indicates the PLN amplitude (unit: $mm/yr^{\kappa/4}$, dependent on the spectral index κ). The parameters from the burn-in period are excluded. The residual intercept of equation 4 in the main text is estimated but not displayed here as it approaches zero and loses physical meaning after pre-processing.

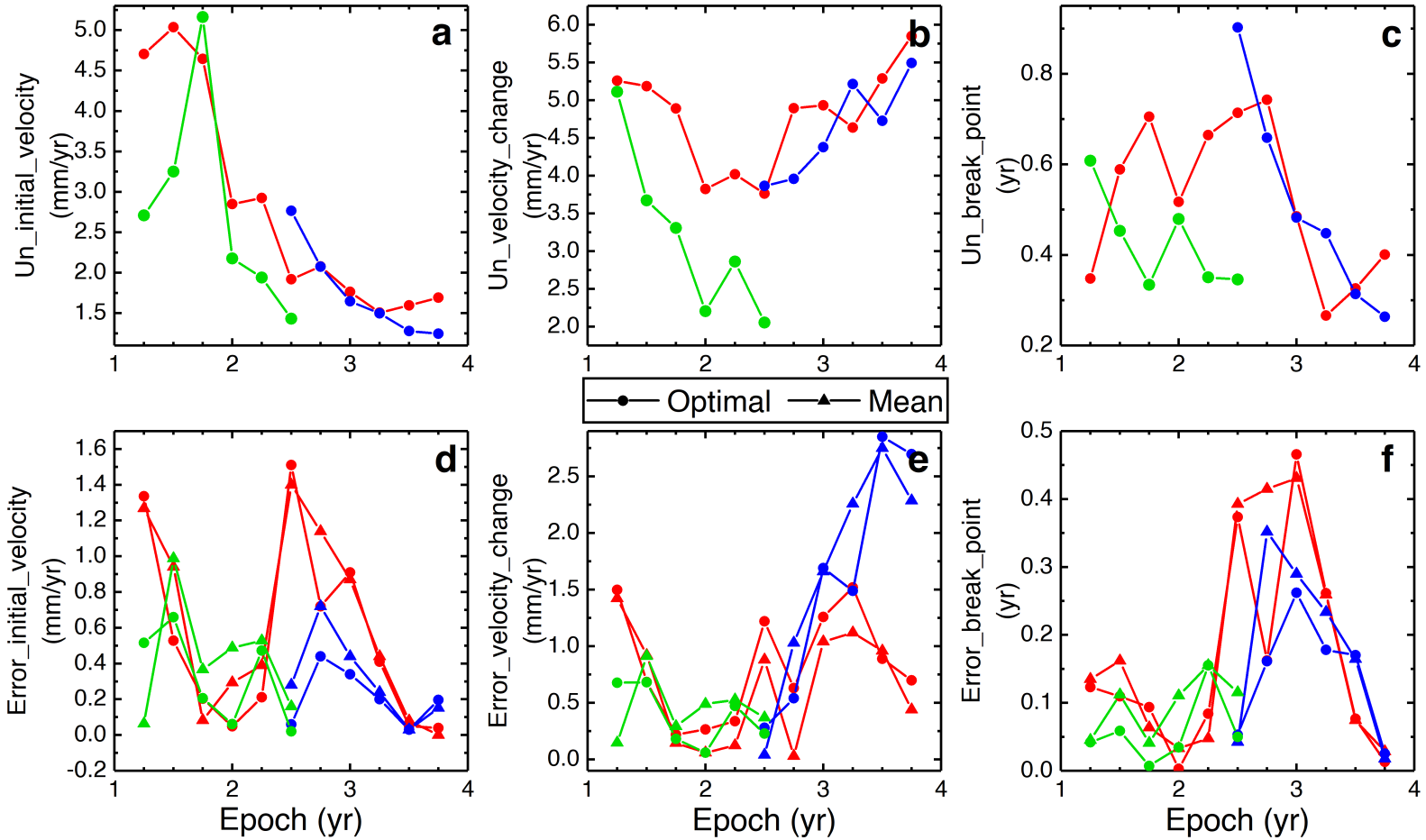


Figure S7. Additional synthetic data experiments with a single break point at different epochs. (a-c) The uncertainties (Un) of initial velocity (a), velocity change (b) and break point (c). (d-f) The estimations errors (Error) of initial velocity (a), velocity change (b) and break point (c). The estimation errors here are the absolute differences between the estimates and the true values. Different colors indicate different sets of noise series generated.

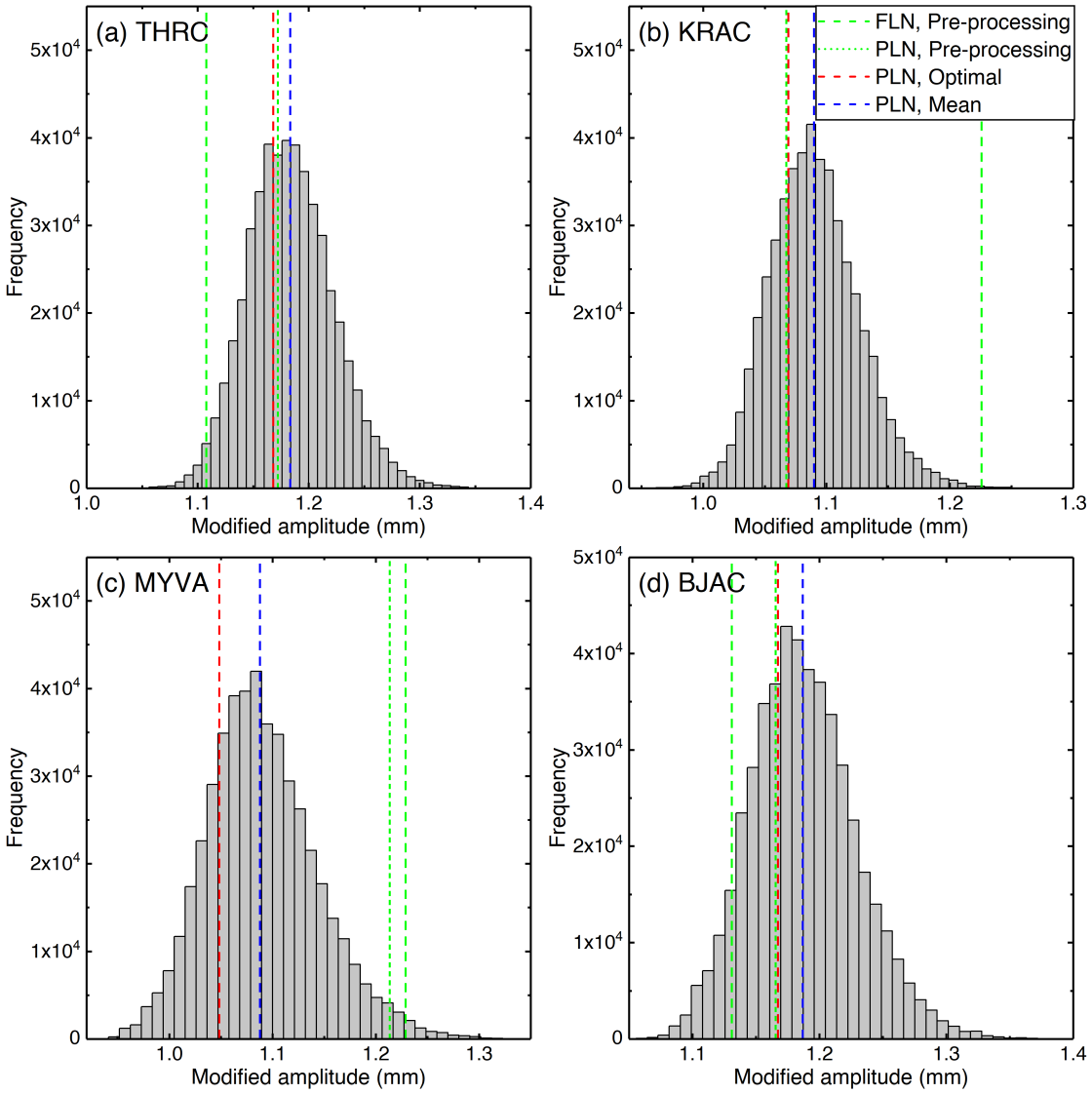


Figure S8. The modified PLN amplitude of observed time series. The histogram showing the posterior distribution of modified PLN amplitude realized by the Bayesian modeling. The green, red and blue vertical lines indicate the noise amplitude derived from pre-processing (Pre-processing), the optimal estimates (Optimal) and the mean estimates (Mean) in the Bayesian estimation, respectively. FLN represents the flicker noise model used in the pre-processing (spectral index of -1) and PLN represents the power-law noise model is used in the Bayesian estimation (spectral index is kept flexible). Detail of the modification of amplitudes is in Text S4.

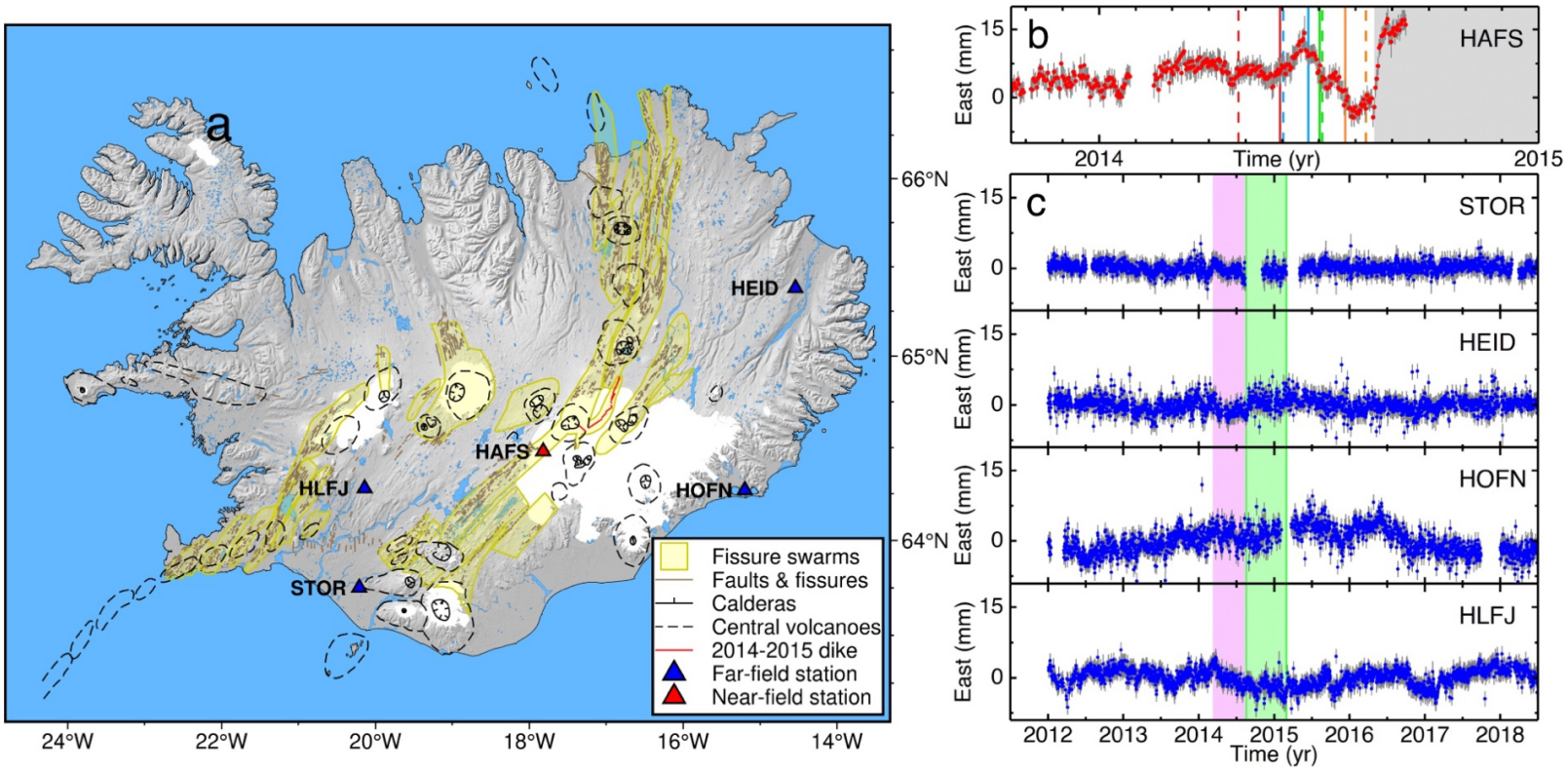


Figure S9. (a) The locations of four far-field cGNSS stations (110-150 km) and a near-field station (23 km) from Bárðarbunga. The geological features are from Jóhannesson & Sæmundsson (2009). B: Bárðarbunga. (b) Detrended time series (red dots) at the near-field station showing similar velocity anomalies before the onset of 2014 Bárðarbunga dike intrusion. The gray lines indicate the uncertainties. The vertical solid and dashed lines indicate the optimal and mean estimates of the first break point, respectively, with their colors indicating the four cGNSS stations as in Figure 4. (c) Detrended time series (blue dots) at the far-field stations showing no similar change before the onset of 2014 Bárðarbunga dike intrusion. The green-shaded area indicates the Bárðarbunga dike and eruption period and the purple-shaded area indicate the break point uncertainty from the three cGNSS stations at Krafla. The linear trend, annual and semi-annual signals are estimated with weighted least square method and removed.

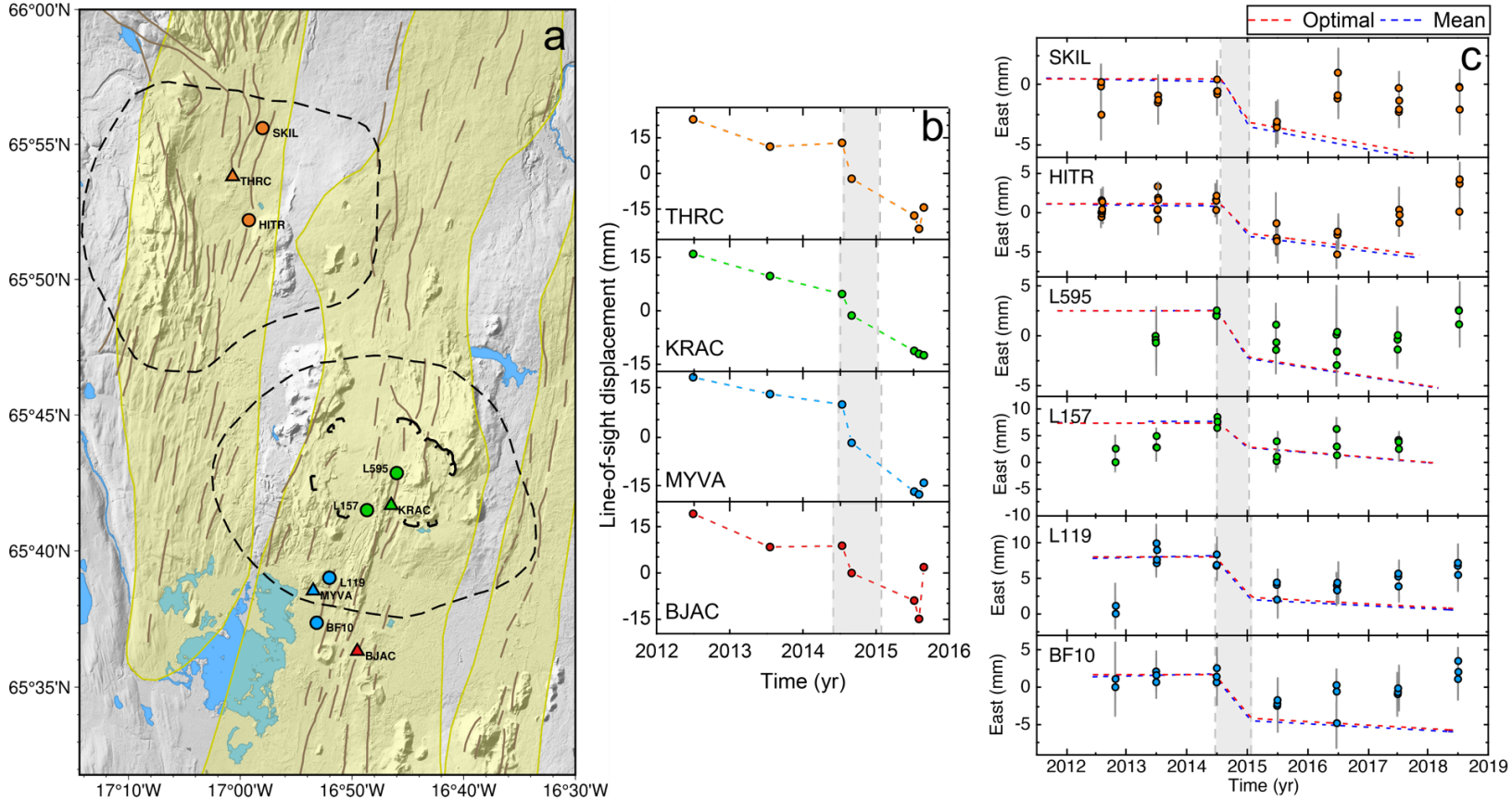


Figure S10. (a) The location of selected campaign GNSS stations (circles) and cGNSS stations (triangles). The colors of circles indicate the nearest cGNSS station (same as in Figure 4). The geological features are from Jóhannesson & Sæmundsson (2009). (b) Averaged InSAR line-of-sight displacements of the pixels nearest to the cGNSS stations with Radarsat-2 mission (Drouin et al., 2017). The nearest four pixels are used for the averaging. (c) Detrended time series at selected campaign GNSS stations. The grey lines indicate the uncertainties. The red and blue dashed lines are the function form of their nearest cGNSS stations (as in Figure 3), with the grey shaded areas being the period of velocity anomalies.

Table S1. Data pre-processing procedure and possible methods.

Procedures[1]	Methods
Outlier removal	Inter-quartile range (IQR) criteria (Nikolaidis, 2002); median absolute deviation (MAD) criteria (Leys et al., 2013)
Step and break point detection	Eye-detection (Gazeaux et al., 2013)
Preliminary estimation of the parameters[2]	Weighted least square estimation
Evaluation of noise parameters	Maximum likelihood estimation (Bos et al., 2013); Allen variance (Hackle et al., 2011)

[1] The outlier removal and step detection can be implemented iteratively for better performance.

[2] The estimation and removal of periodic signals should be implemented carefully to avoid introducing artificial signals.

Table S2. Pre-processing results of the observed GNSS time series. The break points are detected with east-component time series. The FLN and PLN are not assessed simultaneously, and the PLN model are not estimated for north and east components.

Station	Component	Initial velocity (mm/yr)	Velocity change 1 (mm/yr)	Break point 1 (yr)	Velocity change 2 (mm/yr)	Break point 2 (yr)	WN amplitude (mm)	FLN amplitude (mm/yr0.25)	Spectral index κ	PLN amplitude (mm/yrκ)
THRC	N	21.3	-4.5	2014.6600	4.8	2015.0700	0.8	3.5	/	/
	E	-6.0	-8.4		7.6		1.1	3.0	-0.7	2.7
	U	-3.8	-3.8		7.6		0.0	19.4	/	/
KRAC	N	23.1	-6.2	2014.5300	6.5	2015.0900	0.7	3.4		
	E	-0.1	-8.3		7.4		0.8	3.3	-0.7	2.5
	U	-5.0	5.7		-3.2		0.6	17.7	/	/
MYVA	N	24.4	-1.4	2014.5400	0.7	2015.0800	0.7	3.4	/	/
	E	0.7	-14.5		13.3		0.8	3.4	-0.8	3.1
	U	-3.4	7.8		-4.0		0.0	19.4	/	/
BJAC	N	25.2	-1.0	2014.3800	0.3	2015.0900	0.7	4.0	/	/
	E	-2.8	-10.7		10.3		0.9	3.1	-0.7	2.8
	U	-2.3	2.3		-0.7		0.0	19.3	/	/

Table S3. Suggested searching range of the parameters in this study, corresponding to equation 4 in the main text. The search range can be modified to take different conditions of data and users' interests into account.

Parameter[1]	Lower limit	Higher limit[4]
Station position a' (mm)	-5	5
Initial velocity b (mm/yr)	-$\hat{b}$	2$\hat{b}$
Velocity change g (mm/yr)	-$\hat{g}$	2$\hat{g}$
Break point[2] t_k (yr)	$\widehat{t_k}$-1	$\widehat{t_k}$+1
Spectral index[3] κ	-1.5	0
PLN amplitude β (mm/yr$^{\kappa/4}$)	0	1.5$\hat{\beta}$

[1] The parameters with hat operator represent their preliminary estimates from pre-processing.
[2] In the case with two break points, the searching range is changed to $\widehat{t_k}$-0.5 to $\widehat{t_k}$+0.5. The search ranges in synthetic data experiments are extended to the whole time spans of the time series.
[3] This lower limit is set as WN+FLN can represent the noise characteristics well at all four stations in the studied area.
[4] For negative values of initial velocities and velocity changes, the higher and lower limits should be reversed.

Table S4. The results of synthetic data experiments. 95%-low: lower limit of the 95% confidence interval. Optimal: the optimal estimate. Mean: the mean estimate. 95%-high: higher limit of the 95% confidence interval.

Schemes		/	Estimates				
FLN amplitude ($mm/yr^{0.25}$)	Velocity change (mm/yr)	/	Initial velocity (mm/yr)	Velocity change (mm/yr)	Break point (yr)	Spectral index κ	PLN amplitude (mm/yr^{κ})
3	1	95%-low	4.1	-2.6	2019.2319	-1.1	3.0
		optimal	4.9	-1.3	2022.1068	-0.9	3.4
		mean	5.0	-1.1	2021.6919	-0.9	3.6
		95%-high	6.4	0.8	2023.7267	-0.8	4.2
	2.5	95%-low	3.7	-1.0	2019.2028	-1.0	3.0
		optimal	4.1	-0.8	2023.0132	-0.8	3.4
		mean	4.2	-0.4	2021.5341	-0.8	3.6
		95%-high	4.9	0.4	2023.7811	-0.7	4.2
	5	95%-low	4.4	-7.3	2021.3467	-0.9	2.9
		optimal	5.3	-6.2	2021.5035	-0.7	3.2
		mean	5.1	-6.1	2021.6173	-0.8	3.4
		95%-high	5.9	-4.9	2021.8793	-0.7	3.9
	7.5	95%-low	4.3	-8.0	2021.3584	-0.5	2.9
		optimal	4.8	-7.5	2021.5186	-0.4	3.1
		mean	4.8	-7.3	2021.5293	-0.4	3.2
		95%-high	5.3	-6.6	2021.7079	-0.4	3.7
	10	95%-low	4.3	-11.3	2021.3767	-0.8	2.8
		optimal	5.0	-10.2	2021.4615	-0.7	3.2
		mean	5.0	-10.2	2021.4912	-0.7	3.3
		95%-high	5.7	-9.2	2021.6333	-0.6	3.9
	15	95%-low	4.1	-15.8	2021.4580	-0.9	3.1
		optimal	4.9	-14.7	2021.5696	-0.8	3.4
		mean	4.8	-14.7	2021.5699	-0.8	3.5
		95%-high	5.5	-13.5	2021.6550	-0.7	4.1
	20	95%-low	4.3	-22.1	2021.4091	-1.0	2.8
		optimal	5.3	-20.8	2021.4584	-0.8	3.1
		mean	5.2	-20.8	2021.4882	-0.9	3.3
		95%-high	6.0	-19.5	2021.5956	-0.7	3.9
4	1	95%-low	4.6	-4.0	2019.5345	-0.9	4.0
		optimal	5.6	-2.5	2021.8483	-0.8	4.3
		mean	5.7	-2.5	2021.6044	-0.8	4.7
		95%-high	7.3	-0.5	2023.1676	-0.7	5.3
	2.5	95%-low	4.0	-4.7	2021.0570	-0.9	3.9
		optimal	4.9	-3.2	2021.9506	-0.7	4.0
		mean	4.8	-3.1	2021.0154	-0.7	4.4
		95%-high	5.6	-1.4	2022.8844	-0.7	5.2
	5	95%-low	4.1	-7.2	2020.7191	-0.9	4.4
		optimal	5.2	-5.4	2021.3258	-0.7	4.7
		mean	5.3	-5.3	2021.1484	-0.8	5.0
		95%-high	6.7	-3.6	2021.5895	-0.7	5.7
	7.5	95%-low	4.0	-8.5	2021.5067	-0.6	3.6
		optimal	4.6	-7.4	2021.6569	-0.5	4.0
		mean	4.6	-7.4	2021.7157	-0.5	4.1
		95%-high	5.3	-6.4	2021.9164	-0.4	4.7
	10	95%-low	4.0	-11.7	2021.3097	-0.9	3.9
		optimal	5.4	-10.2	2021.4349	-0.7	4.2
		mean	5.2	-9.9	2021.4495	-0.8	4.5
		95%-high	6.4	-8.2	2021.6332	-0.7	5.2

(Continued)

4	15	95%-low	3.7	-16.3	2021.4312	-0.9	4.1
		optimal	4.4	-14.3	2021.5464	-0.8	4.5
		mean	4.6	-14.5	2021.5261	-0.8	4.7
		95%-high	5.7	-12.8	2021.6199	-0.8	5.4
	20	95%-low	4.0	-21.3	2021.4215	-0.8	3.6
		optimal	4.7	-20.0	2021.5109	-0.7	4.0
		mean	4.8	-20.1	2021.4954	-0.7	4.2
		95%-high	5.6	-18.7	2021.5728	-0.6	4.9
5	1	95%-low	4.4	-0.5	2019.1124	-0.9	4.3
		optimal	5.3	-0.4	2019.1046	-0.8	4.8
		mean	5.0	-0.1	2021.5190	-0.8	4.9
		95%-high	5.3	0.2	2023.9054	-0.7	5.6
	2.5	95%-low	3.3	-1.4	2019.1515	-1.1	5.0
		optimal	4.3	-1.3	2022.9883	-0.9	5.6
		mean	4.2	-0.5	2021.6921	-0.9	5.7
		95%-high	5.2	0.6	2023.8378	-0.9	6.5
	5	95%-low	2.9	-7.5	2021.3268	-1.0	4.3
		optimal	3.7	-6.0	2022.7423	-0.8	4.7
		mean	3.7	-5.5	2022.5206	-0.9	4.9
		95%-high	4.8	-2.9	2023.0411	-0.8	5.7
	7.5	95%-low	5.0	-10.5	2021.1775	-0.8	4.4
		optimal	6.6	-9.2	2021.2661	-0.7	4.9
		mean	6.2	-9.0	2021.3590	-0.7	4.9
		95%-high	7.4	-7.4	2021.7030	-0.6	5.6
	10	95%-low	4.2	-13.2	2021.1808	-1.1	5.2
		optimal	5.8	-11.2	2021.4325	-0.9	5.6
		mean	5.7	-10.9	2021.4248	-1.0	6.0
		95%-high	7.2	-8.4	2021.6346	-0.9	6.8
	15	95%-low	4.0	-17.1	2021.4348	-1.0	4.5
		optimal	5.4	-15.2	2021.5453	-0.9	4.9
		mean	5.2	-15.0	2021.5479	-0.9	5.3
		95%-high	6.4	-12.9	2021.6509	-0.8	6.1
	20	95%-low	4.1	-21.0	2021.4293	-0.8	4.4
		optimal	5.1	-19.6	2021.5085	-0.7	4.8
		mean	5.0	-19.5	2021.5127	-0.7	5.0
		95%-high	5.9	-18.1	2021.5979	-0.6	5.7

Table S5. The results of observed time series. 95%-low: lower limit of the 95% confidence interval. Optimal: the optimal estimate. Mean: the mean estimate. 95%-high: higher limit of the 95% confidence interval.

Station	/	Initial velocity (mm/yr)	Velocity change 1 (mm/yr)	Break point 1 (yr)	Velocity change 2 (mm/yr)	Break point 2 (yr)	Spectral index κ	PLN amplitude (mm/yr^{κ})
THRC	95%-low	-6.4	-14.4	16 April 2014 (2014.2877)	3.6	30 November 2014 (2014.9166)	-0.8	2.5
	optimal	-5.8	-7.6	24 July 2014 (2014.5601)	6.6	16 January 2015 (2015.0430)	-0.7	2.7
	mean	-5.9	-8.8	10 August 2014 (2014.6071)	7.9	13 January 2015 (2015.0341)	-0.7	2.8
	95%-high	-5.4	-4.5	28 October 2014 (2014.8223)	13.7	24 March 2015 (2015.2273)	-0.6	3.2
KRAC	95%-low	-0.1	-13.4	5 May 2014 (2014.3409)	5.3	17 November 2014 (2014.8776)	-0.8	2.3
	optimal	-0.1	-8.9	3 July 2014 (2014.5018)	7.9	9 January 2015 (2015.0237)	-0.7	2.5
	mean	0.0	-9.8	5 July 2014 (2014.5083)	8.8	1 January 2015 (2015.0020)	-0.7	2.6
	95%-high	0.1	-6.4	14 August 2014 (2014.6166)	12.4	19 February 2015 (2015.1349)	-0.7	3.0
MYVA	95%-low	0.0	-15.5	9 March 2014 (2014.1860)	5.2	3 November 2014 (2014.8392)	-1.0	2.5
	optimal	-0.2	-9.6	23 June 2014 (2014.4758)	9.1	27 January 2015 (2015.0728)	-0.8	2.7
	mean	-0.6	-9.9	2 June 2014 (2014.4186)	9.3	25 January 2015 (2015.0659)	-0.9	2.9
	95%-high	0.8	-5.7	31 July 2014 (2014.5800)	14.7	4 June 2015 (2015.4240)	-0.8	3.3
BJAC	95%-low	-3.0	-12.0	6 December 2013 (2013.9312)	5.0	18 December 2014 (2014.9633)	-0.8	2.6
	optimal	-3.1	-9.8	31 May 2014 (2014.4114)	9.7	26 January 2015 (2015.0712)	-0.7	2.8
	mean	-4.2	-8.3	26 April 2014 (2014.3167)	8.2	27 March 2015 (2015.2356)	-0.7	2.9
	95%-high	-1.5	-4.6	18 July 2014 (2014.5441)	11.9	30 July 2015 (2015.5770)	-0.7	3.3

Paper II

Role of tectonic stress and topography on repeated lateral dikes: application to the 1975–1984 Krafla and 2023–2025 Svartsengi rifting episodes in Iceland

Bulletin of Volcanology (2025) 87:105
https://doi.org/10.1007/s00445-025-01897-y

RESEARCH ARTICLE

Role of tectonic stress and topography on repeated lateral dikes: application to the 1975–1984 Krafla and 2023–2025 Svartsengi rifting episodes in Iceland

Yilin Yang[1] · Freysteinn Sigmundsson[1] · Halldór Geirsson[1] · Joachim Gottsmann[2]

Received: 7 February 2025 / Accepted: 10 October 2025
© The Author(s) 2025

Abstract

Lateral dike intrusions into rift zones, repeated in temporal sequences, depend on intrinsic and extrinsic factors including pressure build-up where magma accumulates between intrusions, and the local stress regime influenced by tectonic stress and topography. We reexamine these effects by revising a simplified elastic model of rifting by Buck et al. (2006), where topographic gradients and tectonic stress, in addition to magma accumulation, contribute to the driving pressure of dike propagation. Our model (i) introduces a three-section dike geometry, (ii) assumes lateral dike intrusions follow a positive pressure gradient and open in the part of the rift zone where the local maximum of driving pressure occurs, (iii) restricts the amount of dike opening according to tectonic stress stored prior to a rifting episode, and (iv) incorporates magma compressibility to better understand volume change in a magma domain. As successive intrusions redistribute stress, dike opening is favored at different parts along the rift zone. When applied to the 1975–1984 Krafla rifting episode, the model predicts a spatial distribution of dike openings consistent with geophysical observations, with magma flow into the Krafla fissure swarm through an inlet located ~ 2–4 km north of the Krafla caldera center. Inferred magma pressure at the inlet at the initiation of the first dike is ~ 1–10 MPa above lithostatic stress, whereas tectonic stress and topographic effects contributed > 20 MPa to the driving pressure. The failure pressure limit for the first dike is found to be larger than that for later dikes by a factor of 2. The lower failure limit for later dikes and tectonic stress allow magma flow into subsequent dikes when magma pressure at the inlet is below lithostatic. The model is also applied to fit the spatial distribution of dike openings in the beginning of the 2023–2025 Svartsengi rifting episode in SW Iceland. There, topographic effects contribute ~ 2 MPa of driving pressure to the southern propagation of the first dike. Tectonic stress and significant magma buoyancy (up to 9 MPa) enable dike initiations when the overpressure from magma recharge in the domain was below lithostatic. Tectonic stress inhibited eruption from the initial dike of the Svartsengi rifting episode. Our findings demonstrate that tectonic stress and topographic effects are critical factors driving lateral dike propagation, allowing magma flow into dikes or eruptions under low magma pressure, even lower than lithostatic pressure.

Keywords Repeated lateral dikes · Krafla rifting episode · Svartsengi rifting episode · Iceland · Magma overpressure · Tectonic stress · Topography

Introduction

Dike intrusion is a fundamental process transporting magma vertically and laterally in the Earth's crust (e.g., Dahm 2002; Daniels and Menand 2015; Urbani et al. 2018). At extensional plate boundaries, repeated lateral dike intrusions often occur in rifting episodes lasting from months to years, with dikes propagating up to tens of kilometers along rift zones (fissure swarms in Icelandic terminology; e.g., Jóhannesson and Sæmundsson 2009; Hjartardóttir et al. 2012, 2015). Temporal sequences of dikes during rifting episodes release

Editorial responsibility: Editorial responsibility: J.-d. Xu

✉ Yilin Yang
yiy1@hi.is

[1] Nordic Volcanological Center, Institute and Faculty of Earth Sciences, University of Iceland, Reykjavík, Iceland

[2] Department of Earth and Environmental Sciences, Ludwig-Maximilians-Universität München, Munich, Germany

Published online: 04 November 2025

stress accumulated in plate boundary deformation zones over large timescales (centuries) due to plate movements (e.g., Abdallah et al. 1979; Paquet et al. 2007; Wright et al. 2012). Such dikes can cause meter-scale ground deformation, trigger normal faulting, and lead to eruptions (e.g., Björnsson et al. 1977; Biggs et al. 2009; Grandin et al. 2010; Parks et al. 2023; Sigmundsson et al. 2024). Studying their spatial features and controlling factors enhances our understanding of divergent plate tectonics, magma transport, and eruptions and assists in volcanic hazard assessment.

Dike models

Dike propagation models primarily aim to predict the temporal evolution of a single dike, including its geometry, propagation velocity, and magma pressure distribution. Traditionally, there have been two main schools of thought for modeling the vertical propagation of a single dike (Nakashima 1993; Rivalta et al. 2015). One emphasizes the resistance of host rock to fracturing, deriving dike geometry from the minimum fluid pressure to maintain equilibrium of an open fluid-filled crack. The other emphasizes the stress in viscous magma flow to predict dike propagation dynamics. Hybrid models incorporating assumptions from both schools of thought have been developed for complex scenarios (Dahm et al. 2000; Roper and Lister 2007), with some extending to lateral dike propagation. For instance, Rivalta (2010) considered lateral dikes and a magma reservoir coupled by a conduit with viscous magma flow to model the temporal evolution of dike propagation. Townsend et al. (2017) introduced a third school of thought, focusing on the vertical cross-sections of lateral dikes, and their propagating distance and horizontal extent. However, reproducing the spatial features of temporal dike sequences and how they release accumulated stress at divergent plate boundaries require a different modeling approach, which quantifies tectonic stress evolution along the rift zone as dikes intrude.

A simplified numerical model of dike sequence formation was presented by Buck et al. (2006). The model analyzed tectonic and topographic stress along the rift zone and predicted major dike openings by assuming that their associated stress changes are controlled by the difference between magma pressure and stress conditions along the fissure swarm due to tectonic stress and topographic effects. When applied to the 1975–1984 Krafla rifting episode in Iceland, the model predicted dike opening distribution broadly consistent with field observations. However, there is scope for improvement. For example, the model assumes a uniform stress distribution along the dike at the end of an intrusion, with dike opening that can be larger than expected from accumulated tensile stress due to plate spreading prior to a rifting episode. Observations show, however, that a single dike in a rifting episode may only partially release previously accumulated tectonic stress, and the total stress release of a dike sequence may be limited by the magnitude of tectonic stress accumulated prior to a rifting episode (e.g., Wright et al. 2012; Heimisson et al. 2015b; Parks et al. 2023; Sigmundsson et al. 2024; Greiner et al. 2025). Additionally, the Buck et al. (2006) model assumed a vertical dike extent of 10 km at Krafla, whereas geodetic observations suggest a range of 2–5 km (Hollingsworth et al. 2013). Modifying the assumed dike geometry and how the model releases tectonic stress in each dike intrusion can provide further insights into the factors controlling dike sequence behavior during rifting episodes.

Krafla volcano and the 1975–1984 rifting episode

The Krafla volcano is in the Northern Volcanic Zone (NVZ) of Iceland, at the divergent Eurasian North-American plate boundary (Fig. 1). Its volcanic system comprises a central volcano with a diameter of ~ 25 km and a 5–8 km wide transecting fissure swarm extending approximately 40 km to the south and 50 km to the north (Opheim and Gudmundsson 1989; Hjartardóttir et al. 2012; Lanzi et al. 2023). A 9 × 7 km caldera formed ~ 100,000 years ago at the central volcano (Sæmundsson 1991). The average plate spreading rate is 17.4 mm/yr in direction N112° E in this area (DeMets et al. 2010; Drouin et al. 2017). Drilling, seismological, and petrological studies suggest the presence of magma across a wide range of depth beneath the caldera (2.1–19 km; e.g., Mortenson et al. 2014; Einarsson 1978; Tryggavson 1980, Brandsdóttir et al. 1997; Schuler et al. 2015; Kim et al. 2020; Rooyakkers et al. 2024).

The most recent rifting episode at Krafla in 1975–1984 consisted of about 20 rifting events with dike intrusions affecting a portion of the fissure swarm, nine of which led to eruptions (e.g., Björnsson et al. 1979; Tryggvason 1980; Einarsson 1991; Wright et al. 2012). These events generated seismic swarms, faulting, and surface widening. The cumulative surface widening averaged 4–5 m, corresponding to 200–250 years of accumulated spreading, with the maximum cumulative widening up to ~ 8 m north of the Krafla caldera (Tryggvason 1984; Hollingsworth et al. 2012). Geodetic data revealed gradual inflation in the caldera between diking events, followed by sudden deflation beginning at the onset of each dike intrusion (Fig. 1d). The subsidence reached > 1.8 m during the first dike in 1975, which recovered only ~ 40% by inflation before the second dike initiated. Thereafter, the elevation at dike onsets gradually increased and had recovered to the level prior to the rifting episode at the onset of the 1979–1980 events (Tryggvason 1980; Johnsen et al. 1980; Einarsson 1991; Buck et al. 2006). Hollingsworth et al. (2013) derived ground displacements along the Krafla fissure swarm during the rifting episode from aerial photos and inferred the dikes extending from 0–3 to 5 km depth

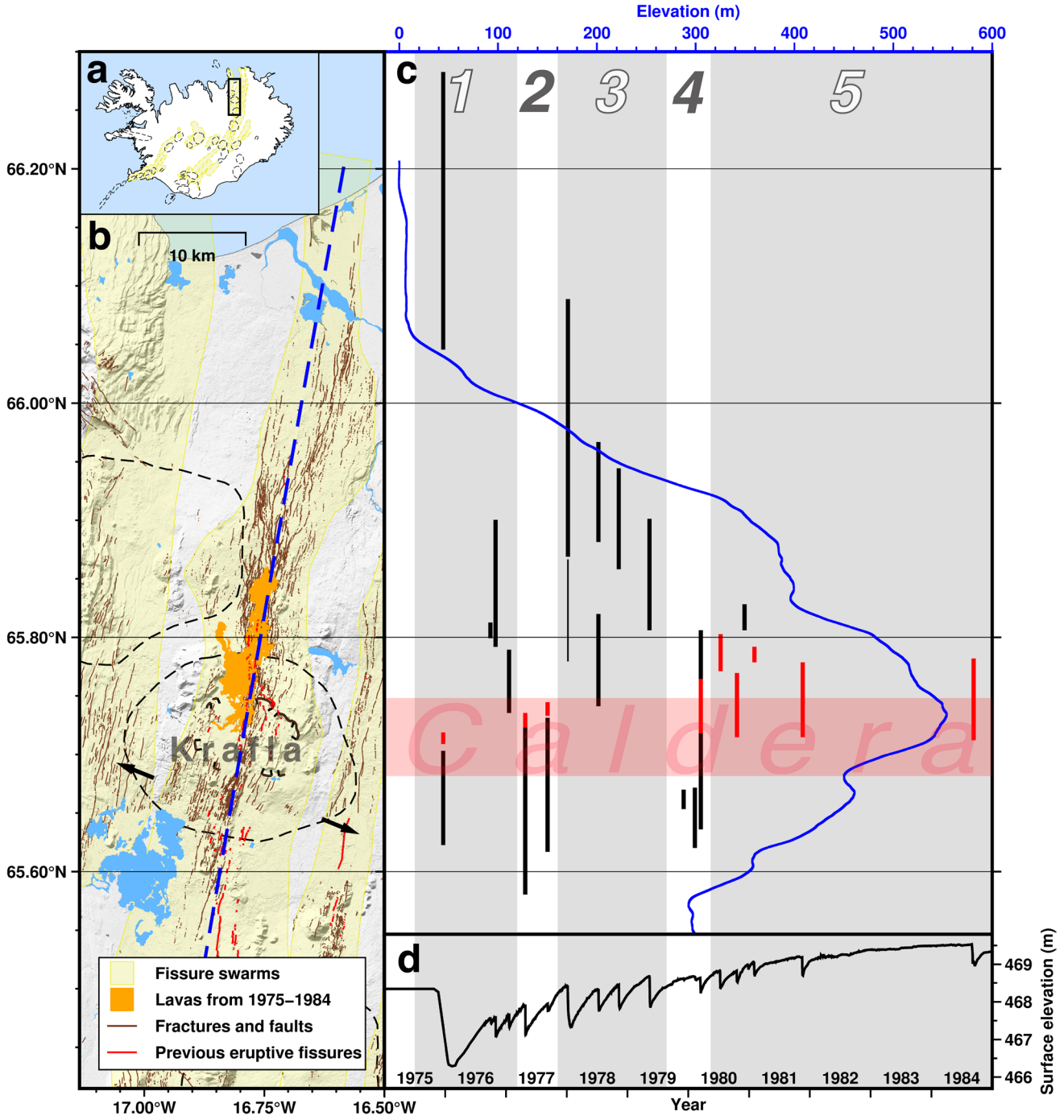


Fig. 1 Krafla volcano and the dikes formed in the 1975–1984 rifting episode. **a** A map of Iceland showing the location of the Krafla volcanic system (black rectangle). **b** A map of the Krafla volcanic system. The black dashed lines indicate central volcanoes and tick-marked lines indicate the outline of the Krafla caldera where mapped. Blue dashed line shows the location of the elevation profile shown in Fig. 1b. The arrows indicate the direction of plate spreading. The topography is from LMÍ (2020). Fractures are from Hjartardóttir et al. (2015). The Krafla fissure swarm, central volcano, and caldera are from Sæmundsson (1991). **c** Elevation profile along the Krafla fissure swarm smoothed with Savitzky-Golay filter (blue line), and the distance range in the Krafla fissure swarm with main dike opening (black) indicated by seismic swarms and eruptions (red), adapted from Einarsson (1991) and Buck et al. (2006). The horizontal red shaded area indicates the latitude range of the Krafla caldera, and the vertical gray and white straps indicate the different sub-sequences of dikes numbered on the top. **d** Elevation change in the Krafla caldera center during 1975–1984 Krafla rifting episode, from Björnsson and Eysteinsson (1998)

in the crust. Geodetic models constrained by leveling and distance measurements, using a point pressure source in a homogeneous elastic half-space (Mogi 1958), estimated the source depth at ~ 3–4.3 km (e.g., Tryggvason 1980; Johnsen et al. 1980; Árnadóttir et al. 1998; Heimisson et al. 2015a).

The spatial distribution of dike openings shows significant first-order regularities (Einarsson 1991; Buck et al. 2006). Several dikes propagated successively mainly in the same direction away from the caldera. Based on their propagation direction, dikes from 1975 to March 1980 can be divided into four sub-sequences (Fig. 1c). Within each sub-sequence, the main dike openings in the fissure swarm manifest a pattern: dikes propagate progressively shorter distances from the Krafla caldera and the length of the main opening also decreases with shorter propagation distance (Fig. 1c). Namely, the first event in each sub-sequence always opens the longest part in the fissure swarm furthest away from the caldera. The pattern is particularly evident for the first sub-sequence events spanning 1975 to January 1977, including the first and largest event of the entire rifting episode. This event most profoundly affected more than 20 km in length of the fissure swarm, > 60 km north of the caldera. The later sub-sequences show the same first-order features with minor deviations (Fig. 1c). After March 1980, the primary character of events shifted to eruptions.

Methodology

To reexamine the role of tectonic stress and topography, we develop a revised version of the Buck et al. (2006) model. The model still aims to identify the most favorable part along the fissure swarm for dike opening in each diking event, dependent on tectonic stress, topographic effects, and magma pressure. Our modifications include restricting tectonic stress relieved by each dike and the entire dike sequence, implementing a three-section dike geometry with variable tectonic stress relief, considering of magma compressibility when applying mass conservation as done by Rivalta (2010), and determining the part of dike opening along the fissure swarm according to the stress profile before resolving opening distribution. Using the revised model, we test if the 1975–1984 Krafla dike sequence can be explained by a scenario where magma flow into all the dikes and eruptions originates from approximately the same horizontal location in the fissure swarm, referred to as the fissure swarm inlet (Fig. 2a).

In the model, the fissure swarm inlet is located at the level of neutral buoyancy (LNB) in the crust, where magma density is similar to crustal density (e.g., Rubin and Pollard 1987; Wilson and Head 2002; Poland et al. 2007; Varugu and Amelung 2021). We define magma overpressure as the

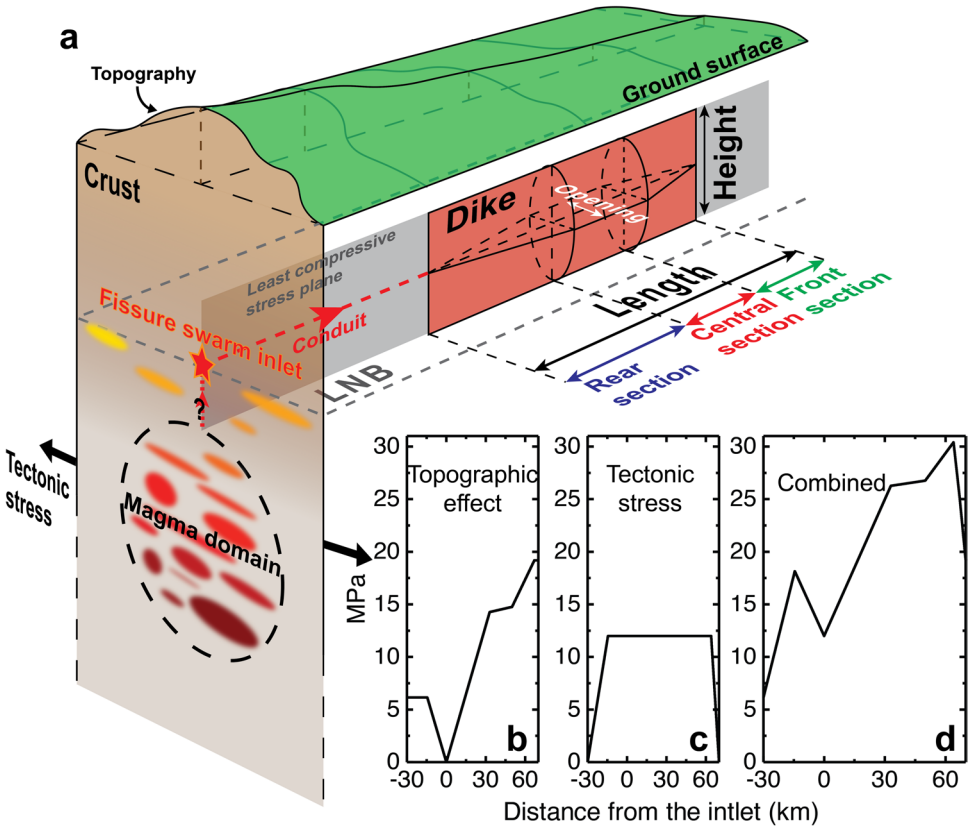


Fig. 2 A schematic figure of the revised dike sequence model. **a** Illustration of magma flow from a magma domain, through the fissure swarm inlet and to a dike on the least compressive stress plane. The figure is not to scale. **b**, **c** Dike driving pressure contributed by topographic effects and tectonic stress prior to the 1975–1984 Krafla rifting episode. The topographic effect is calculated with a simplified piecewise elevation profile along the Krafla fissure swarm shown in Fig. 1c and Fig. S3 in Online Resource 1, and an average host rock density of 2510 kg/m^3 (Scott et al. 2019; see further description in the text). The tensile tectonic stress is assumed to be 12 MPa prior to the first diking event, with two stress barriers on both ends of the Krafla fissure swarm (Buck et al. 2006). **d** Dike driving pressure supplied by the topographic effects and tectonic stress summing up Fig. 2b, c

magma pressure in excess of the lithostatic pressure at the LNB. For simplicity, we define dike opening as its widening perpendicular to the dike plane, dike length as its horizontal scale along the propagation direction, and dike height as its vertical extent. The dike height is assumed to be uniform and centered at the LNB (Fig. 2a). In this study, tensile stress is denoted as negative.

Prior to diking, magma accumulates in a crustal volume we refer to as a magma domain, consisting of partial melt, magma mush and hot solid rock, distributed over a depth interval, as suggested by Sigmundsson et al. (2024). At a certain overpressure, magma begins to flow from the domain and subsequently passes through the inlet to form a dike by lateral flow. Dikes propagate along a plane orthogonal to the direction of least compressive stress (Rubin and Pollard 1988). In the model, tectonic stress accumulation prior to a rifting episode ($\sigma_{t,total}$) reduces normal stress on this plane uniformly. Dike intrusions release tectonic stress by causing elastic deformation of the dike flanks (Pollard et al. 1983; Okada 1985). Each diking event thus modifies the stress along the fissure swarm, shifting the location of the most favorable part for the next dike opening. In contrast to the model by Buck et al. (2006), each dike in our model can only release a percentage (α) of stored tectonic stress, in line with observations from rifting episodes in Iceland and Afar, east Africa, where repeated lateral dikes occur in the same region (Greiner et al. 2025). This restriction allows the model to predict more realistic dike openings and their associated stress changes.

The model may identify dike openings detached from the inlet under specific stress conditions along the fissure swarm. In such cases, we assume the dike opening is connected to the inlet via a zone with limited opening, referred to as a conduit (Fig. 2a; see also supplementary text in Online Resource 1).

The model is implemented in MATLAB® (The MathWorks Inc. 2023), predicting the key features of a dike sequence, e.g., spatial distribution of dike openings, variations in overpressure at the inlet, and the evolution of tectonic stress along the rift zone. All symbols used in the following derivations are listed in Table 1 and Table S1 in Online Resource 1.

To rupture the magma domain and initiate magma flow, magma overpressure in the domain should increase sufficiently that it equals the sum of the host rock failure limit (P_o; e.g., tensile strength) and the external stress (e.g., Blake 1981; Zhan and Gregg 2019; Sigmundsson et al. 2020). Overpressure in the domain results from magma supply into a confined volume, as well as from the buoyancy generated by density contrast between magma and host rock. Assuming that tectonic stress is the only contributor to external stress and that it is uniform with

Table 1 Parameter settings of the revised dike sequence model for the 1975–1984 Krafla rifting episode. The 'value' column indicates the parameter values used to generate the results shown in Figs. 3 and 4. The 'range' column specifies the range of values that produces similar spatial distribution of dike openings in the fissure swarm when variating only one parameter and keep others fixed as in the 'value' column

Parameter		Value	Range	Reference
Tectonic stress $\sigma_{t,\,total}$ [MPa]		−12.0	−11.9 to −12.5	Tryggvason (1984)
Pressure added by upward migration of magma before its lateral propagation (p_u) [MPa]		0	/#	
Failure limit P_o	First dike [MPa]	15.0	13.9–15.9	
	Rest of dikes* [MPa]	7.5	7.2–7.6	
Host rock (< 5 km depth)	Density ρ [kg/m^3]	2510	2216–2540	Scott et al. (2019)
	Poisson's ratio ν	0.20	0.16–0.22	Heap et al. (2020)
	Shear modulus μ [GPa]	10.0	9.4–10.2	Sigmundsson et al. (2024)
Magma domain	Radius R [m]	2400	2361–2422	
	Compressibility β_m [Pa^{-1}]	2.10×10^{-10}	1.97×10^{-10} to 2.15×10^{-10}	
Dike	Height H [m]	3700	3665–3792	Hollingsworth et al. (2013)
	Central depth [m]	3000	/#	
Maximum percentage of tectonic stress relieved by one dike α		60%	59%–73%	Tryggvason (1984); Greiner et al. (2025)
Stress reduction ratio between the far end and the local maximum of dike driving pressure γ		0.30	0.13–0.30	
Tapering factor ε [Pa/m]		130	80–136	

#p_u only changes the inlet overpressure at dike initiations but does not affect the spatial distribution of predicted dike openings. Central depth of dikes only determines the absolute pressure of dike and the inlet but does not affect the spatial distribution of predicted dike openings

*The ratio between the failure limits for the first and rest of dikes is constrained by the elevation curve observed during the Krafla rifting episode, e.g., Einarsson (1991)

depth, the magma overpressure at the inlet (p_i) at dike initiations is expressed as (Buck et al. 2006; Qin and Buck 2008):

$$p_i = P_o + \sigma_{t,i} + p_u \quad (1)$$

where $\sigma_{t,i}$ represents the tectonic stress at the inlet (negative for tension), and p_u accounts for any potential overpressure added by magma upward migration before its lateral propagation (Sigmundsson et al. 2020). Assuming the upward migration is the same during all dike initiations in a rifting episode, p_u is treated as constant. The failure limit is adjustable and is set higher for the first dike than for later dikes, in line with elevation change curves from rifting episodes (Tryggvason 1980; Parks et al. 2025).

After a lateral dike is initiated, the driving pressure for magma flow is contributed by both inlet overpressure and the stress conditions along its path on the least compressive stress plane. The initial magma overpressure is controlled by Eq. (1). The stress conditions along the dike path are determined by two factors: (i) topographic overburden from difference in lithostatic stress between the inlet and the dike path (e.g., Fialko and Rubin 1998; Sigmundsson et al. 2015; Urbani et al. 2017). Using the peak elevation along the Krafla fissure swarm as a reference (latitude of ~ 65.734° N in Fig. 1c), all other points along the profile have negative relative stress due to smaller lithostatic stress, increasing the driving pressure of each dike (Fig. 2b); (ii) accumulated tensile tectonic stress along the dike path that reduces stress acting perpendicularly to the propagating dike (Fig. 2c). The net driving pressure of lateral dike propagation, $P_{driving}$, is given by

$$P_{driving} = p_i - \rho g \Delta h(x) - \sigma_t(x), \quad (2)$$

where x indicates any location in the dike, ρ is average host rock density above the central depth of dikes, $\Delta h(x)$ is the elevation difference above the inlet and other locations along the fissure swarm, $\sigma_t(x)$ is the tectonic stress at each horizontal location along the dike path, and g is the gravitational acceleration. Considering the minimum potential energy principle and that dikes take the path of least resistance (Heimisson et al. 2015b), dikes in the model will propagate in the direction with larger positive gradient of $P_{driving}$ near the inlet, continuing towards an area where $P_{driving}$ reaches its local maximum and no longer increases. With magma extracted from the magma domain, $P_{driving}$ decreases due to reduction in source overpressure (p_i decreases) and in tectonic stress (σ_t becomes less negative). Dike intrusion stops when $P_{driving}$ drops to zero, achieving equilibrium between overpressure at the inlet and the dike.

Stress change scaling with dike openings

Our model assumes that dikes release accumulated tectonic stresses elastically, such that the opening at each mathematically discretized location of the dike scales with the stress release, in accordance with Hooke's law. We derive a scaling relationship (see derivation in Online Resource 1) between average dike opening at each horizontal location, $w(x)$, and change in tectonic stress at that location, $\Delta\sigma_t(x)$, such that

$$w(x) = A\frac{\pi H(1-\nu)}{4\mu}\Delta\sigma_t(x), \quad (3)$$

where ν and μ represent the Poisson's ratio and shear modulus of the host rock, respectively, H indicates the dike height, and A is a constant. The term $\frac{\pi H(1-\nu)}{4\mu}$ is the scaling factor between average opening and stress change of a two-dimensional elliptical crack in an unbounded elastic material (Pollard et al. 1983). However, dikes forming in a rifting episode are highly influenced by their location close to the free surface of the Earth, causing larger opening than anticipated in the full space approximation. Dike opening models (Online Resource 1) suggest $A \sim 2$, used in this study.

Equation (3) with $A = 2$ can be used to derive a relation between the mass (or volume) of a dike and the stress release, assuming negligible variation of magma density within the dike:

$$\Delta M_d = \rho_d \int_L Hw(x)dx \approx \rho_d \frac{\pi \Delta L H^2(1-\nu)}{2\mu} \sum_L \Delta\sigma_t(x) \quad (4)$$

Here L is the dike length, and ρ_d is the magma density in the dike. Integrating the horizontal cross-section area $Hw(x)$ over the dike gives the dike volume, corresponding to the discretization as presented above.

Coupling of dikes and magma domain with mass conservation and elasticity

We infer the variation of $P_{driving}$ by considering the coupling between a dike and a magma domain through the inlet, mass conservation, and elasticity. Mass conservation implies that the magma mass extracted from the magma domain (ΔM_s, the source) equals to that injected into a dike (ΔM_d):

$$-\Delta M_s = \Delta M_d, \quad (5)$$

where ΔM_s is negative and ΔM_d is positive during dike emplacement.

Assuming no additional feeding into the magma domain during diking, loss of mass in the magma domain leads

to its pressure decrease, reducing both its volume and density as the remaining material within it expands. We assume the inlet overpressure drop (Δp_i) is equivalent to the overpressure drop in the magma domain. Assuming the variations of temperature and composition are second order effects, then

$$\Delta M_s = \rho_s V_s \left(\beta_m + \beta_s\right) \Delta p_i, \tag{6}$$

where ρ_s and V_s are the average density of material within the magma domain and the total volume of the magma domain, respectively (e.g., Segall et al. 2001; Rivalta 2010; Sigmundsson 2021). The effective compressibility of material within the magma domain, β_m, and the so-called mechanical compressibility of the magma domain structure within elastic host rock, β_s, together relate the mass change in the magma domain with its volume and pressure variations, where β_m ranges 0.04–1.5 GPa^{-1} (Spera 2000; Segall et al. 2020; Sigmundsson et al. 2020). Assuming the host rock is a homogeneous elastic half-space and approximating the magma domain as a sphere with radius R (volume $V_s = 4\pi R^3/3$), then $\beta_s = 3/4\mu$ (McTigue 1987).

Equations (4), (5), and (6) can be combined to couple together the variations of magma overpressure at the inlet and tectonic stress change in the fissure swarm:

$$\Delta p_i = -\frac{\rho_d}{\rho_s} \frac{H^2 \Delta L (1-\nu)}{2R^3 \left(1 + \frac{\beta_m}{\beta_s}\right)} \sum\nolimits_L \Delta\sigma_t(x) \tag{7}$$

The volume ratio between the dike and the deflation of a magma domain is $1 + \frac{\beta_m}{\beta_s}$ (Rivalta 2010). For any location x in a dike where the driving pressure decreases to zero at the end of the intrusion, the equilibrium condition can be written as

$$P^0_{\text{driving}} - \Delta\sigma_t(x) + \Delta p_s = \left(p_i + \Delta p_i\right) - \rho g \Delta h(x) - \sigma^0_t(x) - \Delta\sigma_t(x) = 0 \tag{8}$$

where P^0_{driving} represents dike driving pressure at its initiation and $\sigma^0_t(x)$ is the initial tectonic stress along the dike path prior to the diking event. The terms $p_i + \Delta p_i$ give the final inlet overpressure.

Three-section dike geometry and numerical implementation of the model

Implementing the above equations requires specifying the dike geometry. We use a simplified geometrical form, with more opening in a central section and less near dike ends, similar as dike opening under constant overpressure in an unbounded elastic material (Pollard et al. 1983). The model divides a lateral dike into three sections: front, central, and rear (Fig. 2a and Fig. S2 in Online Resource 1). The dike propagates along a positive gradient of P_{driving} to the location where P_{driving} reaches its local maximum. There, (i) the dike has its maximum opening, and (ii) the largest reduction in tectonic stress occurs. Beyond this point, dike opening tapers toward its far end because the driving pressure continually drops towards the front. This effect is implemented by prescribing a linear decrease in tectonic stress release, with a tapering factor (ε) being the slope. Dikes will stop propagating when the driving pressure drops below a certain level (Buck et al. 2006), implemented here as the tectonic stress release reduced to a preset fraction (γ) of $\Delta\sigma_{t,max}$, or to zero in cases of a rapid pressure drop in the front section induced by topographic gradients or stress barriers.

The rear section begins at the dike's near end and extends away from the inlet (Fig. 2a). Tectonic stress reduction within this section is variable such that the final dike driving pressure from external contributors becomes uniform, determined by solving for $\Delta\sigma_t(x)$ in Eq. (8). In this model, any individual dike cannot reduce tectonic stress by more than a fixed maximum percentage of the total tectonic stress stored prior to the rifting episode ($\alpha\sigma_{t,total}$). Namely, at any location where $\Delta\sigma_t(x) > \alpha\sigma_{t,total}$, we set $\Delta\sigma_t(x) = \alpha\sigma_{t,total}$. This yields a section of uniform opening, referred to as the central section. It is typically located further away from the inlet than the rear section. The final geometry of the dike is determined by searching for $\Delta\sigma_t(x)$ in the rear section so that equilibrium in Eq. (8) is achieved. That specifies the dike opening, tectonic stress reduction, and the lengths of the three sections (details in Online Resource 1).

For numerical implementation, we discretize the horizontal axis of the dike propagation plane with interval ΔL. When the critical limit in Eq. (1) is reached, a numerical algorithm evaluates the local maxima of P_{driving} and searches for $\Delta\sigma_t(x)$ in the dike rear section. The hydraulic equilibrium between the inlet and the rear section can be written according to Eqs. (7) and (8) for any location x in the rear section:

$$p_i - \frac{\rho_d}{\rho_s} \frac{H^2 \Delta L (1-\nu)}{2R^3 \left(1 + \frac{\beta_m}{\beta_s}\right)} \sum\nolimits_L \Delta\sigma_t(x) = \rho g \Delta h(x) + \sigma^0_t(x) + \Delta\sigma_t(x) \tag{9}$$

The model inputs include the profiles of topography and tectonic stress along the dike path, along with parameters listed in Table 1. The model tests values of $\Delta\sigma_t(x)$ in the rear section and their corresponding dike geometry aiming at fulfilling the condition described in Eq. (9), and from that, derives the distribution of dike opening. The tectonic stress profile is updated considering the stress released by one dike and used as input for the next dike. The modeling steps are (demonstrated by Fig. S2 in Online Resource 1 and the animation in Online Resource 2):

(i) Calculate initial magma overpressure with Eq. (1) and locate where P_{driving} reaches its local maximum nearest to the fissure swarm inlet;
(ii) Set $\Delta\sigma_t(x) = -\alpha\sigma_{t,\text{total}}$ at the location found in (i);
(iii) Determine dike geometry with $\Delta\sigma_t(x)$ and evaluate Eq. (9);
(iv) If the far end locates in an area with positive gradient of driving pressure, move to the next local maximum of P_{driving} further away from the inlet and go back to (ii);
(v) If the left-hand side in Eq. (9) is larger, increase $\Delta\sigma_t(x)$ by a certain searching step (0.05 MPa in this study) and go back to (iii);
(vi) If the left-hand side in Eq. (9) is smaller, decrease $\Delta\sigma_t(x)$ by the searching step and go back to (iii);
(vii) If equilibrium in Eq. (9) is fulfilled, stop the search, and all information of the dike is now available;
(viii) Update the tectonic stress along the fissure swarm and go back to (i) for the next dike intrusion.

One can decide which parameters in Table 1 to fix, depending on available a priori information. In this study, the sensitivity of the free parameters is tested by changing one parameter at a time and evaluating how the spatial distribution of dike openings is modified (see parameter sensitivity analysis in discussion).

Eruption

Equation 1 suggests that higher inlet overpressure is required to initiate dikes in the later stage of a rifting episode compared to the early stage, as tectonic stress near the fissure swarm inlet is progressively reduced by dike intrusions. This conforms to the ground uplift at dike initiations after the first dike intrusion during the Krafla rifting episode.

Increased initial magma overpressure at the inlet may drive upward magma movement and cause eruptions. In our model, eruption occurs when inlet pressure is high enough to drive magma flow, yet significant tectonic stress relief from previous dike intrusions reduces the support for lateral propagation. In step (iii) of the numerical algorithm, a simple condition for eruptions is added:

$$-\Delta p_i \le (1-\gamma)p_i \text{ and } \sigma_{t,i} < (1-\gamma)P_o \tag{10}$$

where Δp_i is evaluated with the dike geometry in step (iii). When the overpressure at the inlet drops to γp_i, the eruption will stop. Dikes that feed eruptions are assumed to only have a front section tapering from the inlet, thus limiting its propagating distance. Due to effects of faulting, as well as variations in physical properties of magma and host rock above the assumed dike top (e.g., Segall et al. 2001; Huppert and Woods 2002; Taisne and Jaupart 2009; Hollingsworth et al. 2013; Magee and Jackson 2020; Townsend and Hubber 2020), our model cannot predict the location of eruptive fissures. Furthermore, predicted dike openings with eruptions are less accurate than those without eruptions.

Results

We evaluate if the first ten dikes of the 1975–1984 Krafla rifting episode, covering four sub-sequences with most surface widening in the fissure swarm, can be explained by the revised dike sequence model. The fissure swarm inlet is assumed to be below the highest elevation along the Krafla fissure swarm in the caldera. The tensile tectonic stress is assumed to be 12 MPa with two stress barriers on both ends of the Krafla fissure swarm (Buck et al. 2006; Fig. 2c). Table 1 lists parameter values we use, constrained by previous research where available and otherwise tested over a range of values to reproduce the observed dike opening distribution (Fig. 1c). The density ratio ρ_d/ρ_s is set to 1 in Eq. (9), assuming the difference between the magma density in the magma domain and dikes is negligible. The failure limit P_o in Eq. (1) to initiate the first dike is set larger than P_o for later dikes in the Krafla rifting episode, scaled according to the ground elevation in the Krafla caldera (Fig. 1d; Einarsson 1991). The maximum percentage of stored tectonic stress that a single dike can release is inferred from surface widening estimates by Tryggvason et al. (1984). Results in Figs. 3 and 4 are from model runs using parameter values in Table 1.

Figure 3 shows the external contributors to dike driving pressure at the onset of the rifting episode and how it evolves with dike intrusions. External factors contribute up to 30 MPa to the driving pressure for the first dike and ~20 MPa for the second and sixth dikes. Dikes relieve tectonic stress and reduce the driving pressure available for later events (see the animation in Online Resource 2). Assuming initial magma overpressure at the inlet is 3 MPa prior to the rifting episode, the model suggests that the topographic effect and tectonic stress account for >90% of the dike driving pressure for its lateral propagation in the early stage of the rifting episode. Tectonic stress relieved by preceding dikes limits the propagation distance of later dikes by shifting the local maxima of dike driving pressure.

Other predictions by the revised dike sequence model are compared with geophysical observations and previous models in Fig. 4. The predicted dike opening distribution and inlet overpressure changes are compared to the Buck et al. (2006) model in Fig. S4 in Online Resources 1. Generally, the predicted dike opening distribution aligns with that indicated from observations (Fig. 4a, b). Dike intrusions from 1975 to 1977 generated ~ 3 m of surface widening over ~ 80 km along the fissure swarm, and dikes from 1978

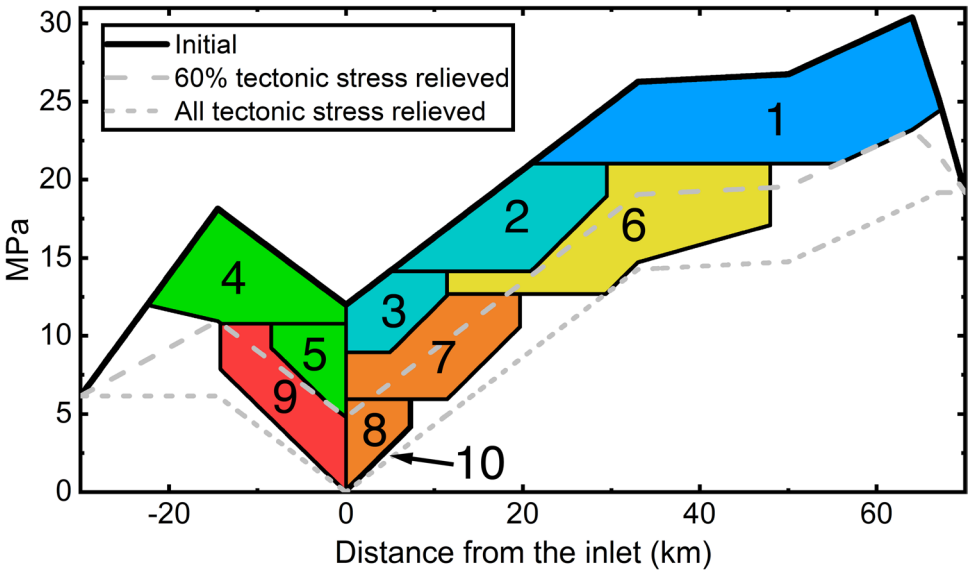


Fig. 3 Variation in dike driving pressure contributed by topographic effects and tectonic stress during the 1975–1984 Krafla rifting episode, predicted by the revised dike sequence model. The numbers indicate the temporal order of the dikes. The thick black line corresponds to the curve in Fig. 2d. The color codes correspond to Fig. 4d. An animation in Online Resource 2 demonstrates the spatio-temporal sequence of diking which contributes to the cumulative data displayed in the figure

to 1979 caused again ~ 2–3 m of surface widening north of the fissure swarm inlet (Fig. 4c, d). The largest cumulative surface widening near the inlet is ~ 6 m in Fig. 4d, smaller than ~ 8 m inferred from ground observations, as shown in Fig. 4c. The model predicts eruptions associated with dike intrusions after 1979 (Fig. 4b) when tectonic stress near the inlet has been mostly relieved (Fig. 3). Figure 4e suggests that the revised dike sequence model, even without direct constraints from ground deformation data, predicts magma volume change in the magma domain that is consistent with geodetic models. Variations of surface elevation and magma overpressure at the inlet in Fig. 4f show similar inflation–deflation cycles and a general increase at dike initiations, except for the first one, as observed during the rifting episode.

Discussion

Implications for the Krafla rifting episode

Comparisons above indicate that the model successfully reproduces the first-order regularities of the 1975–1984 Krafla dike sequence. A relatively low magma overpressure of 3 MPa at the fissure swarm inlet prior to the rifting episode can generate the first and largest dike intrusion of the entire sequence, dominated by topographic effects and tectonic stress (Fig. 3). By 1979, the tectonic stress near the inlet had been mostly relieved, and dikes thereafter are likely to cause eruptions. The dikes after March 1980 are not modeled due to less accurate opening prediction with the involvement of eruptions (see "Eruption" section). Comparing the model-predicted dike openings with the surface widening estimated with the geodetic approach shows that, after 1980, about 25% of cumulative widening occurred in the zone near the magma inlet associated with the unmodeled dikes.

Figure 4f shows that a higher failure limit is required to initiate the first dike than later dikes by a factor of 2, which fits the observed elevation change. Since the first dike intrusion did not significantly reduce the tectonic stress near the inlet, a lower failure limit for later dikes permits their initiations under negative magma overpressure at the inlet, namely when magma pressure is lower than the lithostatic pressure. The predicted inlet overpressure variations (red curve in Fig. 4f) align with the observed elevation changes (blue curve in Fig. 4f). Based onthe predicted inlet overpressure variations, we find that a spherical pressure source with a radius of 2.4 km (Table 1) in an elastic half-space (Mogi 1958) at ~ 3.6 km depth leads to a similar magnitude of elevation changes as the observations. This is consistent with previous geodetic inversions (e.g., Tryggvason 1980; Johnsen et al. 1980; Ewart et al. 1991; Heimisson et al. 2015a).

The magma domain and the location of the fissure swarm inlet

For the Krafla rifting episode, our model suggests that the fissure swarm inlet is offset from the magma domain center, similarly as found for the ongoing Svartsengi rifting episode in Iceland (Sigmundsson et al. 2024). Both our model and the Buck et al. (2006) model (Fig. 4a, b and S4a in Online Resource 1) indicate that an inlet located under the highest surface elevation along the fissure swarm, ~ 3 km north of the Krafla caldera center, explains the spatial distribution of dike openings. This area coincides with the center of the 1975–1984 eruptive fissures (Fig. 1c), the epicenters of seismicity in the beginning of intrusive activities during 1978–1980 (~ 67.5° N; Einarsson and Brandsdóttir 2021),

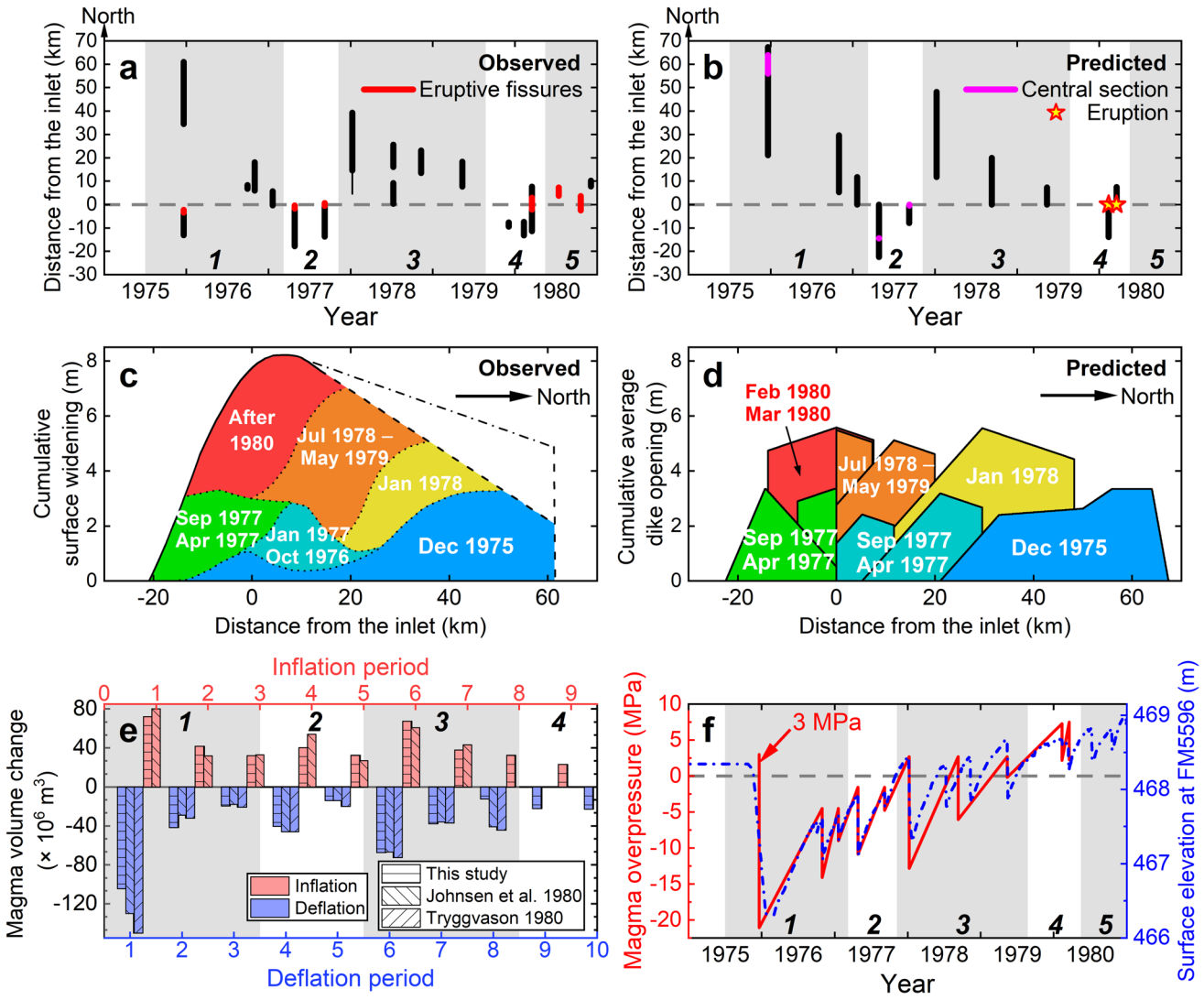


Fig. 4 Comparison between predictions from the revised dike sequence model and geophysical observations and previous models of the 1975–1984 Krafla rifting episode. **a** The distance range in the Krafla fissure swarm with main dike opening (black) indicated by seismic swarms and eruptions (red), adapted from Einarsson (1991) and Buck et al. (2006), same as Fig. 1c. The vertical white and grey straps represent different sub-sequences of dike intrusions numbered at the bottom. The inlet is located 4 km north of the center of the caldera. **b** Spatial distribution of dike openings predicted by the revised dike sequence model. **c** Estimated cumulative surface widening in the fissure swarm with distance measurements, adapted from Tryggvason (1984). **d** Predicted cumulative dike opening (average over the depth range of diking) in the fissure swarm. The color codes correspond to estimates for different period in Fig. 4c. **e** Volume change in the magma domain, predicted by the revised dike sequence model and inverted with a point pressure source within uniform elastic half-space (Mogi 1958) using ground deformation (Johnsen et al. 1980; Tryggvason 1980). **f** Magma overpressure at the inlet (red line) predicted by the revised dike sequence model and observed elevation change in the Krafla caldera (blue dash-dot line; Tryggvason 1984). The horizontal grey dashed line indicates magma pressure equals to lithostatic pressure. Overpressures after each event and at the initiation of next event is connected by straight lines without any indication of dynamic processes of dike emplacement or recharge of the magma domain

and the boundary of bimodal eruptive products across the north caldera rim, where magma mixing and supply from different depths occurred (Rooyakkers et al. 2024). In contrast, geodetic models suggested that the magma domain center is near the caldera center, e.g., with deformation source centers located within 1 km of it (Heimisson et al. 2015a). The offset between the fissure swarm inlet and the magma domain center may result from structural weakness along caldera-bounding faults and local stress regime below caldera rims (Sigmundsson et al. 2020; Corbi et al. 2016).

For the model of Krafla rifting episode presented here, the upward migration of magma before its lateral propagation is assumed to be negligible (p_u being zero), as the point-source pressure at ~ 3–4 km depth, inferred from geodetic models

and Fig. 4f, is close to the assumed LNB at central depth of the dikes (3 km in Table 1). We also vary the value of p_u in the sensitivity test, which does not alter the predicted dike opening patterns but only shifts the estimate of overpressure as a whole.

Magma overpressure change at the fissure swarm inlet is assumed to be the same as the pressure change in the magma domain, represented in our model by a single spherical volume with a radius of 2.4 km. Petrochemistry analyses of eruptive products during the Krafla rifting episode (Rooyakkers et al. 2024) have, however, inferred basaltic magma storage prior to the Krafla eruptions at both ~ 7–9 km (shallow) and ~ 14–19 km (deep). Dike intrusions tapped the shallow and deep storage in a different manner during individual eruptions of Krafla, and primitive magma erupted north of the caldera flowed from the deep storage zone directly to the surface without being stored in the shallow zone. We suggest this distributed storage of basaltic magma may correspond to a magma domain ranging over a depth interval of ~ 5–12 km. In this case, a prolate ellipsoidal volume, with a larger vertical extent than a sphere with a radius of 2.4 km, may better represent the magma domain. Anderson and Segall (2011) demonstrated that the mechanical compressibility difference between a sphere and a prolate ellipsoid within an elastic half-space is less than 25%, whereas the difference between a sphere and a penny-shaped crack is two orders of magnitude. Assuming a prolate ellipsoidal magma domain rather than a spherical one is unlikely to affect the first-order regularities of the dike sequence behavior and variations in inlet overpressure.

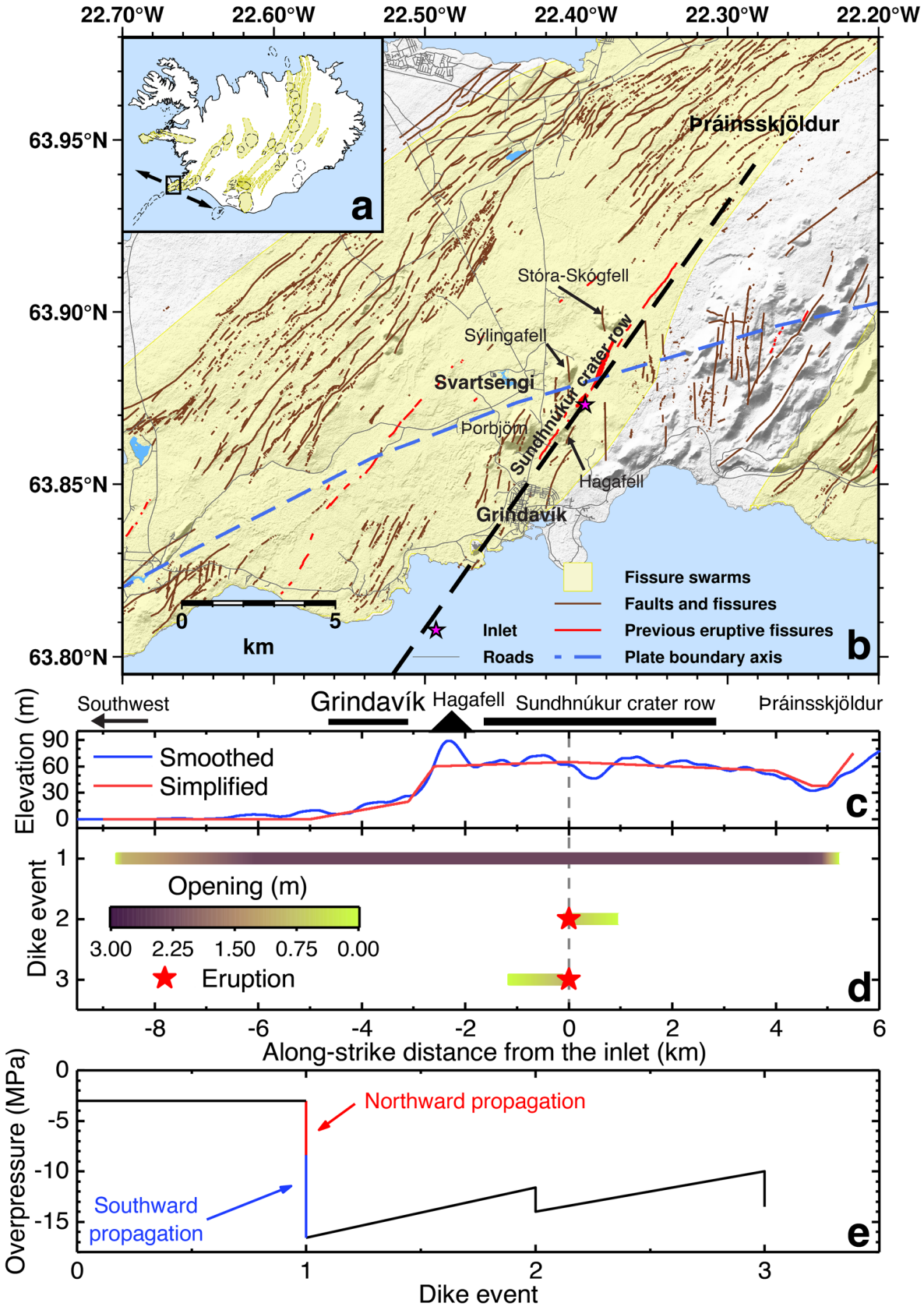
Parameter sensitivity analysis

Equation 9 indicates that most parameters in the model are correlated, among which the most simple and straightforward correlation is between the radius and compressibility of the magma domain. Changing one parameter value may be accommodated by adjusting one or more other parameters to obtain a similar spatial distribution of dike openings. Thus, it is important to constrain as many parameters as possible from previous research (Table 1). The failure limit explored in this study is in the range of ~ 1–20 MPa, comparable to tensile strength indicated by laboratory rock tests (Zhan and Gregg 2019) and dike tensile strength of < 10 MPa constrained by geodetic observations for large-scale strength of rocks inferred by Jónsson (2012). Poisson's ratio in Table 1 is close to the average value in Heap et al. (2020), and its range in Table 1 overlaps largely with values from previous models or experimental data. Shear modulus of 10 GPa has been applied for other volcanological models in Iceland (e.g., Hartley and Maclennan 2018; Juncu et al. 2020; Sigmundsson et al. 2024). Dike height is constrained with ground deformation by Hollingsworth et al. (2013).

We evaluate in particular the sensitivity of free parameters to validate the conclusion that a relatively low magma overpressure at a fissure swarm inlet prior to the Krafla rifting episode can broadly explain the dike sequence behavior. We adjust one individual parameter at a time and fix other parameters at their plausible values in Table 1. The parameter ranges in Table 1 are obtained by testing when the dike opening distribution (Fig. 4b) changes significantly, e.g., any dike propagates in the other direction, or the dikes propagate out of the range of the fissure swarm.

The parameter ranges indicate the model is least sensitive to dike tapering factor ε and pressure change ratio γ since the volume of the front section is small compared to the dike length. The host rock density, which controls the magnitude of dike driving pressure from the topographic effects, also has little influence on the dike pattern prediction. The density range in Table 1 is within a larger range of rock density ~ 1800–2700 kg/m^3 for the Krafla area inferred by petrological and geophysical studies (Eggertsson et al. 2020; Darbyshire et al. 2000). Different assumptions of rock density do not alter the significance of topographic effects driving long-distance dike propagation, and similar dike opening distributions are obtained. Our parameter sensitivity analysis shows that the maximum percentage of tectonic stress relieved by an individual dike (α) should be less than 73%, indicating that individual dikes release only part of the tectonic stress accumulated prior to a rifting episode. Nevertheless, varying the value of α between 59% and 73% does not change the model predictions significantly, since it is not the only factor limiting dike openings, e.g., the size of the magma domain also contributes (Buck et al. 2006).

Our model demonstrates that initially low magma overpressure at the inlet may broadly explain the dike sequence behavior during the 1975–1984 Krafla rifting episode, where the failure limit and tectonic stress play important roles. The failure limit determines the initial disequilibrium in the inlet-dike system in Eq. (9). A higher failure limit requires a larger volume of magma extracted from the inlet to resume equilibrium, influencing the dike opening distribution. With the same percentage of tectonic stress relieved, higher accumulated tectonic stress prior to the rifting episode leads to more lateral dikes and predicts no eruption for the first ten events in the Krafla rifting episode. In Table 1, the highest value of the failure limit of 15.9 MPa for the first dike and the lowest value of tensile tectonic stress of 11.9 MPa still give an inlet overpressure of only 4 MPa prior to the rifting episode. Further trials of parameter combinations give a maximum possible magma overpressure of ~ 10 MPa prior to the rifting episode. The ratio of 1.8–2.2 between the failure limits of the first and later dikes leads to a similar prediction of dike opening distribution. This parameter controls the inlet overpressure difference at the initiations of the first and second


22.70°W
22.60°W
22.50°W
22.40°W
22.30°W
22.20°W
63.95°N
63.90°N
63.85°N
63.80°N
a
Þráinsskjöldur
Stóra-Skógfell
Sýlingafell
Svartsengi
Þorbjörn
Sundhnúkur crater row
Hagafell
Grindavík
0
5
km
Fissure swarms
Faults and fissures
Previous eruptive fissures
Plate boundary axis
Inlet
Roads
b
Southwest
Grindavík
Hagafell
Sundhnúkur crater row
Þráinsskjöldur
Elevation (m)
90
60
30
0
Smoothed
Simplified
c
Dike event
1
2
3
Opening (m)
3.00 2.25 1.50 0.75 0.00
Eruption
d
-8
-6
-4
-2
0
2
4
6
Along-strike distance from the inlet (km)
Overpressure (MPa)
0
-5
-10
-15
Northward propagation
Southward propagation
e
0
1
2
3
Dike event

◂**Fig. 5** A plausible dike sequence model for the first three dikes of the 2023–2025 Svartsengi rifting episode, SW Iceland. **a** A map of Iceland illustrating the location of the Svartsengi area with the black rectangle. The arrows indicate the direction of plate spreading in the Svartsengi area. **b** A map of the Svartsengi area. The black dashed line indicates the approximate strike of the dike intruded in November 2023 from Sigmundsson et al. (2024). Þráinsskjöldur is a lava shield formed around 14,100 years ago with general higher elevation than its surroundings (Jónsson 1978). The faults and fissures are from Clifton and Kattenhorn (2006), the fissure swarms are from Jóhannesson and Sæmundsson (2009), the plate boundary axis is from Sigmundsson et al. (2024) and the topography is from LMÍ (2020). **c** Elevation profile along the strike of the first dike. The smoothed one is derived from the real topography with Savitzkyp-Golay filter. **d** The distribution of dike openings predicted by the revised dike sequence model for the three dike intrusions. **d** Variation of overpressure from the magma supply into the magma domain predicted by the revised dike sequence model

dikes, where a comparison between observed and predicted elevation change in Fig. 4f favors a ratio of 2.

The case of the 2023–2025 Svartsengi rifting episode

A dike sequence similar to the 1975–1984 Krafla rifting episode has occurred at the Sundhnúkur crater row in the Svartsengi volcanic system, SW Iceland (Fig. 5; Sigmundsson et al. 2024; Parks et al. 2025). The first dike intrusion formed a ~ 14-km-long dike in November 2023, ~ 6 km to the north and ~ 8 km from a fissure swarm inlet inferred from all seven dike intrusions during November 2023 and July 2024 (Fig. 5b; Parks et al. 2025). Eight more dike intrusions with seven eruptions manifest alternations between southward and northward propagation.

We applied our revised dike sequence model to the first three events of the rifting episode. Our model inherently assumes unidirectional propagation. However, for the first dike at the Sundhnúkur crater row, the ratio between the northeast and southwest propagation distances is 0.75 (6 km over 8 km), compared to ~ 0.25 between the southward and northward propagation of the first dike at Krafla (~ 15 km over ~ 60 km). Hence, the first dike is modeled with two separate iterations in the numerical implementation—once the central section of the dike reaches the fissure swarm inlet, all remaining overpressure at the inlet is used to calculate the dike opening in the other direction. This is only to predict the final opening distribution of such bilateral dike propagation without any indication of its temporal evolution. The initial propagating direction is imposed by setting the elevation gradient slightly steeper to the north since later events of the rifting episode propagate more to the north (Parks et al. 2025). Topographic stresses are calculated from a simplified elevation profile along the strike of the first dike (Fig. 5c). The parameter settings of one plausible model are listed in Table S2 in Online Resource 1.

Figure 5d, e shows the predictions of the model. Tectonic stress reductions with dike intrusions are presented in Fig. S5 in Online Resource 1. The part in the fissure swarm opened by the first dike is predicted to be 14 km long with the average opening up to ~ 3 m (Fig. 5d), in the magnitude range of ~ 2–7 m by geodetic inversions (Sigmundsson et al. 2024). The second and third events propagate to the north and south, respectively, consistent with the locations of eruptive fissures (Parks et al. 2025). The predicted overpressure variation at the inlet in Fig. 5e indicates that the northward propagation of ~ 5 km reduces ~ 5.3 MPa of inlet overpressure, while the southward propagation of ~ 9 km reduces ~ 8.2 MPa. Considering simple proportion to the propagation distances, the pressure drop from the southward propagation is expected to be ~ 9.5 MPa. A relatively low pressure drop from the southward propagation predicted by the model may relate to the elevation decrease northeast of Grindavík, which contributes some 2 MPa of dike driving pressure, highlighting the importance of topographic effects. In this model, a maximum buoyancy effect of 9 MPa (Sigmundsson et al. 2024) and tectonic stress allow dike initiations when overpressure from magma supply into the domain is ~ −3 MPa. If the accumulated tectonic stress prior to the rifting episode is smaller than 7.7 MPa, the model predicts eruption already for the first dike intrusion. These again highlight the contributions of topography to dike propagation distances, the importance of tectonic stress for relatively low magma overpressure at the inlet to initiate dikes, and possibly for the absence of eruptions in the initial event.

Overpressure added by magma upward migration before its lateral propagation (p_u) is 6 MPa in this case compared to zero in the model for the Krafla rifting episode as presented above. Geodetic models inferred that the magma domain at Svartsengi is ~ 2 km below the intruded dikes, leading to ineligible density difference between the magma and encasing rocks, as well as overpressure increase from upward migration (Sigmundsson et al. 2024). The largest difference in parameter values between the Svartsengi and Krafla dike sequence model is the tapering factor, which is 2000 Pa/m for the Svartsengi case, 15 times larger than that for the Krafla case, possibly indicating varied stress along the oblique rift or dike propagating away from the preexisting weak zone (Jenness and Clifton 2009; Philippon et al. 2015; Greiner et al. 2025).

Conclusions

To reexamine the role of tectonic stress and topography in controlling the spatial distribution of dike openings during the 1975–1984 Krafla rifting episode, north Iceland, we propose a revised version of the Buck et al. (2006) dike sequence model. In our model, a dike starts by lateral flow

of magma from an inlet into a fissure swarm. The dike propagates along a positive gradient of driving pressure until the local maximum of driving pressure is reached. Magma intrusion stops once a pressure equilibrium between the dike and the inlet is re-established, that is, no pressure gradient to drive the dike further. The revised model (i) assumes a three-section dike geometry with tapering toward its far end, (ii) restricts the tectonic stress released by individual dike intrusions as well as by the entire dike sequence, (iii) incorporates magma compressibility in mass conservation between a magma domain and a set of dikes, and (iv) determines where dike tapering begins based on the cumulative stress profile before resolving the spatial distribution of dike opening. The model reproduces realistic dike geometries and magma pressure changes, in agreement with geophysical observations and geodetic models of rifting episodes, and our modeling provides deeper insights into the evolution of tectonic stress at divergent plate boundaries.

Using a plausible parameter setting, our model predicts dike openings and inlet overpressure variations that are consistent with the geophysical observations and previous models for the 1975–1984 Krafla rifting episode. The model indicates the fissure swarm inlet locates 2–4 km north of the Krafla caldera center. Parameter sensitivity analysis suggests a relatively low magma overpressure at the inlet of < 10 MPa prior to the first and the largest dike intrusion of the entire dike sequence, compared to > 20 MPa of initial dike driving pressure contributed by tectonic stress and topographic effects. Modeling results favor a failure pressure limit ratio of 2 between the first and successive dikes. A larger failure limit for the first dike compared to later dikes, a significant tectonic stress component along the dikes' paths, and the compressibility of the magma domain permit magma flow into later dikes even when pressure conditions are below lithostatic at the LNB.

The model is adapted for the first three dikes in the 2023–2025 Svartsengi rifting episode, SW Iceland, during November 2023 to January 2024. Predicted dike openings have comparable magnitudes with those from geodetic inversions, and the predicted propagation directions of dikes causing eruptions are consistent with the locations of eruptive fissures. For the first dike, topographic effects contribute about 2 MPa higher driving pressure for the southward dike propagation than for the northward propagation. A buoyancy effect of 9 MPa and a tensile tectonic stress of 8 MPa allow the first dike to initiate when the overpressure from magma supply in the domain is 3 MPa lower than the lithostatic pressure. The model also indicates that the tensile stress at the plate boundary was at least 7.7 MPa and inhibited eruption during initial dike formation from the magma domain by preferentially channeling magma towards lateral propagation.

Supplementary information The online version contains supplementary material available at https://doi.org/10.1007/s00445-025-01897-y.

Acknowledgements We thank the reviewer and the Editor, Marie Edmonds, for their insightful comments. We acknowledge discussions with Vincent Drouin, Magnús Tumi Gudmundsson, Giuseppe Puglisi, Juliet Biggs, Sæmundur Ari Halldórsson, and John Maclennan. Y.Y. thanks Ana Martinez Garcia, Elisabeth Glück, and Roberto Davoli in the IMPROVE project for discussions on the crustal properties in the Krafla area and thanks Chiara Lanzi for helping with the finite element model in the Supplementary Materials. Figures 1 and 5a are plotted with the Generic Mapping Tools (Wessel et al. 2019).

Funding This study received funding from the European Union's Horizon 2020 research and innovation programme under grant agreement No. 858092 (IMPROVE project). JG's contributions have been supported by Y. Lavallee's European Research Council (ERC) Consolidator Grant MODERATE under grant agreement No. 101001065.

Data availability The study builds on published data.

Code availability The MATLAB scripts of the model are available upon request to the correspondence.

Declarations

Conflict of interest The authors declare no competing interests.

Open Access This article is licensed under a Creative Commons Attribution 4.0 International License, which permits use, sharing, adaptation, distribution and reproduction in any medium or format, as long as you give appropriate credit to the original author(s) and the source, provide a link to the Creative Commons licence, and indicate if changes were made. The images or other third party material in this article are included in the article's Creative Commons licence, unless indicated otherwise in a credit line to the material. If material is not included in the article's Creative Commons licence and your intended use is not permitted by statutory regulation or exceeds the permitted use, you will need to obtain permission directly from the copyright holder. To view a copy of this licence, visit http://creativecommons.org/licenses/by/4.0/.

References

Abdallah A, Courtillot V, Kasser M, Le Dain A-Y, Lépine J-C, Robineau B et al (1979) Relevance of Afar seismicity and volcanism to the mechanics of accreting plate boundaries. Nature 282:17–23. https://doi.org/10.1038/282017a0

Anderson K, Segall P (2011) Physics-based models of ground deformation and extrusion rate at effusively erupting volcanoes. J Geophys Res 116:B07204. https://doi.org/10.1029/2010JB007939

Árnadóttir T, Sigmundsson F, Delaney PT (1998) Sources of crustal deformation associated with the Krafla, Iceland, eruption of September 1984. Geophys Res Lett 25(7):1043–1046. https://doi.org/10.1029/98GL50655

Biggs J, Amelung F, Gourmelen N, Dixon TH, Kim S-W (2009) InSAR observations of 2007 Tanzania rifting episode reveal mixed fault and dyke extension in an immature continental rift. Geophys J Int 179(1):549–558. https://doi.org/10.1111/j.1365-246X.2009.04262.x

Björnsson A, Eysteinsson H (1998) Breytingar á landhæð við Kröflu 1974–1995: Samantekt á landhæðarmælingum [Changes in ground elevation at Krafla 1974–1995: Summary of elevation

measurements]. National Energy Authority, Nordic Volcanological Institute and Landsvirkjun, Report OS-98002, Reykjavík, Iceland (in Icelandic). https://gogn.orkustofnun.is/Skyrslur/OS-1998/OS-98002.pdf

Björnsson A, Saemundsson K, Einarsson P, Tryggvason E, Grönvold K (1977) Current rifting episode in north Iceland. Nature 266:318–323. https://doi.org/10.1038/266318a0

Björnsson A, Johnsen G, Sigurdsson S, Thorbergsson G, Tryggvason G (1979) Rifting of the plate boundary in north Iceland 1975–1978. J Geophys Res 84(B6):3029–3038. https://doi.org/10.1029/JB084iB06p03029

Blake S (1981) Volcanism and the dynamics of open magma chambers. Nature 289:783–785. https://doi.org/10.1038/289783a0

Brandsdóttir B, Menke W, Einarsson P, White RS, Staples RK (1997) Færoe-Iceland Ridge Experiment 2. Crustal structure of the Krafla central volcano. J Geophys Res Solid Earth 102(B4):7867–7886. https://doi.org/10.1029/96JB03799

Buck WR, Einarsson P, Brandsdóttir B (2006) Tectonic stress and magma chamber size as controls on dike propagation: constraints from the 1975–1984 Krafla rifting episode. J Geophys Res Solid Earth 111:B12404. https://doi.org/10.1029/2005JB003879

Clifton AE, Kattenhorn SA (2006) Structural architecture of a highly oblique divergent plate boundary segment. Tectonophysics 419(1–4):27–40. https://doi.org/10.1016/j.tecto.2006.03.016

Corbi F, Rivalta E, Pinel V, Maccaferri F, Acocella V (2016) Understanding the link between circumferential dikes and eruptive fissures around calderas based on numerical and analog models. Geophys Res Lett 43:6212–6219. https://doi.org/10.1002/2016GL068721

Dahm T (2000) On the shape and velocity of fluid-filled fractures in the Earth. Geophys J Int 142:181–192. https://doi.org/10.1046/j.1365-246x.2000.00148.x

Dahm T (2002) Numerical simulations of the propagation path and the arrest of fluid-filled fractures in the Earth. Geophys J Int 141:623–638. https://doi.org/10.1046/j.1365-246x.2000.00102

Daniels KA, Menand T (2015) An experimental investigation of dyke injection under regional extensional stress. J Geophys Res Solid Earth 120:2014–2035. https://doi.org/10.1002/2014JB011627

Darbyshire FA, White RS, Priestley KF (2000) Structure of the crust and uppermost mantle of Iceland from a combined seismic and gravity study. Earth Planet Sci Lett 181(3):409–428

DeMets C, Gordon RG, Argus DF (2010) Geologically current plate motions. Geophys J Int 181:1–80. https://doi.org/10.1111/j.1365-246X.2009.04491.x

Drouin V, Sigmundsson F, Ófeigsson BG, Hreinsdóttir S, Sturkell E, Einarsson P (2017) Deformation in the Northern Volcanic Zone of Iceland 2008–2014: an interplay of tectonic, magmatic, and glacial isostatic deformation. J Geophys Res Solid Earth 122:3158–3178. https://doi.org/10.1002/2016JB013206

Eggertsson GH, Kendrik JE, Weaver J, Wallace PA, Utley JEP, Bedford JD et al (2020) Compaction of hyaloclastite from the active geothermal system at Krafla volcano, Iceland. Geofluids 2020:3878503. https://doi.org/10.1155/2020/3878503

Einarsson P (1978) S-wave shadows in the Krafla Caldera in NE-Iceland, evidence for a magma chamber in the crust. Bull Volcanol 41:187–195. https://doi.org/10.1007/BF02597222

Einarsson P (1991) Umbrotin við Kröflu 1975–89 (The activity of Krafla 1975–1989, in Icelandic). In: Garðarsson A, Einarsson Á (eds), Náttúra Mývayns (Lake Myvatn). Hið íslenska nàttúrufræðifélag (The Icelandic Natural History Society), Reykjavík, pp 97–139

Einarsson P, Brandsdóttire B (2021) Seismicity of the Northern Volcanic Zone of Iceland. Front Earth Sci 9:628967. https://doi.org/10.3389/feart.2021.628967

Ewart JA, Voight B, Björnsson A (1991) Elastic deformation models of Krafla Volcano, Iceland, for the decade 1975 through 1985. Bull Volcanol 53:436–459. https://doi.org/10.1007/BF00258184

Fialko YA, Rubin AM (1998) Thermodynamics of lateral dike propagation: implications for crustal accretion at slow spreading mid-ocean ridges. J Geophys Res 103(B2):2501–2514. https://doi.org/10.1029/97JB03105

Grandin R, Socquet A, Jacques E, Mazzoni N, de Chabalier J-B, King GCP (2010) Sequence of rifting in Afar, Manda-Hararo rift, Ethiopia, 2005–2009: time-space evolution and interactions between dikes from interferometric synthetic aperture radar and static stress change modeling. J Geophys Res Solid Earth 115:B10413. https://doi.org/10.1029/2009JB000815

Greiner SHM, Sigmundsson F, Geirsson H, Burchardt S, Galland O (2025) Tectonic stress as the driving mechanism for dike opening in an oblique rift setting: a deformation model of the 2021 Fagradalsfjall dike, Iceland. Geophys Res Lett 52:e2024GL113970. https://doi.org/10.1029/2024GL113970

Hartley M, Maclennan J (2018) Magmatic densities control erupted volumes in Icelandic volcanic systems. Front Earth Sci 6:29. https://doi.org/10.3389/feart.2018.00029

Heap MJ, Villeneuve M, Albino F, Farquharson JI, Brothelande E, Amelung F, Got J-L, Baud P (2020) Towards more realistic values of elastic moduli for volcano modelling. J Volcanol Geotherm Res 390:106684. https://doi.org/10.1016/j.jvolgeores.2019.106684

Heimisson ER, Einarsson P, Sigmundsson F, Brandsdóttir B (2015a) Kilometer-scale Kaiser effect identified in Krafla volcano, Iceland. Geophys Res Lett 42(19):7958–7965. https://doi.org/10.1002/2015GL065680

Heimisson ER, Hooper A, Sigmundsson F (2015b) Forecasting the path of a laterally propagating dike. J Geophys Res Solid Earth 120:8774–8792. https://doi.org/10.1002/2015JB012402

Hjartardóttir ÁR, Einarsson P, Bramham E, Wright T (2012) The Krafla fissure swarm, Iceland, and its formation by rifting events. Bull Volcanol 74:2139–2153. https://doi.org/10.1007/s00445-012-0659-0

Hjartardóttir ÁR, Einarsson P, Magnúsdóttir S, Björnsdóttir Þ, Brandsdóttir B (2015) Fracture systems of the Northern Volcanic Rift Zone, Iceland: an onshore part of the Mid-Atlantic plate boundary. In: Wright T, Ayele A, Ferguson DJ, Kidane T, Vye-Brown C (eds) Magmatic Rifting and Active Volcanism. Geological Society, London, Special Publications, pp 297–314

Hollingsworth J, Leprince S, Ayoub F, Avouac J-P (2012) Deformation during the 1975–1984 Krafla rifting crisis, NE Iceland, measured from historical optical imagery. J Geophys Res Solid Earth 117:B11407. https://doi.org/10.1029/2012JB009140

Hollingsworth J, Leprince S, Ayoub F, Avoiac JP (2013) New constraints on dike injection and fault slip during the 1975–1984 Krafla rift crisis, NE Iceland. J Geophys Res Solid Earth 118:3707–3727. https://doi.org/10.1002/jgrb.50223

Huppert HE, Woods AW (2002) The role of volatiles in magma chamber dynamics. Nature 420:493–495. https://doi.org/10.1038/nature01211

Jenness MH, Clifton AE (2009) Controls on the geometry of a Holocene crater row: a field study from southwest Iceland. Bull Volcanol 71:715–728. https://doi.org/10.1007/s00445-009-0267-9

Jóhannesson H, Sæmundsson K (2009) Geological map of Iceland (1:600,000) – Tectonics [dataset]. Icelandic Institute of Natural History, Reykjavík, Iceland. https://gatt.lmi.is/geonetwork/srv/eng/catalog.search#/metadata/467EBAA3-E603-4E4C-A61F-2FFE9D19C11D. Accessed 22 Apr 2024

Johnsen G, Bjornsson A, Sigurdsson S (1980) Gravity and elevation changes caused by magma movement beneath the Krafla caldera, Northeast Iceland. J Geophys 47(1):132–140

Jónsson J (1978) Geological map of the Reykjanes Peninsula: notes to geological maps (in Icelandic). National Energy Authority, Report and Map OS-JHD-7831, Reykjavík, Iceland. https://rafhladan.is/handle/10802/4981

Jónsson S (2012) Tensile rock mass strength estimated using InSAR. Geophys Res Lett 39:L21305. https://doi.org/10.1029/2012GL053309

Juncu D, Árnadóttir Th, Geirsson H, Guðmundsson GB, Lund B, Gunnarsson G, Hooper A, Hreinsdóttir S, Michalczewska K (2020) Injection-induced surface deformation and seismicity at the Hellisheidi geothermal field, Iceland. J Volcanol Geotherm Res 391:106337. https://doi.org/10.1016/j.jvolgeores.2018.03.019

Kim D, Brown LD, Árnason K, Gudmundsson Ó, Águstsson K, Flóvenz ÓG (2020) Magma "bright spots" mapped beneath Krafla, Iceland, using RVSP imaging of reflected waves from microearthquakes. J Volcanol Geotherm Res 391:106365. https://doi.org/10.1016/j.jvolgeores.2018.04.022

Lanzi C, Drouin V, Sigmundsson F, Geirsson H, Hersir GP, Ágústsson K, Parks MM, Hreinsdóttir S, Guðmundsson Á (2023) Pressure increase at the magma-hydrothermal interface at Krafla caldera, North-Iceland, 2018–2020: magmatic processes or hydrothermal changes? J Volcanol Geotherm Res 440:107849. https://doi.org/10.1016/j.jvolgeores.2023.107849

LMÍ (2020) ÍslandsDEM útgáfa 1.0. Landmælingar Íslands. https://gatt.natt.is/geonetwork/srv/api/records/e6712430-a63c-4ae5-9158-c89d16da6361. Accessed 18 Mar 2024

Magee C, Jackson CAL (2020) Can we relate the surface expression of dike-induced normal faults to subsurface dike geometry? Geology 49(4):366–371. https://doi.org/10.1130/G48171.1

McTigue DF (1987) Elastic stress and deformation near a finite spherical magma body: resolution of the point source paradox. J Geophys Res Solid Earth 92(B12):12931–12940. https://doi.org/10.1029/JB092iB12p12931

Mogi K (1958) Relation between the eruption of various volcanoes and the deformation of the ground surface around them. Bull Earthquake Res Inst 36:99–134

Mortensen AK, Egilson Þ, Gautason B, Árnadóttir S, Guðmundsson Á (2014) Stratigraphy, alteration mineralogy, permeability and temperature conditions of well IDDP-1, Krafla, NE-Iceland. Geothermics 49:31–41. https://doi.org/10.1016/j.geothermics.2013.09.013

Natashima Y (1993) Static stability and propagation of a fluid–filled crack in rock: implication for fluid transport in magmatism and metamorphism. J Phys Earth 41(3):189–202

Okada Y (1985) Surface deformation due to shear and tensile faults in a half-space. Bull Seismol Soc Am 75(4):1135–1154. https://doi.org/10.1785/BSSA0750041135

Opheim JA, Gudmundsson A (1989) Formation and geometry of fractures, and related volcanism, of the Krafla fissure swarm, northeast Iceland. Geol Soc Am Bull 101(12):1608–1622. https://doi.org/10.1130/0016-7606(1989)101%3c1608:FAGOFA%3e2.3.CO;2

Paquet F, Dauteuil O, Hallot E, Moreau F (2007) Tectonics and magma dynamics coupling in a dyke swarm of Iceland. J Struct Geol 29(9):1477–1493. https://doi.org/10.1016/j.jsg.2007.06.001

Parks M, Sigmundsson F, Drouin V, Hjartardóttir ÁR, Geirsson H, Hooper A (2023) Deformation, seismicity, and monitoring response preceding and during the 2022 Fagradalsfjall eruption, Iceland. Bull Volcanol 85:60. https://doi.org/10.1007/s00445-023-01671-y

Parks M, Drouin V, Sigmundsson F, Hjartardóttir ÁR, Geirsson H, Pedersen GBM et al (2025) 2023–2024 inflation-deflation cycles at Svartsengi and repeated dike injections and eruptions at the Sundhnúkur crater row, Reykjanes Peninsula, Iceland. Earth Planet Sci Lett 658:119324. https://doi.org/10.1016/j.epsl.2025.119324

Philippon M, Willingshofer E, Sokoutis D, Corti G, Sani F, Bonini M, Cloetingh S (2015) Slip re-orientation in oblique rifts. Geology 43(2):147–150. https://doi.org/10.1130/G36208.1

Poland MP, Moats WP, Fink JH (2007) A model for radial dike emplacement in composite cones based on observations from Summer Coon volcano, Colorado, USA. Bull Volcanol 70:861–875. https://doi.org/10.1007/s00445-007-0175-9

Pollard DD, Delaney PT, Duffield WA, Endo ET, Okamura AT (1983) Surface deformation in volcanic rift zones. Developments in Geotectonics 19:541–559, 563, 567–584. https://doi.org/10.1016/B978-0-444-42198-2.50036-5

Qin R, Buck WR (2008) Why meter-wide dikes at oceanic spreading centers? Earth Planet Sci Lett 265:466–474. https://doi.org/10.1016/j.epsl.2007.10.044

Rivalta E (2010) Evidence that coupling to magma chambers controls the volume history and velocity of laterally propagating intrusions. Journal of Geophysical Research: Solid Earth 115:B07203. https://doi.org/10.1029/2009JB006922

Rivalta E, Taisne B, Bunger AP, Katz RF (2015) A review of mechanical models of dike propagation: schools of thought, results and future directions. Tectonophysics 638:1–42. https://doi.org/10.1016/j.tecto.2014.10.003

Rooyakkers SM, Carroll KJ, Gutai AF, Winpenny B, Bali E, Guðfinnsson GH et al (2024) Hydraulically linked reservoirs simultaneously fed the 1975–1984 Krafla Fires eruptions: insights from petrochemistry. Earth Planet Sci Lett 646:118960. https://doi.org/10.1016/j.epsl.2024.118960

Roper SM, Lister JR (2007) Buoyancy-driven crack propagation: the limit of large fracture toughness. J Fluid Mech 580:359–380. https://doi.org/10.1017/S0022112007005472

Rubin AM, Pollard DD (1987) Origins of blade-like dikes in volcanic rift zones. US Geol Surv Prof Pap 1350(2):1449–1470

Rubin AM, Pollard DD (1988) Dike-induced faulting in rift zones of Iceland and Afar. Geology 16(5):413–417. https://doi.org/10.1130/0091-7613(1988)016%3c0413:DIFIRZ%3e2.3.CO;2

Sæmundsson K (1991) Jarðfræði Kröflukerfisins (Geology of the Krafla volcanic system, in Icelandic). In: Garðarsson A, Einarsson A (eds), Náttúra Mývatns (Nature of Mývatn). Hið íslenska náttúrufræðifélag (The Icelandic Natural History Society), Reykjavík, Iceland, pp 24–95

Schuler J, Greenfield T, White RS, Roecker SW, Brandsdóttir B, Stock JM et al (2015) Seismic imaging of the shallow crust beneath the Krafla central volcano, NE Iceland. J Geophys Res Solid Earth 120(10):7156–7173. https://doi.org/10.1002/2015JB012350

Scott SW, Covell C, Júlíusson E, Valfells Á, Newson J, Hranfnkelsson B, Pálsson H, Gudjónsdóttir M (2019) A probabilistic geologic model of the Krafla geothermal system constrained by gravimetric data. Geotherm Energy 7:29. https://doi.org/10.1186/s40517-019-0143-6

Segall P, Cervelli P, Owen S, Lisowski M, Miklius A (2001) Constraints on dike propagation from continuous GPS measurements. J Geophys Res Solid Earth 106(B9):19301–19317. https://doi.org/10.1029/2001JB000229

Segall P, Anderson KR, Pulvirenti F, Wang T, Johanson I (2020) Caldera collapse geometry revealed by near-field GPS displacements at Kīlauea Volcano in 2018. Geophys Res Lett 47:e2020GL088867. https://doi.org/10.1029/2020GL088867

Sigmundsson F (2021) Recent basaltic eruptions in Iceland and the dynamics of co-eruptive subsurface magma flow. In: Papale P (ed) Forecasting and Planning for Volcanic Hazards, Risks, and Disasters. Elsevier, Amsterdam, pp 413–438. https://doi.org/10.1016/B978-0-12-818082-2.00010-X

Sigmundsson F, Hooper A, Hreinsdóttir S, Vogfjörd KS, Ófeigsson BG, Heimisson ER et al (2015) Segmented lateral dyke growth in a rifting event at Bárðarbunga volcanic system, Iceland. Nature 517:191–195. https://doi.org/10.1038/nature14111

Sigmundsson F, Pinel V, Grapenthin R, Hooper A, Halldórsson SA, Einarsson P et al (2020) Unexpected large eruptions from buoyant magma bodies within viscoelastic crust. Nat Commun 11:2403. https://doi.org/10.1038/s41467-020-16054-6

Sigmundsson F, Parks M, Geirsson H, Hooper A, Drouin V, Vogfjörd KS et al (2024) Fracturing and tectonic stress drive ultrarapid magma flow into dikes. Science 383(6688):1228–1235. https://doi.org/10.1126/science.adn2838

Spera FJ (2000) Physical properties of magmas. In: Sigurdsson H (ed) Encyclopedia of volcanoes. Academic Press, San Diego, pp 171–190

Taisne B, Jaupart C (2009) Dike propagation through layered rocks. Journal of Geophysical Research: Solid Earth 114(B9):B09203. https://doi.org/10.1029/2008JB006228

The MathWorks Inc. (2023) MATLAB® (Version R2023b, Update 1) [Software]. Natick, Massachusetts, United States. Retrieved from https://www.mathworks.com

Townsend M, Huber C (2020) A critical magma chamber size for volcanic eruptions. Geology 48(5):431–435. https://doi.org/10.1130/G47045.1

Townsend MR, Pollard DD, Smith RP (2017) Mechanical models for dikes: a third school of thought. Tectonophysics 703:98–118. https://doi.org/10.1016/j.tecto.2017.03.008

Tryggvason E (1980) Subsidence events in the Krafla area, North Iceland, 1975–1979. J Geophys 41(1):141–153.

Tryggvason E (1984) Widening of the Krafla fissure swarm during the 1975–1981 volcano-tectonic episode. Bull Volcanol 47:47–69. https://doi.org/10.1007/BF01960540

Urbani S, Acocella V, Rivalta E, Corbi F (2017) Propagation and arrest of dikes under topography: models applied to the 2014 Bardarbunga (Iceland) rifting event. Geophys Res Lett 44:6692–6701. https://doi.org/10.1002/2017GL073130

Urbani S, Acocella V, Rivalta E (2018) What drives the lateral versus vertical propagation of dikes? Insights from analogue models. J Geophys Res Solid Earth 123:3680–3697. https://doi.org/10.1029/2017JB015376

Varugu B, Amelung F (2021) Southward growth of Mauna Loa's dike-like magma body driven by topographic stress. Sci Rep 11:9816. https://doi.org/10.1038/s41598-021-89203-6

Wessel P, Luis JF, Uieda L, Scharroo R, Wobbe F, Smith WHF, Tian D (2019) The generic mapping tools version 6. Geochem Geophys Geosyst 20:5556–5564. https://doi.org/10.1029/2019GC008515

Wilson L, Head JW (2002) Tharsis-radial graben systems as the surface manifestation of plume-related dike intrusion complexes: models and implications. J Geophys Res 107(E8):5057. https://doi.org/10.1029/2001JE001593

Wright TJ, Sigmundsson F, Pagli C, Belachew M, Hamling IJ, Brandsdóttir B et al (2012) Geophysical constraints on the dynamics of spreading centres from rifting episodes on land. Nat Geosci 5:242–250. https://doi.org/10.1038/ngeo1428

Zhan Y, Gregg PM (2019) How accurately can we model magma reservoir failure with uncertainties in host rock rheology? J Geophys Res Solid Earth 124:8030–8042. https://doi.org/10.1029/2019JB018178

Publisher's Note Springer Nature remains neutral with regard to jurisdictional claims in published maps and institutional affiliations.

Online resource 1: Supplementary text, figures and tables for model set-up and interpretation

Role of tectonic stress and topography on repeated lateral dikes: application to the 1975–1984 Krafla and 2023–2025 Svartsengi rifting episodes in Iceland

Yilin Yang[1] ✉ · Freysteinn Sigmundsson[1] · Halldór Geirsson[1] · Joachim Gottsmann[2]

[1] Nordic Volcanological Center, Institute and Faculty of Earth Sciences, University of Iceland, Reykjavík, Iceland

[2] Department of Earth and Environmental Sciences, Ludwig-Maximilians-Universität München, Munich, Germany

✉ **yiy1@hi.is**

This supplementary material provides additional information for the methodology, including: a list of symbols used in the manuscript (Table S1); the derivation of the relationship between dike opening and tectonic stress reduction for the model ('Derivation of Eq. (3) in the main text' and Fig. S1); the numerical expression of the segmented dike geometry for implementation ('Numerical expression of the segmented dike geometry'); and a demonstration of the searching in the numerical implementation of the model (Fig. S2). To further justify the model assumptions, a discussion on the connectivity between the inlet and rear section is also included. The driving pressure supplied by tectonic stress and topographic effects is referred to as external driving pressure in this text for simplicity.

To provide supplementary information for the model set-up for both applications, this material further includes the comparison between the smoothed and simplified topography along the Krafla fissure swarm (Fig. S3) and the model settings for the Svartsengi rifting episode (Table S2). Figure S4 compares the model predictions between the original and revised models. Figure S5 presents more modeling results for the Svartsengi rifting episode.

Table S1 List of symbols used in the manuscript in addition to model input parameters presented in Table 1. The positive or negative sign in the description column indicates the sign of the value of the parameters as typically used in the model. The last column shows where the parameters are involved; either influencing conditions in the dikes or in the fissure swarm inlet

Symbol	Description	Unit	Component
p_u	Magma overpressure gained during upward migration before lateral propagation (+)	Pa	Fissure swarm inlet
p_i	Magma overpressure at the fissure swarm inlet (+)	Pa	Fissure swarm inlet
Δp_i	Pressure change associated with magma extraction from the magma domain (-)	Pa	Fissure swarm inlet
p_e	Dike driving pressure supplied by topographic effects and tectonic stress (+)	Pa	Dike
$P_{driving}$	Net dike driving pressure including magma overpressure, buoyancy pressure and external contributions of p_e (+)	Pa	Fissure swarm inlet
$\sigma_{t,i}$	Tectonic stress at the fissure swarm inlet (varies with dike injections) (-)	Pa	Fissure swarm inlet
$\sigma_t(x)$	Tectonic stress at a location (x) along the dike path prior to dike intrusion (-)	Pa	Dike
$\Delta\sigma_t(x)$	Tectonic stress reduction at a location along the dike after dike intrusion (+)	Pa	Dike
ρ_d	Magma density in the dike (+)	kg/m^3	Dike
ρ_s	Magma density in the magma domain (+)	kg/m^3	Fissure swarm inlet
g	Gravity acceleration (+)	m/s^2	
$\Delta h(x)$	Surface elevation difference between a point along the dike path (location l) and the fissure swarm inlet (-)	m	Dike
$w(x)$	Dike opening at a location (x) along the dike path (+)	m	Dike
L	Length of the dike (+)	m	Dike
ΔL	Grid size of the dike length for numerical implementation (+)	m	Dike
d	Distance from the local maximum of driving pressure to a point in the front section of a dike (+)	m	Dike
A	A scaling factor used in the relationship between dike opening and tectonic stress reduction (+)	/	Dike
ΔM_d	Mass of a dike (after dike intrusion has ended) (+)	kg	Dike
ΔM_s	Mass change in the magma domain at the end of a dike intrusion (-)	kg	Fissure swarm inlet
β_s	Mechanical compressibility of the magma domain (depending on different assumptions on the magma domain geometry) (+)	Pa^{-1}	Fissure swarm inlet

Derivation of Eq. (3) in the main text

Equation 3 in the main text assumes that dike opening at each location along a dike scales with the release of pre-diking tectonic stress at that location. Qin and Buck (2008) suggested that the two-dimensional elastic model for an elliptical hole in an infinite region approximating the dike cross-section perpendicular to the dike plane (Fig. 2 in the main text) can provide a general guidance for calculating the dike opening. The dike opening (w) in this cross-section can be calculated by rewriting the equation (1B) and (4B) in Pollard et al. (1983) into:

$$w = \pm \frac{\Delta\sigma_e(1-\nu)\sqrt{\left(\frac{H}{2}\right)^2 - z^2}}{\mu}, \tag{S1}$$

where μ and ν are the shear modulus and Poisson's ratio of the host hock, respectively, H is the assumed height of the dike, z represents the vertical distance away from the central point of the dike cross-section, and $\Delta\sigma_e$ is the local tectonic stress change on the dike wall. The square root in Eq. (S1) diminishes to zero at the bottom and top of the dike. To derive the average opening on a dike cross-section, we integrate for Eq. (S1):

$$\int_{-\frac{H}{2}}^{\frac{H}{2}} w\mathrm{d}z = \frac{\Delta\sigma_e(1-\nu)}{\mu} \int_{-\frac{H}{2}}^{\frac{H}{2}} \left[\left(\frac{H}{2}\right)^2 - z^2\right]\mathrm{d}z = \frac{\Delta\sigma_e(1-\nu)}{\mu}\frac{\pi}{4}\left(\frac{H}{2}\right)^2, \tag{S2}$$

where only one side of the dike wall (positive part) is considered. The average of width of the dike is:

$$w_{avg} = \frac{4}{H}\int_{-\frac{H}{2}}^{\frac{H}{2}} w(x)\mathrm{d}z = \frac{\Delta\sigma_e(1-\nu)\pi H}{4\mu}. \tag{S3}$$

However, dikes forming in a rifting episode are highly influenced by their depths close to the free surface of the Earth, causing larger opening than anticipated in the full space approximation. A scaling factor, A, is introduced into Eq. (S3) and we have the Eq. (3) in the main text:

$$w(x) = A\frac{\pi H(1-\nu)}{4\mu}\Delta\sigma_t(x). \tag{S4}$$

To obtain an empirical value for this scaling factor A, we set up a finite element model (FEM) with uniform dike opening in a homogeneous elastic half space (Okada 1985; Pascal et al. 2014), using COMSOL Multiphysics® software v6.1 (2022). The dike is set to 3700 m height and 3000

m depth for the center, the same as estimated for the setting for the Krafla rifting episode. The elastic modulus of the host rock is also set the same as in the main text. We variate the length and the opening of the dike to investigate how the dike opening influence its surrounding stress field. The average normal stress on the dike plane at its central depth (Fig. S1b) within 2 km away from the dike is compared with the stress change derived with Eq. (S4) when $A = 2$ in Fig. S1a. The comparison indicates that for dike length larger than 10 km, normal stress change on the dike plane calculated using Eq. (S4) with $A = 2$ has only <10% difference from the FEM value. This empirical value is therefore taken in the derivation of the main text as the revised dike sequence model predicts dike lengths are in general larger than 10 km for the Krafla rifting episode, except for the ones with eruptions.

Numerical expression of the segmented dike geometry

In the main text, a dike is divided into three sections, the rear, central and front sections, extending from dike near end (nearest to the fissure swarm inlet) to the far end. The rear section features a uniform final external driving pressure. Within the central section, we apply uniform dike opening by assigning the maximum percentage of tectonic stress reduction $\Delta\sigma_t(x) = \alpha\sigma_{t,total}$. The front section starts from the location where dike driving pressure reaches its local maximum, and its opening tapers toward the dike far end.

If we denote a location along the dike as x, for x in the rear section, the external driving pressure (p_e) can be expressed numerically as follow:

$$p_e(x) = -\rho g\Delta h(x) - \sigma_t(x) - \Delta\sigma_t(x) = constant, \quad \text{(S5)}$$

where $\Delta\sigma_t(x)$ is variable. The dike near end would overlap with the inlet when $-\rho g\Delta h(x) - \sigma_t(x) - \Delta\sigma_t(x) \leq -\sigma_{t,i}$, where $\sigma_{t,i}$ is the tectonic stress at the inlet. When $-\rho g\Delta h(x) - \sigma_t(x) - \Delta\sigma_t(x) > -\sigma_{t,i}$, the near end would be located where $\Delta\sigma_t(x) = 0$ (Fig. S2).

For x in the central section,

$$p_e(x) = -\rho g\Delta h(x) - \sigma_t(x) - \alpha\sigma_{t,total}. \quad \text{(S6)}$$

Note that $\alpha\sigma_{t,total}$ is a constant for each dike. This section only exists when $p_e(x) < -(\rho g\Delta h_{max} + \sigma_{t,max}) - \alpha\sigma_{t,total}$ for x in the rear section, where the term $(\rho g\Delta h_{max} + \sigma_{t,max})$ represents the the local maximum value of the external driving pressure.

For x in the front section,

$$p_e(x) = -\rho g \Delta h_{max} - \sigma_{t,max} - \Delta\sigma_{t,max} + \varepsilon d - \rho g(\Delta h(x) - \Delta h_{max}), \quad \text{(S7)}$$

where $\Delta\sigma_{t,max}$ represents the tectonic stress change at the local maximum of dike driving pressure, and d represents the distance further away from that location. Equation S7 implements a linear decay of tectonic stress relief further away from the local maximum of driving pressure, considering a tapering factor (ε) with distance (d) and a local topographic effect. Dike propagation is assumed to stop when

$$\varepsilon d = (1 - \gamma)\Delta\sigma_{t,max}, \quad \text{(S8)}$$

or

$$p_e(x) = -\rho g \Delta h(x) - \sigma_t(x). \quad \text{(S9)}$$

The first condition is usually for positive to minor negative gradients of initial driving pressure in the front section, while the second is for significant negative gradient of initial driving pressure. The far end locates in an area with zero or negative gradient of driving pressure, otherwise the dike will propagate further to next area where driving pressure reaches its local maximum.

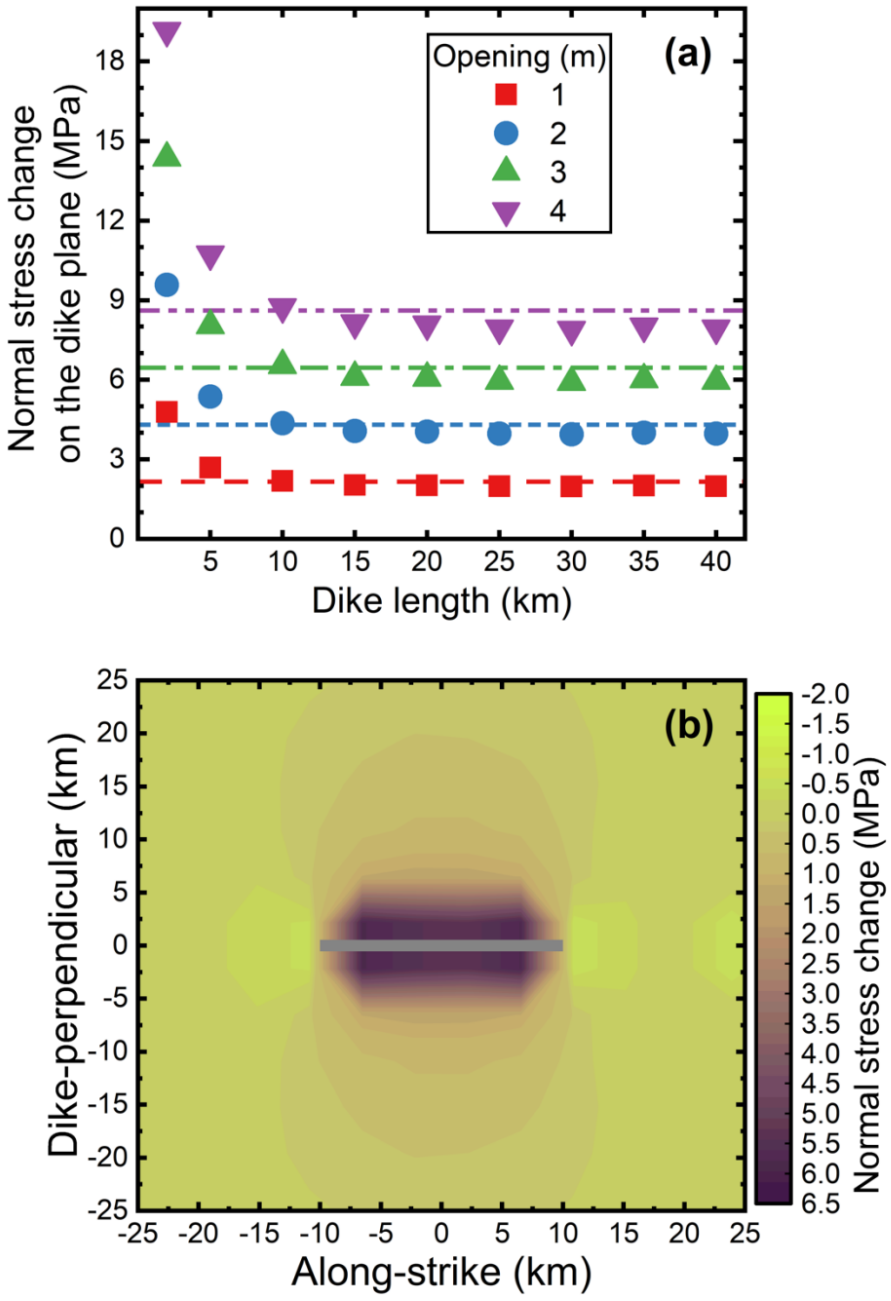


Fig. S1 Stress change induced by a uniform dike opening in a uniform elastic half-space. **a** The relationship between the dike length, dike opening and normal stress change on the dike plane. The dashed lines are calculated with Eq. (S4) and a scaling factor $A = 2$. **b** Exemplified spatial distribution of normal stress change on the dike plane at central depth of the dike, 3000 m. The grey line indicates the location of the dike. The dike has a 20 km length and opens 3 m, corresponding to the middle green triangle in Fig. S1a

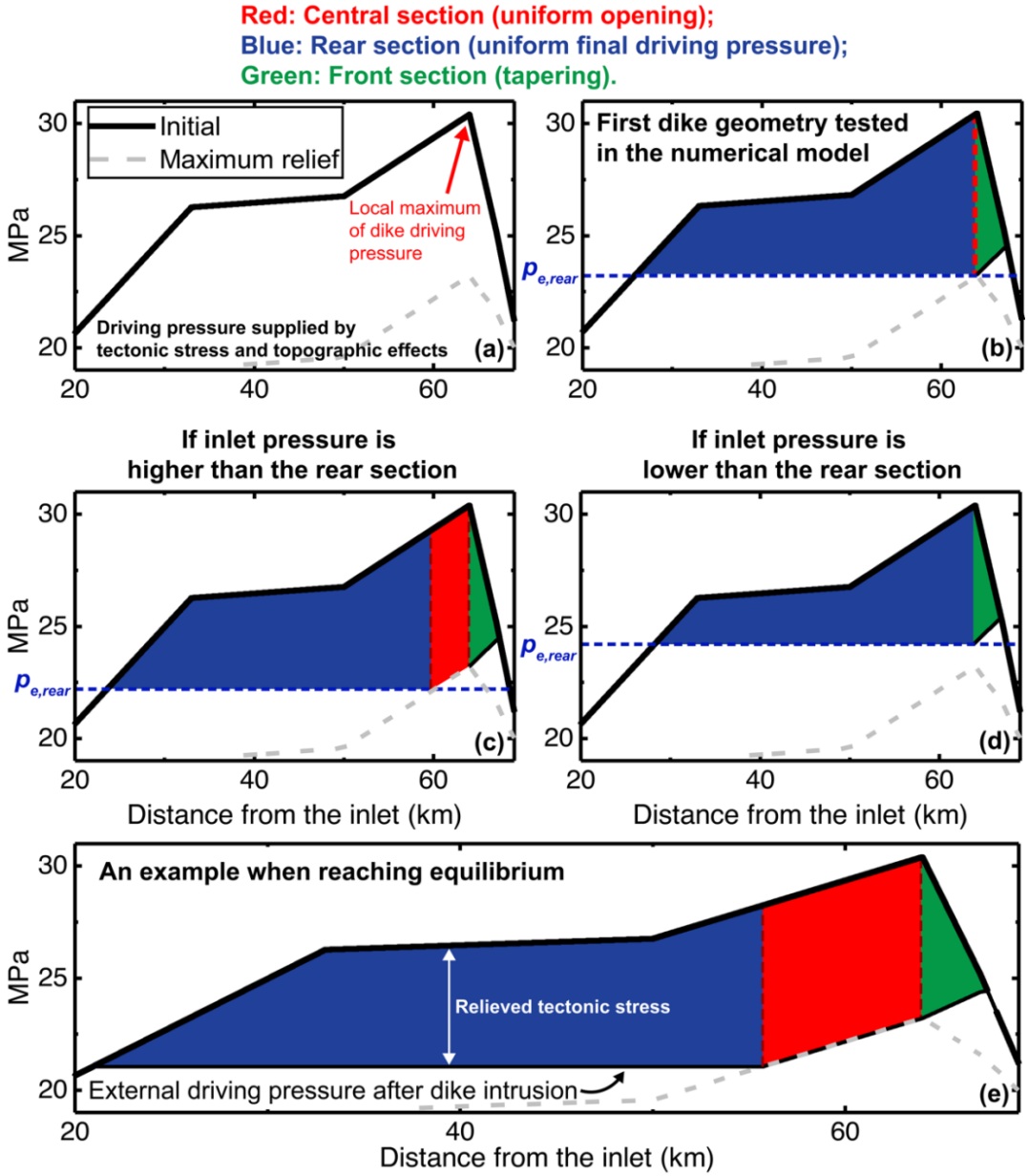


Fig. S2 Demonstration of our numerical modeling scheme and dike geometry indicated by external driving pressure distribution, exemplified with the first diking event of the Krafla rifting episode. **a** Initial external driving pressure. The grey dashed line indicates the external driving pressure level after the maximum percentage of tectonic stress is relieved. **b** The dike geometry first tested in the procedure of numerical modeling, of which the dike only has maximum opening at the local maximum of dike driving pressure (red vertical dashed line). The front section is determined from the local maximum of driving pressure and the tapering parameters. **c** and **d** show how the numerical model continues searching for the final pressure at the inlet and in the rear section. Panel c shows the case when the overpressure at the inlet is higher than the rear section after considering a pressure drop caused by a dike in panel b. Panel d shows the case when the overpressure at the inlet is lower than the rear section after considering a pressure drop caused by a dike in panel b. **e** An example of final external driving pressure when the equilibrium of the inlet-dike system is re-established

Connectivity between the inlet and rear section

Figure 4b in the main text shows that the openings of the first, second and sixth dikes locate offset laterally from the fissure swarm inlet. In this case the magma must travel in the fissure swarm and maintain the connection to the inlet for magma supply. Rivalta (2010) assumed a cylinder conduit with radius of 1 m connecting dike(s) and the feeding source to predict the flow rate variation during a dike intrusion. Tryggvason (1984) assigned ~0.5 m of surface widening between the inlet and the area with widening larger than 1 m. This connectivity is needed to predict the detailed dynamic processes of magma flow, but considered to have a negligible effect on our models for predicting the first-order regularities of a dike sequence.

The connectivity has limited influence on the eventual manifestation of a dike sequence. The magma volume related to this connectivity is small. Assuming the connectivity as a dike with opening of 0.5 m, height of 3700 m and length of 20 km for the first event in Fig. 4b in the main text, the magma volume within is only ~12% of the magma volume for the major dike opening. For the second and sixth dikes, this percentage decreases to ~10% and <6%, respectively. The conduit connectivity assumption in Rivalta (2010) yields smaller magma volume.

How the magma in this connectivity interact with later intrusions is uncertain. Despite that tectonic stress will be released if magma flow through the conduit deforms the host rock, reducing the tectonic stress and providing less driving pressure for later events, these magma conduits may also generate a zone of weakness in the crust supporting magma flow (Jenness and Clifton 2009). The general underestimation of volume loss in the magma domain during the latter two sub-sequences of dikes in Fig. 4e of the main text may demonstrate the complexity of these processes. Considering the connectivity in a detailed manner for this type of dike model we present requires more assumptions than we invoke here, and eventually causes problems in the model implementation.

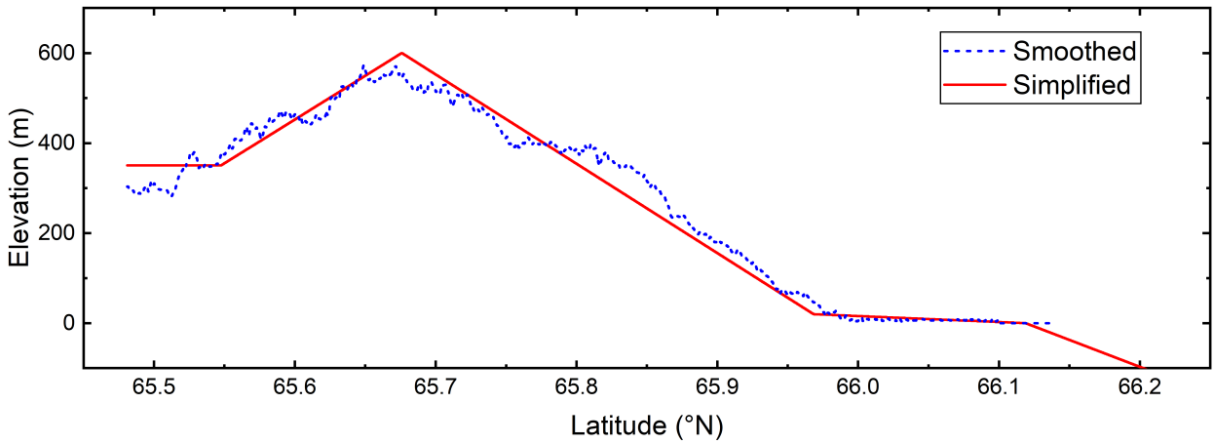


Fig. S3 Comparison between the elevation profile smoothed from actual topography and simplified for the revised dike sequence model. The blue curve is the same as shown in Fig. 1c in the main text

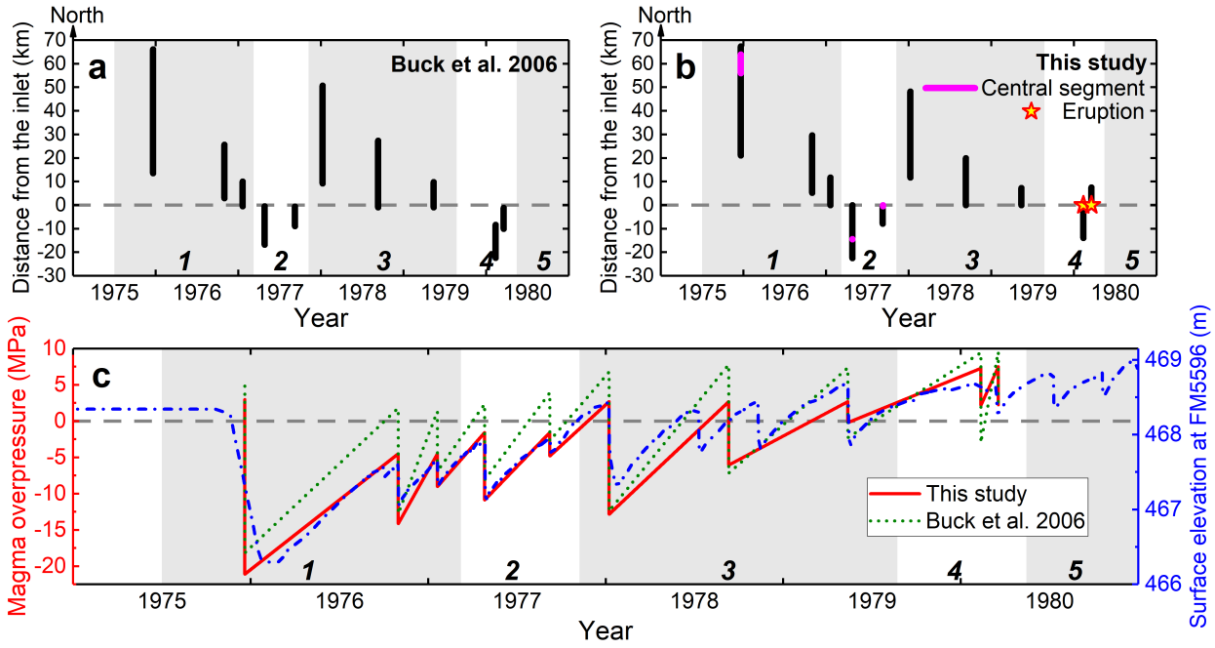


Fig. S4 Comparison between model prediction by the models in Buck et al. (2006) and this study. **a** The spatial distribution of dike openings predicted by the original model, extracted from Fig. 11 in Buck et al. (2006). **b** The spatial distribution of dike openings predicted by the revised model **c** Variation of the magma overpressure at the inlet predicted by the models, compared with the surface elevation change in the Krafla caldera center. The green curve is from Fig. 11 in Buck et al. (2006)

Table S2 A plausible setting of parameters of the revised dike sequence model for the 2023–2025 Svartsengi rifting episodes.

Parameter		Value	Reference
Tectonic stress $\sigma_{t,total}$ [MPa]		-8.0	Sigmundsson et al. (2024)
Pressure added from upward migration of magma before its lateral propagation (p_u) [MPa]		6.0	Sigmundsson et al. (2024)
Tensile strength P_o	First dike [MPa]	20.0	Parks et al. (2025)
	Rest of dikes [MPa]	5.0	
Magma domain	Radius R [m]	2510	Sigmundsson et al. (2024)
	Compressibility β_m [Pa^{-1}]	5.30×10^{-11}	Sigmundsson et al. (2024)
Host rock (<5 km depth)	Density ρ [kg/m^3]	2510	Table 1
	Poisson's ratio ν	0.20	Sigmundsson et al. (2024)
Dike	Height H [m]	3200	Sigmundsson et al. (2024)
	Central depth [m]	3000	Sigmundsson et al. (2024)
Maximum percentage of tectonic stress relieved by one dike α		80%	
Stress reduction ratio between the far end and the local maximum of dike driving pressure γ		0.30	
Tapering factor ε [Pa/m]		2000	

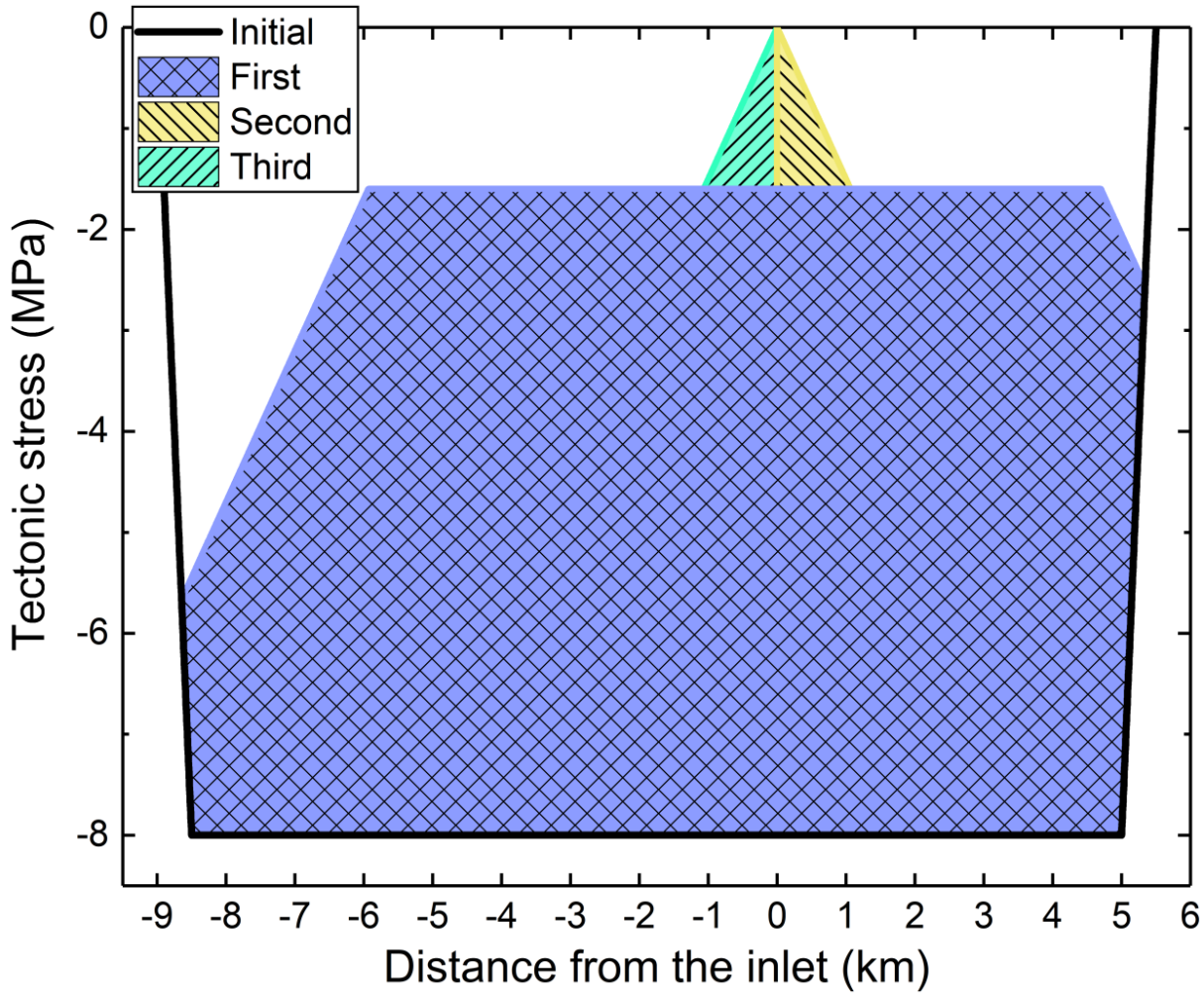


Fig. S5 Variation in tectonic stress predicted by the revised dike sequence model for the first three dike intrusions at the Sundhnúkur crater row. The tensile tectonic stress accumulated prior to the rifting episode is assumed to be 8 MPa with stress barriers on both sides away from the inlet.

References in this supplementary material

COMSOL Multiphysics® (2022) version 6.2. COMSOL AB, Stockholm, Sweden.

Buck WR, Einarsson P, Brandsdóttir B (2006) Tectonic stress and magma chamber size as controls on dike propagation: Constraints from the 1975–1984 Krafla rifting episode. J Geophys Res Solid Earth 111:B12404. https://doi.org/10.1029/2005JB003879

Greiner SHM, Sigmundsson F, Geirsson H, Burchardt S, Galland O (2025) Tectonic stress as the driving mechanism for dike opening in an oblique rift setting: A deformation model of the 2021 Fagradalsfjall dike, Iceland. Geophys Res Lett 52: e2024GL113970. https://doi.org/10.1029/2024GL113970

Jenness MH, Clifton AE (2009) Controls on the geometry of a Holocene crater row: a field study from southwest Iceland. Bull Volcanol 71:715-728. https://doi.org/10.1007/s00445-009-0267-9

Okada Y (1985) Surface Deformation due to Shear and Tensile Faults in a Half-Space. Bulletin of the Seismological Society of America 75:1135-1154. https://doi.org/10.1785/BSSA0750041135

Parks M, Drouin V, Sigmundsson F, Hjartardóttir ÁR, Geirsson H, Pedersen GBM et al (2025) 2023–2024 inflation-deflation cycles at Svartsengi and repeated dike injections and eruptions at the Sundhnúkur crater row, Reykjanes Peninsula, Iceland. Earth Planet Sci Lett 658:119324. https://doi.org/10.1016/j.epsl.2025.119324

Pascal K, Neuberg J, Rivalta E (2014) On precisely modelling surface deformation due to interacting magma chambers and dykes. Geophys J Int 196(1):253-278. https://doi.org/10.1093/gji/ggt343

Pollard DD, Delaney PT, Duffield WA, Endo ET, Okamura AT (1983) Surface Deformation in Volcanic Rift Zones. Developments in Geotectonics 19:541-559. https://doi.org/10.1016/B978-0-444-42198-2.50036-5

Qin R, Buck WR (2008) Why meter-wide dikes at oceanic spreading centers? Earth Planet Sci Lett 265:466-474. https://doi.org/10.1016/j.epsl.2007.10.044

Rivalta E (2010) Evidence that coupling to magma chambers controls the volume history and velocity of laterally propagating intrusions. J Geophys Res Solid Earth 115:B07203. https://doi.org/10.1029/2009JB006922

Tryggvason E (1984) Widening of the Krafla Fissure Swarm during the 1975-1981 Volcano-Tectonic Episode. Bull Volcanol 47:47-69. https://doi.org/10.1007/BF01960540

Parks M, Drouin V, Sigmundsson F, Hjartardóttir ÁR, Geirsson H, Pedersen GBM et al (2025) 2023–2024 inflation-deflation cycles at Svartsengi and repeated dike injections and eruptions at the Sundhnúkur crater row, Reykjanes Peninsula, Iceland. Earth Planet Sci Lett 658:119324. https://doi.org/10.1016/j.epsl.2025.119324

Sigmundsson F, Parks M, Geirsson H, Hooper A, Drouin V, Vogfjörd KS, et al. (2024) Fracturing and tectonic stress drive ultrarapid magma flow into dikes. Science 383(6688):1228-1235. https://doi.org/10.1126/science.adn2838

Paper III

Plate divergence at the Krafla volcanic system, Iceland: Insight from GNSS geodesy and Sentinel-1 Satellite Radar Interferometry in 2002–2024

Plate divergence at the Krafla volcanic system, Iceland: Insight from GNSS geodesy and Sentinel-1 Satellite Radar Interferometry in 2002–2024

Yilin Yang[1], Freysteinn Sigmundsson[1], Halldór Geirsson[1], Juliet Biggs[2], Vincent Drouin[3], Josefa Sepúlveda Araya[4], Sigrún Hreinsdóttir[5], Chiara Lanzi[3], Joachim Gottsmann[6], Taco Broerse[7], Sandra Verhagen[7]

[1] Nordic Volcanological Center, Institute and Faculty of Earth Sciences, University of Iceland, Reykjavík, Iceland.

[2] COMET, School of Earth Sciences, University of Bristol, Bristol, UK.

[3] Icelandic Meteorological Office, Reykjavík, Iceland.

[4] COMET, School of Earth and Environment, University of Leeds, Leeds, UK.

[5] GNS science, Lower Hutt, New Zealand.

[6] Department of Earth and Environmental Sciences, Ludwig-Maximilians-Universität München, Munich, Germany.

[7] Faculty of Civil Engineering and Geosciences, Delft University of Technology, Delft, The Netherlands.

Corresponding author: Yilin Yang (yiy1@hi.is)

Key Points:

- GNSS and InSAR data jointly constrain the North American-Eurasian plate divergence across the Krafla volcanic system, Iceland.
- Locking depth is ~3.5 km beneath the Krafla caldera, deepening to ~4.3 km to the north and ~6.8 km to the south, implying a dome-like crustal structure.
- We identify three local areas of protracted deflation from residuals, related to geothermal activity and lava subsidence.

Abstract

The Krafla volcanic system in Iceland, a subaerial segment of the divergent boundary between the North American and Eurasian plates, offers a unique opportunity to investigate tectonic and volcano-tectonic processes. We present a six-segment kinematic back-slip plate boundary model constrained jointly by long-term deformation velocity fields from GNSS (2002–2024) and Sentinel-1 SAR interferograms (2015–2023). The inferred plate spreading rate is $19.52^{+0.05}_{-0.06}$ mm/yr in an azimuth of $283.4^{+0.1}_{-0.1}$ °, with formal uncertainties corresponding to the 95% confidence interval of the Bayesian inversion results. The inferred plate boundary axis aligns with recent eruptive fissures and fracture orientations, striking N2.5°E–N15.5°E within and south of the central volcano and rotating to NNW-SSE north of it. Locking depth varies significantly along the plate boundary axis: it is shallowest within and just north ($3.52^{+0.03}_{-0.06}$ to $3.64^{+0.05}_{-0.06}$ km) of the Krafla caldera and deepens to $4.27^{+0.15}_{-0.23}$ and $6.81^{+0.11}_{-0.13}$ km to the north and the south, respectively. This variation is consistent with the depth distribution of seismicity and reflects a dome-like crustal structure beneath Krafla. After correcting vertical velocities for GIA and regional subsidence caused by rheological anomalies under extension, residual velocities reveal three areas with local deflation: two related to the Krafla and Bjarnarflag geothermal fields and one at the northernmost part of the 1975–1984 Krafla lava field. InSAR displacement time series indicate that these deflation signals sustain from 2015 to 2023. In addition to resolving plate divergence kinematics, detailed plate boundary models provide insights into crustal rheology, volcano-tectonic interactions and local processes.

1 Introduction

Improved knowledge of processes at divergent plate boundaries, where oceanic crust forms, is important for the general understanding of tectonics and lithospheric evolution (e.g., Smith & Cann, 1993; Toomey et al., 2007; Augustin et al., 2021). The system of mid-ocean ridges (MOR) is the most common type of divergent plate boundary and accounts for about 75% of Earth's volcanism (Bennett et al., 2019). However, less than 2% of MOR are above sea level, posing challenges for measuring their deformation and seismicity. Thus, subaerial portions of MOR, such as Iceland and Afar region in Africa, offer good opportunities for measuring plate spreading and volcano-tectonic processes (e.g., Wright et al., 2012; Pagli et al., 2014; Sigmundsson et al., 2020).

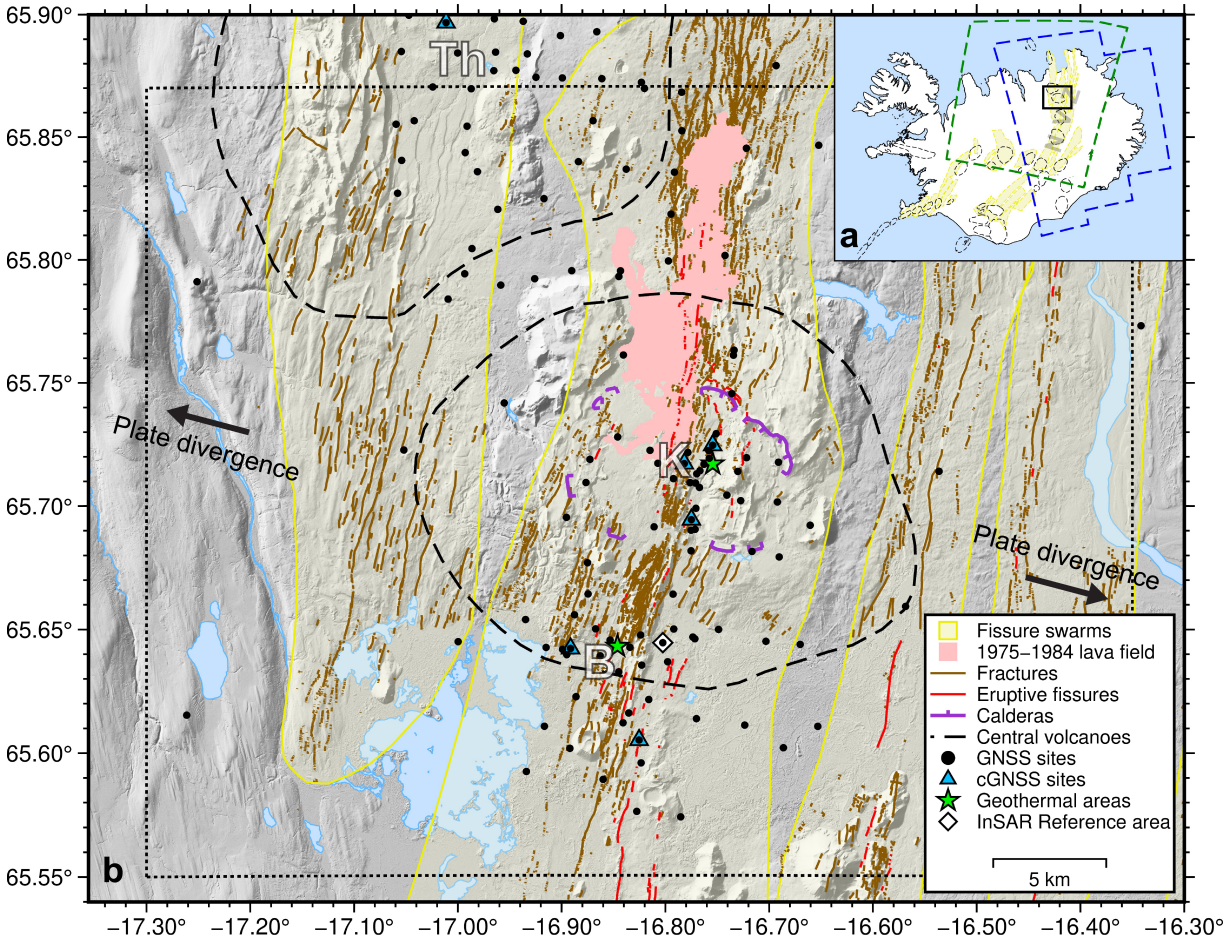


Figure 1. (a) Map of Iceland. The rectangle indicates the study area. The green and blue dashes outline the descending and ascending frames of COMET-LiCS Sentinel-1 InSAR products, respectively, available in 2024 for the Krafla area. **(b)** Map of the study area. Th indicates the Þeistareykir (Theistareykir) volcanic system, K indicates the Krafla volcanic system and B indicates the Bjarnarflag geothermal field. The dotted rectangle indicates the area of InSAR deformation analysis. The topography is from LMÍ (2020), fractures from Hjartardóttir et al. (2015), and fissure swarms, central volcanoes and caldera are from Jóhannesson & Sæmundsson (2009).

The Krafla volcanic system in the Northern Volcanic Zone (NVZ) of Iceland (shown in Figure 1) is well suited for studying plate divergence at the subaerial part of the MOR system, because of the extensive set of geodetic observations available. The system is a segment of the divergent boundary between the Eurasian and North American plates. Global plate motion models give a spreading rate of 16.3–18.6 mm/yr in N283.0°–286.7°E in this area (DeMets et al., 1994; DeMets et al., 2010; Argus et al., 2010). The volcanic system consists of a central volcano with a 9×7 km wide caldera and a 4–10 km wide fissure swarm (rift zone), striking NNE-SSW, and extending 40 km to the south and 50 km to the north from the caldera (Figure 1; Opheim & Gudmundsson, 1989;

Sæmundsson, 1991; Hjartardóttir et al. 2012; Lanzi et al. 2023). Plate spreading occurs at a relatively small angle from the rift-normal direction, featuring minimal obliquity. The volcanic system hosts two high-temperature geothermal fields (Krafla and Bjarnarflag; green stars in Figure 1b), which have been exploited since 1960s. The most recent rifting episode at Krafla occurred in 1975–1984, including about twenty rifting events, nine of which led to eruptions (e.g., Björnsson et al. 1977; Tryggvason, 1980; Einarsson, 1991). The current large-scale deformation at Krafla, dominated by plate spreading and glacial isostatic adjustment (GIA) (e.g., Drouin et al., 2017a).

Quantifying plate divergence at Krafla is important for monitoring volcanic, geothermal, and rift-related activities, as well as for understanding small-scale and small-magnitude deformation patterns superimposed on plate spreading. For instance, Sturkell et al. (2008) suggested that the subsidence from deflation of a shallow magmatic body below Krafla (~2.5 km depth) decayed from 50 mm/yr in 1989–1992 to 3 mm/yr during 2002–2005. Geothermally-related surface deformation in the study area has been generally inferred to be smaller than 6 and 15 mm/yr in horizontal and vertical components, respectively, with sources shallower than 2.5 km (Drouin et al., 2017b; Lanzi et al., 2023). Additionally, Yang et al. (2023) detected a deformation anomaly of 7.6–9.8 mm/yr in the east component during 2014–2015 across the study area. Accurate estimates of background plate spreading enhances our capability to detect and model these small deformation signals.

The Krafla volcanic system also has abundant geodetic observations for studying plate spreading. Global Navigation Satellite System (GNSS) surveys in the area began in 1986 and the GNSS network now contains over 100 benchmarks. Four continuous GNSS (cGNSS) stations have been operating for more than a decade and two additional stations at the Krafla caldera center were installed in 2019. Since 2010, 78 sites have been annually measured during GNSS campaigns. Interferometric analysis of synthetic aperture radar satellite images (InSAR) has also been applied to monitor deformation in the area, using multiple satellite missions (e.g., Ali et al., 2014; Metzger & Jónsson, 2014; Drouin et al., 2017b; Cao et al., 2023).

Previously, several models of plate boundary deformation in the Krafla area have been developed. The first countrywide plate boundary model constrained with GNSS data was presented by Árnadóttir et al. (2009). Later models using data from a denser GNSS network were presented by Metzger et al. (2013), Drouin et al. (2017a) and Barreto et al. (2025), focusing on regional plate spreading including the Krafla area. Metzger & Jónsson (2014) implemented the first joint inversion of GNSS and InSAR data covering the Krafla areas, spanning 1992–2009, to identify plate boundary motion, fault slip rate and volcanic deformation in North Iceland. The countrywide InSAR analyses by Drouin & Sigmundsson (2019) and Cao et al. (2023) have also been used to

constrain the plate boundary models for the whole Iceland. In most of these studies, the plate boundary across the Krafla volcanic system is simplified into two linear segments. However, Metzger & Jónsson (2014) and Drouin et al. (2017a) found that the locking depth of the plate boundary varies significantly at Krafla, ranging at least from ~3 to 6 km. Moreover, the geometric simplification of using long, straight plate boundary segments (Drouin & Sigmundsson, 2019; Cao et al., 2023) causes the inferred plate boundary being offset from the Krafla fissure swarm (Hjartardóttir et al., 2015), and inconsistent with the observed fracture strikes (Corti et al., 2021). These observations suggest that a simplified plate boundary axis cannot adequately represent the local stress field. A spatially variable plate boundary profile along the NVZ, such as in Drouin et al. (2017a), can solve this issue. Their profile, with variable strike, also shows the variability in locking depth across the Krafla area, but it suffers from large uncertainties in locking depth of ~10 km due to the sparse distribution of GNSS sites.

The vast increase in available geodetic data (both GNSS and InSAR) allows us to derive an improved plate boundary model with a more precise description of geometry and locking depths. In earlier studies, Metzger & Jónsson (2014) used 92 interferograms and Drouin et al. (2017) included ~35 GNSS sites from Krafla. Conversely, our current datasets including more than 100 GNSS sites and thousands of SAR interferograms covering the central part of the Krafla volcanic system can provide better constraint on the plate divergence. Integrating these two types of datasets also combines the strengths of the wide spatial coverage from InSAR and three-dimensional displacement measurements from GNSS, leading to more reliable plate boundary models than using only one of them.

In this study, we aim to separate the large-scale plate divergence signal from local deformation patterns, by constraining a plate boundary model using geodetic observations that complies with local stress field and fissure swarm geometries. The model represents the central Krafla volcanic system with six linear segments, of which the geometry is determined by inversion of GNSS and InSAR velocity fields. We then investigate local deformation using residual velocity fields and InSAR line-of-sight (LOS) displacement time series. Finally, we compare the new plate boundary model with plate motions from global and previous regional models, geological features and seismicity in the area, and discuss how plate divergence interacts with volcanic activities.

2 Data

This study analyzes GNSS data collected in 2002–2024 and Sentinel-1 SAR interferograms in 2015–2023 to derive the long-term deformation velocity field of the area. A scaled version of a GIA deformation model of Iceland by Auriac (2014) is incorporated. We adopt a regional

subsidence model by Lanzi et al. (2024) to account for vertical deformation caused by rheological heterogeneities and plate divergence, enhancing our ability to resolve local deformation signals.

2.1 GNSS

We process GNSS data collected at both continuous and campaign sites between 2002 and 2024 jointly at University of Iceland using GAMIT/GLOBK 10.75 to obtain coordinate time series in the ITRF2014 (IGb14) reference frame, using reference stations in Iceland and globally (Herring et al., 2018; Altamimi et al., 2016). The processing uses an elevation mask angle of 10° and IGS14 azimuth and elevation dependent absolute phase center model for all antennas. We use IGS final orbit products as a priori constraint, and solve for satellite orbits, earth rotation parameters, atmospheric zenith delay (every 2 hrs), and three atmospheric gradients per day along with site coordinates. Zenith wet tropospheric delays are derived by scaling slant delays using the Vienna Mapping Function (VMF1; Boehm et al., 2006). Corrections include ocean tidal loading using the FES2004 model (Lyard et al., 2006), solid-Earth and pole tide (Danis et al., 2004). Finally, we convert the derived coordinate time series to topocentric coordinate system (east, north, up) for better representing local deformation (see available campaign GNSS data in Figure S1 and examples of GNSS time series in Figures S2 and S3 in Supplementary Information S1).

Stable GNSS site coordinate time series (i.e., without transient or anomalous deformation signals) can be described as:

$$y = a + bt + \sum_{i=1}^{n} [c_i \sin(2\pi it) + d_i \cos(2\pi it)] + \varepsilon, \quad (1)$$

where y is the coordinate at time t, a represents initial site position, c_i and d_i represent the amplitudes of seasonal signals (Blewitt & Lavallée, 2002) and ε represents the residuals. The linear term, b, represents the long-term site velocity and is here estimated together with other parameters (a, c_i, d_i) using the Weighted Least Square (WLS) method (following the same procedure as in Yang et al., 2023). The number of seasonal signals (n) considered in the velocity estimation is set to $n = 2$ for cGNSS sites (annual and semi-annual signals) and $n = 0$ for campaign sites (no seasonal signal), because the periodicities are mitigated at campaign sites by conducting measurements in the same period each year.

Before velocity estimation, we manually inspect the time series and have detected no significant jump, except at cGNSS site LHNC, where instrument and power failures caused data gaps and jumps. This site is not considered in subsequent analysis. Outliers in cGNSS time series are removed using the inter-quartile range criterion (IQR; Nikolaidis, 2002). For campaign GNSS

sites, we handle outliers after the velocity estimation (see next paragraph) and during the inversion scheme (section 3.3) since statistical methods cannot handle sparse time series.

Several studies have identified transient deformation signals in the study area during the period 2002–2024 (Metzger et al., 2013; Lanzi et al., 2023; Yang et al., 2023; Gudnason et al., 2024). However, these signals usually last less than two years with magnitudes below 10 mm/yr in the horizontal components, and their impact on velocity estimation at campaign GNSS sites is generally smaller than 2 mm/yr (see synthetic data experiments in Figure S4 in Supplementary Information S1), comparable to the fitting errors (Leonard et al., 2007). To reduce biases from insufficient observations and outliers at campaign sites, we do not consider sites with vertical velocity uncertainties larger than 3 mm/yr, representing approximately the 95% confidence limit of stable stations. Vertical velocities are used for site selection for their larger uncertainties and more sensitivity to noise than horizontal velocities. Finally, we use the Euler pole and rotation rate of the Eurasian plate from ITRF2014 plate motion model to evaluate the expected displacement rate at each site, thereby referencing GNSS horizontal velocity field to the stable Eurasian plate (Altamimi et al., 2017).

2.2 InSAR

We conduct a Small Baseline Subset (SBAS) time series analysis using Sentinel-1 radar interferograms from 2015 to 2023 using the COMET-LICS system (Lazecký et al., 2020; Morishita et al., 2020). The spatial extent (dotted rectangle in Figure 1b) was chosen to encompass the region of plate spreading deformation and the full variation in the satellite line-of-sight (LOS) velocity field. Interferogram products are generated with the LiCSAR software (Lazecký et al., 2020), and were multilooked by factors of 5 (range) and 20 (azimuth) to improve the signal-to-noise ratio, achieving a pixel size of ~100×100 m. The topographic correction is derived using Copernicus Digital Elevation Model at 90 m resolution (ESA, 2020).

We perform time series analysis of one ascending track (T147) and one descending track (T9) using LiCSBAS software (Morishita et al., 2020), which follows the New SBAS approach (e.g., López-Quiroz et al., 2009; Doin et al., 2011). This approach incorporates a linear deformation constraint, allowing the estimation of InSAR displacement time series despite gaps in its spatiotemporal baseline network (Figure S5 in Supplementary Information S1). This assumption of linear displacements is appropriate for the Krafla area, where the long-term deformation is significant and relatively stable over the observation period. We correct atmospheric errors using the Generic Atmospheric Correction Online Service for InSAR (GACOS; Yu et al., 2018). Because the interferograms from early fall to late spring in the study area have low coherence due

to snow cover, we only include images acquired between May and late September to maximize the use of high-quality interferograms.

The derived InSAR LOS velocity fields (Figure S6 in Supplementary Information S1) are referenced to nearest pixel of benchmark FM15 (white diamond in Figure 1b), where GNSS time series shows minimal vertical displacement. This benchmark has also served as the reference point for leveling measurements over decades (Sturkell et al., 2008). Assuming that the displacement in north-component has a negligible contribution to LOS velocities, we decompose the LOS velocities into approximate estimates of eastward (near-east) and vertical (near-up) components (Wright et al., 2004; Motagh et al., 2017). We reference InSAR near-east and near-up velocity fields to the stable Eurasian plate by subtracting the median difference between InSAR and GNSS velocities (10.62 mm/yr and 1.64 mm/yr for the near-east and near-up components, respectively).

To reduce computational cost of inversion, we down-sample the near-east InSAR velocity map uniformly from a pixel size of ~100×100 m to ~600×1000 m, resulting in 2464 pixels. The smaller pixel size in the X-direction (Easting) helps preserve deformation variations across the plate boundary deformation zone. All data point coordinates are projected into a local Cartesian coordinate system (X, Y).

2.3 Deformation from Glacial Isostatic Adjustment

GIA deformation due to retreat of Icelandic ice caps since 1890 is widespread in Iceland. To remove its imprint in the observed velocity fields, we use surface deformation predicted by the model developed by Auriac (2014). It is a numerical model using a finite element method, with two elastic layers overlying a viscoelastic half-space. The upper elastic layer is 1 km thick, with a Young's modulus (E) of 14 GPa and a Poisson's ratio (ν) of 0.17. The lower elastic layer and the viscoelastic half-space share the same elastic properties, $E = 74$ GPa and $\nu = 0.25$. The model calculates deformation based on an ice thinning model for 1890–2010. Auriac (2014) inverted for the thickness of the lower elastic layer and the viscosity (η) of the viscoelastic half-space by using GNSS and InSAR velocity fields from 1993 to 2004, inferred to be 21 km thick and $\eta = 8.4 \times 10^{18}$ Pa s, respectively.

Although this time-varying model predicts GIA deformation velocities in 2008–2010, it was constrained with data spanning 1993–2004 and the model does not account for the variable and accelerated glacier retreat in recent years (The GlaMBIE Team, 2025). The model tends to underestimate GIA signals in observed velocity fields after 2004. To preserve the spatial

deformation pattern while increasing the predicted velocities in line with observations, we follow the same approach as several previous studies (Drouin et al., 2017a; Drouin & Sigmundsson, 2019; Li et al., 2022). This approach estimates a scaling factor for the Auriac (2014) model outputs for the 2008–2010 period and we then subtract the scaled outputs from our observed velocity fields. The scaling results in maximum horizontal GIA corrections of ~1–2 mm/yr and vertical corrections up to ~4–8 mm/yr at Krafla reported by Drouin et al. (2017a).

3 Methods

This study models horizontal velocity fields with the kinematic back-slip concept of plate boundary deformation within a Bayesian inversion framework. Section 3.1 and 3.2 describe the principles of the back-slip model and the Bayesian inversion, respectively. Then section 3.3 details the inversion strategies. Vertical velocity fields are analyzed independently and are not included in the inversion of the plate boundary model. Instead, they are corrected for GIA deformation and the regional subsidence due to rheological anomalies undergoing extension (section 3.4), and then used qualitatively to interpret local deformation patterns in combination with the horizontal residual velocities.

3.1 Kinematic modeling of plate boundary deformation

We assume that two tectonic blocks (plates) are locked from the surface to a certain depth and move freely below. The locking produces elastic strain, resulting in deformation velocity gradient across the plate boundary. We describe the plate boundary deformation using the kinematic back-slip model (Savage & Prescott, 1978), which has been previously applied to north Iceland (Ali et al., 2014; Metzger & Jónsson, 2014; Drouin & Sigmundsson, 2019; Barreto et al., 2025). The model assigns half spreading rate on each side of the plate boundary axis (black arrows in Figure 2a) to simulate the free movement at depth and superimposes the deformation field produced by a vertical fault dislocation at the plate boundary axis from the surface to the locking depth, assuming a uniform elastic half-space (Okada, 1992). The dislocation moves opposite to the spreading at the same rate (namely the back-slip) to simulate the locking at shallow crust.

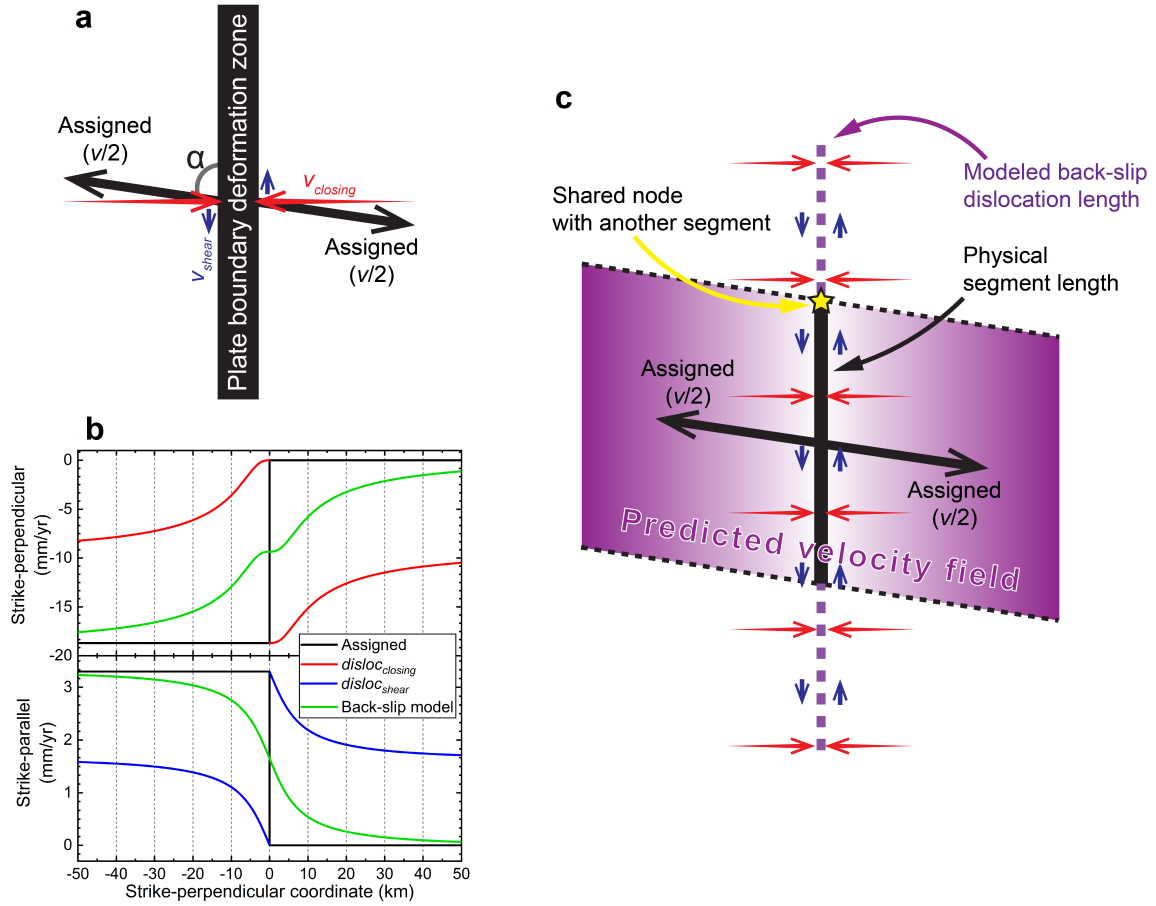


Figure 2. Illustration of the kinematic back-slip model for plate boundary deformation. **(a)** Schematic figure of the back-slip model for plate spreading. **(b)** Example deformation velocity profiles of the back-slip model. The full spreading rate is 19 mm/yr with $\alpha = 80°$. The locking depth is set to 6 km. **(c)** Implementation of the back-slip model for a plate boundary axis segment. Blue and red arrows have the same meaning as in panel a. The modeled dislocation plane is extended to ten times the physical segment length along strike to approximate an effectively infinite fault (not to scale in the figure), while only the predicted displacements within the segment range are retained to avoid edge effects. The shared node with an adjacent segment can be located at either end, depending on the segment position along the plate boundary.

At regional scale, the plate spreading direction is not necessarily perpendicular to the strike of the central axis, and a shallow back-slip dislocation with only strike-normal motion cannot accommodate the strike-parallel component of deformation. To account for this obliquity, we incorporate both strike-normal and strike-parallel components of the back-slip dislocation. These components can be calculated from the angular difference (α) between the plate spreading direction and the axis strike:

$$v_{closing} = -v \sin \alpha, \qquad v_{shear} = -v \cos \alpha, \tag{2}$$

where $v_{closing}$ and v_{shear} represent the dislocation in the strike-normal and strike-parallel directions, respectively, and v represents the spreading rate (opening and right-lateral are positive). An example of the deformation profile from a back-slip model is illustrated in Figure 2b. In this study, we implement the back-slip dislocation as an effectively infinite strike-parallel fault plane by setting its model length to ten times the physical segment length and retain only the predicted displacements within the spatial range of the segment (Figure 2c). This approach minimizes edge effects from the finite length of plate boundary axis segments. To ensure a consistent reference system in the inversion, we also reference the modeled velocity fields to the stable Eurasian plate by subtracting half of the spreading rate in the spreading direction. When applying the back-slip concept to a divergent plate boundary, we only use the horizontal component of the assigned plate motion and back-slip dislocation. The vertical deformation predicted by the model is not used; instead, we use the model of Lanzi et al. (2024) to account for potential subsidence at the plate boundary.

3.2 Bayesian inversion framework

Given the nonlinearity of the back-slip model problem and the trade-off among parameters, we apply a Bayesian inversion scheme to establish the plate boundary model. With a nonlinear model function ($\mathbf{G}$) with its parameters ($\mathbf{m}$), the observations ($\mathbf{d}$) can be written as:

$$\mathbf{d} = \mathbf{G}(\mathbf{m}) + \boldsymbol{\epsilon}, \tag{3}$$

where $\boldsymbol{\epsilon}$ represents errors. Here $\mathbf{d}$ is the vector of geodetic observations. Bayesian inversion calculates the probability of each parameter $\mathbf{m}$ given the data, $\mathrm{p}(\mathbf{m}|\mathbf{d})$, which according to Bayes theorem can be written as:

$$\mathrm{p}(\mathbf{m}|\mathbf{d}) = \frac{\mathrm{p}(\mathbf{d}|\mathbf{m})\mathrm{p}(\mathbf{m})}{\mathrm{p}(\mathbf{d})}, \tag{4}$$

where $\mathrm{p}(\mathbf{m})$ is the prior probability of parameter values, usually assumed to conform to a joint uniform distribution within their bounds (Jeffreys, 1939; Ulrych et al., 2001). Given a sample of model parameters $\mathbf{m}$, and assuming that the errors conform to a multivariate Gaussian distribution, a likelihood function evaluating the probability of the geodetic observations $\mathbf{d}$, $\mathrm{p}(\mathbf{d}|\mathbf{m})$ can be calculated.:

$$\mathrm{p}(\mathbf{d}|\mathbf{m}) = (2\pi)^{-N/2}|\boldsymbol{\Sigma}_\mathbf{d}|^{-\frac{1}{2}} \times \exp\left[-\frac{1}{2}\big(\mathbf{d}-\mathbf{G}(\mathbf{m})\big)^{\mathrm{T}}\boldsymbol{\Sigma}_\mathbf{d}{}^{-1}\big(\mathbf{d}-\mathbf{G}(\mathbf{m})\big)\right], \tag{5}$$

where N is the number of observations and $\boldsymbol{\Sigma}_\mathbf{d}$ is the covariance matrix of the observations $\mathbf{d}$. The marginal probability of the observations $\mathrm{p}(\mathbf{d})$ is a constant to normalize the posterior probability distribution. A specific iterative sampling can achieve an estimate of a posterior joint probability distribution function (PDF) of unknown parameters $\mathbf{m}$, providing all their statistics. For instance,

estimates can be derived from the mean, median, maximum probability, and 95% confidence intervals of the marginal posterior PDF for each parameter.

The sampling method is crucial for the estimation of $p(\mathbf{m}|\mathbf{d})$. We follow the framework proposed by Bagnardi & Hooper (2018) by modifying the Geodetic Bayesian Inversion Software (GBIS) in MATLAB®. This framework iteratively samples on the unknown parameters $\mathbf{m}$ using Markov chain Monte Carlo (MCMC) method with the Metropolis-Hastings algorithm and automatic step size selection. The method is flexible to modify for different scenarios (e.g., Yang et al., 2023). We assess the convergence of an inversion by monitoring the stability of the posterior distributions and the variation of the Markov chain. A chain is considered converged when the mean and variance of the sampled parameters remain stable. Otherwise, the inversion fails to converge, which can be caused by model non-uniqueness, weak data constraints, or inappropriate priories or step sizes.

3.3 Inversion strategies

GNSS horizontal velocities and InSAR near-east velocities jointly constrain the plate boundary model. We divide the plate boundary axis into multiple segments and use a two-step inversion scheme to avoid model non-uniqueness. The first-step inversion infers the location and geometry of the plate boundary. Each segment is inverted independently for using only the data points within its spatial extent along the spreading direction (Figure 2c). The inversion estimates the segment strike, locking depth, spreading rate and direction, along with two individual GIA scaling factors for GNSS and InSAR velocities. Priories and step sizes of parameters are adjusted through multiple trials to avoid inappropriate settings that could hinder convergence. To ensure continuity of the plate boundary axis, adjacent segments are connected through shared nodes: the connecting node of each segment is fixed to the endpoint of the previous one. Therefore, we invert only for the X-coordinate at one endpoint of an initial segment and calculate the other from the inferred strikes and the prescribed segment length. The locations of the remaining segments are then determined sequentially from their segment lengths, inferred strikes and fixed connecting nodes. Segment lengths are initially set to 3 km along the Y-direction (northing) and increased by 1 km if the inversion fails to converge due to weak data constraints. This approach results in six segments across the study area, ranging from 3 to 9 km in length along Y-direction, depending on local data quality and spatial coverage (Figure 4a). Our inversion allows potential local spreading obliquity by estimating the strike and spreading direction as two individual parameters for each segment, rather than assuming the plate boundary axis to be perpendicular to the spreading direction a priori. In this study, the initial segment is a 3-km-long segment covering the southern half of the Krafla caldera.

The second-step inversion estimates a uniform spreading rate, spreading direction, and GIA scaling factor for the entire study area, while allowing segment-specific locking depths. This approach avoids inconsistency in plate spreading and discontinuities in the GIA deformation field that could arise from segment-wise estimates. We estimate a single GIA scaling factor for both GNSS and InSAR, even though the data period us not the same, because separate estimations for each dataset leads to unrealistic differences in the InSAR-derived estimates across segments. Although all the segments are jointly inverted in the second-step inversion, the model deformation field of each segment is calculated individually and only applied within its spatial extent along the spreading direction (Figure 2c). That is, each observation is always explained by model prediction of one single segment.

Weighting is applied to balance the contributions of InSAR and GNSS datasets, and the north and east components, on the derived values for the model parameters. The observations can be written as:

$$\mathbf{d} = \begin{pmatrix} \mathbf{d}^{\mathrm{n}}_{\mathrm{GNSS}} \\ \mathbf{d}^{\mathrm{e}}_{\mathrm{GNSS}} \\ \mathbf{d}^{\mathrm{e}}_{\mathrm{InSAR}} \end{pmatrix} \tag{6}$$

where the superscripts denote the data type (GNSS or InSAR) and the subscripts denote the velocity component (north n or east e). We weight the $\mathbf{d}^{\mathrm{n}}_{\mathrm{GNSS}}$ and $\mathbf{d}^{\mathrm{e}}_{\mathrm{GNSS}}$ by the standard deviations of the linear velocity estimates derived from WLS (denoted as $\boldsymbol{\sigma}^{\mathrm{n}}_{\mathrm{GNSS}}$ and $\boldsymbol{\sigma}^{\mathrm{e}}_{\mathrm{GNSS}}$, respectively). For $\mathbf{d}^{\mathrm{e}}_{\mathrm{InSAR}}$, we assign a spatially uniform weight (e.g., Funning et al., 2007; Guglielmino et al., 2011), derived from the standard deviation of the fitted semi-variogram at zero lag distance ($\sigma^{\mathrm{e}}_{\mathrm{InSAR}} = 0.25$ mm/yr; see Supplementary Information S1 for more explanation).

Since north-component deformation is constrained only by GNSS velocities (~100 sites in total), whereas both GNSS (~100 sites) and InSAR (>2400 pixels) data constrain the east-component deformation, the east component will dominate the likelihood function. To compensate, we up-weight $\mathbf{d}^{\mathrm{n}}_{\mathrm{GNSS}}$ by a factor κ_1, defined as:

$$\kappa_1 = \frac{N^{\mathrm{e}}_{\mathrm{GNSS}} + N^{\mathrm{e}}_{\mathrm{InSAR}}}{N^{\mathrm{n}}_{\mathrm{GNSS}}}, \tag{7}$$

where N denotes the number of observations with superscripts and subscripts having the same meaning as in Eq. (6). This factor varies between 10 to 40 across sampling iterations of MCMC and between the two inversion steps, e.g., $\kappa_1 = 13.5$ for the second-step inversion with 2464 InSAR pixels and 183 GNSS sites. To ensure comparable overall contributions from InSAR and

GNSS to the likelihood function after this adjustment, we further scale the weight of $\mathbf{d}^{\mathrm{e}}_{\mathrm{InSAR}}$ by another factor κ_2 ($\kappa_2 = 2$ in this study). Accordingly, the covariance matrix $\mathbf{\Sigma_d}$ can be written as:

$$\mathbf{\Sigma_d} = \begin{pmatrix} \frac{1}{\kappa_1}\mathrm{diag}[(\boldsymbol{\sigma}^{\mathrm{n}}_{\mathrm{GNSS}})^2] & 0 & 0 \\ 0 & \mathrm{diag}[(\boldsymbol{\sigma}^{\mathrm{e}}_{\mathrm{GNSS}})^2] & 0 \\ 0 & 0 & \frac{1}{\kappa_2}(\sigma^{\mathrm{e}}_{\mathrm{InSAR}})^2\mathbf{I} \end{pmatrix}, \quad (8)$$

where diag( ) indicates diagonal matrix, and $\mathbf{I}$ represents the identity matrix.

In our study, we first derive the plate divergence deformation and then evaluate local deformation patterns. This is different from the approach of Drouin et al. (2017a), where they corrected for known local deformation sources before inferring plate spreading. Given the minimal obliquity of plate spreading at Krafla, the east-component velocities primarily control the inversion of spreading parameters and locking depths. Our approach is justified because (i) We find no evidence of a deep deflation source at 21.5 km in the east-component velocity profile (Figure S7a in the Supplementary Information S1), and (ii) synthetic data experiments suggest that deformation originating from sources at 2.5 km or shallower affects the locking depth estimates by less than 15% (Figure S7b in the Supplementary Information S1).

To further minimize the influence of local deformation and ensure a robust estimation, we apply targeted data filtering and exclusion. This also aims at the following challenges: (i) InSAR velocities, even after down-sampling, may still be affected by topography-related errors due to radar imaging geometry; (ii) campaign GNSS velocities may be biased by low-quality or sparse observations; and (iii) up-weighting north-component GNSS velocities can amplify the impact of (ii) and local deformation. We apply outlier removal at each sampling iteration of the MCMC method using a Median Absolute Deviation (MAD) criterion with a 95% confidence threshold (Wilcox, 2005), based on the residuals within each dataset. We exclude GNSS sites within 2.5 km from both sides of the plate boundary axis if their residuals to the modeled displacements from the priori parameter values exceed 1.3 mm/yr, corresponding to approximately three times of the largest standard deviation in GNSS north-component velocities. In the first-step inversion of the northernmost segment, we further exclude GNSS sites located in the Þeistareykir volcanic system (more than 5 km west of the estimated plate boundary axis) to avoid bias in the axis geometry from another volcanic system. These sites are added back in the second-step inversion since the local variations have limited effects on the inversion with a fixed plate boundary axis.

To obtain the posterior PDFs, we run 100,000 sampling iterations in the Bayesian inversion. We determined parameter search bounds and initial values according to a prior knowledge of the plate boundary and adjusted through multiple inversion trials (see Table S1 and S2 in Supplementary Information S1). Visual inspection on the Markov chain suggests the first 30,000 iterations as burn-in, where the Marko chain has not converged to the target posterior distribution, and are not considered in the PDFs.

3.4 Corrections of the vertical velocity fields

Accurate interpretation of vertical deformation requires correcting observed velocity fields for long-wavelength signals. In this study, we account for GIA and regional subsidence associated with rheological anomalies undergoing extension.

3.4.1 GIA

GIA scaling factor for the vertical component is estimated using WLS, with the velocities in the eastern part of the study area (longitude 16.35°W–16.72°W), where uplift larger than in other parts of the study area is observed (Figure 3b). We increased the weight of GNSS velocities by the ratio between the GNSS sites and InSAR pixels involved, in a similar manner as in Eq. (5). The estimated GIA scaling factor is 1.89, consistent with the value of 1.8 reported by Drouin et al. (2017a).

3.4.2 Regional subsidence due to rheological anomalies undergoing extension

Rheological anomalies within the subvolcanic crustal structure, altered by magma and hot rock, can influence the deformation styles (e.g., Dragoni and Magnanensi, 1989; Liao et al., 2018; Head et al., 2021). Strain localization associated with crustal extension in the presence of such anomalies can cause long-term subsidence in volcanic systems (Lanzi et al., 2024). To account for this effect, we incorporate the finite element model of Lanzi et al. (2024) to represent regional subsidence in the vertical deformation field. The model consists of a regional 7-km-thick elastic upper crust with $E = 30$ GPa, overlying a viscoelastic half-space with $E = 60$ GPa and $\eta = 5 \times 10^{18}$ Pa s. Three key rheological heterogeneities are implemented (Figure S8 in Supplementary Information S1): (i) a low-modulus elastic volume with $E = 7$ GPa representing caldera infill, tapering from a 9×7 km area at the surface to 6×6 km at 2 km depth, (ii) a viscoelastic up-doming volume beneath the caldera with $E = 30$ GPa and $\eta = 5 \times 10^{18}$ Pa s, extending from 9×9 km at 7 km depth to 6×6 km at 2 km depth, and (iii) a 9-km-wide zone representing the Krafla fissure swarm, extending 50 km north and 40 km south of the caldera, where the elastic-viscoelastic interface ramps from 2 km to 7 km depth along its length.

A uniform extension rate of 19.52 mm/yr (the median estimate from section 3.3) is applied across its domain. The model is implemented using COMSOL Multiphysics 6.1® (COMSOL, 2022). We resample the model-derived vertical velocity field onto the InSAR pixel and GNSS site locations, where we estimate a constant offset to the modeled velocities to cancel out the overall thinning of the crust in the model, instead of imposing an upward boundary velocity at the bottom of the model as in Lanzi et al. (2024), for a better fitting between the model and the observations. The offset is calculated by comparing the modeled and InSAR-derived vertical velocities at two pixels located in northwest and southeast corners of the study area (Figure 3b), yielding a value of 27.2 mm/yr. This represents a first-order correction, as these two points are selected in areas of observed subsidence while avoiding broader areas that may be influenced by the topography-related errors.

4 Results

We first present the long-term deformation velocity fields from GNSS and InSAR, and then the new plate boundary model for the central part of the Krafla volcanic system, constrained by the horizontal velocity fields. Because geophysical processes often induce coupled horizontal and vertical deformation, we jointly analyze both components to better resolve local deformation. Horizontal velocities are corrected for the plate divergence and GIA, while the vertical velocities are corrected for GIA and regional subsidence due to rheological anomalies under extension (see section 3.4). The derived residual velocity fields reveal local deformation patterns, of which the temporal evolution is investigated using InSAR displacement time series.

4.1 Long-term deformation velocity fields at Krafla

Both GNSS horizontal and InSAR near-east velocity fields (shown in Figure 3a) reveal a clear extensional deformation pattern across the Krafla volcanic system. Deformation velocities referenced to the stable Eurasian plate increase from near zero in the eastern part of the study area to over 17 mm/yr in the west. The transition from low to high velocities appears more gradual south of the Krafla central volcano than in the north, as indicated by the wider zone with yellow to green colors in Figure 3a. In addition, GNSS horizontal velocity vectors indicate stronger northward motion (6–10 mm/yr) south of the Krafla central volcano and within the Þeistareykir central volcano than elsewhere (<6 mm/yr).

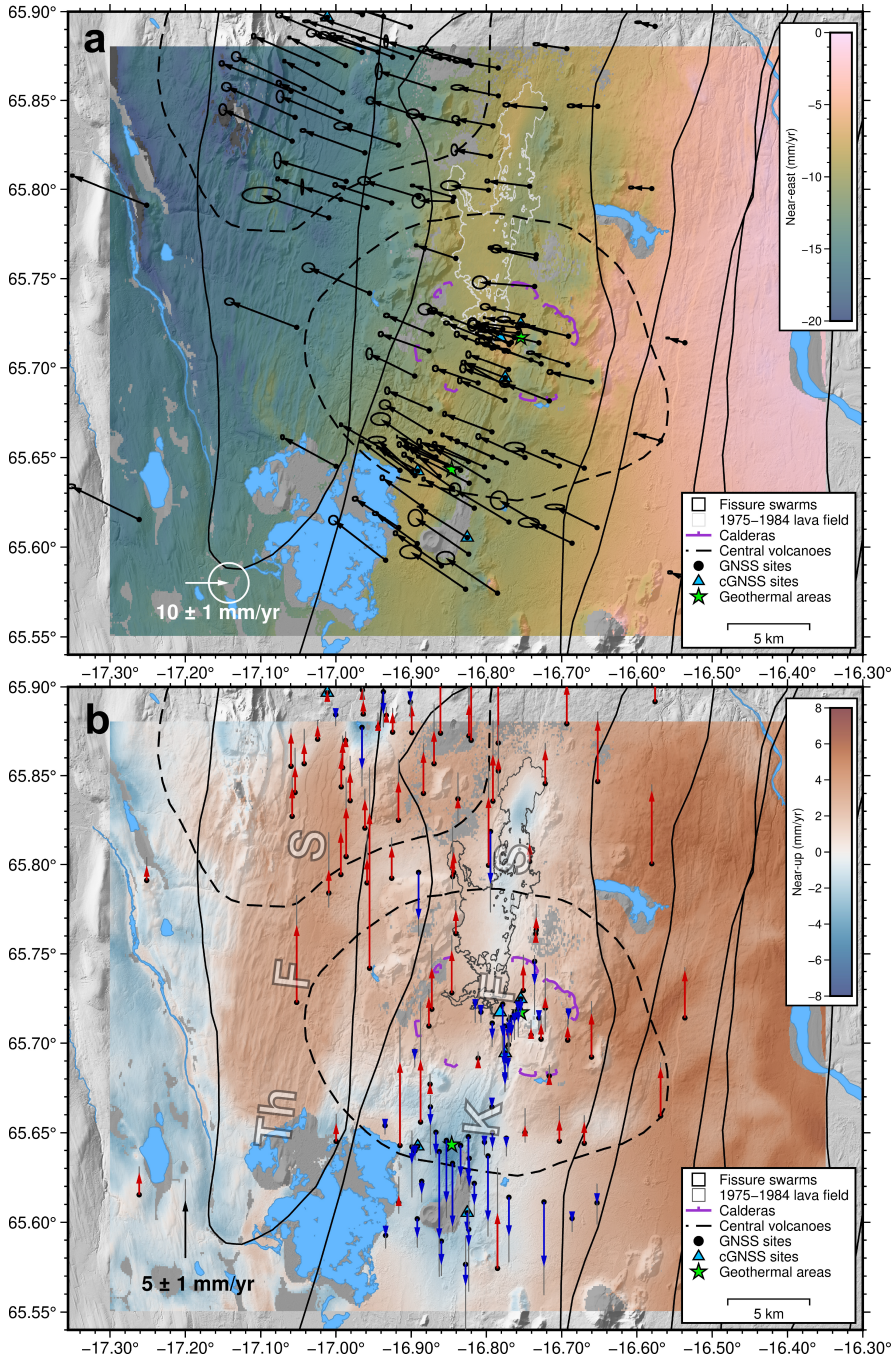


Figure 3. Long-term deformation velocity fields in the central part of the Krafla volcanic system from GNSS (2002–2024) and InSAR (2015–2023). **(a)** Horizontal velocity fields. Black arrows show GNSS horizontal velocities with ellipses indicating uncertainties (95% confidence) and the color map shows the InSAR near-east velocity field. **(b)** Vertical velocity fields. GNSS velocities are shown with red (uplift) and blue (subsidence) arrows, and their uncertainties (95% confidence) are shown with gray lines, centered symmetrically at the arrow tips. Half of the uncertainty bar may be covered by the arrow body due to overlap. ThFS: Þeistareykir fissure swarm. KFS: Krafla fissure swarm.

Observed GNSS vertical displacements (arrows in Figure 3b) show overall uplift, with millimeter-level yearly subsidence concentrated in the Bjarnarflag area and the Krafla caldera center. The fastest uplift in GNSS velocities is observed northwest and east of the Krafla central volcano, reaching up to ~5 mm/yr. InSAR near-up velocity field (color map in Figure 3b) are consistent with the GNSS displacement pattern but also provide additional detail on the spatial variability of deformation. It further suggests two main areas of uplift, within the Þeistareykir fissure swarm (~3 mm/yr) and east of the Krafla fissure swarm (5–6 mm/yr). The westwern most part of the study area shows minor vertical deformation, ~1 mm/yr uplift at the two westernmost GNSS sites and InSAR velocities there range from -1 to 1 mm/yr.

We also extract the InSAR velocities from pixels nearest to GNSS sites and compare them with corresponding GNSS velocities in Figure S9 in Supplementary Information S1 to further demonstrate the consistency between GNSS and InSAR results. To summarize, GNSS horizontal and InSAR near-east velocity fields are consistent with each other and effectively capture the plate boundary deformation. Their consistency suggests relatively stable long-term deformation at Krafla and supports the usage of both datasets in a joint inversion of the plate boundary model.

4.2 Plate boundary model of the Krafla area

The inferred plate boundary axis is shown as a segmented line with a color gradient from light to dark blue (south to north) in Figure 4a and e, divided by the white diamonds. The segments are denoted as S1–S6 from south to north. Table 1 and Figure 4b–d show the median estimates and 95% confidence interval of model parameters. Two strike changes of the inferred plate boundary axis are notable: one from S1 to S3, where the strike gradually increases from a value below N3.8°–6.8°E to N7.5°–15.5°E; and the other between S5 and S6, where the strike rotates from NE-SW to NW-SE by 6.4°–17.3° to the west near the northern boundary of the Krafla central volcano. The locking depth of the plate boundary axis exhibits significant variation, illustrating an asymmetric deepening trend of locking depth laterally away from the caldera along the south-north direction (discussed in section 5.4). The marginal PDFs of all model parameters are shown in Figure S10 and S11 in Supplementary Information S1. Table S4 displays the coordinates of the inferred plate boundary axis.

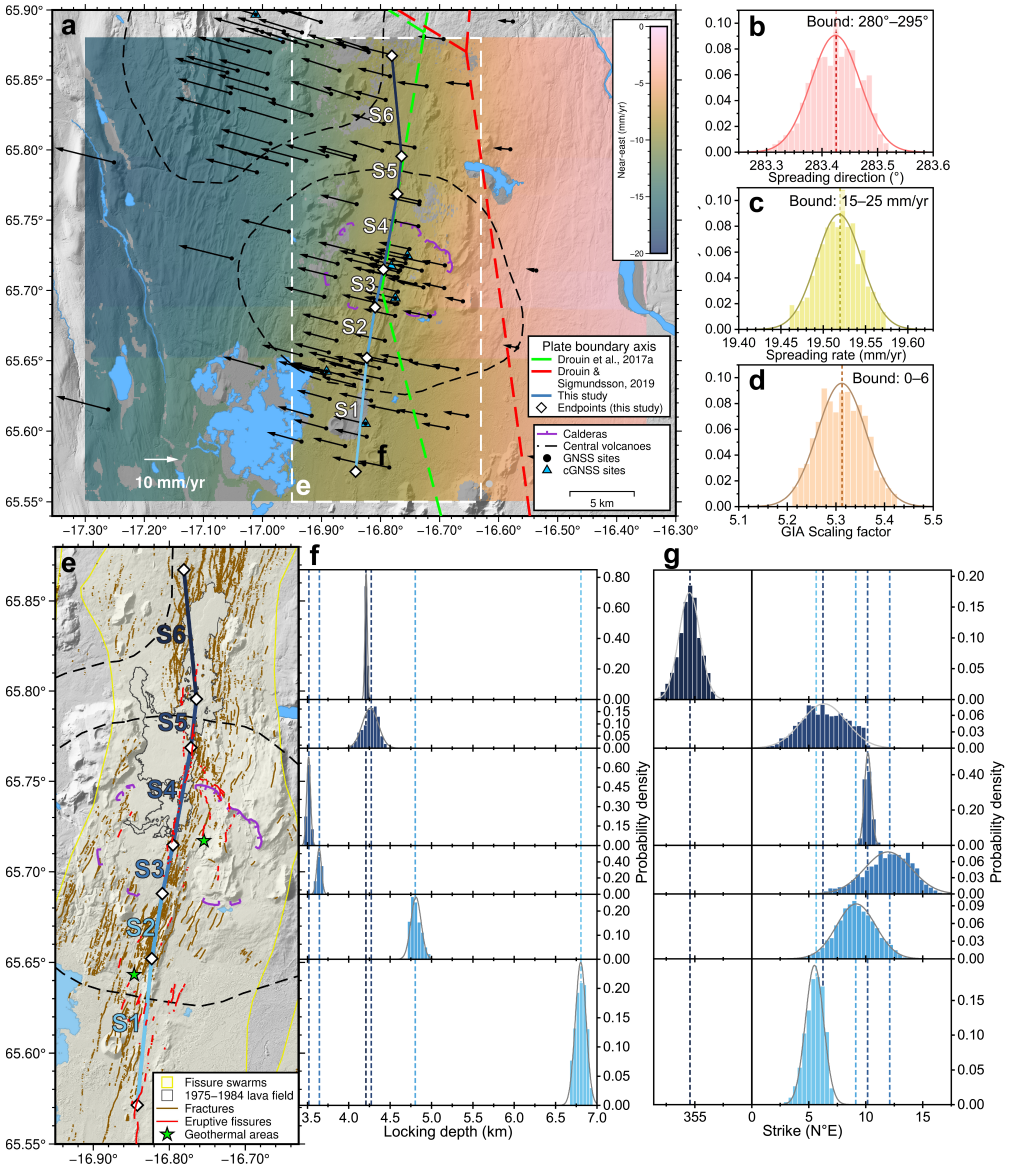


Figure 4. Plate boundary model constrained from GNSS and InSAR velocity fields. **(a)** Map showing modeled plate boundary displacements, arrows for horizontal velocities at GNSS sites and colormap for InSAR near-east velocities. The color from light to dark blue indicates segment location from south to north for visual distinction, also applied for Figure 4e, f and g. The green and red dashed lines indicate the plate boundary central axis previously constrained from either GNSS-only or InSAR-only data, respectively (Drouin et al., 2017a; Drouin and Sigmundsson, 2019). The white dashed rectangle shows the area in Figure 4e. **(b)–(d)** Marginal posterior PDFs of the spreading parameters and horizontal GIA scaling factor. Vertical dashed lines indicate the medians of the PDFs. **(e)** Zoomed-in view of the inferred plate boundary axis. **(f)** Marginal posterior probability density functions (PDF) of the locking depth for each plate boundary segment. The vertical extent of each panel corresponds to their latitude range in Figure 4e. Vertical dashed lines indicate the median of the PDFs. **(g)** Marginal posterior probability density functions (PDF) of the strike for each plate boundary segment. Vertical dashed lines indicate the medians of the PDFs.

Table 1. Inferred plate boundary model across the central part of the Krafla volcanic system in this study. Parameter estimates are the median of the marginal posterior PDFs and the formal uncertainties are inferred from corresponding 95% confidence intervals. Uncertainties in the brackets are inferred from an alternative approach (see Section 5.1 and Text S2 in the Supplementary Information S1). The reference point of the local Cartesian coordinate system is 16.83°W, 65.67°N. The southern endpoint of segment S3 is inferred from the inversion, while the other is calculated from its length and strike. Other segments are then connected sequentially: one endpoint is fixed to the adjacent segment, and the other is calculated from its segment length and strike.

Segment	Length in Y-axis (km)	Strike	X-coordinate of the southern endpoint (km)	Locking depth (km)
S1	9	$\mathrm{N}5.6^{+1.2}_{-1.8}$°E	/	$6.81^{+0.11\ (+0.28)}_{-0.13\ (-0.28)}$
S2	4	$\mathrm{N}9.1^{+3.4}_{-3.4}$°E	/	$4.80^{+0.15\ (+0.31)}_{-0.08\ (-0.26)}$
S3	3	$\mathrm{N}12.1^{+3.4}_{-4.6}$°E	$0.96^{+0.39}_{-0.38}$	$3.64^{+0.05\ (+0.13)}_{-0.06\ (-0.13)}$
S4	6	$\mathrm{N}10.2^{+0.6}_{-0.6}$°E	/	$3.52^{+0.03\ (+0.09)}_{-0.06\ (-0.12)}$
S5	3	$\mathrm{N}6.2^{+3.6}_{-3.7}$°E	/	$4.27^{+0.15\ (+0.45)}_{-0.23\ (-0.41)}$
S6	8	$\mathrm{N}354.6^{+1.5}_{-2.1}$°E	/	$4.21^{+0.04\ (+0.08)}_{-0.02\ (-0.05)}$

Parameters	Estimate
Spreading direction	$\mathrm{N}283.4^{+0.1\ (+0.1)}_{-0.1\ (-4.5)}$°E
Spreading rate (mm/yr)	$19.52^{+0.05\ (+1.33)}_{-0.06\ (-2.42)}$
GIA scaling factor – GNSS & InSAR	$5.31^{+0.10}_{-0.09}$

The median estimate of horizontal GIA scaling factor (5.31) is higher than the value of 3.2 reported by Drouin et al. (2017a). This larger horizontal GIA scaling factor is possibly caused by (i) regional mismatch between the GIA deformation and the countrywide model by Auriac (2014), (ii) possible bias from velocity errors given the small magnitude of horizontal GIA deformation, (iii) different datasets and data timespans used in this study. Even scaled by a factor of 5.31, the predicted GIA horizontal deformation remains less than 1 mm/yr in east component and ~2 mm/yr in north component (see Figure S12 in Supplementary Information S1) and generally should not influence the estimation of locking depth and spreading parameters.

Figure 5 compares the observed and modeled deformation velocities along the spreading direction for all six segments. For the east component, the model fits the observations well and reproduces specifically the observed flattened velocity gradient near the plate boundary axis. GIA correction yields only minimal shift. For the north component, segment S3 and S4 show the best fit qualitatively, while other segments show systematic misfits: the model underestimates northward

motions in northern segments (S5–S6), while overestimates northward motions in southern segments (S1–S2). This pattern is consistent with the north-south contraction towards the Krafla caldera along the fissure swarm. Although such contraction was explained using a deep deflation source by Drouin et al. (2017a), the east-component velocity profiles in Figure 5 do not show corresponding systematic misfits. An alternative explanation for this contraction could be crustal heterogeneity along the fissure swarm, where variation in viscosity or rigidity generates strike-parallel stress gradients and localized contraction toward the caldera. Because the second-step inversion applies a single set of spreading parameters across the whole area, trade-offs among segments are inevitable. Such a systematic pattern produces opposite effects north and south of the source, which tend to cancel out in the inversion and therefore should not considerably affect the inferred spreading parameters.

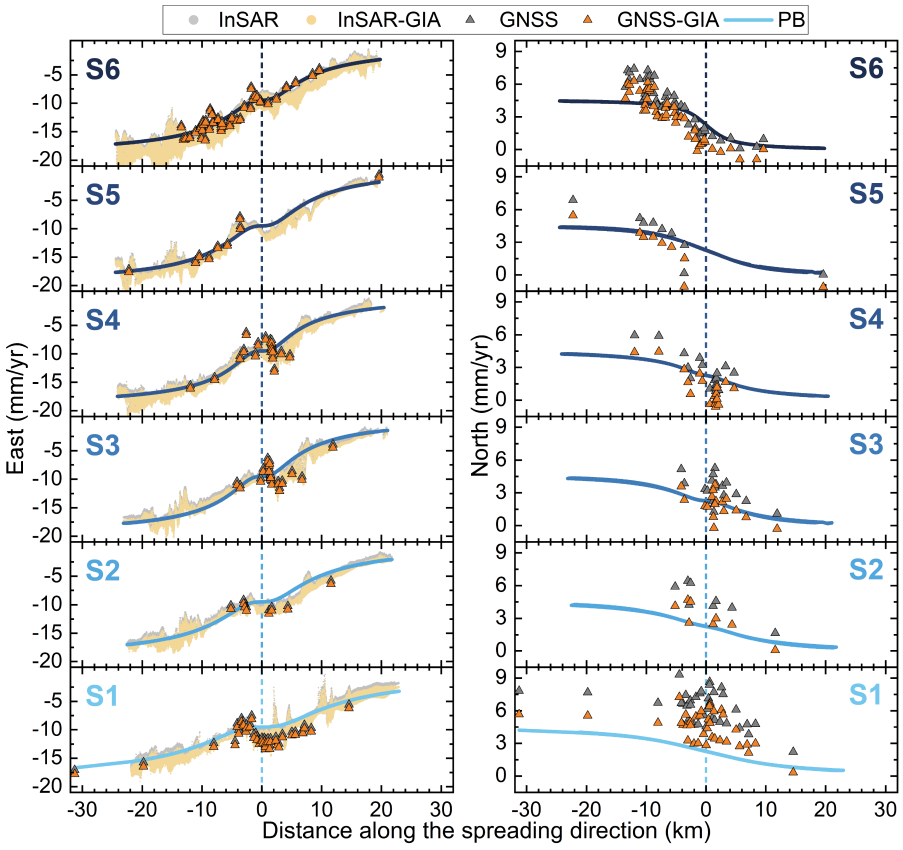


Figure 5. Profiles of observed and predicted velocities along the inferred spreading direction for all segments of the inferred plate boundary axis. For each segment, all GNSS sites and InSAR pixels located within its spatial extent are grouped and plotted as a one-dimensional profile across the plate boundary, aligned with the spreading direction. Notice the difference in scale in left and right panels. InSAR-GIA and GNSS-GIA indicate the InSAR and GNSS velocities corrected for GIA displacements, respectively. PB indicates the plate boundary model predictions. Orange dots and triangles overlaps with gray dots and triangles. Notice the different y-axis scale for east and north components of displacements.

4.3 Residual velocity fields

Residual velocity fields are shown in Figure 6 and additional comparisons among observed, modeled and residual velocities are shown in Figure S13–S15 in Supplementary Information S1. In the area north of ~65.65°N, both horizontal and vertical residual velocities are generally within ±2 mm/yr, suggesting that the model accounts for the plate boundary and GIA deformation. However, in the southeastern part of the study area (dashed rectangle 2 in Figure 6a), GNSS horizontal velocities show residual northwest motion, with an average magnitude of 2.0 mm/yr and a maximum of 3.9 mm/yr. Vertical residual velocities in this area mostly show subsidence, with GNSS residuals averaging -5.2 mm/yr and reaching a minimum of -10.8 mm/yr.

Since we implement infinitely long fault planes for the back-slip dislocation (Figure 2c) to minimize deformation gradients at the ends of plate boundary segments, these residual velocities are unlikely to be artifacts from model configuration. Two possible explanations may account for this systematic residual pattern. One is an extra rotation south of the Krafla central volcano, related to the transition of plate spreading from the Krafla volcanic system to systems further southeast. The other is a local mismatch between the large-scale GIA model and the deformation pattern. For instance, GIA deformation may differ between the two plates, whereas the model assumes a continuous response across the plate boundary. This is supported by the fact that the GIA model predicts peak uplift in the southwest (Figure S13b in the Supplementary Information S1), whereas the InSAR near-up velocity field (Figure 3b) shows largest uplift in the eastern part of the study area.

Additionally, Figure 6 highlights three local deflation areas. These deformation signals feature horizontal contraction, with GNSS horizontal residual vectors in Figure 6a pointing inward to these areas, InSAR near-east residual velocities showing eastward motion (yellow color) in their western part and westward motion (blue color) in the east, and vertical residual fields indicating subsidence. Two of such deflating signals are located near the geothermal fields of Bjarnarflag and Krafla (shown in Figure 6c–f), possibly associated with geothermal activity under exploitation (e.g., Sturkell et al., 2008; Drouin et al., 2017b). The vertical residuals in the Krafla caldera (Figure 6e) show discrepancies between InSAR and GNSS, likely due to their different time spans, especially an inflation period during 2018–2022 reported by Lanzi et al. (2023) (further supported by the InSAR displacement time series in section 4.4).

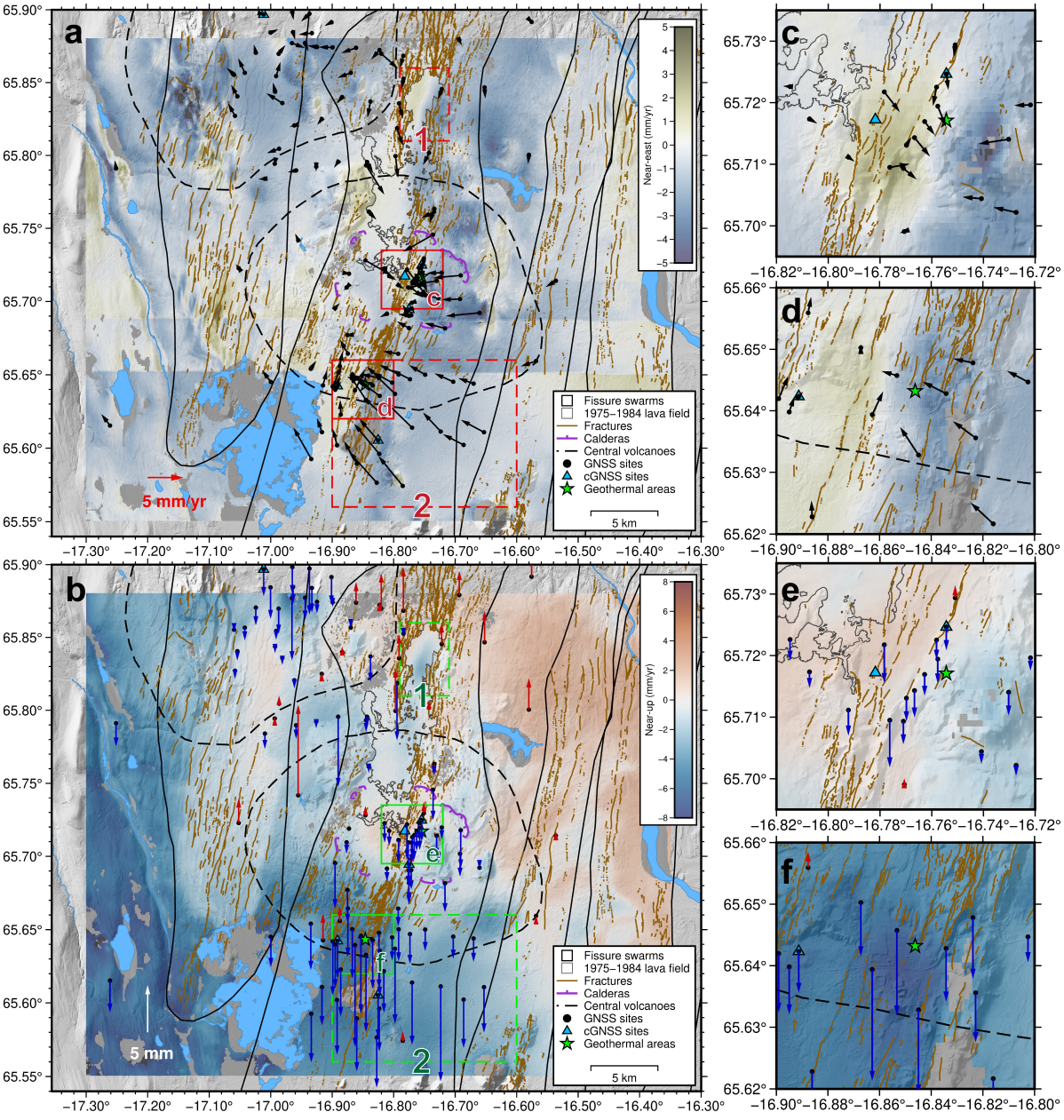


Figure 6. Horizontal **(a)** and vertical **(b)** residual velocity fields from GNSS (arrows) and InSAR (colormaps). The solid rectangles correspond to Figure 6c–6f. **(c)–(d)** Zoomed-in view of the horizontal residual velocity fields at the geothermal fields. Symbols and colormaps have the same meaning as in Figure 6a. **(e)–(f)** Zoomed-in view of the horizontal residual velocity fields at the geothermal fields.

The third area is located at the northernmost part of the lava field formed in 1975–1984 (dashed rectangle 1 in Figure 6a and 6b), possibly caused by continued thermal contraction (Sigmundsson et al., 1997), mechanical compaction (Ebmeier et al., 2012) or loading effects on the Earth's surface (e.g., Grapenthin et al., 2010) of the lava. Additionally, the deep deflation source inferred

from the velocity profiles in section 4.2 (Figure 4f) may also be reflected in the residual velocity fields. Residual vectors at GNSS sites in and near the Krafla central volcano (Figure 6a) generally point into the caldera, accompanied by broad subsidence within the central volcano, consistent with a small-magnitude, large-area deflation process beneath the Krafla caldera.

4.4 Temporal variation of local deformation

We extract the InSAR LOS displacement time series along profiles across the three areas showing local deformation to inspect their temporal variation. Three-dimensional velocities predicted by the plate boundary, regional subsidence, and GIA models are projected into the satellite LOS directions. To isolate local deformation signals, the LOS velocity difference between the profile points and the reference area predicted by the combined model is subtracted from the displacement time series. We analyze LOS displacements, rather than near-east and near-up components, to avoid the influence of the residual north-component velocities. Figure 7 shows the profiles with residual LOS displacement time series, with positive values indicating motions of ground points towards the satellite relative to the reference area, and negative values indicating motions away.

Residual displacement time series in the Bjarnarflag area (Figure 7b) show clear and steady trends on both satellite tracks. The residual time series from the Bjarnarflag geothermal field (red circles) show clear decreasing trend, suggesting the local deflation. In contrast, the Krafla caldera center (Figure 7c) exhibits non-linear deformation during 2015–2023. Prior to 2018, most residual displacement series show minimal trends, indicating that the caldera center has similar movements as the reference area (shown in Figure 1 and Figure 7a). After 2018, a significant increase in LOS displacements is observed from the descending track for the center (yellow squares) and easternmost (green inversed triangles) of the caldera, which is consistent with the inflation period reported by Lanzi et al. (2023). However, the eastern part of the Krafla geothermal field (red circles) shows weaker increase in the LOS displacements from the descending track, possibly indicating that a shallow deflation source remains active during the broader inflation. However, linear deformation constraint in LiCSBAS processing may cause underestimation of the transient signals, and future research to better quantify them is needed.

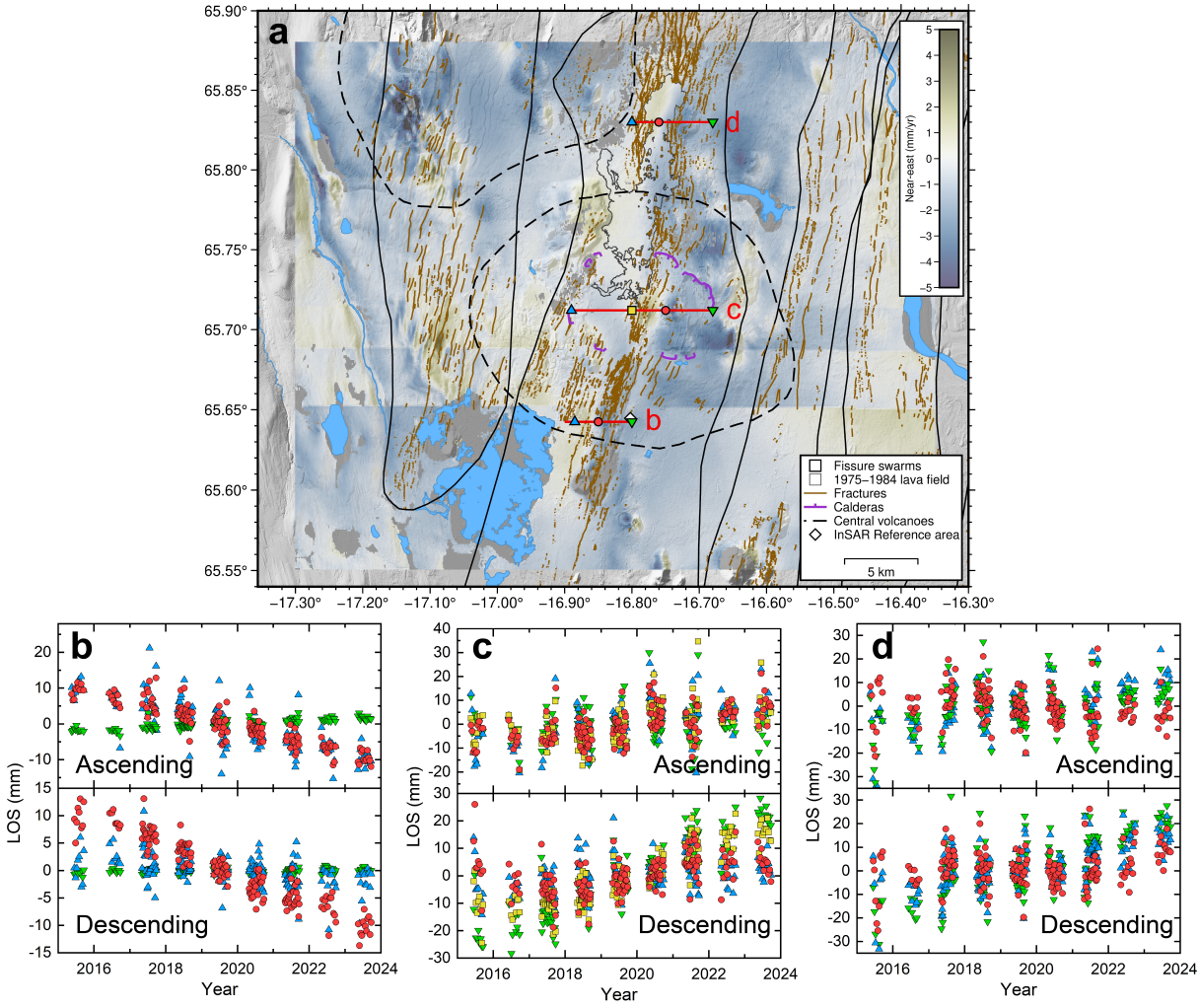


Figure 7. (a) Horizontal residual velocity field from InSAR (same as in Figure 6a) with three profiles across areas of local deformation. Colored symbols mark the locations where InSAR residual line-of-sight (LOS) displacement time series are extracted. Note that the white diamond is partly covered by the green inverted triangle near Bjarnarflag. Profiles labels correspond to the time series plots. **(b)–(d)** Residual InSAR LOS displacement time series along the three profiles. Colors and symbols correspond to those in Figure 7a: Red circles from the centers of the local deformation, and green inverted triangles and blue triangles from the east and west ends of the profiles, respectively. We subtract the mean value from each time series for centering. Note different scales in different panels. Positive (negative) LOS displacements indicate ground points moving towards (away from) the satellite relative to the reference area. The reference area has residual subsidence and northwestward motion both lower than <2 mm/yr in Figure 6. Linear trends in the time series suggest stable deformation signals through the observation period.

To the east and west of the 1975–1984 lava field (blue and green triangles in Figure 7d), residual LOS displacements suggest no clear trend in ascending track and a gradual increase in descending track, reflecting the residual uplift as in Figure 6b. Conversely, residual LOS displacements in the

descending track show less increase in the northern part of the lava field (red circles), mostly within -10–10 mm, compared to -20–30 mm for the blue and green triangles. This coincides with the deflation of the lava field. However, the data points in Figure 7b are more scattered than Figure 7d and the trends are less clear, probably indicating that the deflation at the northern part of the lava field is small and comparable to the residual motion in the reference area after subtracting the modeled deformation. The temporal variation of these local deformation patterns is further supported by residual velocity fields over different time spans, as shown in Figure S16 in Supplementary Information S1.

5 Discussion

5.1 Model limitations

The back-slip model is a kinematic representation of plate boundary deformation and involves several simplifying assumptions. It represents all plate boundary deformation on a single vertical plane along the rift axis, without explicitly representing shallow rift-zone deformation or ductile processes at depth. In nature, ductile processes separate the plates over a finite width, whereas the model idealizes this by directly prescribing the relative displacement of the plates. In addition, deformation at each ground point is assumed to be controlled by only one plate boundary segment, simplifying the mechanical coupling between adjacent segments. These simplifications enable efficient regional-scale modeling but limit the model's ability to reflect dynamic processes and fine-scale tectonic features.

The formal uncertainties of the plate boundary model inferred from the Bayesian inversion are relatively small since the second-step inversion fixes the plate boundary axis, without propagating the uncertainty from the first-step inversion. In addition, they do not account for the limited coverage of the velocity fields in the far field. Consequently, the formal uncertainties primarily reflect the data noise and model misfit after outlier removal, rather than the full model uncertainty. Ideally, one should sample axis geometries from the PDFs of the first-step inversion and implement multiple second-step inversions to obtain the complete PDFs of the plate spreading parameters. However, this approach is computationally prohibitive. As an approximation, we use representative samples from the first-step PDFs to perform maximum likelihood estimation in the second step to evaluate the model uncertainty (see Text S2 in the Supplementary Information S1). The uncertainties from this evaluation are presented in Table 1.

5.2 Inferred plate boundary axis

Figure 4e shows that the modeled plate boundary axis aligns with the recent eruptive fissures mapped by Hjartardóttir et al. (2015). This alignment may reflect an interplay between tensile stress accumulation and crustal weakness at these fissures, as stress tends to localize there while magma intrusions further exploit these structures (e.g., Greiner et al., 2023; Greiner et al., 2025). Compared to previous two-segment boundary models constrained solely by GNSS or InSAR data (green and red dashed lines in Figure 4a; Drouin et al., 2017; Drouin & Sigmundsson, 2019), our inferred plate boundary axis better captures the local stress field. The strikes of inferred axis segments range from N7.5°W to N15.5°E, consistent with fracture orientations summarized by Corti et al. (2021), which have an average of N10.1°E and a standard deviation of 17.5°. Specifically, the south-to-north increase in strike angles for axis segments south of the Krafla central volcano (S1–S3 in Figure 4a) corresponds well with the observed trend of increasing fracture azimuths. The strikes of axis segments S4–S6 in Figure 4a change from NNE-SSW to NNW-SSE, consistent with greater abundance of NNW-SSE oriented fractures north of the Krafla central volcano than in the south (Corti et al., 2021). This may reflect a local stress regime influenced by the intersection between the Krafla fissure swarm and the prolongation of the transform Húsavík-Flatey Fault.

Additionally, we evaluate a potential plate boundary axis that includes a transverse structure within the Krafla caldera. Árnason (2020) identified a possible transverse structure striking WNW-ESE in the southern half of the Krafla caldera (Figure S17 in Supplementary Information S1), based on a resistive anomaly in the resistivity model and a low-density structure in the gravity model. Seismic tomography also suggests a high P-wave to S-wave velocity ratio in this area (Schuler et al., 2015). We adjust the segment S3 to represent such structure (see Figure S17) and rerun the second-step inversion. The resulting model infers a spreading rate differing by <0.5 mm/yr and a spreading direction differing by <1° from the model presented in section 4. The estimated locking depth pattern remains generally similar with the minimum in the north of the caldera. However, the segment corresponding to the transverse structure, though located within the caldera, yields a locking depth of 4.84–5.46 km, deviating from the general variation of locking depth in section 4.2. Moreover, this adjusted model fits the deformation statistically poorer, with a smaller likelihood value than the model presented in section 4 (larger lieklihood value indicates better fit). Although the structure remains debated, our result suggests that it does not significantly influence the regional deformation. Possible explanations include that the feature is too small to be resolved in this study (~1.5 km wide and <5 km long; Martinez-Garcia et al., 2025), or that it only affects the shallowest crust above the locking depth (Schuler et al., 2015; Glück et al., 2025).

5.3 Inferred spreading parameters

Figure S18 in Supplementary Information S1 further compares the inferred spreading parameters with global plate motion and regional plate boundary models. The inferred spreading direction falls within the range of 273°–292° predicted by global plate motion models but is smaller than the 288°–296° range derived from earlier regional models (Metzger et al., 2011; Metzger & Jónsson, 2014; Drouin et al., 2017a; Barreto et al., 2025). This discrepancy may be explained by the relatively large scaling factor (5.31) for GIA horizontal deformation in our model, compared to 3.2 in Drouin et al. (2017a). A higher scaling factor means that more of the observed northward motions are attributed to GIA in the inversion, thereby reducing the inferred spreading azimuth (more E-W oriented). Note that some regional models did not account for GIA deformation because of the long distance from glaciers and uncertainties in GIA models, as they focused on a more northern region (e.g., Metzger & Jónsson, 2014; Barreto et al., 2025), while Drouin et al. (2017a) applied a uniform scaling factor for GIA deformation over about 150 km distance. Our results may highlight the need for more accurate GIA model.

Our inferred spreading rate lies near the lower end of the 19–21 mm/yr range suggested by regional models (Metzger et al., 2011; Metzger et al., 2013; Metzger & Jónsson, 2014; Barreto et al., 2025) but is ~13% higher than the average estimate from global models. Two causes may explain the larger spreading rate inferred across the Krafla volcanic system: (i) Decayed post-rifting viscoelastic relaxation of the 1975–1984 rifting episode may continue contributing millimeter-level extension every year up to ~60 km away from the rift (e.g., Hofton & Foulger, 1996; Ali et al., 2014; Li et al., 2022). The regionally elevated spreading rate may induce minor contraction further away from the rift. However, the contraction associated with a rate difference of only 1–2 mm/yr distributed over a large area is likely below the observational precision, beyond the spatial extent of this study, or accommodated by existing tectonic structures at shallow crust such as normal faults (Ducrocq et al., 2024) or by ductile processes at depth. (ii) Ground deformation associated with glacial unloading, if not fully modeled, may influence the estimation of regional spreading parameters, especially near plate boundaries where the crust is weak and heterogeneous and the lithospheric thickness varies spatially (e.g., Klemann et al., 2008; Vardić et al., 2022; Yuan & Zhong, 2025).

5.4 Inferred locking depth variation

Figure 8 compares the spatial variations in the inferred locking depth with the seismicity during 2002–2022 and the surface widening during the 1975–1984 Krafla rifting episode. Two profiles are outlined based on the depth distribution of seismicity inferred by Guðnason et al. (2023), one indicating the depth range where most (~90%) earthquakes occur, and the other approximating the

maximum depth of seismicity (orange and brown lines in Figure 8, respectively). The inferred locking depth is referenced to the ground surface in above sections, while the seismicity distribution in Guðnason et al. (2023) is referenced to the sea level. For better comparison, we add the surface elevation to the inferred the locking depth in Figure 8.

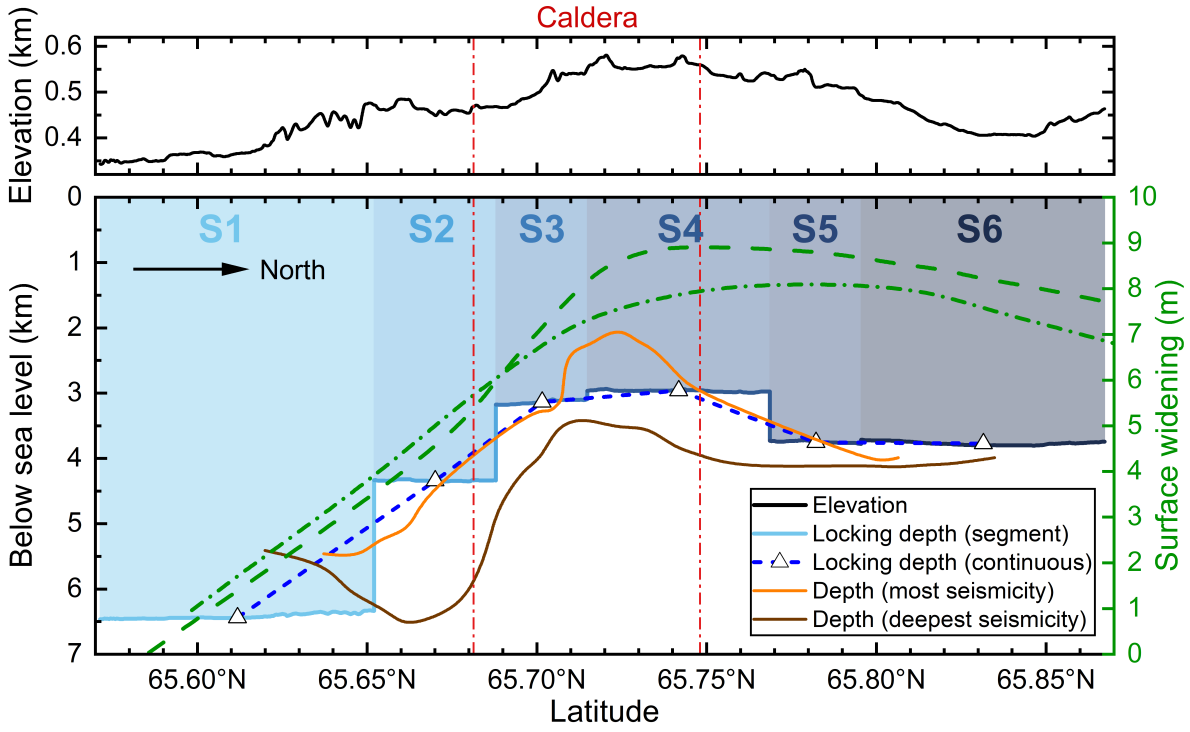


Figure 8. Comparison between the inferred plate boundary locking depth, the depth distribution of seismicity during 2006–2022 and the surface widening during the 1975–1984 rifting episode. The vertical dash-dotted red lines indicate the north and south rims of the Krafla caldera. The blue lines with varying intensity represent the inferred locking depth of different axis segments, where more southern segments correspond to lighter the blue color. Above the blue lines are boxes filled to the top with the same color, showing the depth range of the back-slip dislocation. The triangles are the midpoints of the segments at their locking depths, connected with the blue dashed line to form an indicative continuous locking depth profile. Depth (most seismicity) indicates that most earthquakes occur shallower than this depth, while depth (deepest seismicity) outlines the deepest seismicity at Krafla. Dashed and dash-dotted green lines shows the surface widening during the 1975–1984 rifting episode estimated by Tryggvason (1984) and Hollingsworth et al. (2012), respectively, referring to the right vertical axis. The depth of seismicity is drawn from Guðnason et al. (2023). The surface elevation is extracted along the plate boundary axis from the Digital Elevation Model by LMÍ (2020).

Both locking depth of plate boundary and depth distribution of seismicity reflect the brittle-ductile transition within the crust. The general trends of the blue, orange and brown lines in Figure 8 show mutual consistency, with shallowest depths beneath the Krafla caldera, and deepening laterally

away from the caldera. The inferred shallowest locking depth of ~3 km below sea level within and north of the Krafla caldera, together with most seismicity above ~2 km depth, suggests shallow rheological changes. This is probably caused by high temperature and high pore pressure in the crust in the Krafla geothermal field, related to supercritical geothermal fluids and shallow magma bodies (e.g., Mortenson et al., 2010; Scott et al., 2015; Eggertsson et al., 2020; Andajani et al., 2023). Although the locking depth is ~1 km deeper than the depth of most earthquakes, this segment (S4 in Figure 4a) extends from the center of the Krafla caldera to ~1.5 km north of its rim, and therefore likely represents a spatial average across the segment rather than fine-scale variations. Our results validate the deepened elastic-viscoelastic interface away from the Krafla caldera along the fissure swarm assumed in the regional subsidence model by Lanzi et al. (2024).

Locking depth at a divergent plate boundary affects the style of stress accumulation: shallow locking depths produce steep gradients of horizontal deformation velocity, leading to rapid strain accumulation and concentrated tensile stress. Localized tensile stress facilitates magma intrusions. Figure 8 illustrates that both the inferred shallowest locking depth and the maximum cumulative surface widening during the 1975–1984 rifting episode occurs within and north of the Krafla caldera. Seismic observations and a model of repeated lateral dikes have indicated that dikes started lateral propagation in the northern part of the Krafla caldera during its 1975–1984 rifting episode (Einarsson & Brandsdóttir, 2021; Yang et al., in review). Petrochemical evidence of bimodal eruptive products across the north caldera rim from the Krafla rifting episode further suggests magma mixing and supply from different depths (Rooyakkers et al., 2024). Magma intrusions into such a stress-localized area promote the development of a magma domain, consisting of partial melt, magma mush and hot solid rock (Sigmundsson et al., 2024). The inferred shallowest locking depth (~3.5 km) within the caldera coincides with such a magma domain, inferred from geodetic, seismological, petrochemical and drilling observations (e.g., Einarsson 1978; Tryggvason, 1980; Mortenson et al., 2010; Heimisson et al. 2015; Schuler et al. 2015; Kim et al. 2020; Rooyakkers et al., 2024). Stress localization further aids the maintenance of this domain by reducing confining pressure (Eichelberger & Carrigan, 2023). Conversely, dike intrusions and the presence of the magma domain weaken the crust and influence rheology around the caldera, reinforcing tensile stress accumulation. Together, these highlights the volcano-tectonic interactions in controlling ground deformation at volcanoes in a plate boundary zone.

6 Conclusion

We evaluate plate divergence and volcano-tectonic interaction along the Krafla volcanic system by constraining a six-segment plate boundary model using long-term deformation velocity fields from GNSS data (2002–2024) and Sentinel-1 SAR interferograms (2015–2023). The model is established through a kinematic back-slip model and a two-step Bayesian inversion strategy. The

model considers GIA deformation and jointly solves for the axis geometry, spreading parameters and segmental locking depths. The inferred plate boundary axis strikes N2.5°E to N15.5°E within and south of the Krafla central volcano, and changes to N$5.4^{+2.1}_{-1.5}$°W north of it, aligning with mapped fracture orientation and recent eruptive fissures. The inferred spreading rate is $19.52^{+0.05}_{-0.06}$ mm/yr in an azimuth of $283.4^{+0.1}_{-0.1}$° (formal uncertainties). Locking depths are inferred to be shallowest beneath and north of the Krafla caldera at ~3.5 km below surface, increasing to ~4.2 and ~6.8 km north and south of the central volcano, respectively. Such variation is consistent with the depth distribution of seismicity, indicating a dome-like crustal structure across the Krafla volcanic system. The shallowest locking depth coincides with the maximum surface widening during the 1975–1984 rifting episode and the area where dikes started lateral propagation, implying that tensile stress accumulation along the plate boundary facilitates dike intrusions. Residual velocity fields reveal three local deflation patterns, two related to geothermal activities at Krafla and Bjarnarflag geothermal fields and another related to 1975–1984 lava field. Qualitative analysis on InSAR displacement time series further suggests that the local deformation at Bjarnarflag and the lava field are relatively stable through 2015–2023, and the deflation in the Krafla geothermal field might remain active during the 2018–2022 inflation, causing an area with reduced inflation rate.

Acknowledgments

This study received funding from the European Union's Horizon 2020 research and innovation programme under grant agreement No. 858092 (IMPROVE project). We acknowledge Landsvirkjun for collaboration and partial financial support on this research and the GNSS campaigns. We thank Sveinbjörn Steinþórsson for excellent field support for the GNSS measurements, and collaboration on the Krafla GNSS surveys in 2012–2024 with Delft University of Technology, through their summer course program, led by Sandra Verhagen, Paco Lopez Dekker, Freek van Leijen, Taco Broerse and others. COMET is the UK Natural Environment Research Council (NERC)'s Centre for the Observation and Modelling of Earthquakes, Volcanoes and Tectonics, a partnership between UK Universities and the British Geological Survey (https://comet.nerc.ac.uk). We acknowledge Milan Lazecky (University of Leeds), Tianyuan Zhu and Simon Orrego Astudillo (University of Bristol) for supports on InSAR data processing. We thank Corné Kreemer and Raphaël Grandin for suggestions to improve the manuscript. We thank Andrew Hooper, Alejandra Barreto, Þorbjörg Ágústsdóttir, Egill Árni Guðnasson, Elisabeth Glück, Patricia Fehrentz for discussions. The global plate motions are calculated with GAGE Plate Motion Calculator (https://www.unavco.org/software/geodetic-utilities/plate-motion-calculator/plate-motion-calculator.html). Maps are plotted with the Generic Mapping Tools (Wessel et al., 2019).

References

Ali, S. T., Feigl, K. L., Carr, B. B., Masterlark, T., & Sigmundsson, F. (2014). Geodetic measurements and numerical models of rifting in Northern Iceland for 1993–2008. Geophysical Journal International, 196(3), 1267–1280. https://doi.org/10.1093/gji/ggt462

Altamimi, Z., Métivier, L., Rebischung, P., Rouby, H., & Collilieux, X. (2017). ITRF2014 plate motion model. Geophysical Journal International, 209(3), 1906–1912. https://doi.org/10.1093/gji/ggx136

Altamimi, Z., Rebischung, P., Métivier, L., & Collilieux, X. (2016). ITRF2014: A new release of the International Terrestrial Reference Frame modeling nonlinear station motions. Journal of Geophysical Research: Solid Earth, 121, 6109–6131. https://doi.org/10.1002/2016JB013098

Andajani, R. D., Tsuji, T., Ikeda, T., & others (2023). Tracking supercritical geothermal fluid distribution from continuous seismic monitoring. Scientific Reports, 13, 8370. https://doi.org/10.1038/s41598-023-35159-8

Argus, D. F., Gordon, R. G., Heflin, M. B., Ma, C., Eanes, R. J., Willis, P., Peltier, W. R., & Owen, S. E. (2010). The angular velocities of the plates and the velocity of the Earth's centre from space geodesy. Geophysical Journal International, 180(3), 913–960. https://doi.org/10.1111/j.1365-246X.2009.04463.x

Árnadóttir, T., Lund, B., Jiang, W., Geirsson, H., Björnsson, H., Einarsson, P., & Sigurdsson, T. (2009). Glacial rebound and plate spreading: Results from the first countrywide GPS observations in Iceland. Geophysical Journal International, 177(2), 691–716. https://doi.org/10.1111/j.1365-246X.2008.04059.x

Árnason, K. (2020). New conceptual model for the magma-hydrothermal-tectonic system of Krafla, NE Iceland. Geosciences, 10(1), 34. https://doi.org/10.3390/geosciences10010034

Augustin, N., van der Zwan, F.M., Devey, C.W., & Brandsdóttir, B. (2021). 13 million years of seafloor spreading throughout the Red Sea Basin. Nature Communications, 12, 2427. https://doi.org/10.1038/s41467-021-22586-2

Auriac, A. (2014). Solid Earth response to ice retreat and glacial surges in Iceland inferred from satellite radar interferometry and finite element modelling, Ph.D. thesis, University of Icenad, Reykjavík, Iceland.

Bagnardi, M., & Hooper, A. (2018). Inversion of surface deformation data for rapid estimates of source parameters and uncertainties: A Bayesian approach. Geochemistry, Geophysics, Geosystems, 19, 2194–2211. https://doi.org/10.1029/2018GC007585

Barreto, A., Viltres, R., Matrau, R., Metzger, S., Ófeigsson, B. G., Liu, S., et al. (2025). Interseismic deformation of the Húsavík–Flatey fault (North Iceland) from two decades of GNSS data. Geophysical Journal International, 241(3), 1663–1679. https://doi.org/10.1093/gji/ggaf106

Bennett, E.N., Jenner, F.E., Millet, M.-A., Cashman, K.V., & Lissenberg, C.J. (2019). Deep roots for mid-ocean-ridge volcanoes revealed by plagioclase-hosted melt inclusions. Nature, 572, 235–239. https://doi.org/10.1038/s41586-019-1448-0

Björnsson, A., Saemundsson, K., Einarsson, P., Tryggvason, E., & Grönvold, K. (1977). Current rifting episode in north Iceland. Nature, 266(5597), 318–323. https://doi.org/10.1038/266318a0

Blewitt, G., & Lavallée, D. A. (2002). Effect of annual signals on geodetic velocity. Journal of Geophysical Research: Solid Earth, 107(B7), ETG 9-1–ETG 9-11. https://doi.org/10.1029/2001JB000570

Boehm, J., Werl, B., & Schuh, H. (2006). Troposphere mapping functions for GPS and very long baseline interferometry from European Centre for Medium-Range Weather Forecasts operational analysis data. Journal of Geophysical Research: Solid Earth, 111, B02406. https://doi.org/10.1029/2005JB003629

Cao, Y., Jónsson, S., & Hreinsdóttir, S. (2023). Iceland kinematics from InSAR. Journal of Geophysical Research: Solid Earth, 128, e2022JB025546. https://doi.org/10.1029/2022JB025546

COMSOL. (2022). COMSOL Multiphysics® v6.1. COMSOL AB. Retrieved from https://www.comsol.com

Corti, N., Bonali, F. L., Pasquaré Mariotto, F., Tibaldi, A., Russo, E., Hjartardóttir, Á. R., Einarsson, P., Rigoni, V., & Bressan, S. (2021). Fracture Kinematics and Holocene Stress Field at the Krafla Rift, Northern Iceland. Geosciences, 11(2), 101. https://doi.org/10.3390/geosciences11020101

Denis, D., McCarthy, D. D., & Petit, G. (2004). IERS Conventions (2003). IERS Technical Note 32. Frankfurt am Main: IERS Convention Center.

DeMets, C., Gordon, R. G., & Argus, D. F. (2010). Geologically current plate motions. Geophysical Journal International, 181(1), 1–80. https://doi.org/10.1111/j.1365-246X.2009.04491.x

DeMets, C., Gordon, R. G., Argus, D. F., & Stein, S. (1994). Effect of recent revisions to the geomagnetic reversal time scale on estimates of current plate motions. Geophysical Research Letters, 21(20), 2191–2194. https://doi.org/10.1029/94GL02118

Doin, M.-P., Lodge, F., Guillaso, S., Jolivet, R., Lasserre, C., Ducret, G., et al. (2011). Presentation of the small baseline NSBAS processing chain on a case example: The Etna deformation monitoring from 2003 to 2010 using Envisat data. In Proceedings of the FRINGE 2011 Workshop, Frascati, Italy, 19–23 September. ESA SP-697.

Drouin, V., & Sigmundsson, F. (2019). Countrywide observations of plate spreading and glacial isostatic adjustment in Iceland inferred by Sentinel-1 radar interferometry, 2015–2018. Geophysical Research Letters, 46, 8046–8055. https://doi.org/10.1029/2019GL082629

Drouin, V., Sigmundsson, F., Ófeigsson, B. G., Hreinsdóttir, S., Sturkell, E., & Einarsson, P. (2017a). Deformation in the Northern Volcanic Zone of Iceland 2008–2014: An interplay of tectonic, magmatic, and glacial isostatic deformation. Journal of Geophysical Research: Solid Earth, 122, 3158–3178. https://doi.org/10.1002/2016JB013206

Drouin, V., Sigmundsson, F., Verhagen, S., Ófeigsson, B. G., Spaans, K., & Hreinsdóttir, S. (2017b). Deformation at Krafla and Bjarnarflag geothermal areas, Northern Volcanic Zone of Iceland, 1993–2015. Journal of Volcanology and Geothermal Research, 344, 92–105. https://doi.org/10.1016/j.jvolgeores.2017.06.013

Ducrocq, C., Árnadóttir, Þ., Einarsson, P., Jónsson, S., Drouin, V., Geirsson, H., & Hjartardóttir, Á. R. (2024). Widespread fracture movements during a volcano-tectonic unrest: The Reykjanes Peninsula, Iceland, from 2019–2021 TerraSAR-X interferometry. Bulletin of Volcanology, 86, 14. https://doi.org/10.1007/s00445-023-01699-0

Ebmeier, S. K., Biggs, J., Mather, T. A., Elliott, J. R., Wadge, G., & Amelung, F. (2012). Measuring large topographic change with InSAR: Lava thicknesses, extrusion rate and

subsidence rate at Santiaguito volcano, Guatemala. Earth and Planetary Science Letters, 335–336, 216–225. https://doi.org/10.1016/j.epsl.2012.04.027

Eggertsson, G. H., Lavallée, Y., Kendrick, J. E., & Markússon, S. H. (2020). Improving fluid flow in geothermal reservoirs by thermal and mechanical stimulation: The case of Krafla volcano, Iceland. Journal of Volcanology and Geothermal Research, 391, 106351. https://doi.org/10.1016/j.jvolgeores.2018.04.008

Eichelberger, J. C., & Carrigan, C. R. (2023). What is the confining pressure of magma and what does this mean about depth and eruption? AGU Fall Meeting Abstracts, 2023(195), V23D-0195. https://agu.confex.com/agu/fm23/meetingapp.cgi/Paper/1271150

Einarsson, P. (1978). S-wave shadows in the Krafla Caldera in NE-Iceland, evidence for a magma chamber in the crust. Bulletin of Volcanology, 41, 187–195. https://doi.org/10.1007/BF02597222

Einarsson, P. (1991). Umbrotin við Kröflu 1975–89 (in Icelandic). In A. Garðarsson & Á. Einarsson (Eds.), Náttúra Mývatns (pp. 97–139). Reykjavík: Hið íslenska náttúrufræðifélag.

Einarsson, P., & Brandsdóttir, B. (2021). Seismicity of the Northern Volcanic Zone of Iceland. Frontiers in Earth Science, 9, 628967. https://doi.org/10.3389/feart.2021.628967

European Space Agency (ESA). (2020). Copernicus Digital Elevation Model (DEM) – 2020 release [Data set]. European Space Agency. https://doi.org/10.5270/ESA-c5d3d65

Funning, G. J., Bürgmann, R., Ferretti, A., Novali, F., & Fumagalli, A. (2007). Creep on the Rodgers Creek fault, northern San Francisco Bay area from a 10 year PS-InSAR dataset. Geophysical Research Letters, 34, L19306. https://doi.org/10.1029/2007GL030836

Glück, E., Garambois, S., Vandemeulebrouck, J., Muzellec, T., Virieux, J., Mortensen, A. K., Gudnason, E. Á., Ágústsdóttir, T. (2025). Seismicity patterns and multi-scale imaging of Krafla, N–E Iceland, with local earthquake tomography. Journal of Geophysical Research: Solid Earth, 130, e2024JB030425. https://doi.org/10.1029/2024JB030425

Grapenthin, R., Ófeigsson, B. G., Sigmundsson, F., Sturkell, E., & Hooper, A. (2010). Pressure sources versus surface loads: Analyzing volcano deformation signal composition with an application to Hekla volcano, Iceland. Geophysical Research Letters, 37, L20310. https://doi.org/10.1029/2010GL044590

Greiner, S. H. M., Burchardt, S., Sigmundsson, F., Óskarsson, B. V., Galland, O., Geirsson, H., & Rhodes, E. (2023). Interaction between propagating basaltic dikes and pre-existing fractures: A case study in hyaloclastite from Dyrfjöll, Iceland. Journal of Volcanology and Geothermal Research, 442, 107891. https://doi.org/10.1016/j.jvolgeores.2023.107891

Greiner, S. H. M., Galland, O., Sigmundsson, F., Burchardt, S., Geirsson, H., Pedersen, R., & Wen, X. (2025). The influence of variable host rock cohesion and magma viscosity on intrusion-fault interaction: Insights from laboratory models. Journal of Geophysical Research: Solid Earth, 130, e2024JB029870. https://doi.org/10.1029/2024JB029870

Guðnason, E. Á., Ágústsdóttir, Þ., Magnússon, R. L., & Gunnarsson, K. (2023). Seismic monitoring in Krafla, Þeistareykir and Námafjall: October 2022 to November 2023 (LV-2023-060). Landsvirkjun. http://hdl.handle.net/10802/34603

Gudnason, E. Á., Drouin, V., Yang, Y., Sigmundsson, F., Ágústsdóttir, T., & Mortensen, A. K. (2024). Changes in seismicity and observed deformation related to inflation at the Theistareykir high-temperature geothermal field, NE Iceland, in 2023–2024. EGU General Assembly 2024, Vienna, Austria, 14–19 April 2024, EGU24-19913. https://doi.org/10.5194/egusphere-egu24-19913

Guglielmino, F., Nunnari, G., Puglisi, G., & Spata, A. (2011). Simultaneous and integrated strain tensor estimation from geodetic and satellite deformation measurements to obtain three-dimensional displacement maps. IEEE Transactions on Geoscience and Remote Sensing, 49(6), 1815–1826. https://doi.org/10.1109/TGRS.2010.2103078

Heimisson, E. R., Einarsson, P., Sigmundsson, F., & Brandsdóttir, B. (2015). Kilometer-scale Kaiser effect identified in Krafla volcano, Iceland. Geophysical Research Letters, 42(19), 7958–7965. https://doi.org/10.1002/2015GL065680

Herring, T. A., King, R. W., Floyd, M. A., & McClusky, S. C. (2018). Introduction to GAMIT/GLOBK. Massachusetts Institute of Technology. Retrieved from http://geoweb.mit.edu/gg/Intro_GG.pdf

Hjartardóttir, Á. R., Einarsson, P., Bramham, E., & Wright, T. (2012). The Krafla fissure swarm, Iceland, and its formation by rifting events. Bulletin of Volcanology, 74, 2139–2153. https://doi.org/10.1007/s00445-012-0659-0

Hjartardóttir, Á. R., Einarsson, P., Magnúsdóttir, S., Björnsdóttir, Þ., & Brandsdóttir, B. (2015). Fracture systems of the Northern Volcanic Rift Zone, Iceland: An onshore part of the Mid-Atlantic plate boundary. In T. Wright, A. Ayele, D. J. Ferguson, T. Kidane, & C. Vye-Brown (Eds.), Magmatic rifting and active volcanism (Vol. 420, pp. 297–314). Geological Society of London. https://doi.org/10.1144/SP420.1

Hofton, M. A., & Foulger, G. R. (1996). Postrifting anelastic deformation around the spreading plate boundary, north Iceland: 1. Modeling of the 1987–1992 deformation field using a viscoelastic Earth structure. Journal of Geophysical Research: Solid Earth, 101(B11), 25403–25421. https://doi.org/10.1029/96JB02466

Hollingsworth, J., Leprince, S., Ayoub, F., & Avouac, J.-P. (2012). Deformation during the 1975–1984 Krafla rifting crisis, NE Iceland, measured from historical optical imagery. Journal of Geophysical Research: Solid Earth, 117, B11407. https://doi.org/10.1029/2012JB009140

Jeffreys, H. (1939). Theory of probability. Oxford, UK: Clarendon Press.

Jóhannesson, H., & Sæmundsson, K. (2009). Jarðfræðikort af Íslandi 1:600,000, höggun: Geological map of Iceland 1:600,000 – Tectonics. Icelandic Institute of Natural History.

Kim, D., Brown, L. D., Árnason, K., Gudmundsson, Ó., Ágústsson, K., & Flóvenz, Ó. G. (2020). Magma "bright spots" mapped beneath Krafla, Iceland, using RVSP imaging of reflected waves from microearthquakes. Journal of Volcanology and Geothermal Research, 391, 106365. https://doi.org/10.1016/j.jvolgeores.2018.04.022

Landmælingar Íslands (LMÍ). (2020). ÍslandsDEM, version 1.0, Landmælingar Íslands (National Land Survey of Iceland), available at https://gatt.natt.is/geonetwork/srv/api/records/e6712430-a63c-4ae5-9158-c89d16da6361

Lanzi, C., Drouin, V., Sigmundsson, F., Geirsson, H., Hersir, G. P., Ágústsson, K., et al. (2023). Pressure increase at the magma-hydrothermal interface at Krafla caldera, North-Iceland, 2018–2020: Magmatic processes or hydrothermal changes? Journal of Volcanology and Geothermal Research, 440, 107849. https://doi.org/10.1016/j.jvolgeores.2023.107849

Lanzi, C., Sigmundsson, F., Parks, M. M., Geirsson, H., & Drouin, V. (2024). Strain localization at volcanoes undergoing extension: Investigation of long-term deformation at Krafla and Askja volcanic systems in North Iceland. Geophysical Research Letters, 51, e2024GL110299. https://doi.org/10.1029/2024GL110299

Lazecký, M., Spaans, K., González, P. J., Maghsoudi, Y., Morishita, Y., Albino, F., et al. (2020). LiCSAR: An Automatic InSAR Tool for Measuring and Monitoring Tectonic and Volcanic Activity. Remote Sensing, 12(15), 2430. https://doi.org/10.3390/rs12152430

Leonard, L. J., Hyndman, R. D., Mazzotti, S., Nykolaishen, L., Schmidt, M., & Hippchen, S. (2007). Current deformation in the northern Canadian Cordillera inferred from GPS measurements. Journal of Geophysical Research: Solid Earth, 112(B11), B11401. https://doi.org/10.1029/2007JB005061

Li, S., Grapenthin, R., Sigmundsson, F., Drouin, V., Hreinsdóttir, S., & Ófeigsson, B. G. (2022). Post-rifting relaxation during 2015–2020 following the Bárðarbunga-Holuhraun dike intrusion and eruption in Iceland. Geophysical Research Letters, 49, e2022GL098977. https://doi.org/10.1029/2022GL098977

López-Quiroz, P., Doin, M.-P., Tupin, F., Briole, P., & Nicolas, J.-M. (2009). Time series analysis of Mexico City subsidence constrained by radar interferometry. Journal of Applied Geophysics, 69(1), 1–15. https://doi.org/10.1016/j.jappgeo.2009.02.006

Lyard, F., Lefevre, F., Letellier, T., & Francis, O. (2006). Modelling the global ocean tides: Modern insights from FES2004. Ocean Dynamics, 56, 394–415. https://doi.org/10.1007/s10236-006-0086-x

Martinez-Garcia, A., Gottsmann, J., Wookey, J., Rust, A., Gudmundsson, M. T., & Lavallée, Y. (2025). 3D model of the shallow crustal density distribution of the Krafla volcanic system in Iceland. Journal of Geophysical Research: Solid Earth, 130, e2025JB031670. https://doi.org/10.1029/2025JB031670

Metzger, S., & Jónsson, S. (2014). Plate boundary deformation in North Iceland during 1992–2009 revealed by InSAR time-series analysis and GPS. Tectonophysics, 634, 127–138. https://doi.org/10.1016/j.tecto.2014.07.027

Metzger, S., Jónsson, S., & Geirsson, H. (2011). Locking depth and slip-rate of the Húsavík Flatey fault, North Iceland, derived from continuous GPS data 2006–2010. Geophysical Journal International, 187(2), 564–576. https://doi.org/10.1111/j.1365-246X.2011.05176.x

Metzger, S., Jónsson, S., Danielsen, G., Hreinsdóttir, S., Jouanne, F., Giardini, D., & Villemin, T. (2013). Present kinematics of the Tjörnes Fracture Zone, North Iceland, from campaign and continuous GPS measurements. Geophysical Journal International, 192(2), 441–455. https://doi.org/10.1093/gji/ggs032

Morishita, Y., Lazecky, M., Wright, T. J., Weiss, J. R., Elliott, J. R., & Hooper, A. (2020). LiCSBAS: An Open-Source InSAR Time Series Analysis Package Integrated with the LiCSAR Automated Sentinel-1 InSAR Processor. Remote Sensing, 12(3), 424. https://doi.org/10.3390/rs12030424

Mortensen, A., Grönvold, K., Gudmundsson, Á., Steingrímsson, B., & Egilson, T. (2010). Quenched silicic glass from well KJ-39 in Krafla, North-Eastern Iceland. In Proceedings of the World Geothermal Congress (pp. 1–6).

Motagh, M., Shamshiri, R., Haghshenas Haghighi, M., Wetzel, H.-U., Akbari, B., Nahavandchi, H., Roessner, S., & Arabi, S. (2017). Quantifying groundwater exploitation induced subsidence in the Rafsanjan plain, southeastern Iran, using InSAR time-series and in situ measurements. Engineering Geology, 218, 134–151. https://doi.org/10.1016/j.enggeo.2017.01.011

Nikolaidis, R. (2002). Observation of geodetic and seismic deformation with the Global Positioning System. Ph.D. thesis, University of California, San Diego, La Jolla, CA, USA.

Okada, Y. (1992). Internal deformation due to shear and tensile faults in a half-space. Bulletin of the Seismological Society of America, 82(2), 1018–1040. https://pubs.geoscienceworld.org/ssa/bssa/article/82/2/1018/119251

Opheim, J. A., & Gudmundsson, A. (1989). Formation and geometry of fractures, and related volcanism, of the Krafla fissure swarm, northeast Iceland. Geological Society of America Bulletin, 101(12), 1608–1622. https://doi.org/10.1130/0016-7606(1989)101<1608:FAGOFA>2.3.CO;2

Pagli, C., Wang, H., Wright, T.J., Calais, E., & Lewi, E. (2014). Current plate boundary deformation of the Afar rift from a 3-D velocity field inversion of InSAR and GPS. Journal of Geophysical Research: Solid Earth, 119(11), 8562–8575. https://doi.org/10.1002/2014JB011391

Rooyakkers, S. M., Carroll, K. J., Gutai, A. F., Winpenny, B., Bali, E., Guðfinnsson, G. H., et al. (2024). Hydraulically linked reservoirs simultaneously fed the 1975–1984 Krafla Fires eruptions: Insights from petrochemistry. Earth and Planetary Science Letters, 646, 118960. https://doi.org/10.1016/j.epsl.2024.118960

Sæmundsson, K. (1991). Jarðfræði Kröflukerfisins (in Icelandic). In A. Garðarsson & A. Einarsson (Eds.), Náttúra Mývatns (pp. 24–95). Icelandic Nature Science Society, Reykjavík.

Savage, J. C., & Prescott, W. H. (1978). Asthenosphere readjustment and the earthquake cycle. Journal of Geophysical Research: Solid Earth, 83(B7), 3369–3376. https://doi.org/10.1029/JB083iB07p03369

Schuler, J., Greenfield, T., White, R. S., Roecker, S. W., Brandsdóttir, B., Stock, J. M., et al. (2015). Seismic imaging of the shallow crust beneath the Krafla central volcano, NE Iceland. Journal of Geophysical Research: Solid Earth, 120(10), 7156–7173. https://doi.org/10.1002/2015JB012350

Scott, S., Driesner, T., & Weis, P. (2015). Geologic controls on supercritical geothermal resources above magmatic intrusions. Nature Communications, 6, 7837. https://doi.org/10.1038/ncomms8837

Sella, G. F., Dixon, T. H., & Mao, A. (2002). REVEL: A model for recent plate velocities from space geodesy. Journal of Geophysical Research: Solid Earth, 107(B4), 2081. https://doi.org/10.1029/2000JB000033

Sigmundsson, F., Einarsson, P., Hjartardóttir, Á. R., Drouin, V., Jónsdóttir, K., Árnadóttir, Þ., et al. (2020). Geodynamics of Iceland and the signatures of plate spreading. Journal of Volcanology and Geothermal Research, 391, 106436. https://doi.org/10.1016/j.jvolgeores.2018.08.014

Sigmundsson, F., Parks, M., Geirsson, H., Hooper, A., Drouin, V., Vogfjörd, K. S., et al. (2024). Fracturing and tectonic stress drive ultrarapid magma flow into dikes. Science, 383(6688), 1228–1235. https://doi.org/10.1126/science.adn2838

Sigmundsson, F., Vadon, H., & Massonnet, D. (1997). Readjustment of the Krafla spreading segment to crustal rifting measured by satellite radar interferometry. Geophysical Research Letters, 24(15), 1843–1846. https://doi.org/10.1029/97GL01934

Smith, D., & Cann, J. (1993). Building the crust at the Mid-Atlantic Ridge. Nature, 365, 707–715. https://doi.org/10.1038/365707a0

Sturkell, E., Sigmundsson, F., Geirsson, H., Ólafsson, H., & Theodórsson, T. (2008). Multiple volcano deformation sources in a post-rifting period: 1989–2005 behaviour of Krafla, Iceland constrained by levelling, tilt and GPS observations. Journal of Volcanology and Geothermal Research, 177(2), 405–417. https://doi.org/10.1016/j.jvolgeores.2008.06.013

The GlaMBIE Team. (2025). Community estimate of global glacier mass changes from 2000 to 2023. Nature, 639(3982), 382–388. https://doi.org/10.1038/s41586-024-08545-z

Toomey, D., Jousselin, D., Dunn, R., Williams, S.D.W., & Detrick, R.S. (2007). Skew of mantle upwelling beneath the East Pacific Rise governs segmentation. Nature, 446, 409–414. https://doi.org/10.1038/nature05679

Tryggvason, E. (1980). Subsidence events in the Krafla area, North Iceland, 1975–1979. Journal of Geophysics, 41(1), 141–153. Retrieved from https://journal.geophysicsjournal.com/JofG/article/view/76

Tryggvason, E. (1984). Widening of the Krafla fissure swarm during the 1975–1981 volcano-tectonic episode. Bulletin of Volcanology, 47, 47–69. https://doi.org/10.1007/BF01960540

Ulrych, T. J., Sacchi, M. D., & Woodbury, A. (2001). A Bayes tour of inversion: A tutorial. Geophysics, 66(1), 55–69. https://doi.org/10.1190/1.1444923

Wessel, P., Luis, J. F., Uieda, L., Scharroo, R., Wobbe, F., Smith, W. H. F., & Tian, D. (2019). The Generic Mapping Tools version 6. Geochemistry, Geophysics, Geosystems, 20, 5556–5564. https://doi.org/10.1029/2019GC008515

Wilcox, R. R. (2005). Introduction to robust estimation and hypothesis testing (2nd ed.). Elsevier Academic Press.

Wright, T. J., Parsons, B. E., & Lu, Z. (2004). Toward mapping surface deformation in three dimensions using InSAR. Geophysical Research Letters, 31, L01607. https://doi.org/10.1029/2003GL018827

Wright, T.J., Sigmundsson, F., Pagli, C., Belachew, M., Hamling, I.J., Brandsdóttir, B., et al. (2012). Geophysical constraints on the dynamics of spreading centres from rifting episodes on land. Nature Geoscience, 5, 242–250. https://doi.org/10.1038/ngeo1428

Yang, Y., Sigmundsson, F., & Geirsson, H. (2023). Joint Bayesian modeling of velocity break points, noise characteristics, and their uncertainties in GNSS time series: Far-field velocity anomalies concurrent with magmatic activity in Iceland. Geophysical Research Letters, 50, e2023GL103432. https://doi.org/10.1029/2023GL103432

Yang, Y., Sigmundsson, F., Geirsson, H., Gottsmann, J. (2025). Role of tectonic stress and topography on repeated lateral dikes: application to the 1975–1984 Krafla and 2023–2025 Svartsengi rifting episodes in Iceland. In review, Bulletin of Volcanology.

Yu, C., Li, Z., Penna, N. T., & Crippa, P. (2018). Generic atmospheric correction model for interferometric synthetic aperture radar observations. Journal of Geophysical Research: Solid Earth, 123, 9202–9222. https://doi.org/10.1029/2017JB015305

Yuan, T., & Zhong, S. (2025). Effects of glacial forcing on lithospheric motion and ridge spreading. Nature, 641(122), 122–128. https://doi.org/10.1038/s41586-025-08846-x

Journal of Geophysical Research: Solid Earth

Supporting Information for

Plate divergence at the Krafla volcanic system, Iceland: Insight from GNSS geodesy and Sentinel-1 Satellite Radar Interferometry in 2002–2024

Yilin Yang[1], Freysteinn Sigmundsson[1], Halldór Geirsson[1], Juliet Biggs[2], Vincent Drouin[3], Josefa Sepúlveda Araya[4], Sigrún Hreinsdóttir[5], Chiara Lanzi[3], Joachim Gottsmann[6], Taco Broerse[7], Sandra Verhagen[7]

[1]. Nordic Volcanological Center, Institute of Earth Sciences, University of Iceland, Reykjavík, Iceland

[2]. COMET, School of Earth Sciences, University of Bristol, Bristol, UK.

[3]. Icelandic Meteorological Office, Reykjavík, Iceland.

[4]. COMET, School of Earth and Environment, University of Leeds, Leeds, UK.

[5]. GNS science, Lower Hutt, New Zealand.

[6]. Department of Earth and Environmental Sciences, Ludwig-Maximilians-Universität München, Munich, Germany.

[7]. Faculty of Civil Engineering and Geosciences, Delft University of Technology, Delft, The Netherlands.

Contents of this file

Text S1
Figures S1 to S18
Table S1 to S3

Introduction

This supporting information includes supplementary text, figures and tables of data processing and inversions. Text S1 justifies the spatially uniform uncertainty assigned for InSAR velocity field and Text S2 describe the alternative approach to evaluate the uncertainty of the plate boundary model. Figure S1 shows all available campaign GNSS data for the study area. Figure S2 and S3 show the derived GNSS coordinate time series in north, east and up components at four

continuous GNSS stations and four campaign GNSS sites, respectively. Figure S4 illustrates the influence of transient deformation on velocity estimation with synthetic data experiments. Figure S5 and S6 shows the spatiotemporal baseline networks of InSAR processing and the average InSAR line-of-sight displacement velocity fields, respectively. Figure S7 demonstrates, through synthetic data experiments, that the influence of local deformation on the plate boundary model is minor, thereby justifying our approach not applying explicit corrections in this study. Figure S8 illustrates the three-dimensional set-ups of the regional subsidence model. Figure S9 compares the GNSS velocities with InSAR velocities at grid points nearest to the GNSS sites to further illustrate their consistency. Figure S10 and S11 present the inversion results from the two-step inversion. Figure S12 shows the scaled horizontal GIA deformation from the Auriac (2014) model. Figure S13 show the vertical deformation velocity fields predicted from the scaled Auriac (2014) model and the regional subsidence model of Lanzi et al. (2024). Figure S14 to S15 gives additional comparisons among the observed, modeled and residual velocity fields. Figure S16 shows the velocity fields in different periods to investigate the temporal evolution of the localized deformation patterns. Figure S17 illustrates the possible transverse structure within the Krafla caldera and the adjusted plate boundary axis to test. Figure S18 compares the inferred plate spreading parameters with those from global plate motion models and previous regional plate boundary models. Table S1 and S2 show the search bounds and initial values of model parameters in the two-step inversion scheme. Table S3 shows the coordinates of the inferred plate boundary axis in this study.

Text S1: InSAR velocity uncertainty

InSAR velocities are known to be affected by spatially correlated errors, and their uncertainties are often estimated empirically based on spatial variability in areas that are not expected to deform (e.g., Sudhaus & Jónsson, 2009; Bagnardi & Hooper, 2018; Wang et al., 2024). In the main text, we apply a spatially uniform uncertainty to the InSAR velocity field when weighting data within the Bayesian inversion. This simplification is justified for several reasons:

(i) Downsampling effect: The InSAR velocity field is downsampled from a pixel size of ~100×100 m to ~600×1000 m prior to inversion. This may obscure small-scale spatial noise features, reducing the influence of spatial variability.

(ii) Correlation length scale vs deformation scale: The fitted exponential semi-variogram of the InSAR near-east velocity field suggests a spatial correlation length of ~9 km, which is comparable to the ~20 km zone of concentrated plate boundary deformation. This complicates separating real deformation from spatial variability. Moreover, the full plate boundary signal spans ~40 km and is also constrained by GNSS data, so the inferred regional deformation pattern should be robust, while local features should be interpreted with caution.

(iii) Relative weight variation: Inverse squared uncertainties are used as initial weights. The estimated uncertainty range for InSAR grid points is 0.5–1.4 mm/yr, while GNSS east-component velocities have uncertainties ranging from 0.1–1.0 mm/yr. Consequently,

weights within the InSAR dataset vary less (within a factor of ~8) than those of GNSS data (up to a factor of ~100). Thus, the spatial correlated error in InSAR uncertainty is not the dominant factor influencing the weighting scheme.

(iv) Computational efficiency: Using a diagonal covariance matrix improves computational efficiency in the Bayesian inversion, especially for large datasets.

Text S2: An alternative approach to estimate uncertainty of the plate boundary model

Since the formal uncertainties from the second-step Bayesian inversion are obtained under the assumption that the plate boundary geometry derived from the first step is known without uncertainty, we implement an alternative approach to propagate the uncertainty from the first-step inversion into the second step and approximate a more realistic total model uncertainty. This approach samples 100 realizations of plate boundary geometries from the first-step PDFs and performs a maximum likelihood estimation (MLE) for each to derive the locking depths, spreading rate and spreading direction. Because Figure S11 shows correlation between GIA scaling factor and the spreading direction, we randomly sample from the 95% confidence interval of the GIA scaling factor instead of inverting for it here.

(i) Sampling: A Monte Carlo sampling of the plate boundary segment strikes and the X-coordinate of the southern endpoint of segment S3 is conducted using a Latin Hypercube Sampling method, which efficiently explore the multidimensional parameter space with a limited number of samples (McKay et al., 1979). Each parameter is assumed to follow a normal distribution defined by its median and 95% confidence interval from the first-step inversion.

(ii) MLE: For each sampled geometry, we implement MLE using the Nelder-Mead simplex algorithm (Nelder & Mead, 1985) with up to 1000 iterations. The input data for the MLE is the down-sampled InSAR near-east velocity field and the GNSS velocities sampled using a Bootstrap method. The objective function minimizes the weighted least-square misfit between the model and the observed velocity fields, with additional exponential penalty terms enforcing smooth boundary constraints. The weighted least-square misfit is consistent with the likelihood function of the Bayesian inversion. We adopt the boundary constraints to stabilize convergence and prevent unrealistic estimates, with the boundaries being the upper and lower limit of the 95% confidence interval from the second-step Bayesian inversion and the constraint intensity adjusted to allow parameters to explore a certain extent beyond the limits.

(iii) Combination: Because the formal uncertainties of the second-step inversion are smaller than the variability of the MLE results, we combined the two to form an approximate total uncertainty range.

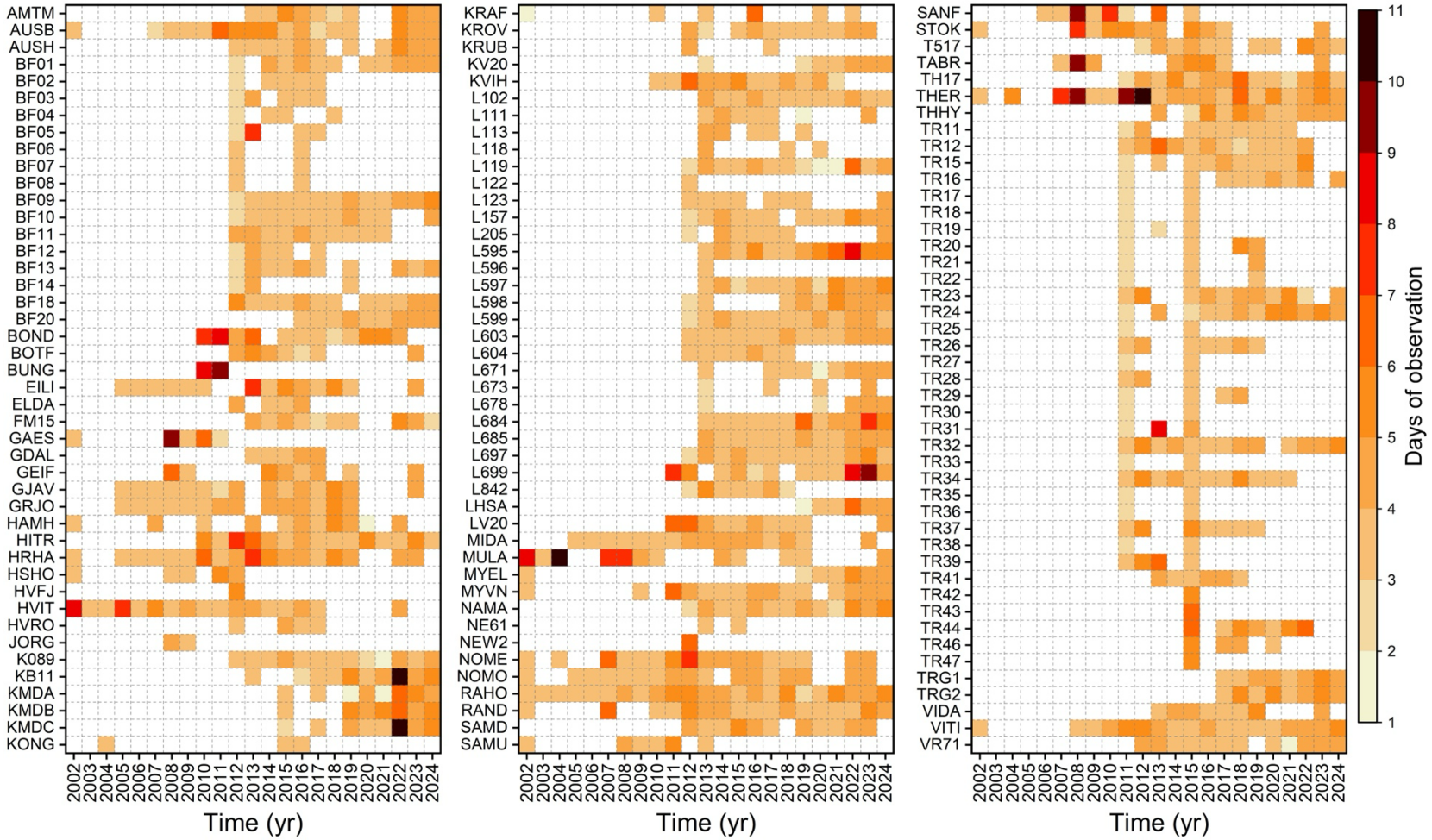


Figure S1. Summary of campaign GNSS data available in the central part of the Krafla volcanic system. All the sites are within the range of Figure 1b in the main text. The color codes indicate how many days of observation each campaign site has in different years.

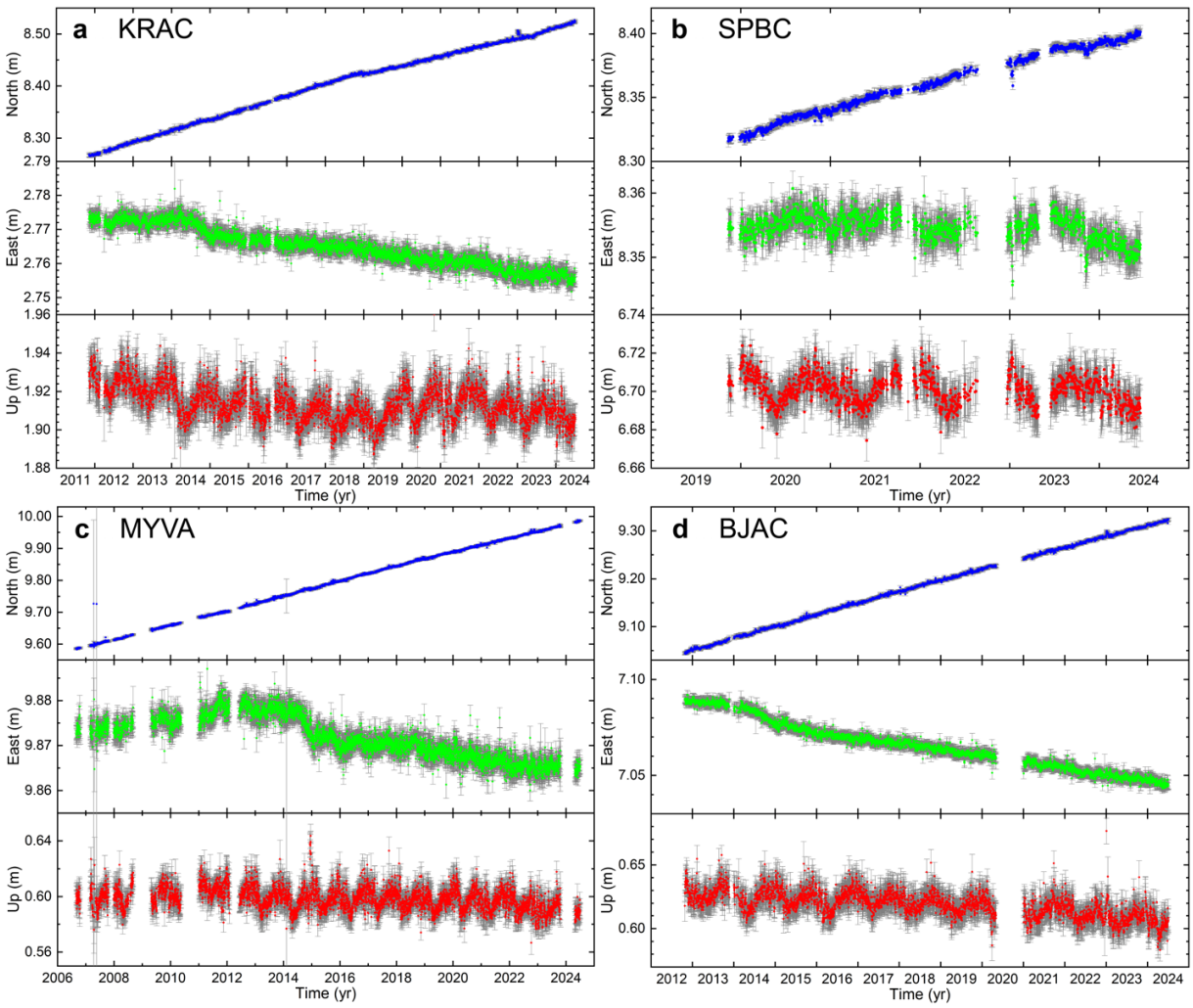


Figure S2. GNSS coordinate time series at four cGNSS stations, referenced to ITRF2014. The dots indicate the coordinates and the gray error bars indicate the corresponding formal errors from GNSS data processing.

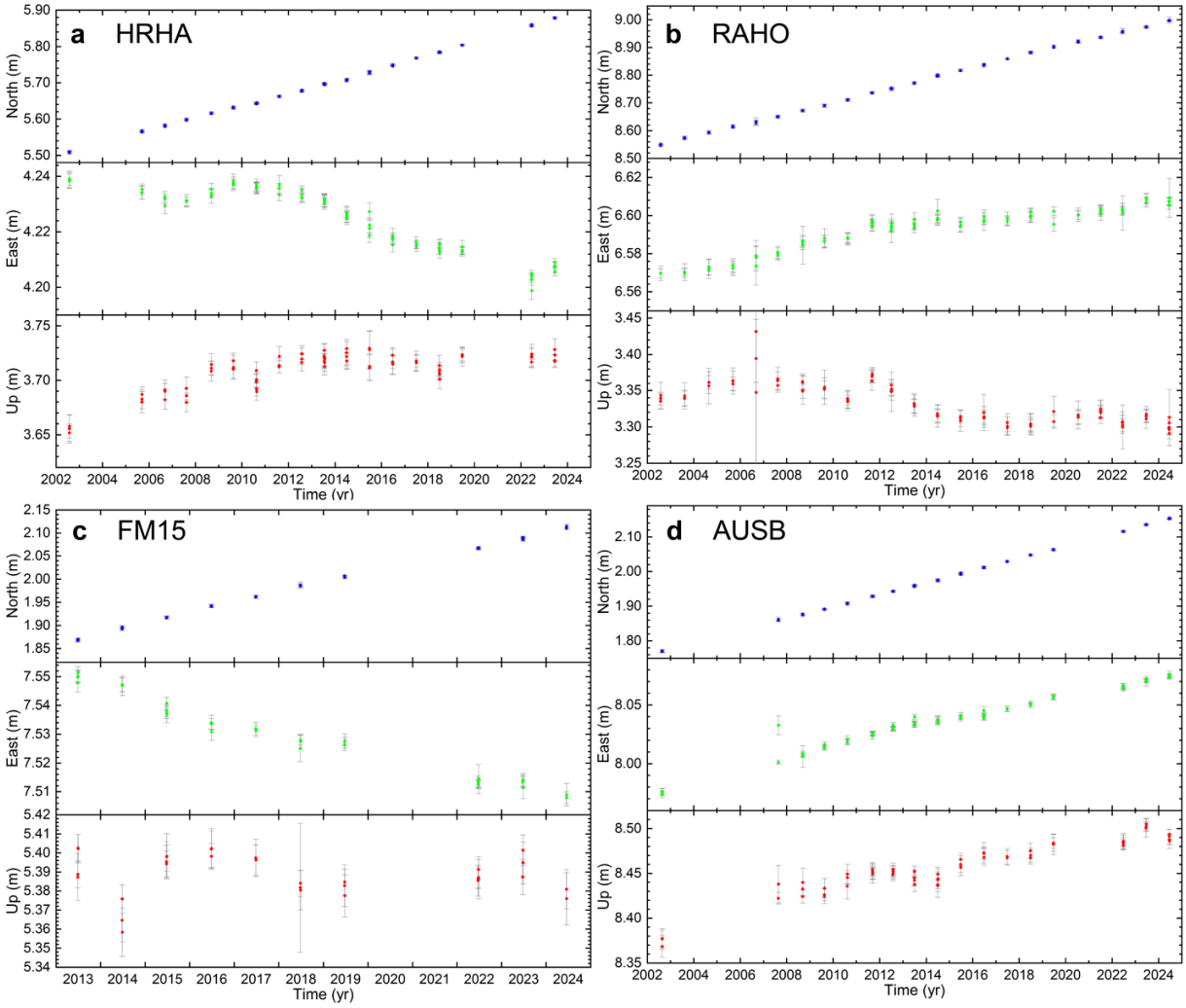


Figure S3. GNSS coordinate time series at four campaign GNSS stations, referenced to ITRF2014. The dots indicate the coordinates and the gray error bars indicate the corresponding formal errors from GNSS data processing. Site FM15 is the reference area of InSAR velocity fields (white diamond in Figure 1 in the main text). Site HRHA and AUSB, locate north and east of the Krafla central volcano, respectively. Site RAHO locates near the Krafla caldera center.

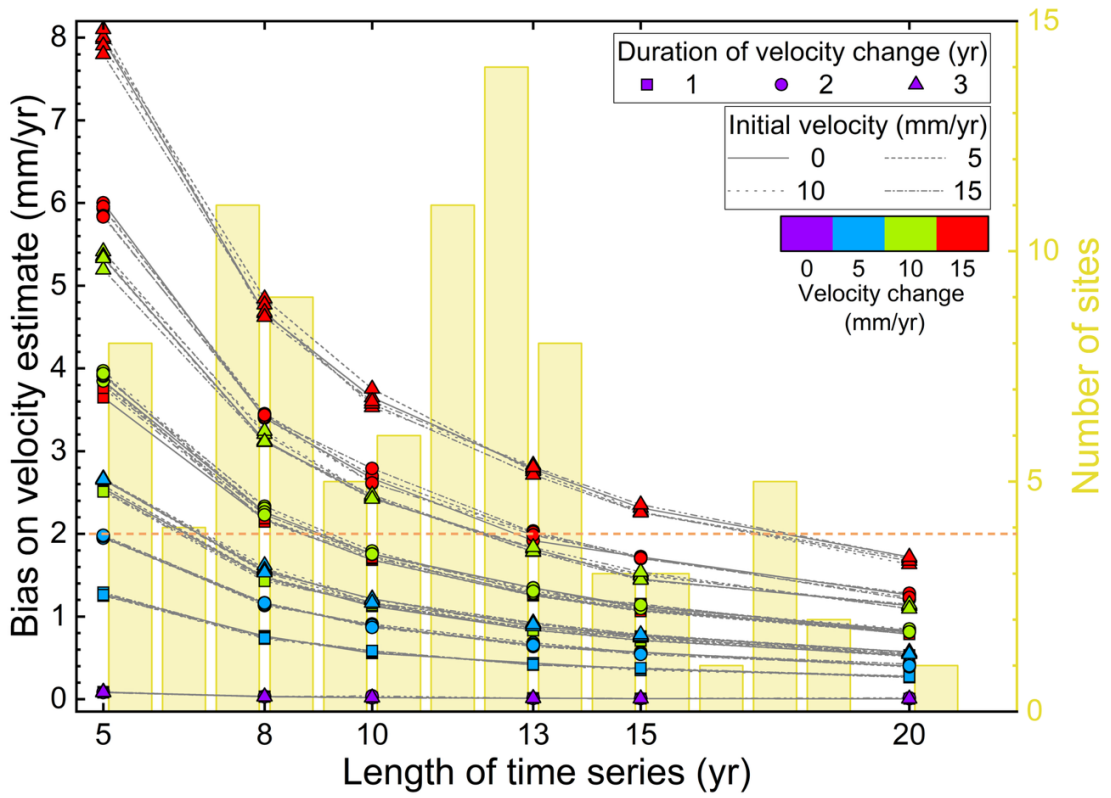


Figure S4. Bias in long-term velocity estimates caused by transient deformation, based on synthetic data experiments. The right vertical axis and the histogram show the distribution of time series lengths at campaign GNSS sites with observations longer than 5 years. Synthetic daily time series are generated using model parameters (legends in the figure), white noise of 1 mm, and flicker noise with an amplitude of 3.2 mm/yr0.25 (Yang et al., 2023). Three to five continuous data points are randomly sampled in June of each year, mimicking the annual campaign measurements. Lines representing results from different initial velocities but identical noise and transient deformation signals overlap, indicating that the bias is insensitive to the initial velocity. Given transient velocity changes of 6–10 mm/yr lasting 1–3 years (Yang et al., 2023; Lanzi et al., 2023), and considering the actual time series spans, we infer that velocity bias in our campaign GNSS velocity field is generally less than 2 mm/yr.

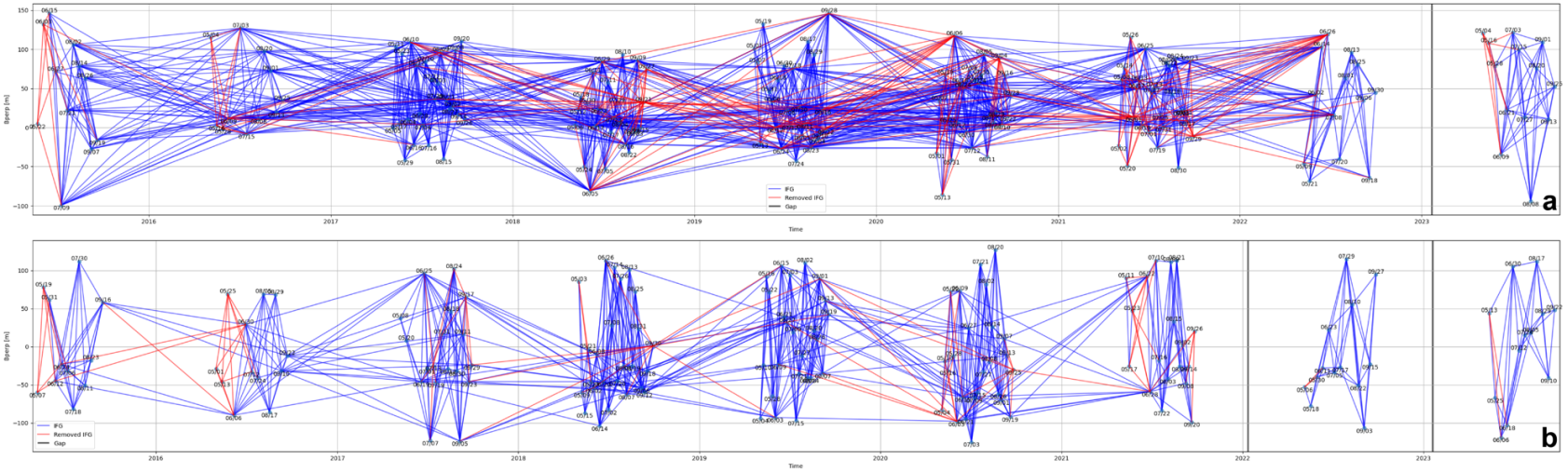


Figure S5. Spatio-temporal baseline networks of Sentinel-1 satellite from descending T9 (a) and ascending T147 (b) tracks. The vertical axis indicates the physical distance between two vantage points where SAR images are acquired, namely perpendicular baselines (Bperp). The horizontal axis indicates time in year. The dates of acquisitions are annotated by the data points. The blue lines represent interferograms used in the final InSAR time series, while the red ones are removed.

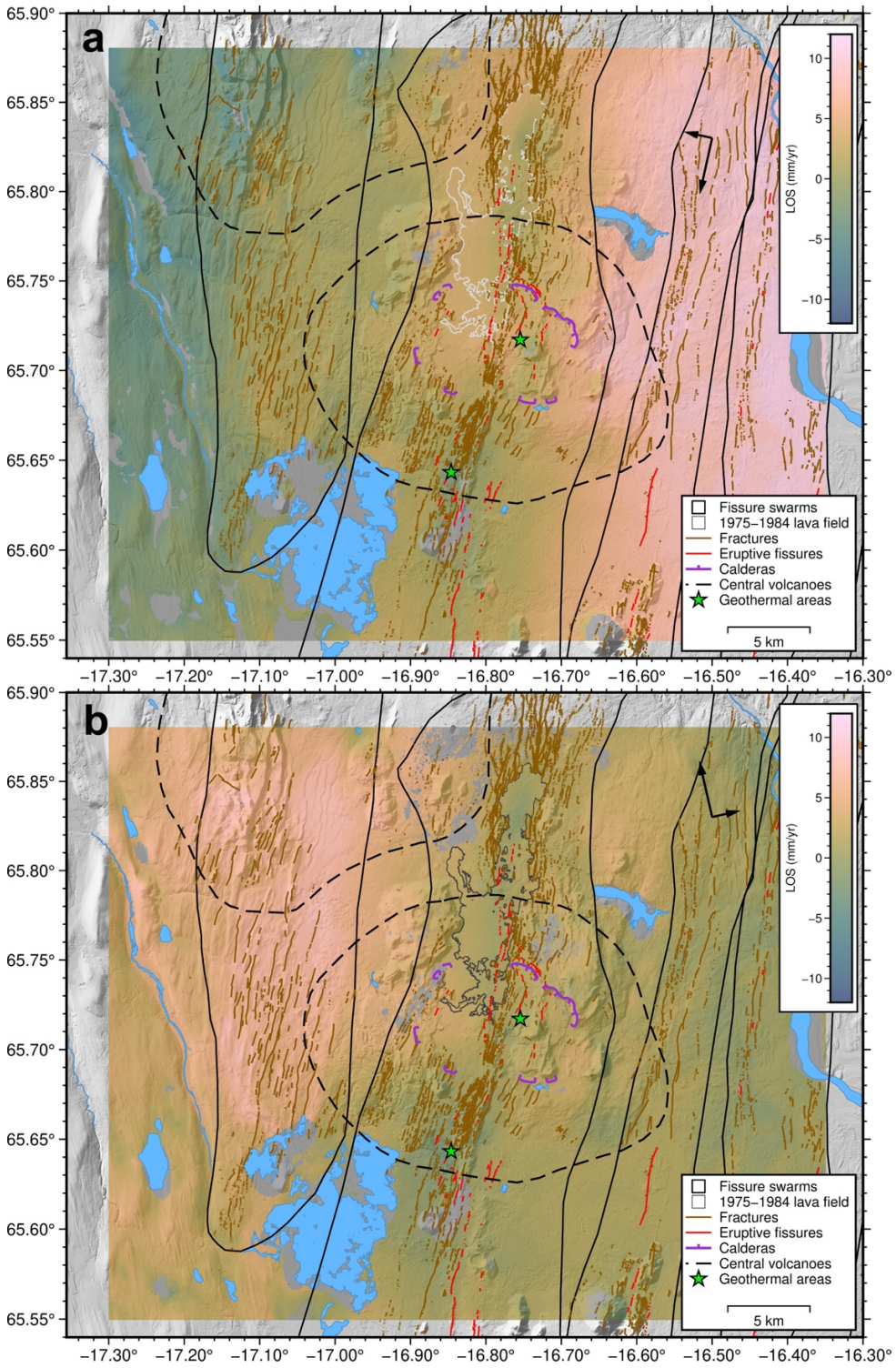


Figure S6. InSAR line-of-sight (LOS) displacement velocity fields from descending T9. (a) and ascending T147 (b) tracks. The arrows indicate the satellite heading (long arrows) and look (short arrows) directions.

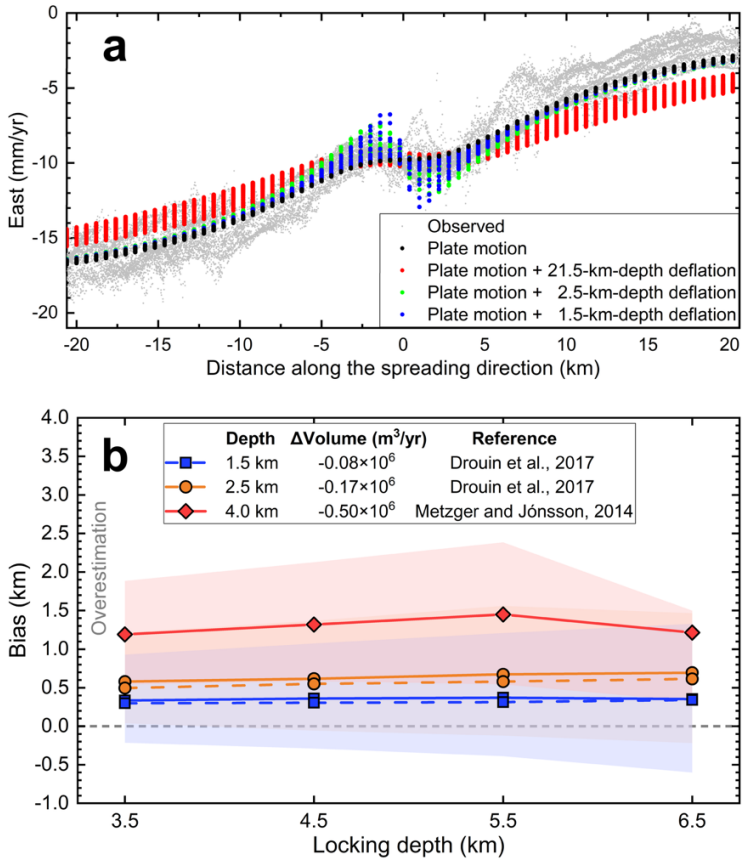


Figure S7. (a) Comparison between the profiles from InSAR near-east velocity (stacked from left panels of Figure 5 in the main text) and from synthetic deformation fields. The zero value on the horizontal axis indicates the location of the plate boundary axis. Volume changes of the deflation sources are -11.2 × 10^6 m3/yr for the 21.5-km-depth deflation, -0.17 × 10^6 m3/yr for the 2.5-km-depth deflation, and -0.08 × 10^6 m3/yr for the 1.5-km-depth deflation (Drouin et al., 2017). Plate motion is simulated using a back-slip model with a spreading rate of 20 mm/yr in a spreading direction of 292° azimuth (Barreto et al., 2025). The red dots indicate that a deflation source at 21.5 km can shift the observed east velocities by ~2 mm/yr at both the east and west ends of the study area while the plate motion with shallow deflation sources (2.5 and 1.5 km) better reproduced the observed east velocities. **(b)** Effect of local deformation signals on the estimation of plate boundary locking depth. Symbols with lines indicate the median estimates from Bayesian inversion. Solid lines correspond to cases where the local deformation source is located beneath the center of the plate boundary axis segment, and dashed lines correspond to sources beneath the segment endpoint. Shaded areas indicate 95% confidence intervals. The synthetic deformation field is generated using the back-slip model with a spreading rate of 20 mm/yr. We sample the synthetic deformation field within a 40 km × 6 km domain at a 600 m × 1000 m resolution, comparable to our down-sampled InSAR dataset. The plate boundary axis is fixed in the inversion, consistent with the second-step inversion in section 3.3 of the main text. We test only deflation sources, as inflation sources would have the opposite effect. The deformation from the 4-km-depth source has decayed and is not accounted for in recent studies (e.g., Drouin et al., 2017; Barreto et al., 2024).

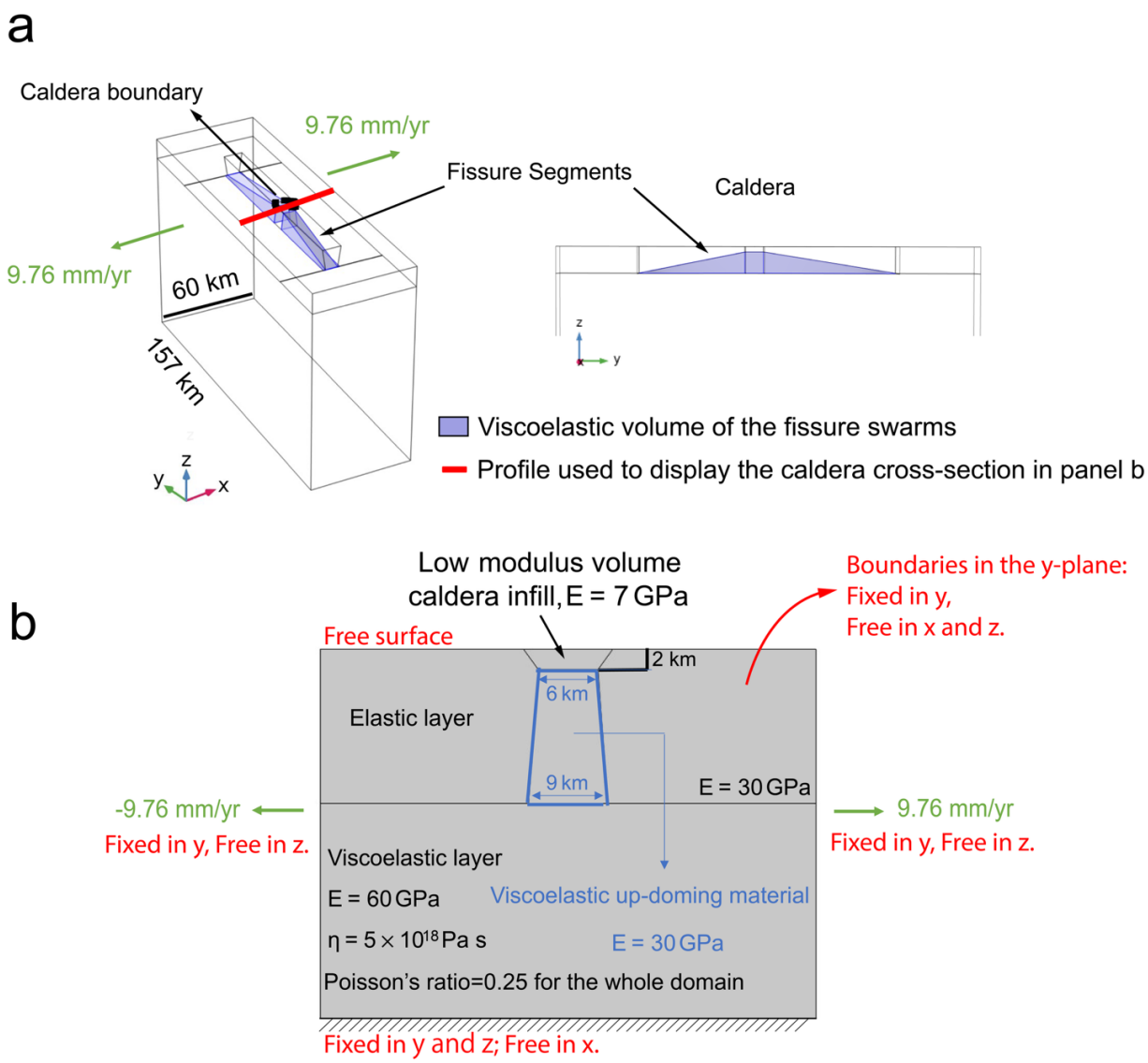


Figure S8. Illustration of the set-ups of the regional subsidence model. (a) Three-dimensional view of the model and its cross-section along the fissure swarm. **(b)** Model cross-section at the Krafla caldera showing material properties. Modified from Lanzi et al. (2024). The red text shows all the boundary conditions applied in the model.

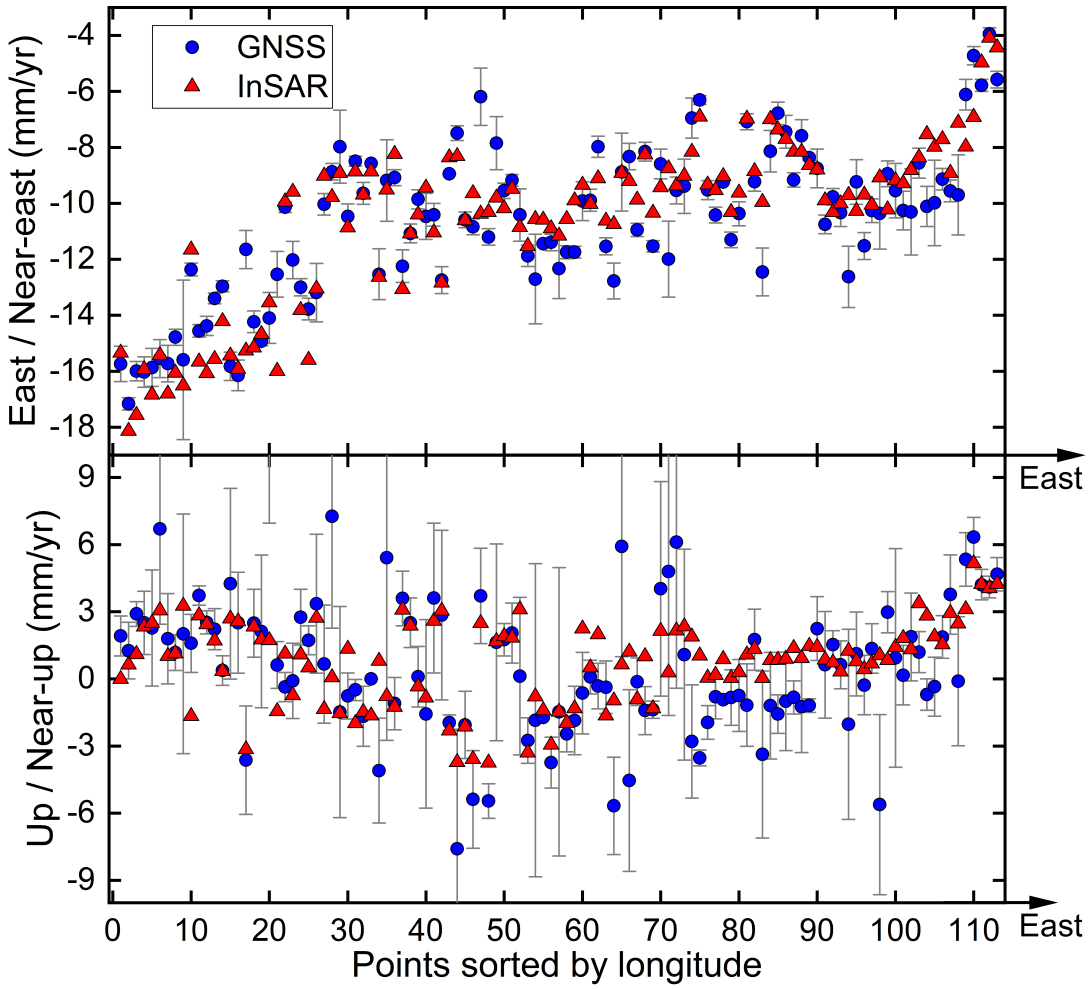
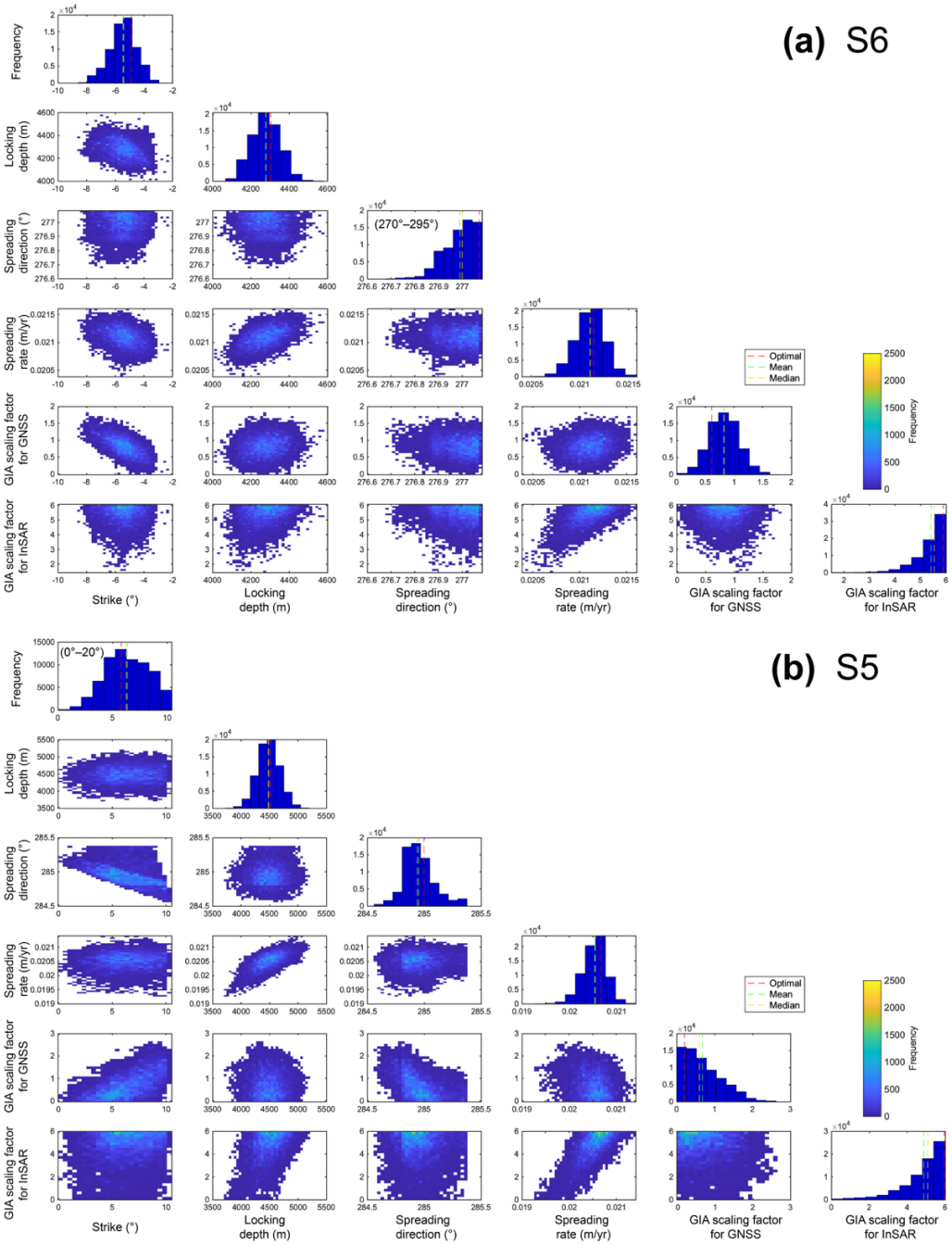
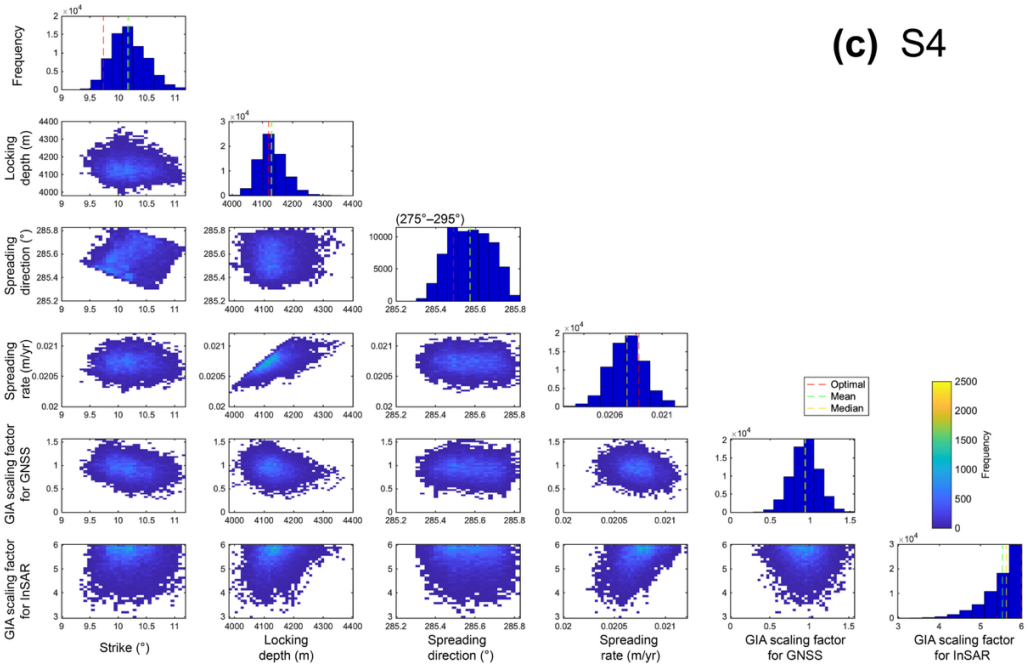
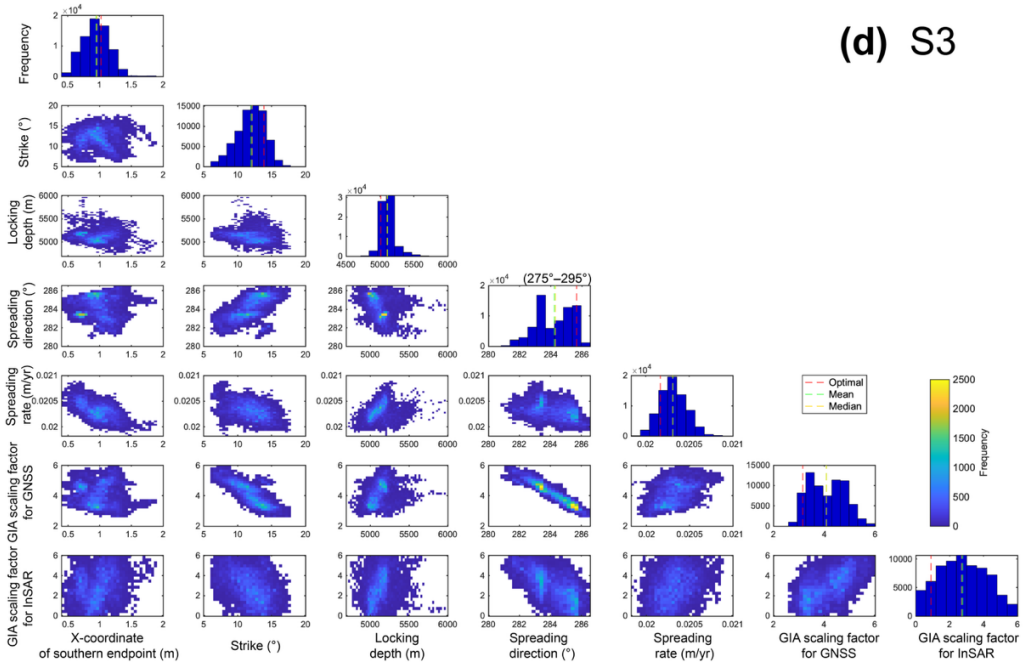


Figure S9. Comparison between GNSS velocities and InSAR velocities at nearest pixels to GNSS sites in east (near-east) component (a) and vertical (near-up) component (b). The GNSS velocity uncertainties are calculated with 3 times the standard deviation of corresponding velocity estimates from WLS (99.73% confidence interval). The root mean square for east (near-east) component is 1.28 mm/yr, consistent with the InSAR velocity uncertainty of ~1.36 mm/yr estimated from the semi-variogram function. The root mean square for vertical (near-up) component is 2.48 mm/yr, consistent with the average GNSS velocity uncertainty of 2.10 mm/yr.


(a) S6
Frequency
Locking depth (m)
Spreading direction (°)
(270°–295°)
Spreading rate (m/yr)
GIA scaling factor for GNSS
GIA scaling factor for InSAR
Optimal
Mean
Median
Frequency
Strike (°)
Locking depth (m)
Spreading direction (°)
Spreading rate (m/yr)
GIA scaling factor for GNSS
GIA scaling factor for InSAR
(b) S5
(0°–20°)
Frequency
Locking depth (m)
Spreading direction (°)
Spreading rate (m/yr)
GIA scaling factor for GNSS
GIA scaling factor for InSAR
Optimal
Mean
Median
Frequency
Strike (°)
Locking depth (m)
Spreading direction (°)
Spreading rate (m/yr)
GIA scaling factor for GNSS
GIA scaling factor for InSAR


(c) S4
Frequency
Locking depth (m)
Spreading direction (°)
(275°–295°)
Spreading rate (m/yr)
GIA scaling factor for GNSS
GIA scaling factor for InSAR
Optimal
Mean
Median
Frequency
Strike (°)
Locking depth (m)
Spreading direction (°)
Spreading rate (m/yr)
GIA scaling factor for GNSS
GIA scaling factor for InSAR


(d) S3
Frequency
Strike (°)
Locking depth (m)
Spreading direction (°)
(275°–295°)
Spreading rate (m/yr)
GIA scaling factor for GNSS
GIA scaling factor for InSAR
Optimal
Mean
Median
Frequency
X-coordinate of southern endpoint (m)
Strike (°)
Locking depth (m)
Spreading direction (°)
Spreading rate (m/yr)
GIA scaling factor for GNSS
GIA scaling factor for InSAR

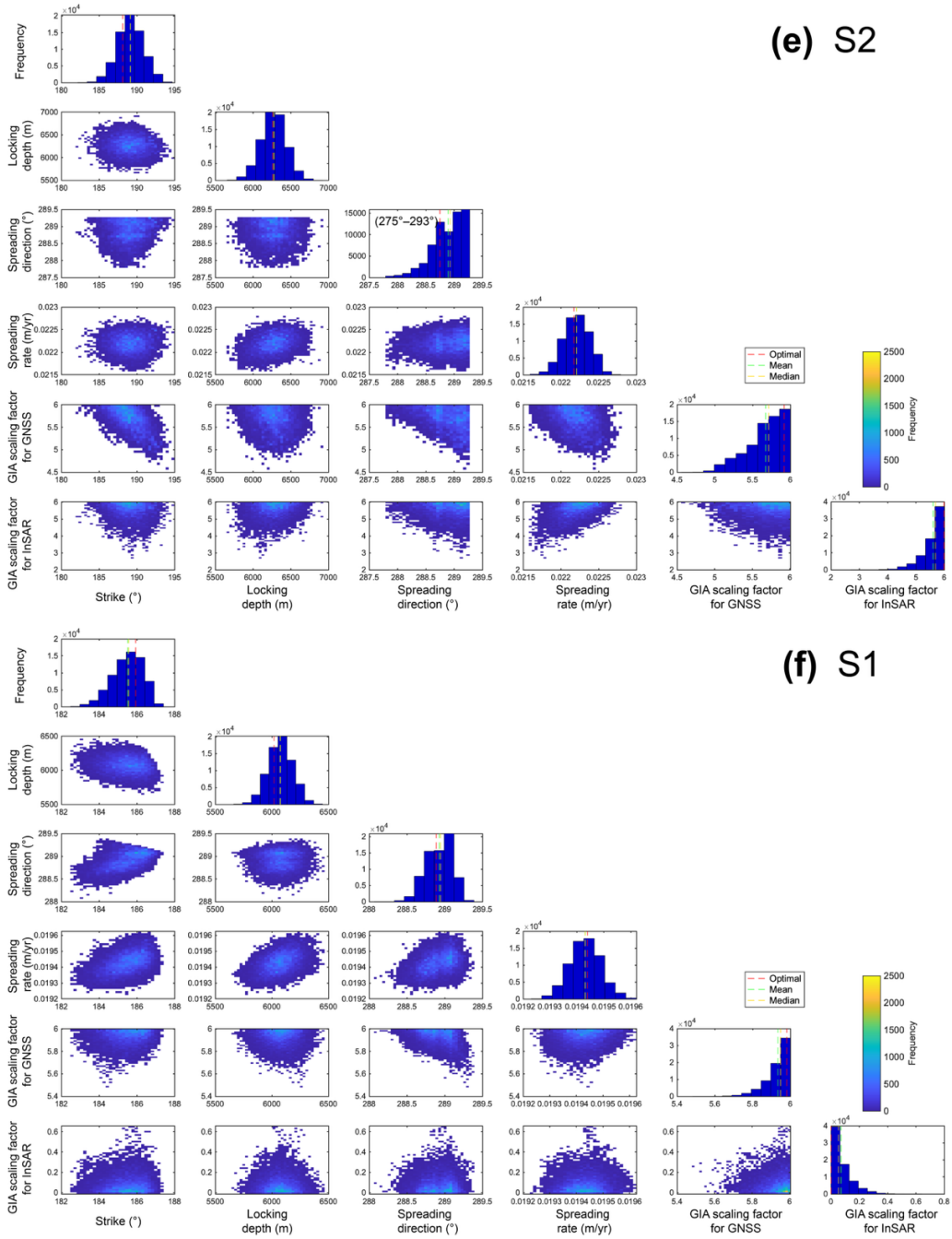


Figure S10. Histogram of posterior samples for model parameters (diagonal panels) and density maps of joint posterior samples (non-diagonal panels) with 95% confidence intervals in the second-step inversion. The color contours indicate the frequency. The GIA scaling factor is for the horizontal deformation predicted by the Auriac (2014) model, of which the scaling factor is limited between 0 and 6 for reasonable results. The parameter search range is annotated when the probability distribution reaches the bound of the horizontal axis.

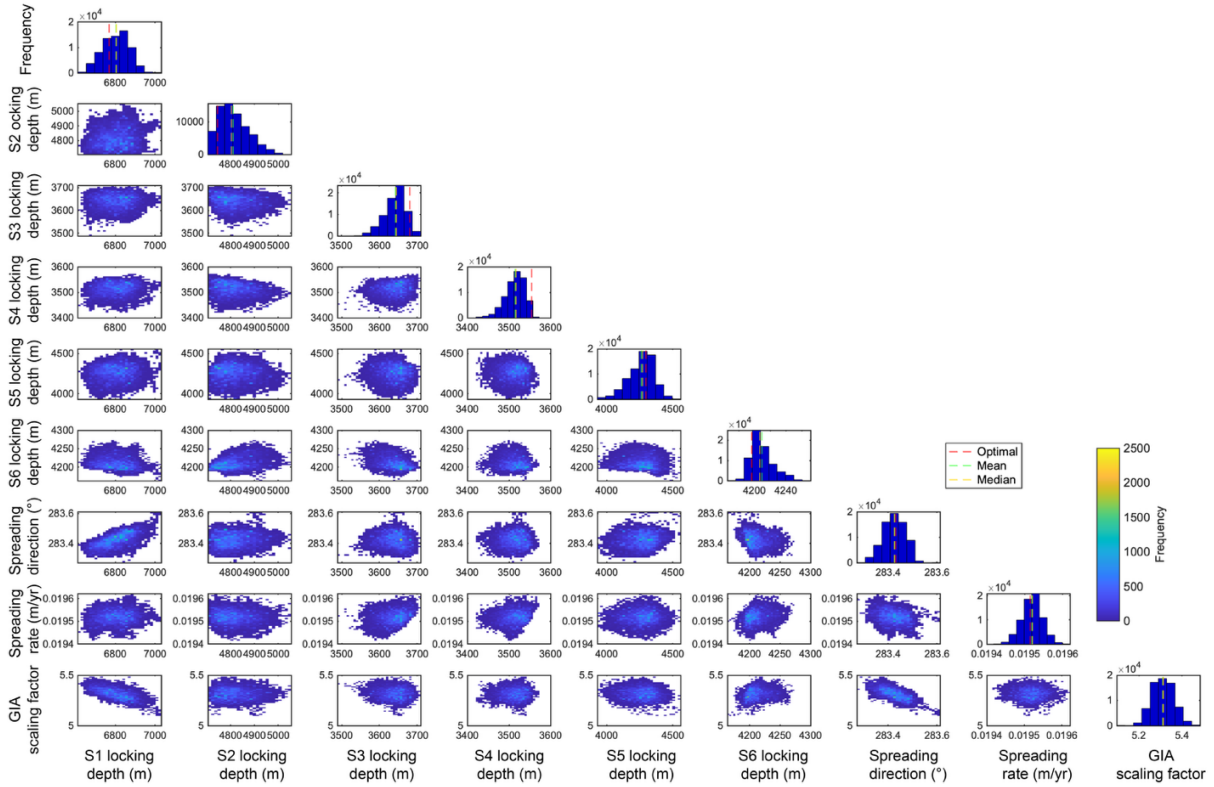


Figure S11. Histogram of posterior samples for model parameters (diagonal panels) and density maps of joint posterior samples (non-diagonal panels) with 95% confidence intervals in the second-step inversion. The color contours indicate the frequency. The GIA scaling factor is for the horizontal deformation predicted by the Auriac (2014) model. The search ranges of parameters are much wider than presented, where horizontal axes are zoomed in for better visualization.

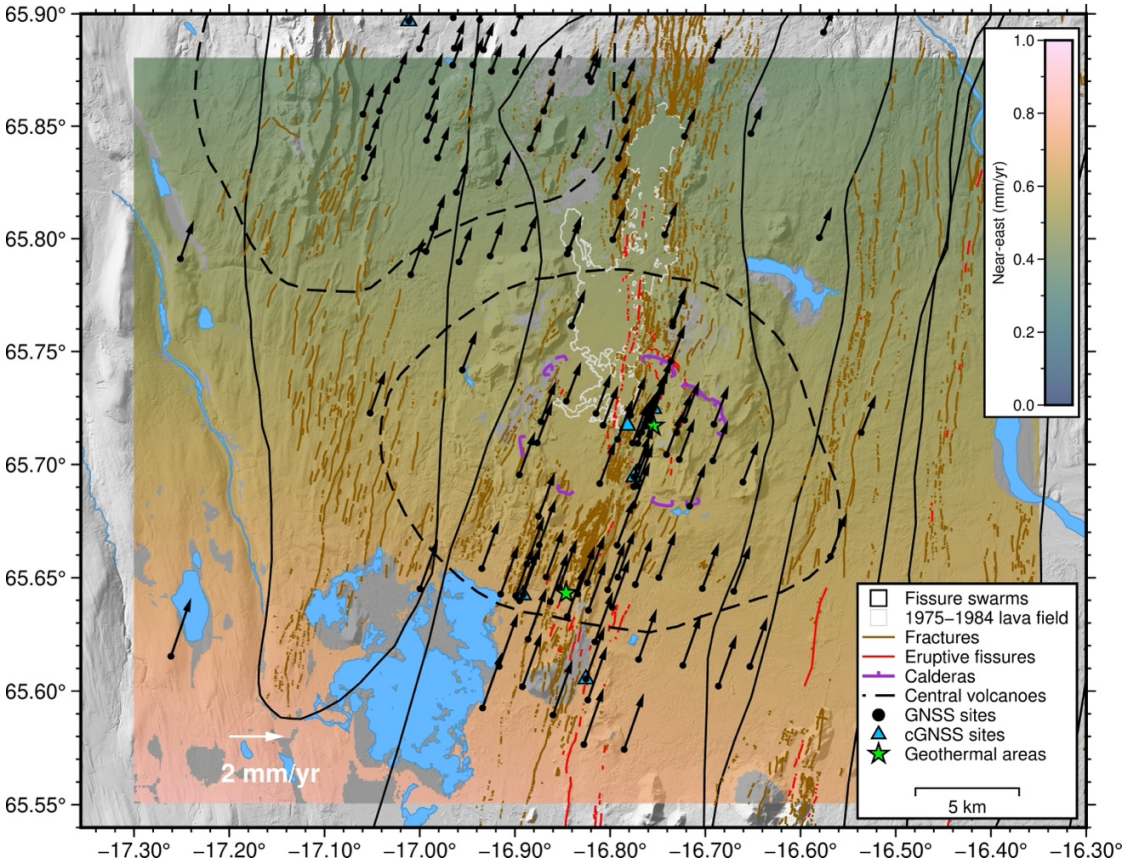


Figure S12. Horizontal GIA deformation velocity field. GIA deformation is derived from the Auriac (2014) model with a scaling factor of 5.31.

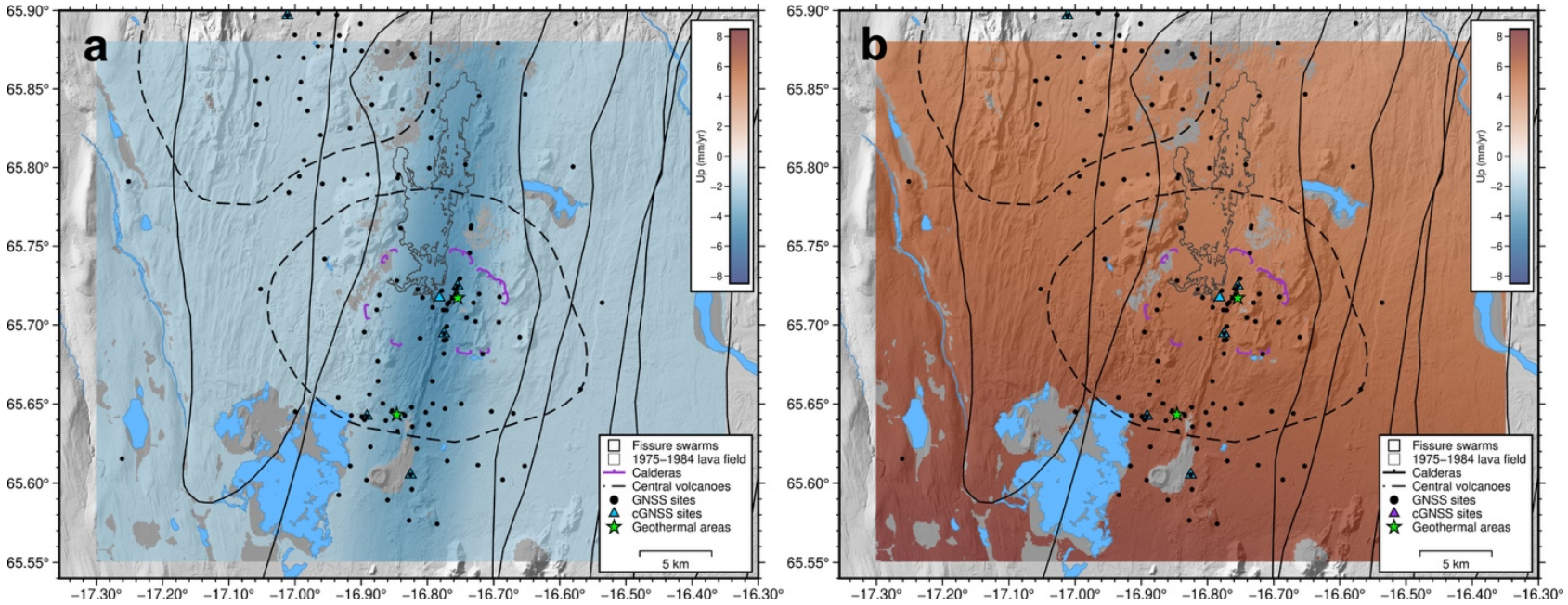


Figure S13. Vertical deformation velocity fields used for corrections. (a) Regional subsidence model incorporating rheological heterogeneities in the Krafla volcanic system (Lanzi et al., 2024), with constant offset of 27.2 mm/yr to align with the observations. The regional subsidence model predicts a background subsidence of ~2 mm/yr outside of the Krafla fissure swarm, while the Krafla fissure swarm and caldera exhibit stronger subsidence up to ~4 and ~5 mm/yr, respectively, due to a shallower brittle-ductile transition beneath the fissure swarm and mechanically weaker crust beneath the caldera. **(b)** Vertical GIA deformation model presented in Auriac (2014), scaled by a factor of 1.89. GIA model predicts overall uplift in the area, decreasing gradually from ~8 mm/yr in the southwest to ~4 mm/yr in the northeast.

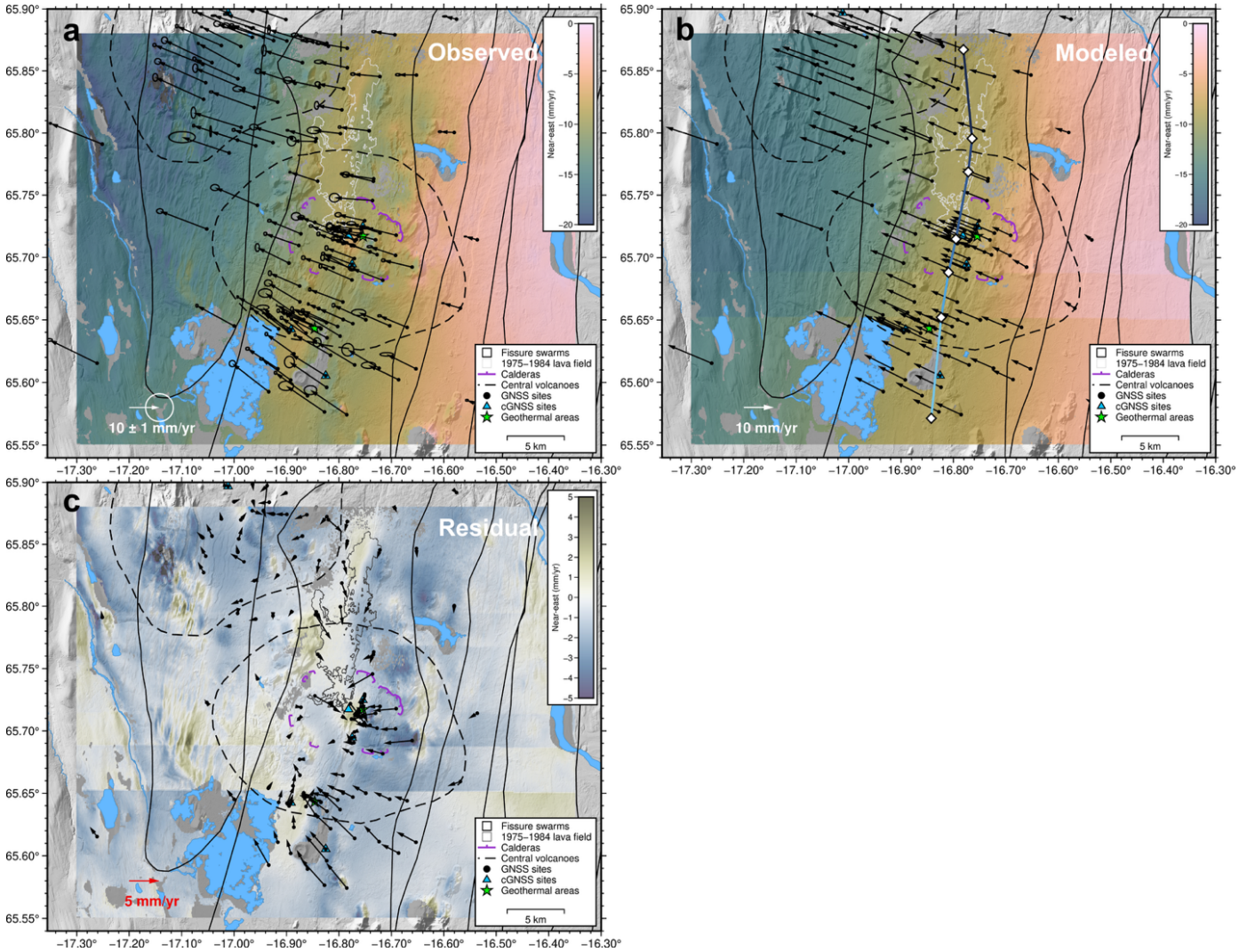


Figure S14. Comparison between the observed and modeled horizontal deformation velocity fields. (a) Horizontal velocity fields derived from GNSS (arrows) and InSAR (colormap) data. **(b)** Horizontal velocity fields predicted by the inverted plate boundary model (Figure 4a in the main text) and the GIA model (Figure S12). **(c)** Residuals. Same as Figure 6a in the main text.

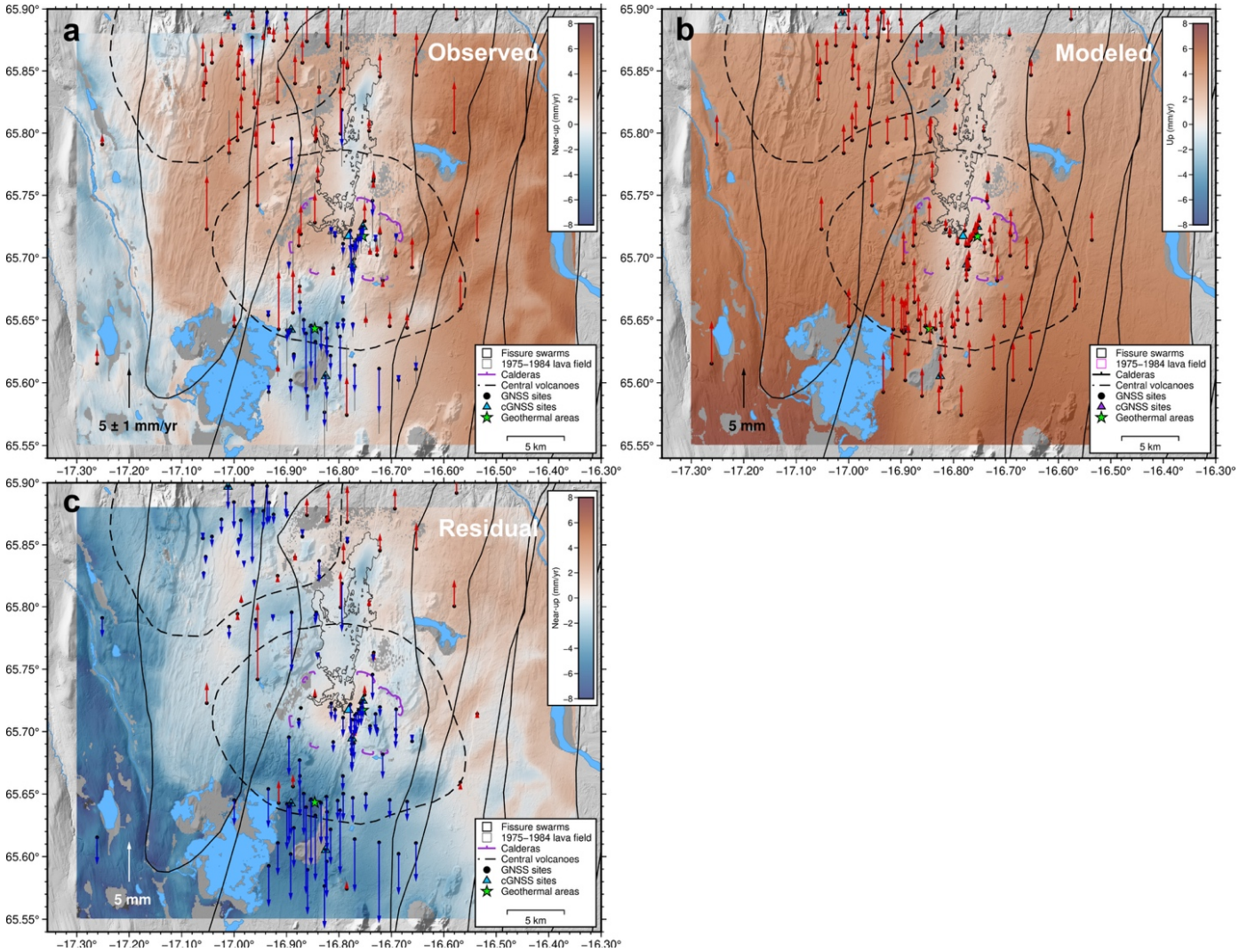


Figure S15. Comparison between the observed and modeled vertical deformation velocity fields. (a) Vertical velocity fields derived from GNSS (arrows) and InSAR (colormap) data. **(b)** Vertical velocity fields predicted by the GIA model and regional subsidence model (Figure S13). **(c)** Residuals. Same as Figure 6b in the main text.

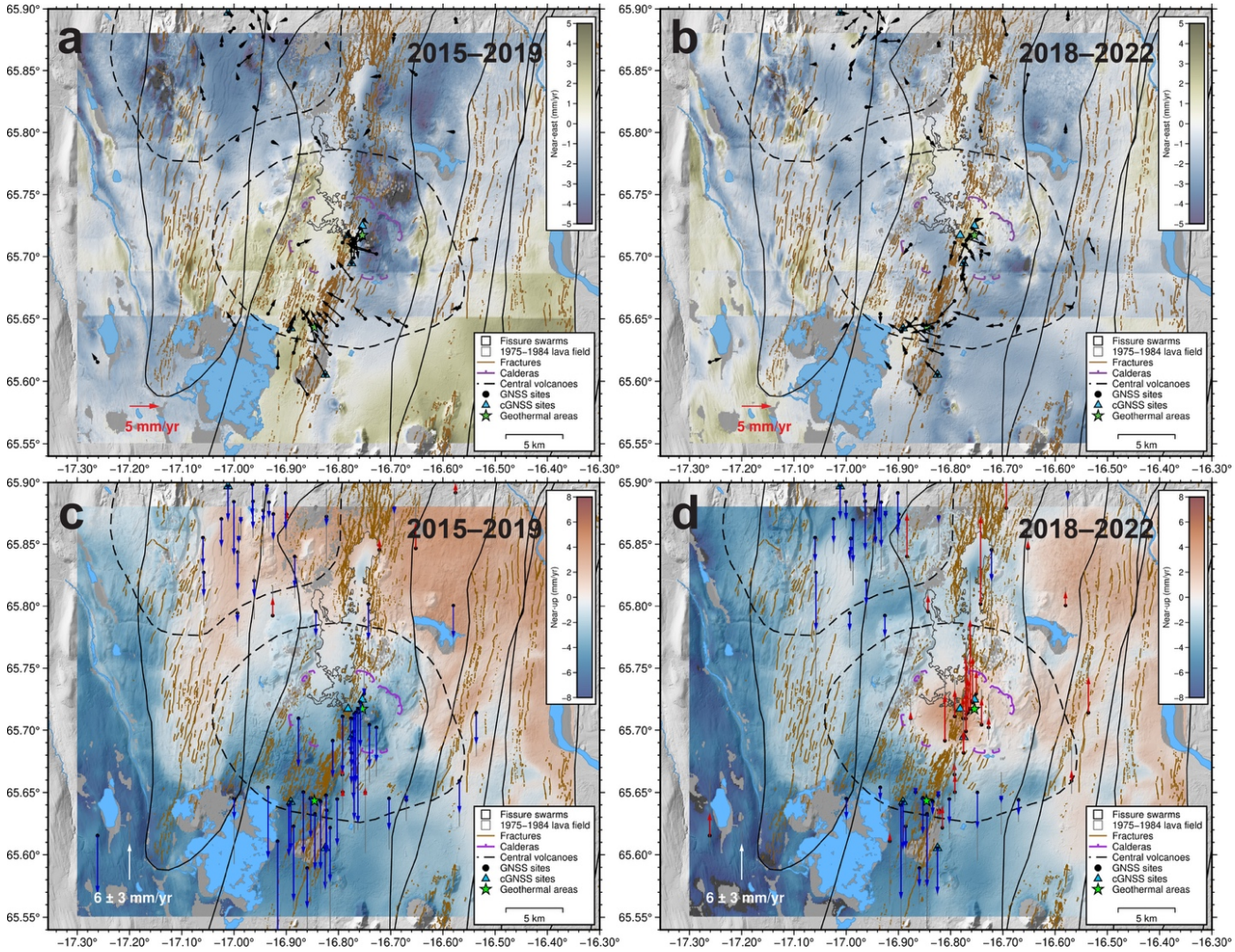


Figure S16. Horizontal (a–b) and vertical (c–d) residual velocity fields from GNSS and InSAR data for 2015–2019 and 2018–2022. Horizontal velocities are corrected for plate spreading and GIA deformation while vertical velocities are corrected for GIA deformation and regional subsidence model.

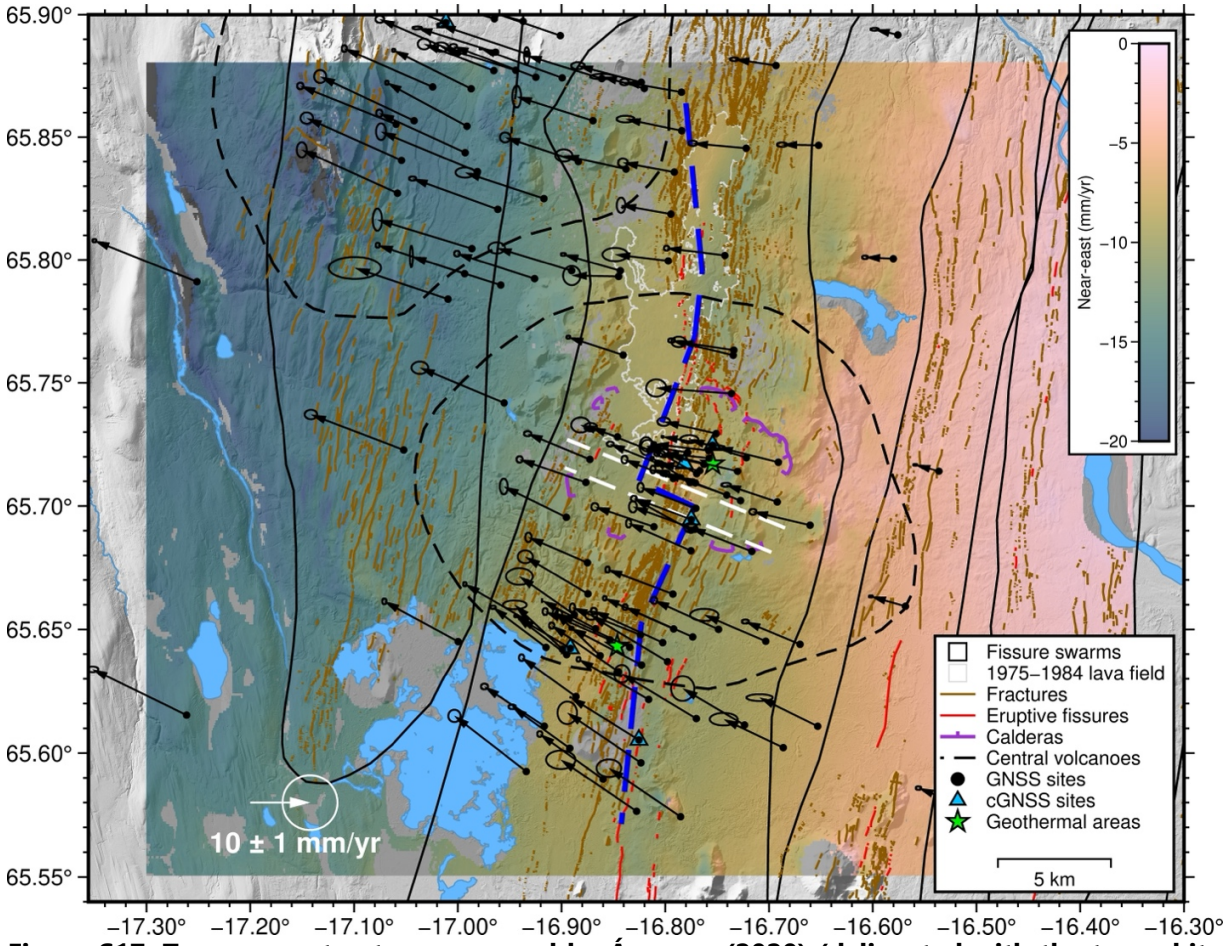


Figure S17. Transverse structure proposed by Árnason (2020) (delineated with the two white dashed lines) and adjusted plate boundary axis (blue dashed lines) in the central part of the Krafla volcanic system. The arrows and colormap are the long-term horizontal deformation velocity fields in the study area from GNSS (arrows) in 2002–2024 and InSAR (color maps) in 2015–2023, same as in Figure 3a in the main text. The transverse structure is extracted from Glück et al. (2025).

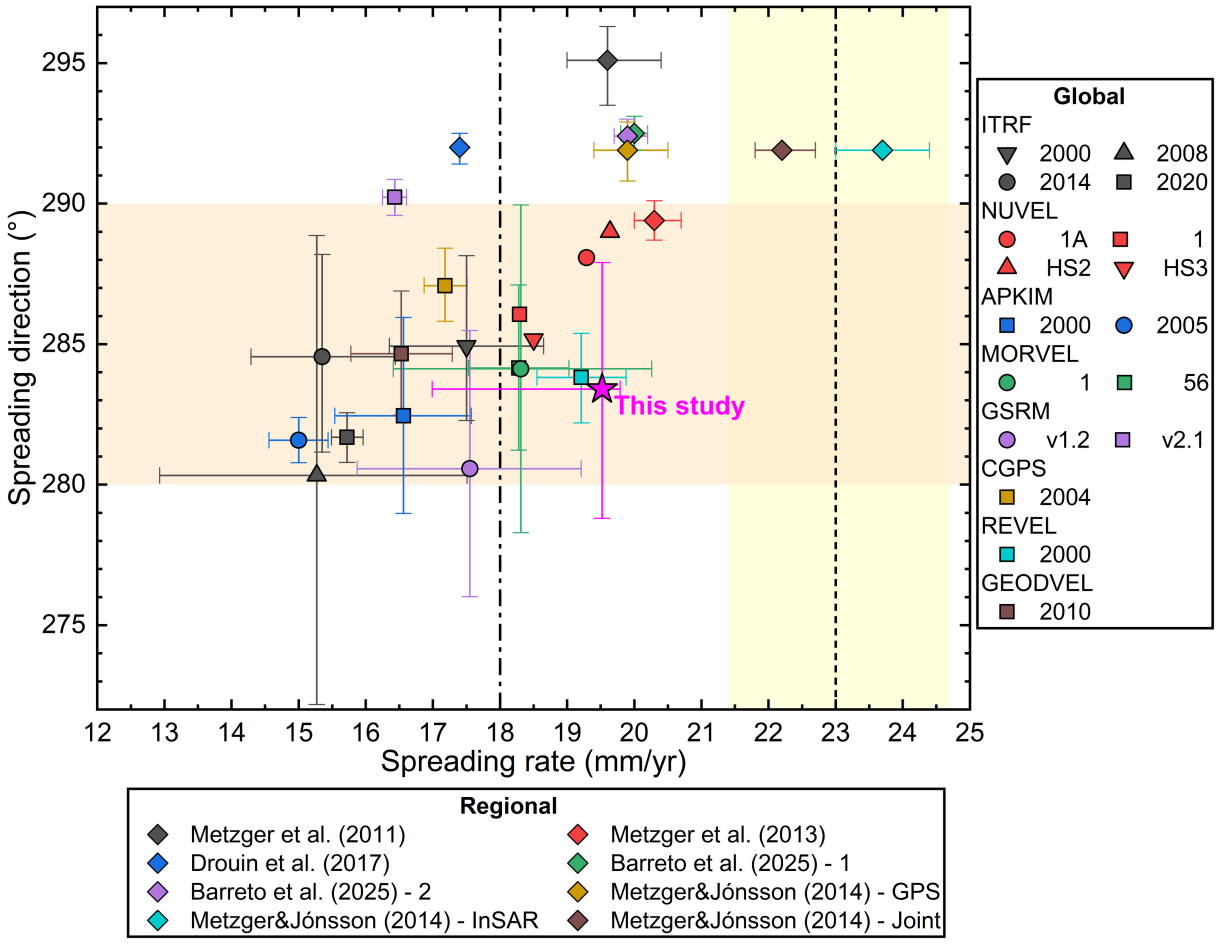


Figure S18. Plate spreading rates and directions in the Krafla volcanic system predicted from different global plate motion models and regional plate boundary models. Krafla caldera center (16.80°W, 65.71°N) is used to calculate the horizontal velocities from the global plate motion models. Thin lines indicate the uncertainties of the model predictions. Shapes without thin lines indicate the corresponding models do not have uncertainty or the uncertainties are too large and thereby omitted. Magenta thin lines for uncertainties of spreading parameters inferred in this study are covered by the star. The vertical dashed and dash-dotted lines are the plate spreading rates from Árnadóttir et al. (2009) and Cao et al. (2023), respectively. The yellow shaded area is the uncertainty of Árnadóttir et al. (2009) spreading rate while the orange shaded area is the range of spreading direction given by Cao et al. (2023). Barreto et al. (2025) has two solutions, depending on whether the Húsavík-Flatey fault is modeled as one or two segment(s). Euler pole location uncertainties are omitted for APKIM2005 and REVEL2000 since they lead to rather large uncertainty in plate spreading. Global models are: ITRF2000 (Altamimi et al., 2002), ITRF2008 (Altamimi et al., 2012), ITRF2014 (Altamimi et al., 2017), ITRF2020 (Altamimi et al., 2023), NUVEL-1 (Argus and Gordon, 1991), NUVEL-1A (DeMets et al., 1994), NUVEL-HS2 (Gripp and Gordon, 1990), NUVEL-HS3 (Gripp and Gordon, 2002), APKIM2000 (Drewes, 1998), APKIM2005 (Drewes, 2009), MORVEL1 (DeMets et al., 2010), MORVEL56 (Argus et al., 2011), GSRMv1.2 (Kreemer et al., 2003), GSRMv2 (Kreemer et al., 2014), CGPS2004 (Prawirodirdjo and Bock, 2004), REVEL2000 (Sella et al., 2002), and GEODVEL2010 (Argus et al., 2010). The global plate motions are calculated with GAGE Plate Motion Calculator (https://www.unavco.org/software/geodetic-utilities/plate-motion-calculator/pla te-motion-calculator.html).

Table S1. Search bounds and initial values of model parameters in the first-step inversion. For each segment, the left and right columns show the lower and upper search bound, respectively, and the central column shows the initial values of parameters (values for the first sample iteration in Bayesian inversion). The longitude of segment S3 is for its southern endpoint, where other segments are connected sequentially by fixing the longitudes of their connecting endpoints. The bounds and values are based on the prior information from previous studies and adjusted through multiple trials of inversions. The reference point of the local Cartesian coordinate system is 16.83°W, 65.67°N.

Parameter	**S1**			**S2**			**S3**		
X-coordinate of the southern endpoint (km)		Fixed			Fixed		0	1.5	3
Strike	-20°	10°	30°	-5°	15°	30°	2°	10°	18°
Locking depth (km)	5.0	6.5	8.0	4.0	6.0	8.0	3.0	4.0	6.0
Spreading direction	280°	289°	300°	275°	288°	293°	275°	290°	295°
Spreading rate (mm/yr)	15	20	25	15	20	25	15	20	25
GIA scaling factor – GNSS	0.0	3.2	6.0	0.0	4.0	6.0	0.0	3.2	6.0
GIA scaling factor – InSAR	0.0	3.2	6.0	0.0	4.0	6.0	0.0	3.2	6.0
Parameter	**S4**			**S5**			**S6**		
X-coordinate of the southern endpoint (km)		Fixed			Fixed			Fixed	
Strike	5°	15°	20°	0°	6°	20°	-15°	-3°	20°
Locking depth (km)	3.0	4.0	6.0	3.0	4.4	7.0	3.0	4.5	7.0
Spreading direction	275°	290°	295°	275°	285°	295°	270°	287°	295°
Spreading rate (mm/yr)	15	20	25	15	20	25	5	20	25
GIA scaling factor – GNSS	0.0	3.2	6.0	0.0	3.2	6.0	0.0	0.1	6.0
GIA scaling factor – InSAR	0.0	3.2	6.0	0.0	3.2	6.0	0.0	0.1	6.0

Table S2. Search bounds and initial values of model parameters in the second-step inversion. The bounds and values are based on the results from the first-step inversion.

Parameter	Lower bound	Initial value	Upper bound
Locking depth S1 (km)	4.0	6.0	7.5
Locking depth S2 (km)	4.0	5.0	7.5
Locking depth S3 (km)	1.0	4.0	6.5
Locking depth S4 (km)	1.0	3.0	6.0
Locking depth S5 (km)	3.0	4.0	6.0
Locking depth S6 (km)	3.0	4.0	6.0
Spreading direction	280°	285°	295°
Spreading rate (mm/yr)	15	20	25
GIA scaling factor – GNSS & InSAR	0.0	3.0	6.0

Table S3. Coordinates of the inferred plate boundary axis. The medians of the marginal PDFs from the first-step inversion are adopted.

Segment	Southern endpoint		Northern endpoint	
	Longitude	**Latitude**	**Longitude**	**Latitude**
S1	16.842°W	65.571°N	16.823°W	65.652°N
S2	16.823°W	65.652°N	18.809°W	65.688°N
S3	16.809°W	65.688°N	16.795°W	65.715°N
S4	16.795°W	65.715°N	16.772°W	65.769°N
S5	16.772°W	65.769°N	16.764°W	65.795°N
S6	16.764°W	65.795°N	16.780°W	65.867°N

References

Árnadóttir, T., Lund, B., Jiang, W., Geirsson, H., Björnsson, H., Einarsson, P. and Sigurdsson, T. (2009). Glacial rebound and plate spreading: results from the first countrywide GPS observations in Iceland. Geophysical Journal International, 177: 691-716. https://doi.org/10.1111/j.1365-246X.2008.04059.x

Árnason, K. (2020). New conceptual model for the magma-hydrothermal-tectonic system of Krafla, NE Iceland. Geosciences, 10(1), 34. https://doi.org/10.3390/geosciences10010034

Altamimi, Z., Métivier, L., & Collilieux, X. (2012). ITRF2008 plate motion model. Journal of Geophysical Research: Solid Earth, 117(B07402). https://doi.org/10.1029/2011JB008930

Altamimi, Z., Métivier, L., Rebischung, P., Collilieux, X., Chanard, K., & Barnéoud, J. (2023). ITRF2020 plate motion model. Geophysical Research Letters, 50(18), e2023GL106373. https://doi.org/10.1029/2023GL106373

Altamimi, Z., Métivier, L., Rebischung, P., Rouby, H., & Collilieux, X. (2017). ITRF2014 plate motion model. Geophysical Journal International, 209(3), 1906–1912. https://doi.org/10.1093/gji/ggx136

Altamimi, Z., Sillard, P., & Boucher, C. (2002). ITRF2000: A new release of the International Terrestrial Reference Frame for earth science applications. Journal of Geophysical Research: Solid Earth, 107(B10), 2214. https://doi.org/10.1029/2001JB000561

Argus, D. F., & Gordon, R. G. (1991). No-net-rotation model of current plate velocities incorporating plate motion model NUVEL-1. Geophysical Research Letters, 18(11), 2039–2042. https://doi.org/10.1029/91GL01532

Argus, D. F., Gordon, R. G., & DeMets, C. (2011). Geologically current motion of 56 plates relative to the no-net-rotation reference frame. Geochemistry, Geophysics, Geosystems, 12(11). https://doi.org/10.1029/2011GC003751

Argus, D. F., Gordon, R. G., Heflin, M. B., Ma, C., Eanes, R. J., Willis, P., Peltier, W. R., & Owen, S. E. (2010). The angular velocities of the plates and the velocity of the Earth's centre from space geodesy. Geophysical Journal International, 180(3), 913–960. https://doi.org/10.1111/j.1365-246X.2009.04463.x

Auriac, A. (2014). Solid Earth response to ice retreat and glacial surges in Iceland inferred from satellite radar interferometry and finite element modelling, Ph.D. thesis, University of Icenad, Reykjavík, Iceland.

Bagnardi, M., & Hooper, A. (2018). Inversion of surface deformation data for rapid estimates of source parameters and uncertainties: A Bayesian approach. Geochemistry, Geophysics, Geosystems, 19, 2194–2211. https://doi.org/10.1029/2018GC007585

Barreto, A., Viltres, R., Matrau, R., Metzger, S., Ófeigsson, B. G., Liu, S., et al. (2025). Interseismic deformation of the Húsavík–Flatey fault (North Iceland) from two decades of GNSS data. Geophysical Journal International, 241, 1663–1679. https://doi.org/10.1093/gji/ggaf106

Cao, Y., Jónsson, S., & Hreinsdóttir, S. (2023). Iceland kinematics from InSAR. Journal of Geophysical Research: Solid Earth, 128, e2022JB025546. https://doi.org/10.1029/2022JB025546

DeMets, C., Gordon, R. G., & Argus, D. F. (2010). Geologically current plate motions. Geophysical Journal International, 181, 1–80. https://doi.org/10.1111/j.1365-246X.2009.04491.x

DeMets, C., Gordon, R. G., Argus, D. F., & Stein, S. (1990). Current plate motions. Geophysical Journal International, 101(2), 425–478. https://doi.org/10.1111/j.1365-246X.1990.tb06579.x

DeMets, C., Gordon, R. G., Argus, D. F., & Stein, S. (1994). Effect of recent revisions to the geomagnetic reversal time scale on estimates of current plate motions. Geophysical Research Letters, 21(20), 2191–2194. https://doi.org/10.1029/94GL02118

Drewes, H. (1998). Combination of VLBI, SLR, and GPS determined station velocities for actual plate kinematic and crustal deformation models. In Geodynamics (pp. 254–259). Springer. https://doi.org/10.1007/978-3-642-72245-5_59

Drewes, H. (2009). The Actual Plate Kinematic and Crustal Deformation Model APKIM2005 as basis for a non-rotating ITRF. In Geodetic Reference Frames (Vol. 134, pp. 95–99). Springer. https://doi.org/10.1007/978-3-642-00860-3_15

Drouin, V., Sigmundsson, F., Ófeigsson, B. G., Hreinsdóttir, S., Sturkell, E., & Einarsson, P. (2017). Deformation in the Northern Volcanic Zone of Iceland 2008–2014: An interplay of tectonic, magmatic, and glacial isostatic deformation. Journal of Geophysical Research: Solid Earth, 122(4), 3158–3178. https://doi.org/10.1002/2016JB013206

Glück, E., Garambois, S., Vandemeulebrouck, J., Muzellec, T., Virieux, J., Mortensen, A. K., et al. (2025). Seismicity patterns and multi-scale imaging of Krafla, N–E Iceland, with local earthquake tomography. Journal of Geophysical Research: Solid Earth, 130, e2024JB030425. https://doi.org/10.1029/2024JB030425

Gripp, A. E., & Gordon, R. G. (1990). Current plate velocities relative to the hotspots incorporating the NUVEL-1 global plate motion model. Geophysical Research Letters, 17(8), 1109–1112. https://doi.org/10.1029/GL017i008p01109

Gripp, A. E., & Gordon, R. G. (2002). Young tracks of hotspots and current plate velocities. Geophysical Journal International, 150(2), 321–361. https://doi.org/10.1046/j.1365-246X.2002.01627.x

Kreemer, C., Blewitt, G., & Klein, E. C. (2014). A geodetic plate motion and global strain rate model. Geochemistry, Geophysics, Geosystems, 15(10), 3849–3889. https://doi.org/10.1002/2014GC005407

Kreemer, C., Holt, W. E., & Haines, A. J. (2003). An integrated global model of present-day plate motions and plate boundary deformation. Geophysical Journal International, 154(1), 8–34. https://doi.org/10.1046/j.1365-246X.2003.01917.x

Lanzi, C., Sigmundsson, F., Parks, M. M., Geirsson, H., & Drouin, V. (2024). Strain localization at volcanoes undergoing extension: Investigation of long-term deformation at Krafla and Askja volcanic systems in North Iceland. Geophysical Research Letters, 51, e2024GL110299. https://doi.org/10.1029/2024GL110299

McKay, M. D., Beckman, R. J., & Conover, W. J. (1979). A Comparison of Three Methods for Selecting Values of Input Variables in the Analysis of Output from a Computer Code. Technometrics, 21(2), 239–245. https://doi.org/10.2307/1268522

Metzger, S., & Jónsson, S. (2014). Plate boundary deformation in North Iceland during 1992–2009 revealed by InSAR time-series analysis and GPS. Tectonophysics, 634, 127–138. https://doi.org/10.1016/j.tecto.2014.07.027

Metzger, S., Jónsson, S., & Geirsson, H. (2011). Locking depth and slip-rate of the Húsavík Flatey fault, North Iceland, derived from continuous GPS data 2006–2010. Geophysical Journal International, 187(2), 564–576. https://doi.org/10.1111/j.1365-246X.2011.05176.x

Metzger, S., Jónsson, S., Danielsen, G., Hreinsdóttir, S., Jouanne, F., Giardini, D., et al. (2013). Present kinematics of the Tjörnes Fracture Zone, North Iceland, from campaign and continuous GPS measurements. Geophysical Journal International, 192, 441–455. https://doi.org/10.1093/gji/ggs032

McKay, M. D., Beckman, R. J., & Conover, W. J. (1979). A Comparison of Three Methods for Selecting Values of Input Variables in the Analysis of Output from a Computer Code. Technometrics, 21(2), 239–245. https://doi.org/10.2307/1268522

Prawirodirdjo, L., & Bock, Y. (2004). Instantaneous global plate motion model from 12 years of continuous GPS observations. Journal of Geophysical Research: Solid Earth, 109, B08405. https://doi.org/10.1029/2003JB002944

Sella, G. F., Dixon, T. H., & Mao, A. (2002). REVEL: A model for recent plate velocities from space geodesy. Journal of Geophysical Research: Solid Earth, 107(B4), ETG 11-1–ETG 11-30. https://doi.org/10.1029/2000JB000033

Sudhaus, H., & Jónsson, S. (2009). Improved source modelling through combined use of InSAR and GPS under consideration of correlated data errors: Application to the June 2000 Kleifarvatn earthquake, Iceland. Geophysical Journal International, 176(2), 389–404. https://doi.org/10.1111/j.1365-246X.2008.03989.x

Wang, C., Chang, L., Wang, X.-S., Zhang, B., & Stein, A. (2024). Interferometric synthetic aperture radar statistical inference in deformation measurement and geophysical inversion: A review. IEEE Geoscience and Remote Sensing Magazine, 12(1), 8–35. https://doi.org/10.1109/MGRS.2023.3344159